Localising the gamma-ray emission in Flat Spectrum Radio Quasars and an extragalactic population study for the Cherenkov Telescope Array

ATREYA ACHARYYA

Localising the gamma-ray emission in Flat Spectrum Radio Quasars and an extragalactic population study for the Cherenkov Telescope Array

Atreya Acharyya

A thesis presented for the degree of

Doctor of Philosophy

Centre for Advanced Instrumentation

The University of Durham

United Kingdom

September 2021

Localising the gamma-ray emission in Flat Spectrum Radio Quasars and an extragalactic population study for the Cherenkov Telescope Array

Atreya Acharyya

Abstract

This thesis is concerned with localising the gamma-ray emission region in Flat Spectrum Radio Quasars (FSRQs) and assessing the extragalactic source populations that will be detectable with the Cherenkov Telescope Array (CTA).

An analysis of the gamma-ray flux from the nine brightest FSRQs detected with the *Fermi*-Large Area Telescope (LAT) during its first 8 years of operation is undertaken. Three different methods are employed to constrain the location of the emission region during identified flare periods, namely, measuring the shortest variability timescales, searching for evidence of a cut-off in the spectra and investigating the energy dependence in cooling timescales. Monte Carlo simulations are then implemented to constrain the very high energy (VHE) photon emission from the sample during the entire observation period. The combined findings of all the approaches suggest that the gamma-ray emission in the brightest FSRQs originates in multiple compact emission regions throughout the jet, within both the broad-line region and the molecular torus.

The remainder of this thesis describes a detailed investigation of the extragalactic AGN sources that will be detectable with the CTA when in operation. The spectra from a sample of 1551 *Fermi*-LAT detected AGN having a known redshift measurement are extrapolated to the energy range 30 GeV - 200 TeV and the detection significance for each source is obtained using the anticipated instrument response of the CTA. The results reveal that the CTA will detect over 300 sources in 20 hours of observation and a list of promising candidates from each AGN class is presented. The improved statistics will allow a range of scientific topics to be explored including obtaining a reliable estimate of the luminosity function in the VHE regime for the first time. A preliminary evaluation of the evolutionary parameters using the expected CTA blazar source count distributions is discussed in this thesis.

Supervisors: Prof. Paula M. Chadwick and Prof. Anthony M. Brown

Acknowledgements

My four year journey towards a PhD has been the most enriching, illuminating and pleasurable experience I have ever undertaken. A number of people are responsible for this and I shall try my best to thank all of them here.

I couldn't possibly start anywhere other than my supervisors, Prof. Paula Chadwick and Prof. Anthony Brown. You not only gave me the opportunity of doing this despite my lack of experience in gamma-ray astronomy, but also believed in me and encouraged me every step of the way. Among many other things, you taught me to always ask questions, try to explain things in the simplest way possible and never to be afraid of being wrong because "that's how we learn!". These lessons helped me overcome the challenges I faced during the PhD and will remain with me always and forever.

A special thanks should also go to Dr. Cameron Rulten. You taught me a lot about transitioning to postgraduate research in my early days, have always answered my numerous questions in an approachable manner and helped me set up my simulations on the Hamilton supercomputer.

I now move on to the amazing people I have had the pleasure of sharing an office with: Dr. Jamie Graham, Dr. Sheridan Lloyd and no doubt soon to follow, Max Harvey and Alberto Rosales de León. You have all made coming in to work everyday something I have genuinely looked forward to. It has been my absolute pleasure discussing physics ideas and papers, spending time at conferences and socialising together at the pub (after work of course!). I have learned so much from each of you, feel privileged to have formed friendships I will always cherish and am sure we will always remain close together over the coming years.

I also want to thank the people in the CTA Consortium I have had the pleasure of collaborating with for the Extragalactic population study: Tarek Hassan, Jean-Philippe Lenain and Santiago Pita. Thanks a lot for teaching me so much about our project and also experience

first hand how rewarding it can be to share ideas and work together as a team. I am also grateful to you for the opportunity to present my first ever plenary talk at the CTA Consortium meeting in October 2020.

I genuinely believe everyone we meet during the course of our lives teaches us valuable lessons and make us the people we turn out to be. So if you are reading this now and I have met you at some point, thank you from the bottom of my heart. It is impossible to name all the people I want to thank but, in no particular order, special mention to Callum, Jack, Kish, Mathew, Scott (and the entire Young family), Sirdas, Tom C, Tom W, Vincent, Will FB and Yue. I would also like to thank all the wonderful folks I met at the *Fermi* summer school, the amazing young men I have had the pleasure of mentoring at Castle and of course all the students I have been privileged to interact with at tutorials, workshops and drop-ins.

That just leaves me with the people I am most grateful for and without whom I would not be here today: Mum, Dad, both my uncles and all four of my grandparents (Ma, Baba, Babji, Roni, Aa-dadu, D-dadu, Nano and Attama). Whatever I have accomplished so far and will do in the future is for you, with you and because of you. My one goal in life is to make you as proud of me as I am of you. Thank you for all your love and support these 27 years. Love you to the farthest galaxy and back.

Audere est Facere

To my grandparents

Contents

Declaration

The work in this thesis is based on research carried out at the Centre for Advanced Instrumentation, Department of Physics, University of Durham, England. No part of this thesis has been submitted elsewhere for any other degree or qualification, and it is the sole work of the author unless referenced to the contrary in the text.

Some of the work presented in this thesis has been published in journals and conference proceedings - the relevant publications are listed below.

Publications

Chapter 3: Acharyya, A., Chadwick, P. M., & Brown, A. M. (2020). Locating the gamma-ray emission region in the brightest Fermi-LAT flat-spectrum radio quasars. Monthly Notices of the Royal Astronomical Society,500(4)

Chapter Header Images

For aesthetic reasons a header image has been placed at the start of each chapter. The captions for these are as follows:

Active Galactic Nuclei: *An artist's representation of the central regions of an AGN. Credit: NASA/Goddard Space Flight Center Conceptual Image Lab (*https://imagine.gsfc.nasa.gov*, accessed on 29/07/2020).*

Spaced based gamma-ray astronomy: *An artist's impression of the Fermi Gamma-ray Space Telescope in orbit. Credit: NASA/Goddard Space Flight Center (*https://fermi.gsfc.nasa.gov*, accessed on 28/10/2020).*

Locating the gamma-ray emission region in the brightest *Fermi*-LAT Flat Spectrum Radio Quasars: *An artist's impression of the Flat Spectrum Radio Quasar 3C 279. Credit: ESO/M. Kornmesser (*https://www.eso.org/public/images/eso1229a*, accessed on 28/10/2020).*

Ground-based gamma-ray astronomy: *An artist's representation of the Cherenkov Telescope Array, hit by an air shower produced by cosmic rays. Credit: DESY/Milde Science Communication (*https://www.desy.de*, accessed on 25/08/2020).*

Extragalactic source population studies for the CTA: *An artist's rendering of the three types of telescopes planned for CTA South at Paranal Observatory, Chile. Credit: CTA/M-A. Besel/IAC (G.P. Diaz)/ESO (*https://www.eso.org/public/images/eso1841a/*, accessed on 27/11/2020).*

Summary and Future work: *The LST-1, one of the four LSTs of the CTA Northern array located on the existing site of the Roque de los Muchachos Observatory in La Palma, Spain. Credit: Tomohiro Inada, CTAO (*https://www.appec.org/news/cta-prototype-lst-1-detects-very-high-energyemission-from-the-crab-pulsar*, accessed on 16/02/2021).*

List of Figures

List of Tables

3.5 Results of the LCCF study between the 0.1 - 1 GeV and the 1 - 300 GeV lightcurves during the flare periods. This includes the times corresponding to the peaks of the Gaussian fit along with the associated uncertainties and their significance in percentile derived from Monte Carlo simulations. The final two columns list the spectral slopes, β where the power spectral density PSD $\propto \nu^{-\beta}$, of the original lightcurves and the mean and 95% confidence intervals of the simulated lightcurves respectively. 114

3.6 The average flux and test statistic (TS) values (see equation 3.1) obtained from a likelihood analysis of the eight year (MJD 54682.66 - MJD 57604.66) *Fermi*-LAT observations of each source above an energy threshold of $E_\gamma \geq 20$ GeV, $E_\gamma \geq 50$ GeV and $E_\gamma \geq 100$ GeV respectively. Only sources having a TS $\geq$ 10 in each energy range are shown. 121

3.7 Summary of the results from the different methods used to constrain the location of the emission region for both flare periods from each source investigated in this work. These methods are the measurement of the shortest variability timescales for the flare periods, the search for evidence of a cut-off in the flare spectra and an investigation into energy dependence in cooling timescales. The final column lists whether the VHE ($E_\gamma \geq 20$ GeV) photon emission observed with the *Fermi*-LAT is compatible with BLR origin. Inconclusive results are due to the flare spectra favouring neither a power law nor a log parabolic model or due to the lack of statistics at high energies preventing obtainment of LCCFs. Multi-zone indicates evidence of multiple emission regions but no physical constraints on the location. 122

Chapter 1

Active Galactic Nuclei

Active Galactic Nuclei (AGN) are compact objects, found in the central regions of some galaxies, having a luminosity much higher than expected solely due to the stars accompanying them. Some of the most extreme phenomena in the Universe, AGN emit energy over many orders of magnitude in frequency from the radio to the gamma-ray end of the electromagnetic spectrum.

Furthermore, AGN are often found to exhibit variability on daily and even hourly timescales indicating that the large energy output comes from extremely small regions. It is believed that AGN are powered by the accretion of surrounding matter into a central supermassive black hole (SMBH) and the extreme energies are attributed to the acceleration of these particles due to relativistic jets.

This chapter begins with a brief historical overview of the discovery of AGN before proceeding to a study of the current AGN model and unification theories and concludes with a discussion on the gamma-ray emission and absorption mechanisms in AGN. The

objective of this chapter is also to set the scene for later chapters in which the location of the gamma-ray emission regions as well as the potential of future AGN surveys are studied in detail.

1.1 Historical Context

The study of AGN has spanned over a century and advancements in technology have led to a remarkable improvement in the sensitivity, angular and spectral resolution across the electromagnetic spectrum. This has also coincided with an enhanced understanding of the underlying physics, in particular quantum mechanics and relativity, which has aided the interpretation of these observations.

It had been believed at the start of the 20^{th} century that the emission from galaxies was simply the aggregate of emission from the stellar objects. This conventional view was first challenged by Fath (1909) whose spectroscopic observations of the spiral galaxy NGC 1068 revealed a discontinuous spectrum with "both bright and absorption lines". This is believed to be the first documented observation of an AGN and was later investigated by Slipher (1917) who found evidence of the emission over a range of wavelengths. The presence of a central gravitational engine was first suggested by Seyfert (1943) in a study of 6 galaxies which indicated the presence of highly-ionised emission lines with varying levels of broadening, thought to be a consequence of gas moving at high velocities.

The advancements of radio astronomy, in particular the seminal papers of Karl Jansky (for example Jansky (1933)), subsequent sky surveys (for example Reber (1944)) and the identification of multiple radio sources (for example Ryle and Smith (1948), Ryle et al. (1950), Smith (1951)) played a crucial role in the study of AGN. Among the other important discoveries over the next decade was the observed structure in Cygnus A, a bright radio source resolved to two separate lobes (Jennison and Das Gupta (1953)), the suggestion of synchrotron radiation as the source of the radio emission (Burbidge (1956)) and the publication of the third Cambridge (3C) survey (Edge et al. (1959), Bennett (1962))

providing the accurate positions of many more radio sources along with, in some cases, their optical counterparts.

AGN were by then being observed at different wavelengths. A major breakthrough came as a result of contemporary studies of 3C 48 (Matthews and Sandage (1963)) and 3C 273 (Hazard et al. (1963)) which revealed broad emission lines at previously unfamiliar wavelengths. This conundrum was solved six weeks later in the adjoining papers published in *Nature* (Schmidt (1963), Oke (1963), Greenstein (1963)) suggesting the sources were both extragalactic and the large redshifts a consequence of Hubble expansion.

The next mystery was finding the origin of the extreme energies observed in AGN towards which Hoyle and Fowler (1963) suggested the idea of a supermassive star. This then led to the first proposals of the accretion of matter onto a SMBH as the source of the emission (Salpeter (1964), Zel'dovich and Novikov (1964)). Lynden-Bell (1969) took this idea further and argued that different black hole masses and accretion rates might explain the observed phenomenon in a variety of AGN from quasars to Seyfert galaxies (see Section 1.2.2).

3C 273, by then categorised as a "quasi-stellar object" (QSO; Burbidge and Burbidge (1969)), also showed optical and radio variability (Smith and Hoffleit (1963), Dent (1969)). The observed rapid variability in radio sources led to the suggestion of relativistic motion and the associated beaming effects being a dominant factor in the emission (Rees (1966)). This was also supported in Hoyle (1966) who noted the possibility of Inverse Compton (IC) scattering of photons by relativistic electrons to higher energies. Further confirmation of relativistic effects came through the apparent superluminal (faster than light) velocities observed in such objects (for example Cohen et al. (1971)).

The study of AGN has continued to progress through the following decades and the evidence, put together, favours models which invoke the presence of a SMBH (Rees (1984)). There are still many unanswered questions especially in relation to the geometry of the emission regions and the acceleration mechanisms involved. This thesis attempts to study some of these questions among AGN using observations in the gamma-ray regime.

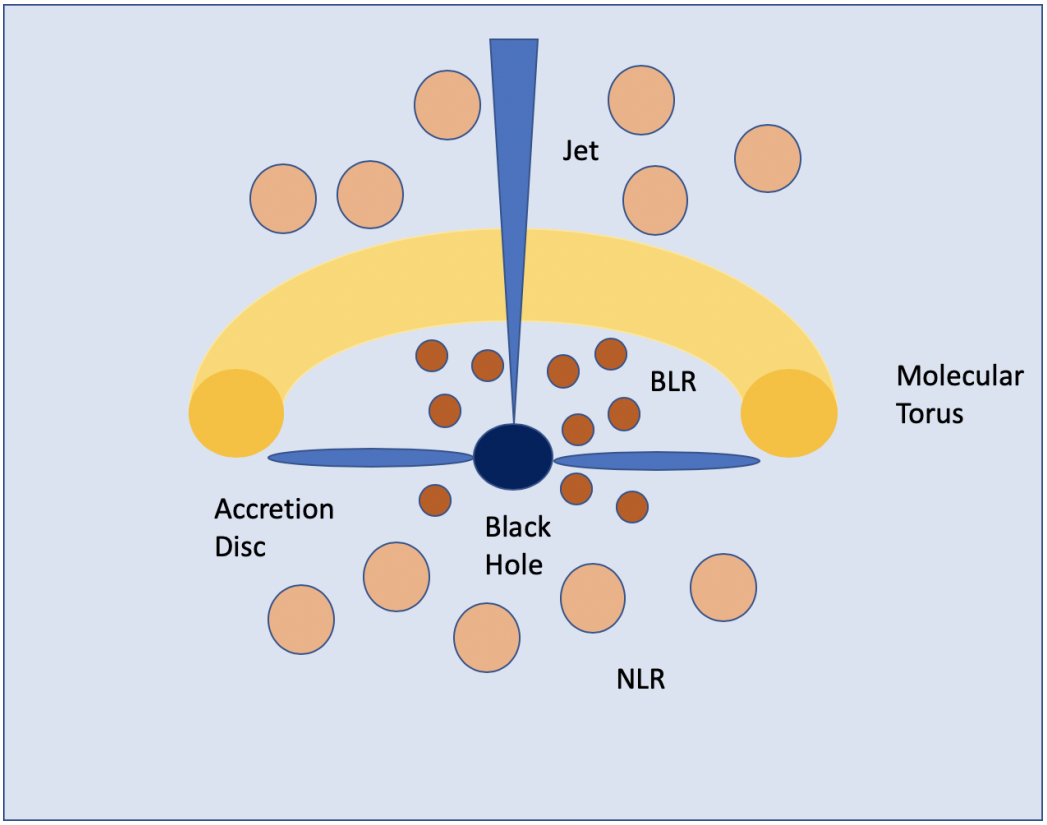

Figure 1.1: A schematic of the main features of an AGN based on the current model.

1.2 AGN: Current Model, Taxonomy and Unification

1.2.1 Current Model

The current accepted model for AGN was proposed by Urry and Padovani (1995) and is shown in Figure 1.1. AGN are believed to contain a central SMBH having mass of the order of $10^6 - 10^9 M_\odot$ and powered by the surrounding accretion disc. The accretion disc is formed from gas falling into the central nucleus while losing its angular momentum as a result of viscous forces. A consequence of Kepler's third law, the inner regions of the accretion disc rotate at a faster velocity than the outer regions producing a large amount of friction between the particles. This friction can result in the gas heating up and emitting thermal radiation at longer wavelengths while also self-sustaining the accretion of matter through the transport of angular momentum out of the system.

In some AGN, collimated outflows of relativistic particles in the form of jets, first detected by Curtis (1918) and proposed by Blandford and Rees (1974), are present and transport mass, momentum, energy and magnetic flux to Mpc scale distances. The physical mechanisms responsible for the origin of jets are not yet fully understood. The Blandford-Znajek mechanism (Blandford and Znajek (1977)) suggests the acceleration is powered by the rotational energy of the SMBH and that strong magnetic field lines within the accretion flow get wound up by the rotating central engine, leading to the formation of magnetically dominated jets.

The physical structure of the jet depends on the balance between the internal and external pressure, and therefore is linked to the properties of the plasma (Romero et al. (2017)). Studies of the radio galaxy M87 (Asada and Nakamura (2012); Potter and Cotter (2013)) have found evidence of a parabolic, magnetically dominated accelerating base transitioning into a conical, kinetically dominated structure which slowly decelerates due to interacting with the surroundings.

For example in the Potter and Cotter (2013) model, a magnetic pressure gradient causes the magnetic energy to be converted to kinetic energy. The plasma within the jet is accelerated until an equipartition is reached between the magnetic and particle energies. At this point the bulk Lorentz factor of the jet reaches its maximum value and the jet transitions from parabolic to conical geometry (McKinney (2006)).

The physical properties of the jet can be modelled using the Lorentz factor, Γ, an intrinsic parameter describing the speed of the jet flow. The Lorentz factor can be calculated from the Doppler factor of the jet and the apparent speed of the jet, determined using combined X-ray and Very Long Baseline Interferometry (VLBI) observations (for example Jorstad et al. (2005), Piner et al. (2007)).

The accretion disc, in addition to continually feeding the SMBH, is also the source of the continuum emission needed to maintain the two distinct populations of dense gas clouds - the broad line region (BLR) and the narrow line region (NLR) surrounding it. The BLR and NLR are distinguished by the width of their emission lines, suggested to be a

consequence of differential Doppler broadening (Krolik (1999)). The BLR gives rise to the broad emission lines observed in some AGN and the close proximity to the central engine results in the gas clouds in the BLR, with electron densities up to $N_e \sim 10^9$ being hotter and denser than those in the NLR, believed to have $N_e \sim 10^2 - 10^6$ (Peterson (2006)).

The radius of the BLR can be observationally measured by reverberation mapping (for example Blandford and McKee (1982), Kaspi et al. (1996)). This technique measures the size of the BLR by using cross correlation studies to determine the time delays between the variations in the continuum flux arising from in the vicinity of the accretion disk and the variations in the flux of the broad emission lines.

The molecular torus (MT), composed primarily of dust, extends to parsec scale distances and obscures the central regions when viewed from certain angles (Krolik and Begelman (1988)). Some of the ultra-violet (UV) radiation emitted from the inner regions of the AGN is believed to be absorbed by the MT and re-emitted in the infrared resulting in an observed bump seen in some AGN spectra. The MT has also been invoked to explain the anisotropic distribution of emission features observed in some AGN and is a pivotal component in AGN unification models (see Section 1.2.3).

The emission region in jets can be modelled using either single-zone or multi-zone models. Single-zone models consider a single, homogeneous emission region and have been successfully applied to describe the Spectral Energy Distribution (SED) of blazars (for example Ghisellini et al. (1998), Böttcher and Chiang (2002)), using a relatively small number of free parameters. However, one-zone models have been unable to fully reproduce the rapid flare events and correlations between data at different frequencies observed in some AGN (for example Begelman et al. (2008), Costamante et al. (2009)).

This has led to proposals invoking the presence of multi-zone emission. These models assume multiple compact emission regions moving relativistically within the reference frame of the jet, resulting in large Doppler factors of the jet, as seen in the observers frame. The rapid variability can be explained by assuming that the emission is produced within compact recollimated turbulent cells (for example Bromberg and Levinson (2009))

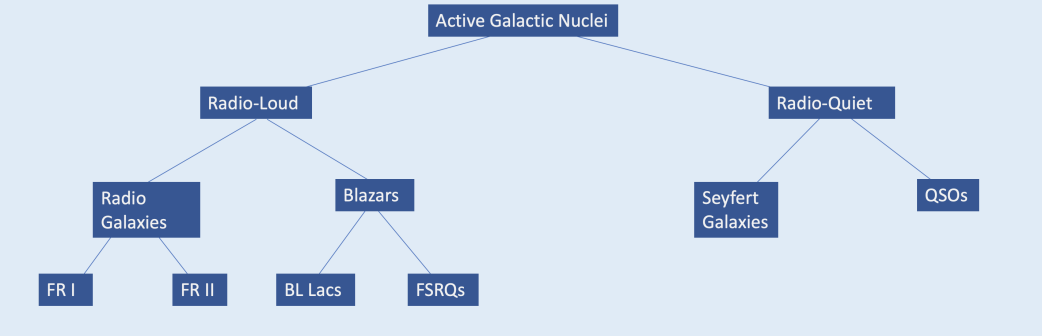

Figure 1.2: Family tree of the AGN classification scheme.

or plasmoids produced from magnetic reconnection events (for example Giannios (2013)).

Bromberg and Levinson (2009) demonstrate that radiative cooling can lead to reconfinement of the outflow in extremely compact regions, capable of producing rapid variability at large distances from the SMBH via reflections of the converging recollimation shock. Giannios (2013) propose a "jets-in-a-jet" model and show that if a large fraction of the Poynting flux luminosity gets magnetically dissipated through reconnection, the outflow can efficiently power observed AGN flares in the TeV regime. The location of the emission region(s) in AGN is investigated in Chapter 3.

1.2.2 Taxonomy

The diverse nature of the observational and spectral properties of AGN has resulted in a wide range of classification summarised in Figure 1.2. AGN can be categorised on the basis of their radio-loudness, R, defined as the ratio of the radio to the optical flux densities as either radio-loud or radio-quiet. Further levels of classification can be made based on the angle between the line of sight of the observer and the source as well as the width of the observed emission lines.

Radio Galaxies

Radio galaxies are typically elliptical galaxies having strong radio brightness and are often accompanied by the presence of extended jets. Fanaroff and Riley (1974) classified radio galaxies on the basis of morphology into two subcategories known as FR I and FR II

respectively, with FR I sources being less luminous than FR II sources. Furthermore, while FR I sources have their peak brightness near the central regions, the radio emission in FR II galaxies is dominated in regions within the outer lobe of the jets.

Blazars

Blazars are a subset of AGN having jets closely orientated to our line-of-sight, leading to bright emission across the electromagnetic spectrum. Arguably the most interesting group of sources, blazars also exhibit rapid variability and high optical polarisation. The small angle to our line-of-sight also results in strongly Doppler boosted emission making blazars a prime candidate in the study of high energy phenomena.

Blazars are further grouped into two main subcategories: BL Lacs and Flat spectrum radio quasars (FSRQs). The key difference is that unlike BL Lacs which exhibit featureless optical spectra, FSRQs have strong broad emission lines (Padovani (2007)). Despite dominating the extragalactic sky at high energies, the close orientation of the jet to the line-of-sight renders the resolution of structures within the jet difficult, and consequently uncovering the location and origin of the emission in blazars remains one of the most active areas of research. This open question is investigated in Chapter 3 where I present a study of some of the brightest FSRQs with the aim of determining the location of the gamma-ray emission region.

Seyfert Galaxies

Unlike the radio-loud sources described previously, the AGN in Seyfert galaxies have relatively low luminosity making the host galaxy easily detectable. Distinguished from other AGN by the presence of strongly ionised emission lines (Peterson (1997)), Seyfert galaxies are subdivided into two groups: Seyfert 1 and Seyfert 2 galaxies (Khachikian and Weedman (1974)). The spectra of Seyfert 1 galaxies show both broad and narrow emission lines while those of Seyfert 2 galaxies contain only narrow emission lines. The broad and narrow emission lines are believed to originate in gas clouds within the BLR and NLR respectively (see Section 1.2.1).

QSOs

Radio-quiet QSOs show similar observational properties to Seyfert galaxies with the only major difference being the absence of stellar absorption lines. This overlap has led to the suggestion that the two form a continuous sequence in luminosity and are a result of the same phenomenon (see Weedman (1976) for a detailed discussion).

1.2.3 Unification

As discussed previously, it is believed that the observational properties of AGN are strongly linked to the angle to our line-of-sight. This is the main motivation behind the schemes for AGN unification (Antonucci (1993), Urry and Padovani (1995)). Unification models can be classified as either strong or weak based on the number of allowed fundamental parameters with strong models requiring fewer parameters and attributing the majority of the observational differences to differences in orientation.

The diverse AGN presented in Section 1.2.2 can be unified by the following arguments (Urry and Padovani (1995), Peterson (1997)):

- Seyfert galaxies and quasars differ primarily in the luminosity of the central source.
- Seyfert 1 and Seyfert 2 galaxies are phenomenologically the same source with the only difference being the favourable line-of-sight of Seyfert 1 galaxies.
- Similarly for radio-loud AGN, blazars (unlike radio galaxies) are closely aligned to our line-of-sight leading to the strongly beamed bright emission observed.
- Furthermore, among blazars, both BL Lacs and FSRQs exhibit rapid variability, strong continuum emission and mainly differ in the presence of strong emission lines in the case of FSRQs.

While this unification scheme has been largely evidenced by observations, there still remain some unanswered questions. For example, unified models of radio-loud and radio-quiet AGN (for example Scheuer and Readhead (1979)) have yet to fully explain the observed properties. There is also evidence that some Seyfert 2 galaxies may not contain an obscured

BLR (Tran (2001)), suggesting that not all the differences are a consequence of orientation alone. Nevertheless, the Urry and Padovani (1995) model remains the generally accepted model for AGN and will be taken as standard for the purpose of this thesis.

1.3 Gamma-rays from AGN

Gamma-rays are the most energetic form of electromagnetic radiation and can be defined as the energy band corresponding to photons having energies $E_\gamma \geq 100$ keV (Longair (2011)). The study of gamma-ray astronomy allows us to understand the physics of the extreme environments in space, for example AGN, responsible for the acceleration of particles to such high energies. Furthermore, unlike cosmic rays, gamma-rays being neutral particles do not suffer from deflections due to strong magnetic fields in the Galaxy and can be traced back to their source. It is believed that cosmic rays and gamma-rays have the same origin for some objects and therefore gamma-rays also help trace the source of cosmic ray acceleration.

1.3.1 Gamma-ray production

In general, gamma-ray production in AGN is a result of either electromagnetic interactions or hadronic acceleration. An illustration of some examples of the electromagnetic production processes is given in Figure 1.3.

1.3.1.1 Electromagnetic interactions

Synchrotron radiation

Synchroton radiation occurs when a charged particle, for example an electron, is deflected by the presence of a magnetic field. As shown in Figure 1.3, if the charged particle has a component of motion perpendicular to the direction of the magnetic field, a Lorentz force correction causes gyration about the field lines. Under the resulting constant acceleration and energy loss, momentum is conserved by the charged particle emitting a beamed cone of

highly polarised emission. Synchroton radiation is responsible for the majority of the non-thermal emission and in particular the X-ray emission from AGN. The term non-thermal emission is conventionally used in astronomy to refer to continuum emission having a non-Maxwellian energy spectrum (Longair (2011)).

Bremsstrahlung

The term Bremsstrahlung, coined by Nikola Tesla in the 1880s, comes from the German word for 'braking radiation' (Longair (2011)). It occurs when a charged particle, for example an electron, is deflected by the strong electric field of an atomic nucleus as seen in Figure 1.3. Energy is conserved by the emission of radiation and the energy released is proportional to the deceleration of the charged particle. In the context of high-energy astronomy, Bremsstrahlung interaction is believed to be responsible for the diffuse gamma-ray emission near the Galactic centre (Yusef-Zadeh et al. (2013)). Furthermore, as will be seen in Chapter 4, this process also produces secondary photons in the development of air showers within the atmosphere.

Inverse Compton Scattering

Inverse Compton (IC) scattering refers to the interaction of an unbound high energy electron with a lower energy photon. Physically the same as Compton scattering, in which case the photon has higher energy than the electron, IC scattering results in the photon being boosted to higher energies and is thought to be the dominant mechanism for the production of gamma-rays in astrophysical sources like AGN (Weekes (2003)). Compton scattering also forms the basis of the detectors used in Compton telescopes, for example *COMPTEL* aboard the Compton Gamma Ray Observatory (*CGRO*; see Section 2.1.2).

In the rest frame of the electron, the energy of the scattered photon after IC interaction, $E_{\text{scattered}}$, is given by the following equation derived from conservation of energy and momentum considerations:

$$E_{\text{scattered}} \approx \gamma E_{\text{primary}}(1 + \beta\cos\theta) \tag{1.1}$$

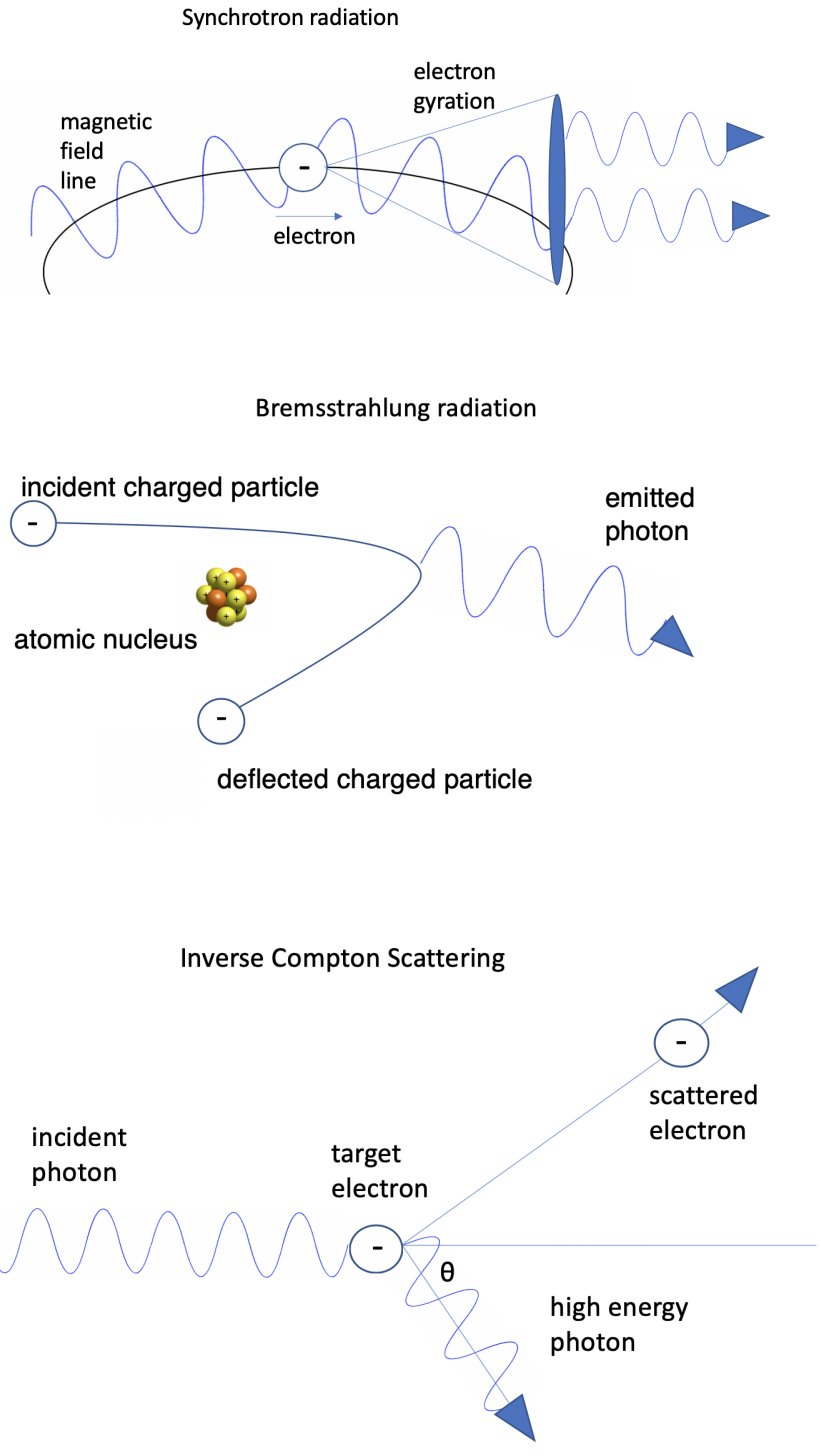

Figure 1.3: Examples of the electromagnetic processes responsible for the production of gamma-rays in AGN, namely, Synchrotron radiation (top), Bremsstrahlung radiation (middle) and Inverse Compton scattering (bottom).

where E_{primary} is the energy of the incident photon, γ is the Lorentz factor for the electron, $\beta = \frac{v}{c}$ is the velocity of the electron divided by the speed of light and θ the scattering angle. When transferred back to the observer's frame, this implies the energy gain of the photon is proportional to γ^2.

Synchrotron Self Compton model

Synchrotron radiation is often believed to act as a precursor to gamma-ray emission at high energies. Under the Synchrotron Self Compton (SSC) model, the photons emitted through synchrotron emission are believed to be up-scattered by IC interactions with the same electron population that produced them.

1.3.1.2 Hadronic interactions

Gamma-rays can also be produced through hadronic processes, for example the interaction of a high energy proton with matter, which results in both charged and neutral pions. The neutral pions can decay into gamma-rays through the following mechanisms:

$$\pi^0 \longrightarrow \gamma\gamma; \pi^0 \longrightarrow \gamma + e^+ + e^- \tag{1.2}$$

It is believed that pion decay is the main source of the diffuse very high energy emission from the Galactic plane (Abramowski et al. (2014)).

1.3.2 Gamma-ray absorption and attenuation

Having discussed the main mechanisms responsible for the production of gamma-rays in AGN, I now present some processes by which gamma-rays may be absorbed and attenuated.

1.3.2.1 Pair production processes

One of the most important energy loss mechanisms in high energy astronomy, pair production can occur when gamma-rays interact with lower energy photons. This occurs when

the two interacting photons have a total energy greater than the rest mass of two electrons, $E_{\gamma+\gamma} > 2m_e c^2$, where m_e is the mass of an electron and c is the speed of light. This interaction results in the gamma-ray being completely annihilated and produces an electron positron pair:

$$\gamma + \gamma \longrightarrow e^+ + e^- \tag{1.3}$$

A similar interaction can occur when a gamma-ray photon interacts with matter within the field of atomic nuclei:

$$\gamma + \text{nucleus} \longrightarrow e^+ + e^- + \text{nucleus} \tag{1.4}$$

Pair production generally occurs in regions of high photon density, for example inside the BLR in AGN as will be discussed in Chapter 3. It is also responsible for the attenuation of gamma-rays from distant sources due to interaction with the Extragalactic Background Light (EBL). Furthermore, when gamma-rays enter the Earth's atmosphere, they interact with atmospheric nuclei to produce electron positron pairs which ultimately give rise to electromagnetic air showers. The study of these air showers forms the basis of the observational techniques used in ground-based gamma-ray astronomy and is discussed in Chapter 4.

1.3.2.2 Extragalactic Background Light

The Extragalactic Background Light (EBL) is the cosmic diffuse radiation mainly composed of the emission from stars throughout the entire history of our Universe (Inoue et al. (2014)). There is also evidence to suggest additional contributions from accretion processes in AGN (Shankar et al. (2016)). Furthermore, Murase and Beacom (2012) reported an excess in the $E_\gamma > 100$ GeV regime which could be explained by dark matter particle decay. The Spectral Energy Distribution (SED) of EBL emission is characterised by a double peak; the first peak is at optical and UV wavelengths due to star formation processes, while the

second peak is at longer wavelengths, such as near infrared, due to the re-emission of these photons after absorption by interstellar dust.

Put together, the EBL comprises the second most energetic radiation field in the Universe after the cosmic microwave background, thereby making an improved understanding and measurement of the EBL crucial. The direct measurement of the EBL using photometry is hindered by the strong foreground due to zodiacal light, as well as light from our own Galaxy (for example Arendt et al. (1998)) while lower limits on the EBL obtained from deep galaxy surveys (for example Madau and Pozzetti (2000), Keenan et al. (2010), Driver et al. (2016)) suffer from systematic uncertainties due to cosmic variance (Somerville et al. (2004)).

Modelling the EBL therefore requires the use of multiple complementary strategies which have been categorised into four different classes (see Domínguez et al. (2011) for a detailed discussion):

- Forward evolution models, which begin with the initial conditions at the start of the Universe and then extrapolate forwards using semi-analytical models of galaxy formation (for example Gilmore et al. (2012)).
- Backward evolution models, which take local galaxy data and extrapolate to higher redshifts i.e. back in time (for example Franceschini et al. (2008)).
- Inferred evolution of galaxy populations from star formation processes (for example Finke et al. (2010)).
- Evolution of galaxy populations based on measured broadband SEDs (for example Domínguez et al. (2011)).

In the context of gamma-ray astronomy, high energy photons from distant sources interact with and get attenuated by the EBL photons due to photon-photon pair production. Hence a good understanding of the EBL is required to recover the unattenuated spectrum from

extragalactic sources. For any given source at redshift z, the observed spectrum, $dN/dE_{\rm obs}$, is related to the intrinsic spectrum, $dN/dE_{\rm int}$, by:

$$\frac{dN}{dE}_{\rm obs} = \frac{dN}{dE}_{\rm int} e^{-\tau(E,z)} \tag{1.5}$$

where $\tau(E,z)$, the EBL opacity, depends on both the redshift of the source and the energy of the gamma-ray photon. For the purpose of this thesis, I use the values of τ stated in Domínguez et al. (2011) to calculate the likely attenuation to the spectrum from extragalactic sources in Chapter 3 and Chapter 5. This model has been found to be compatible with the upper limits from gamma-ray astronomy (for example Mazin and Raue (2007), MAGIC Collaboration et al. (2008)). Figure 1.4 shows the flux attenuation as a function of energy for sources at different redshifts using the Domínguez et al. (2011) EBL model.

1.4 AGN: Spectral Energy Distribution and the Blazar Sequence

The physical properties of AGN can be studied by investigating the broadband spectral energy distribution (SED) across a range of frequencies (for example Fossati et al. (1998), Abdo et al. (2010a)). An example of a SED for a typical blazar, 3C 279, is shown in Figure 1.5 and comprises two distinct peaks. The first peak occurs in the radio to the X-ray regime and is attributed to synchrotron emission from relativistic electrons within the jet interacting with magnetic field lines. The origin of the second peak, seen in the gamma-ray energy regime, is still a matter of debate but is widely believed to be a result of IC emission from a source of seed photons, either the same photons emitted through synchrotron emission (SSC) or photon populations external to the jet (external Compton (EC)).

In addition, some AGN also have a significant thermal component of emission originating, for example, from matter falling into the SMBH being strongly heated in the inner regions

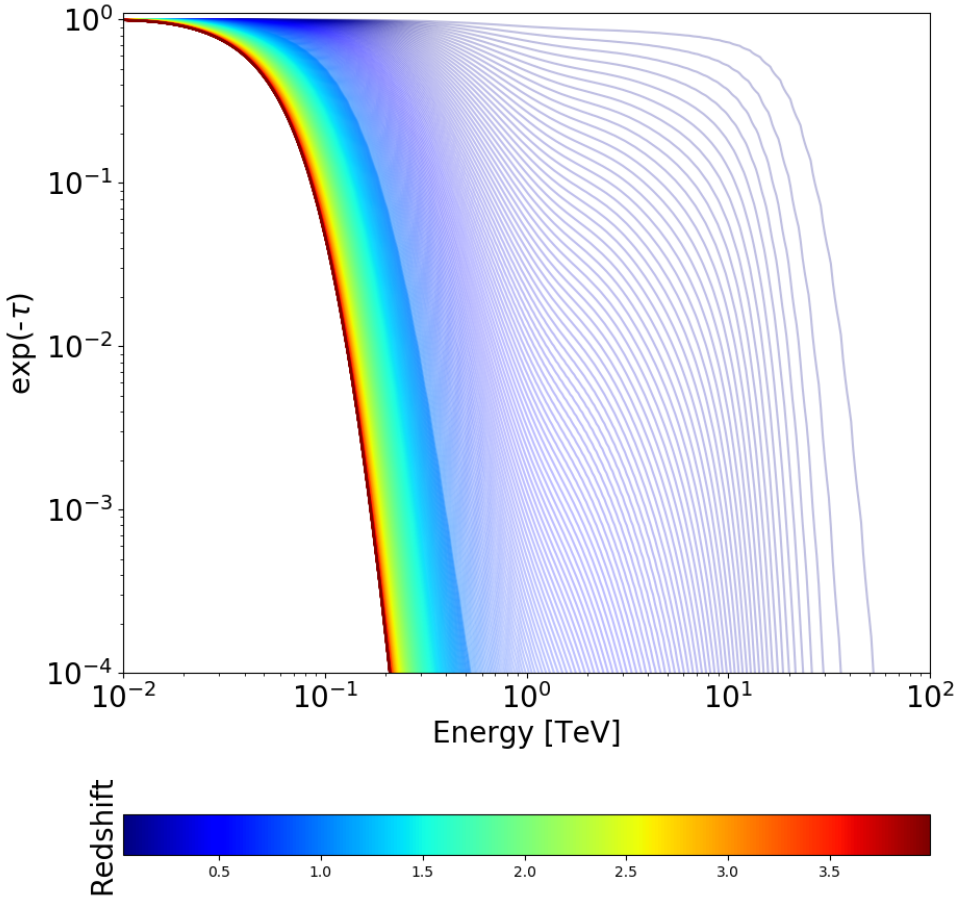

Figure 1.4: Flux attenuation as a function of observed energy for gamma-rays from sources at different redshift (shown as colourbar) using the Domínguez et al. (2011) EBL model.

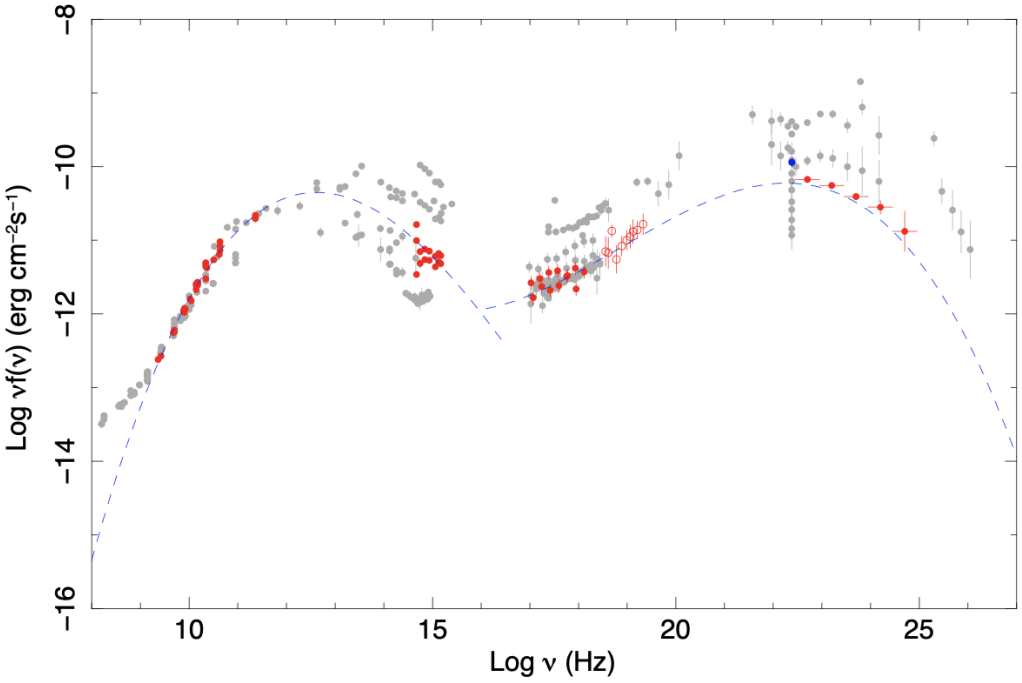

Figure 1.5: An example of a broadband SED for 3C 279, showing the two distinct peaks. The plot was obtained from Abdo et al. (2010a). The large filled red symbols represent quasi-simultaneous data, while the small grey points are non-simultaneous archival measurements. The dashed lines are the best fit to the synchrotron and IC components of the quasi-simultaneous SED.

of the accretion disk. The thermal radiation is believed to be Comptonized by the hot corona, leading to the X-ray emission. AGN which are energetically dominated by thermal radiation in the optical and X-ray band compared to the nuclear radio emission are classified as thermal dominated AGN and include Seyfert galaxies and QSOs.

BL Lac objects can be classified into the following sub-categories based on the synchrotron-peak frequency, $\nu^s_{\rm peak}$,of the broadband SED (Abdo et al. (2010a)):

- High-synchrotron-peaked blazars (HSPs) if $\nu^s_{\rm peak} > 10^{15}$Hz;
- Intermediate-synchrotron-peaked blazars (ISPs) if 10^{14}Hz $< \nu^s_{\rm peak} < 10^{15}$Hz;
- Low-synchrotron-peaked blazars (LSPs) if $\nu^s_{\rm peak} < 10^{14}$Hz.

Fossati et al. (1998) investigated the SED for a sample of 126 blazars and found evidence of

an anti-correlation between the synchrotron peak frequencies and the bolometric luminosity of the sample. The blazars with the higher bolometric luminosity had smaller peak frequencies i.e redder SEDs and a more prominent high energy peak. Blazars with lower bolometric luminosity were found to exhibit larger peak frequencies i.e bluer SEDs with the two peaks having roughly the same luminosity. However, the existence of this trend has been questioned, for example in Padovani (2007), who suggest that the observed sequence might result from selection biases in the sample.

Nevertheless, any observed trend would lead to the suggestion of a sequence in blazar sub-classes, FSRQ $\rightarrow$ LSP $\rightarrow$ ISP $\rightarrow$ HSP, in order of increasing synchrotron peak frequencies and decreasing bolometric luminosity, with LSPs and ISPs as intermediates between FSRQs and HSPs (Böttcher (2007)). This sequence may be interpreted as evidence of a genetic link between BL Lacs and FSRQs as suggested by Cavaliere and D'Elia (2002) who argue that the two classes differ in their accretion rates, $\dot{M}$. FSRQs have accretion rates ranging from $\dot{M} \sim$ 1-10 $M_{\odot}$ per year while BL Lacs have a lower accretion rate of $\dot{M} << 1\ M_{\odot}$ per year. Under this assumption, BL Lacs represent the final, inefficiently accreting and long-term state formed from a short-lived and gas-rich FSRQ.

Furthermore, FSRQs are observationally distinguished from steep-spectrum radio quasars (SSRQs) based on the value of their radio spectral indices at a few GHz, α_r, with $\alpha_r = 0.5$ being the dividing line (Padovani (1999)). This difference is due to the differences in the size of the radio emission region. FSRQs are thought to have compact, nuclear emission regions predominantly from within the core while the radio emission in SSRQs originates from extended regions mainly within the lobes.

1.5 AGN: Some Open Questions

Despite recent advancements in the field of AGN research, there still remain many un-answered questions. A non-exhaustive sample of these are discussed in this section, describing why AGN continue to be interesting objects for study.

The physical mechanisms responsible for the second high energy peak in the broadband SED is still a matter of debate. Leptonic models (for example Blandford and Levinson (1995), Georganopoulos et al. (2002), Zdziarski et al. (2014)) assume that only electrons and positrons are accelerated and contribute to the high energy radiation. On the other hand, lepto-hadronic models (for example Romero et al. (2003), Reynoso et al. (2011), Böttcher et al. (2013)) suggest that the second peak may be a result of protons being accelerated to ultra-relativistic energies.

Understanding the physical mechanisms responsible for the emission will help understand the nature of the relativistic particles, the properties of the regions within the jet where the emission is produced and the physical interactions involved in the emission. For example, a hadronic origin of the high energy emission (Mannheim (1993)) would potentially make AGN prime candidate sources of astrophysical neutrinos (Halzen and Zas (1997)). The existence of a correlation between gamma-ray emission in AGN and the emission of high energy neutrinos has been investigated (for example Kadler et al. (2016), Abeysekara et al. (2018)) and invoked to explain observations of high energy neutrinos with the IceCube Neutrino Observatory (Aartsen et al. (2017)).

Moreover, another open question relates to how the cosmic history of SMBH accretion in AGN compares to the star formation history of the host galaxies. It has been suggested from data tracking investigations of active and star forming galaxies over cosmic time (for example Merloni (2004), Delvecchio et al. (2014), Shankar et al. (2016)) that black hole accretion and star formation peak at similar epochs. This finding can be interpreted as evidence that SMBH and their host galaxies are co-evolving and could indicate a physical connection between the evolution of the SMBH and their host galaxy.

The evolutionary properties of AGN, especially in the TeV regime, are poorly understood. This is primarily due to the intrinsic biases involved in observations with current generation experiments. Investigating the gamma-ray observations from AGN will allow to study the properties of different classes of AGN and help reveal how these sources are distributed in space and also how they evolve over cosmic time. A preliminary investigation towards this is undertaken in Section 5.5.

Finally, AGN also offer an unique and exciting window to investigate areas of physics beyond the observational study of the AGN itself. Recent studies include investigating the physical properties of the central SMBH (for example Reynolds (2019)), understanding the nature and composition of the intergalactic medium in the early Universe (for example Cooke and Fumagalli (2018)) and testing theories of general relativity (for example Mizuno et al. (2018)).

Chapter 2

Space based gamma-ray astronomy

The field of gamma-ray astronomy includes observations from both space based satellites as well as ground-based telescopes. An important attribute of space based gamma-ray detectors is the wide field of view, typically of the order of a few steradians (sr), making it possible to observe almost the entire visible sky while not being constrained by a fixed point of observations, as is the case for ground-based instruments.

This chapter begins with a review of some of the early experiments used to detect gamma-rays from space before proceeding to a detailed description of the *Fermi* Large Area Telescope (LAT) focusing on the design and methodology. I conclude with an overview of the methods implemented in a typical *Fermi*-LAT data analysis, with the aim of setting the scene for Chapter 3, where I investigate the gamma-ray emission region in the nine brightest FSRQs observed with the *Fermi*-LAT.

2.1 Space based Instruments

Among the first recorded observations in the gamma-ray regime, the estimation of source strengths by Morrison (1958) was made using instruments on balloons. The weak source spectra observed in the initial investigations led to the realisation that extended observations were required using larger equipment from space. I now briefly discuss some of the other space based detectors before moving on to a detailed description of the *Fermi*-LAT.

2.1.1 *Cos-B*

Cos-B was launched in August 1975 and was the first ever mission operated by the European Space Agency (ESA) to investigate gamma-ray sources. The satellite included a spark chamber which converted the incoming photons into an electron positron pair, the paths of which were then traced back in order to determine the origin of the gamma-rays. The data collected using *Cos-B* helped produce an initial gamma-ray map of the Milky Way (Mayer-Hasselwander et al. (1980)) and also compile a list of 25 sources, referred to as the 2CG catalogue (Swanenburg et al. (1981)).

2.1.2 *CGRO*

The Compton Gamma-Ray Observatory (*CGRO*) was launched by NASA in April 1991 and operated for almost nine years. The mission comprised four main instruments in one spacecraft and was sensitive to photons spanning over an unprecedented six orders of magnitude in the energy range between 20 keV - 30 GeV. The telescopes, ordered by increasing energy coverage, were:

BATSE

The Burst and Transient Source Experiment (*BATSE*) investigated gamma-ray bursts having timescales ranging from 0.1 - 100 seconds. Located at each of the eight corners were identical detector modules and the experiment detected, on average, one burst per day over

the course of the entire mission. The telescope was surrounded by an anti-coincidence plastic scintillator capable of rejecting background signals from cosmic rays.

OSSE

The Oriented Scintillation Spectrometer Experiment (*OSSE*) was sensitive to gamma-ray photons in the energy range 50 keV - 10 MeV. It comprised four detector modules typically operating two at a time with one from each pair measuring the source and background levels respectively. Each detector had a central spectrometer crystal along with a CsI crystal which acted as the anti-coincidence shield.

COMPTEL

The Imaging Compton Telescope (*COMPTEL*) covered an energy range from 750 keV - 30 MeV with an angular resolution of within 1° and a field of view of 1 sr. The incoming gamma-ray photons would Compton scatter in the front detector module before being absorbed in one of the rear detectors. The time, location and energy of the two interactions was then used to then calculate the direction and energy of the incoming photon and compute the energy spectrum of the source.

EGRET

The Energetic Gamma Ray Experiment Telescope (*EGRET*) was sensitive to gamma-ray photons in the energy range 30 MeV - 30 GeV. *EGRET* comprised a spark chamber used to convert the incoming photon into an electron positron pair, a calorimeter capable of measuring the energy deposited from these secondary particles and a plastic anti-coincidence dome acting as a shield to prevent contamination from background cosmic rays.

Among the key scientific achievements of the *CGRO* were the first all sky survey above 100 MeV (Fichtel et al. (1993)), observations of the gamma-ray properties of individual AGN (for example Schoenfelder (1994)) and the discovery of large scale isotropy in gamma-rays bursts (Briggs et al. (1996)).

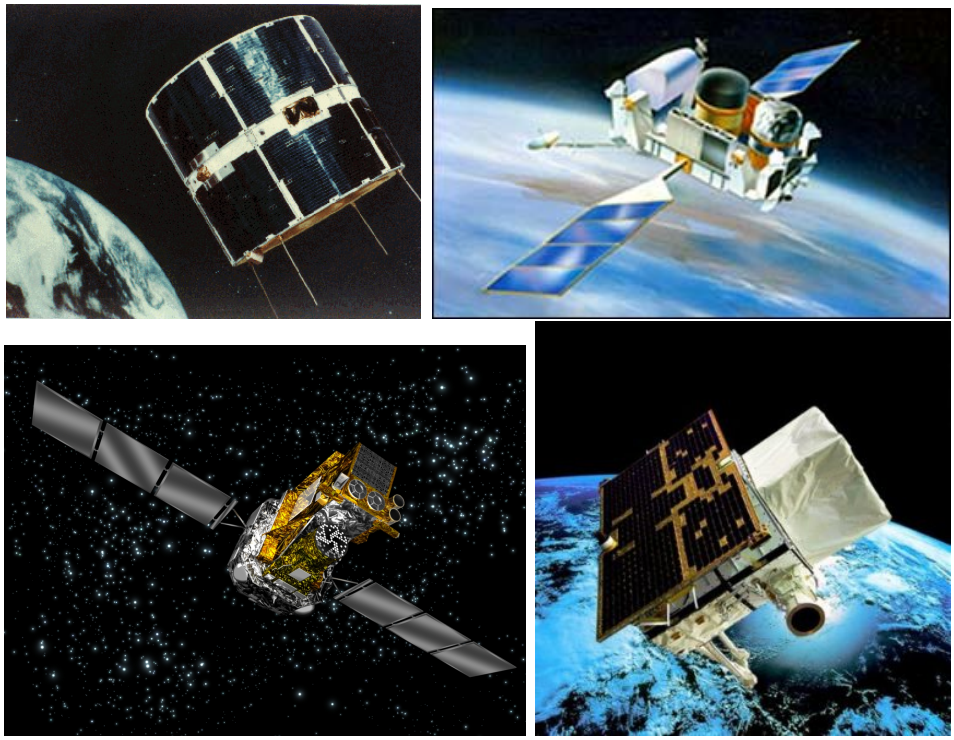

Figure 2.1: Top left: The *Cos-B* satellite. Credit: NASA (https://imagine.gsfc.nasa.gov/Images/cosb/, accessed on 12/11/2020). Top right: The Compton Gamma-Ray Observatory (*CGRO*). Credit: NASA (https://heasarc.gsfc.nasa.gov/docs/cgro/cossc/, accessed on 12/11/2020). Bottom left: The *INTEGRAL* Observatory. Credit: ESA (http://www.esa.int/ESA_Multimedia/Images/, accessed on 12/11/2020). Bottom right: The *AGILE* satellite. Credit: INAF (https://www.media.inaf.it/2017/05/29/agile-successo-italiano/, accessed on 12/11/2020).

2.1.3 *INTEGRAL*

The INTERnational Gamma-Ray Astrophysics Laboratory (*INTEGRAL*), operated by the ESA, was launched in October 2002. It consists of a spectrometer (SPI) and an on-board imager (IBIS), capable of observing photons in the energy range 15 keV - 10 MeV within an angular resolution of 12 arcmin.

INTEGRAL has been responsible for some important discoveries including localising the brightest gamma-ray line in the galaxy, the 511 keV electron-positron annihilation line (Knödlseder et al. (2005)), the first observation of high energy flux from a source coincident with Sagittarius A^* at the heart of the Milky Way (Bélanger et al. (2006)) and the detection of soft gamma-ray emission from a number of sources (for example Petry et al. (2009)).

Furthermore, there have been recent advancements in the field of photon polarimetry in the soft gamma-ray regime making it possible to measure the linear polarization parameters (Chauvin et al. (2013)). These have provided a new avenue of study aimed at understanding the non-thermal emission mechanisms involved in some of the most energetic sources in the Universe (see Ilie (2019) for a review).

2.1.4 *AGILE*

AGILE (short for Astro-rivelatore γ a Immagini LEggero) is an Italian mission launched in April 2007 and funded by the Italian Space Agency (ASI). It comprises three detectors, namely a gamma-ray imaging detector (GRID), a detector for hard X-rays (super *AGILE*) and a mini-calorimeter. The GRID is sensitive to photons in the energy band from 30 MeV - 50 GeV and has a field of view of $\sim$ 3 sr.

AGILE has been successful in detecting a range of gamma-ray sources. Among FSRQs, this includes the December 2009 flare from 3C 454.3 (Vercellone et al. (2008)) and the June 2010 flare from 4C 21.35 (Striani et al. (2010)); both these flares are later investigated using *Fermi*-LAT observations in Chapter 3. Finally, *AGILE* has also confirmed gamma-ray emission from a number of pulsars previously detected with *EGRET* including the detection of the Vela pulsar wind nebula in the energy range 100 MeV - 50 GeV (Pellizzoni et al. (2010)).

2.2 The *Fermi*-LAT

The *Fermi* Gamma-ray Space Telescope was launched by NASA in June 2008. It comprises two instruments, namely the Gamma-ray Burst Monitor (GBM; Meegan et al. (2009)), capable of investigating transient sources in the energy range 8 keV - 40 MeV, and the Large Area Telescope (LAT; Atwood et al. (2009)) used to obtain the gamma-ray observations from AGN studied in this thesis. While benefiting from the extensive knowledge gained from the experiments mentioned so far, the *Fermi*-LAT, as seen in this section, incorporates

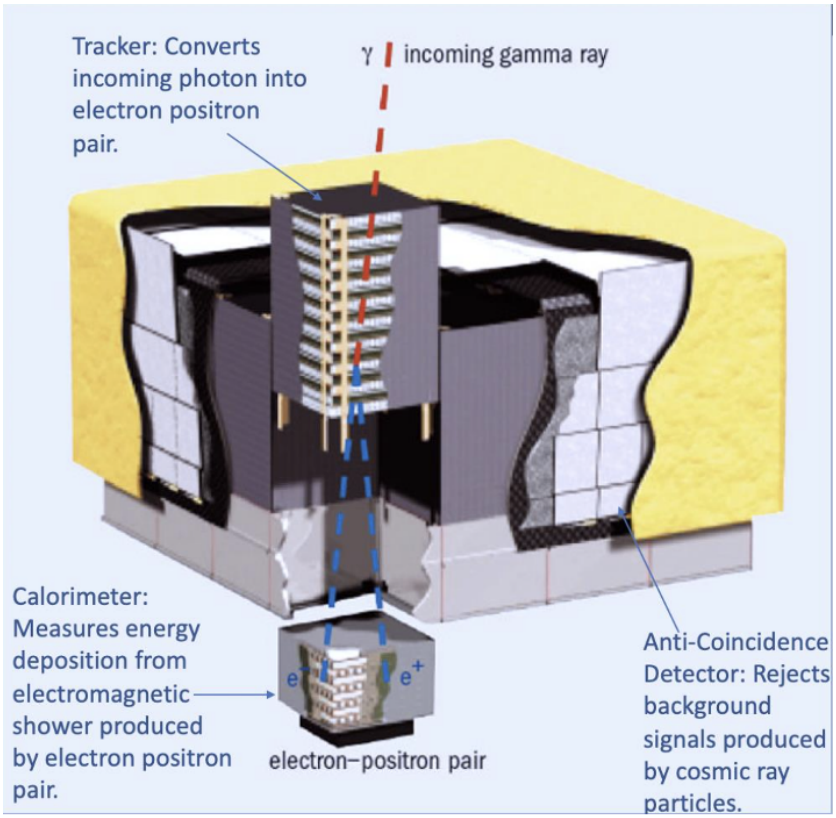

Figure 2.2: A schematic of the *Fermi*-LAT showing the various components: the tracker, calorimeter and the anti-coincidence detector. Adapted from Atwood et al. (2009).

a significant change in approach and improvements in performance when compared to preceding instruments.

The *Fermi*-LAT, schematic shown in Figure 2.2, is a pair conversion telescope having a wide field of view of ~ 2.4 sr (roughly corresponding to 20 % of the sky) capable of detecting photons in the energy range from ~ 20 MeV to above 300 GeV*. While in scanning mode, the *Fermi*-LAT alternates between pointing above and below the orbital plane and completes a full scan of the sky in two orbits (approximately three hours), allowing for an unbiased view of the whole gamma-ray sky.

The following section describes the components of the *Fermi*-LAT instrument and includes a discussion on how the incoming gamma-ray photons are detected and a summary of the performance and sensitivity of the telescope. This is followed by a walk-through of the

*`https://fermi.gsfc.nasa.gov/ssc/data/analysis/documentation/Cicerone/Cicerone_Introduction/LAT_overview.html`, accessed on 17/11/2020.

steps involved in a typical data analysis pipeline using the example of 3C 279, a FSRQ source investigated in Chapter 3.

2.2.1 Design and Methodology

As seen in Figure 2.2, the *Fermi*-LAT consists of an array of 16 tracker modules, 16 calorimeter modules, and a segmented anti-coincidence detector.

Every tracker module consists of a four-by-four array of silicon-strip detectors interleaved with foils of tungsten, a high Z material which facilitates the conversion of any incoming gamma-ray photon from within the field of view of the instrument into an electron positron pair and the paths of which is tracked by the silicon-strip detectors.

Due to the fact that the gamma-ray has a much larger energy than the rest masses of both the electron and positron, both secondary particles travel predominantly in the direction of the incident photon until striking the calorimeter at the bottom. It should be noted, that charged secondary particles resulting from less energetic incoming photons do not always reach the calorimeter and get deposited in the tracker instead.

The primary purpose of the calorimeter module is to measure the energy deposited by the electron positron pair. It is composed of eight alternating orthogonal layers of cesium iodide crystals which generate flashes of light having an intensity proportional to the energy of the incoming particle. The calorimeter is also capable of shower imaging and this allows for better background rejection and improved energy resolution at high energies through an estimation of shower leakage fluctuations.

As discussed in Chapter 4, cosmic rays which far outnumber the gamma-rays can also lead to the production of secondary particles like electrons, positrons, pions, muons and kaons, and therefore form a source of background events The anti-coincidence detector (ACD) surrounds the *Fermi*-LAT and is composed of 89 specially formulated plastic tiles which when hit by charged cosmic rays issue a veto signal.

It should be noted, charged particles from the shower created by the incident gamma-ray photons after striking the calorimeter can ricochet back up the tracker and reach the ACD.

This backsplash effect, which could have potentially reduced the sensitivity (as happened in *EGRET*), is overcome due to the segmented nature of the ACD.

The Data Acquisition System (DAQ) then performs a preliminary event triggering and on-board filtering of the data collected from the other components. A detailed description of the steps involved in determining which events make it to the final data sample can be found in Ackermann et al. (2012).

To summarise, the triggering procedure gets initiated when six consecutive silicon planes detect a signal above a pre-defined threshold value of 0.25 minimum ionizing particles (MIPs). The calorimeter module then classifies this potential trigger as being either at low energies (having a nominal threshold of $\sim$ 100 MeV) or at high energies (having a nominal threshold of $\sim$ 1 GeV). Finally, the ACD inspects the trigger event and issues a veto signal if any of the tiles are above a threshold of 0.45 MIPs, indicating the presence of a charged particle.

The on-board filtering process involves three different filtering algorithms: the *GAMMA* filter which is programmed to select gamma-ray events, the *HIP* filter which accepts heavy ion particle events primarily for the calibration of the calorimeter and the *DIAGNOSTIC* filter used to monitor the performance of the sensor and investigate the presence of selection biases. During the filtering process, any event having patterns consistent with cosmic rays as well as events not having a significant energy deposition (defined as 350 MeV (Ackermann et al. (2012))) in the calorimeter are rejected and the filtered data is telemetered to the ground for further processing.

2.2.2 Performance and Sensitivity

In addition to the design, the performance and sensitivity of the *Fermi*-LAT also depends on the algorithms used in event reconstruction and background rejection. This can be described by the Instrument Response Functions (IRFs) which show the performance of the instrument as a function of different parameters such as the photon energy and incidence angle.

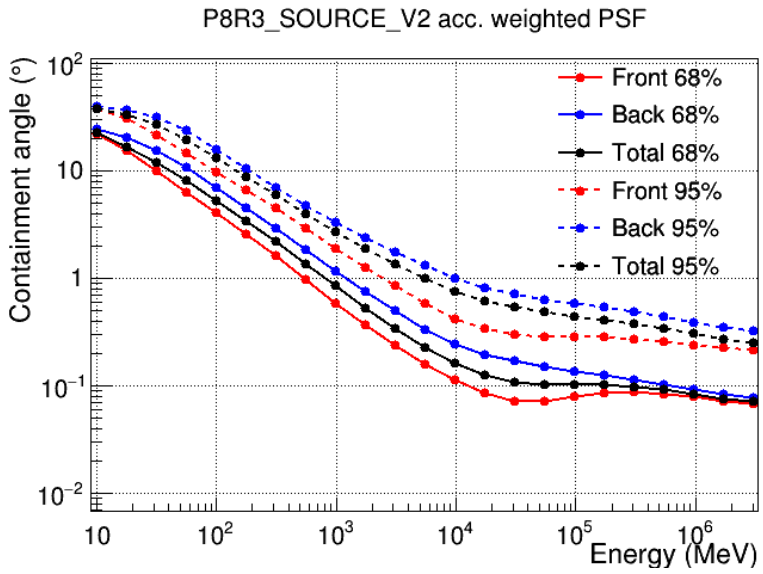

Figure 2.3: The 68 % and 95 % containment angles of the acceptance weighted PSF as a function of energy. The plots show results for both FRONT and BACK event types (in red and blue respectively) in addition to the total (shown in black). Credit: The *Fermi*-LAT Collaboration. The curves represent the performance at the time of writing; for the latest performance plots see `https://www.slac.stanford.edu/exp/glast/groups/canda/lat_Performance.htm`, accessed on 18/11/2020.

Furthermore, the event selection algorithms themselves are periodically updated using Monte Carlo simulations in order to correspond to the improved understanding of the telescope. These updates are called *Passes* with the *PASS* 6 IRFs being released at launch, followed by the *PASS* 7 IRFs in August 2011. The following discussion as well as all the analysis presented in this thesis considers the most recent release, the *PASS* 8 IRFs (Atwood et al. (2013)).

A single photon event is classified as either FRONT or BACK depending on the location within the tracker where the gamma-ray is converted into an electron positron pair. FRONT events get converted in the first 12 tracking planes which are farthest from the calorimeter and have thin converters while BACK events get converted in the next 4 tracking planes for which the tungsten converters are ~ 6 times thicker. The division of the tracker module into two distinct regions was motivated by the need for a trade-off between achieving great angular resolution while still having a high probability of conversion.

As seen in Figure 2.3, FRONT and BACK events differ in their point spread functions

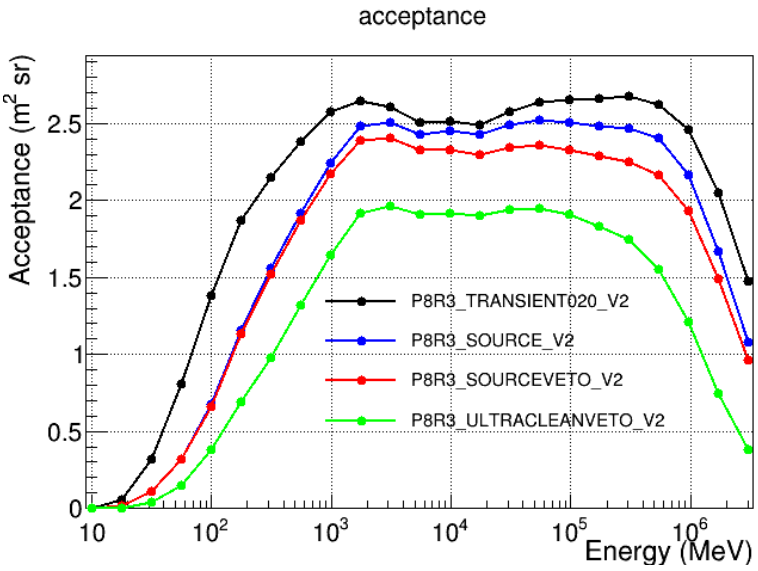

Figure 2.4: The acceptance for the different *PASS* 8 event classes as a function of energy. Credit: The *Fermi*-LAT Collaboration. The curves represent the performance at the time of writing; for the latest performance plots see `https://www.slac.stanford.edu/exp/glast/groups/canda/lat_Performance.htm`, accessed on 18/11/2020.

(PSF) defined here as the containment angle covering 68 % and 95 % of events from a point source with FRONT class events having an inherently better PSF by a factor of ~ 2 than BACK events due to multiple scattering being more prominent in the latter, resulting from the presence of thicker converters. On the other hand, the thicker converters in the BACK section provide larger effective area especially at energies beyond 1 GeV, therefore increasing the conversion probability. Moreover, the design of the tungsten foils allow for the conversion of identical numbers of incoming gamma-ray photons in both sections of the tracker.

Furthermore, the instrument response also varies with how the events are classified by the *Fermi*-LAT Collaboration and is dependent on the types of constraints placed on event reconstruction. A comparison of the acceptance, defined as the effective area integrated over the solid angle, for each class of event is shown in Figure 2.4.

The categories include *SOURCE* class events which provide a combination of good sensitivity and a relatively low field of view background contamination rate of less than ~ 1 Hz. This allows for a high signal-to-background ratio without compromising source detection

and characterisation. *SOURCE* class events are the recommended class for most analyses, including all investigations carried out in this thesis.

The *TRANSIENT* class of events contain the least number of cuts and is designed for investigations of short duration phenomena such as gamma-ray bursts. These studies benefit from the increased photon statistics provided even at the expense of higher background rates. Only a few cuts are applied to this event class allowing to maintain high gamma-ray efficiency while limiting the background contamination rate to a few Hz.

The *CLEAN* class of events contain tighter cuts than *SOURCE* class events with the field of view background contamination rate reduced to $\sim$ 0.1 Hz. This is below the rate of extragalactic gamma-ray background at all energies. For comparison, the total contribution from Galactic diffuse emission is $\sim$ 1 Hz (Ackermann et al. (2012)). Moreover, *CLEAN* class events have a 1.3 to 2 times lower background rate than *SOURCE* class events above 3 GeV making them more sensitive to the study of hard spectrum sources at high Galactic latitudes.

Finally, the most restrictive class of events, *ULTRACLEANVETO* can be used in the analysis of large regions more sensitive to the effects of instrumental backgrounds. This includes the study of extragalactic diffuse emission, as well as investigations of cosmic ray induced systematics. The residual contamination rate of *ULTRACLEANVETO* events is $\sim$ 40 % lower than that of *CLEAN* class events at 100 MeV, with the levels becoming comparable with increasing energy and the same above 10 GeV.

The effective area of the *Fermi*-LAT depends on the energy and angle of incidence of the incoming photon, the position where pair conversion occurs (i.e. whether FRONT or BACK event) and the spatial properties of the detector. Figure 2.5 plots the effective area of the *Fermi*-LAT as a function of energy for photons striking the detector at normal incidence ($\theta = 0$) and this can be seen to peak in the energy range 2 - 100 GeV.

Figure 2.6 shows the acceptance weighted energy resolution of the *Fermi*-LAT as a function of energy for both FRONT and BACK events. The energy resolution reduces at lower energies due to the charged secondary particles not reaching the calorimeter (being deposited

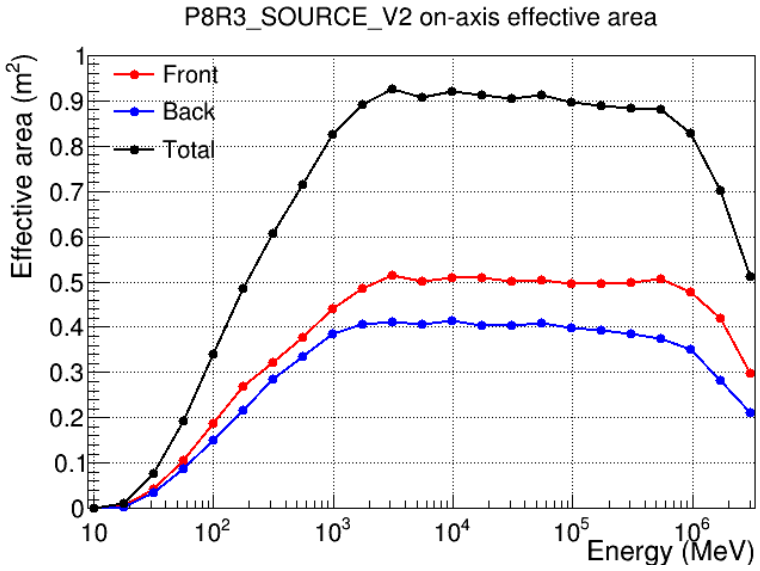

Figure 2.5: The effective area as a function of energy for normally incident photons ($\theta = 0$). The plots show results for both FRONT and BACK event types (in red and blue respectively) in addition to the total (shown in black). Credit: The *Fermi*-LAT Collaboration. The curves represent the performance at the time of writing; for the latest performance plots see `https://www.slac.stanford.edu/exp/glast/groups/canda/lat_Performance.htm`, accessed on 18/11/2020.

in the tracker instead) and also at higher energies due to leakage of the shower out of the calorimeter. Furthermore, the energy resolution is dependent on the angle of incidence of the incoming photons and improves slightly with increasing angle before reducing sharply at large angles from the z axis.

2.3 The *Fermi*-LAT data analysis pipeline

The following section describes the steps involved in a typical *Fermi*-LAT data analysis pipeline using the example of 3C 279, one of the FSRQs later investigated in Chapter 3. The steps are summarised in Figure 2.8. Throughout all the analysis presented in this thesis, I use the *Fermi* Science Tools version 11 – 05 – 03 * and *FERMIPY* version 0.18.0 † (Wood et al. (2017)) in conjunction with the latest *PASS* 8 IRFs (Atwood et al. (2013)).

*`http://fermi.gsfc.nasa.gov/ssc/data/analysis/software`, accessed on 17/03/2021.
†`http://fermipy.readthedocs.io`, accessed on 17/03/2021.

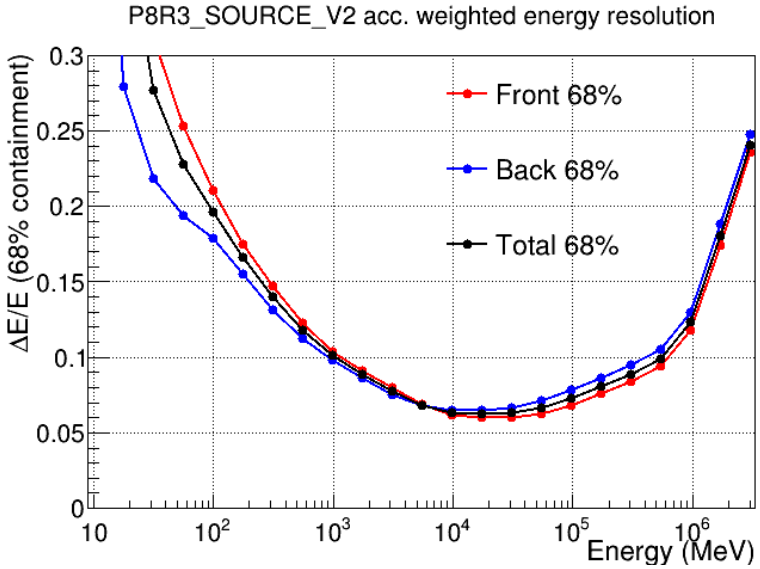

Figure 2.6: The 68 % containment half width of the reconstructed incoming gamma-ray photon energy as a function of energy for both FRONT and BACK event types (in red and blue respectively) and the total (shown in black). Credit: The *Fermi*-LAT Collaboration. The curves represent the performance at the time of writing; for the latest performance plots see `https://www.slac.stanford.edu/exp/glast/groups/canda/lat_Performance.htm`, accessed on 18/11/2020.

2.3.1 Data Extraction and Filtering

Fermi-LAT data, in the form of events files, are obtained from the *Fermi* Science Support Center's data server [‡]. These include a list of all the recorded events corresponding to a specified region of interest (RoI) surrounding the source in a particular time interval and energy range. Also obtained from the server is a single spacecraft file containing the positional information of the *Fermi*-LAT in time intervals of 30 seconds.

For the purpose of this walk-through, I select observations made between modified Julian dates (MJD) 54682.66 and 55047.66, which correspond to midnight on the August 4, 2008 until midnight on August 4, 2009. An energy range between 100 MeV - 300 GeV is considered along with a RoI of radius 15° centred on 3C 279.

The choice of energy range is dependent on the specific analysis undertaken. In this case, a lower limit of 100 MeV is chosen because, as seen in Figure 2.3, the PSF of the

[‡] `https://fermi.gsfc.nasa.gov/cgi-bin/ssc/LAT/LATDataQuery.cgi`, accessed on 10/03/2021.

Fermi-LAT increases to above 6° at lower energies which makes a point source analysis difficult. Furthermore, FSRQs have relatively soft gamma-ray spectra and are not expected to be significantly detected with the *Fermi*-LAT at energies above 300 GeV. The choice of radius of RoI is based on having a sufficient knowledge of the background while at the same time keeping computation times manageable and to reduce the effects of background systematics.

The first step in the analysis involves applying the *gtselect* routine to make specified cuts to the events files obtained from the server. For a point source analysis, I include events having a high probability of being photons by selecting only *SOURCE* class events (specified by setting the event class = 128) from both the FRONT and BACK of the detector (specified by setting event type = 3).

Furthermore, a maximum zenith angle cut of 90° is applied to exclude time intervals in which any part of the RoI is too close to the Earth's limb. The Earth's limb lies at a zenith angle of 113° and is a bright source of gamma-ray photons produced by the interaction of cosmic rays with the upper atmosphere. Two representative plots showing the result of implementing the above cuts in event class and zenith angle are given in Figure 2.7.

It is then necessary to apply time selection cuts to the data in order to obtain Good Time Intervals (GTIs), time periods in which the telescope was in survey mode. For instance, the *Fermi*-LAT does not collect data when crossing the South Atlantic Anomaly, a region 120 miles above sea level where the inner Van Allen belt comes closest to the Earth's surface.

This region has very high levels of radiation, a consequence of the increased levels of flux from trapped high energy particles and has affected a number of spacecrafts in orbit around the Earth. The *gtmktime* routine uses the information in the spacecraft file and the filter expression DATA_QUAL==1 && LAT_CONFIG==1 is applied to obtain good data collected when the instrument is in nominal science configuration.

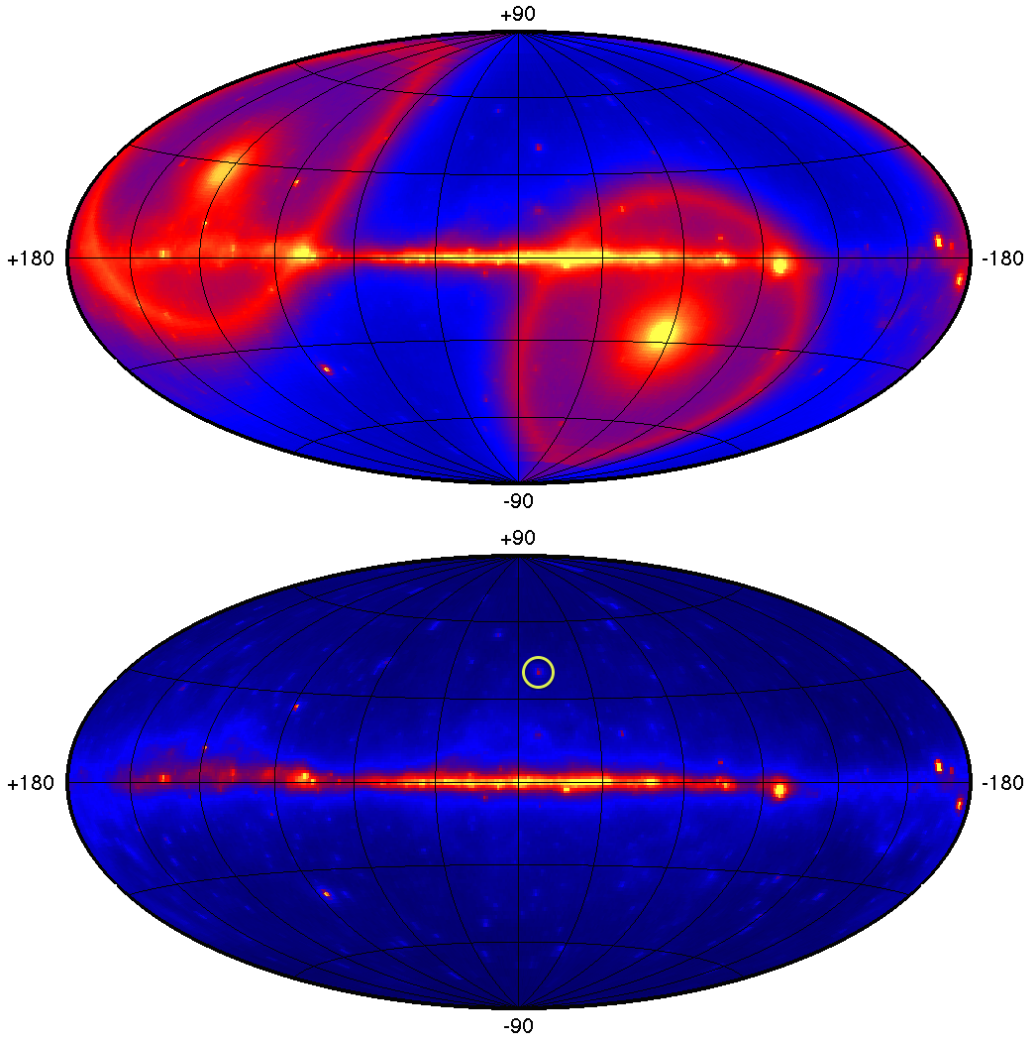

Figure 2.7: Top: An all-sky image, in Galactic co-ordinates, of gamma-rays in the energy range 100 MeV - 300 GeV captured by the *Fermi*-LAT after 4.8 years of operation. Bottom: The same all-sky image after selecting only *SOURCE* class events and applying a maximum zenith angle cut of 90°. The circle shows the location of 3C 279. Credit: Jeremy S. Perkins, NASA Goddard Space Flight Center (`https://github.com/FermiSummerSchool/fermi-summer-school/tree/master/Likelihood_Analysis/images`, accessed on 19/03/2021).

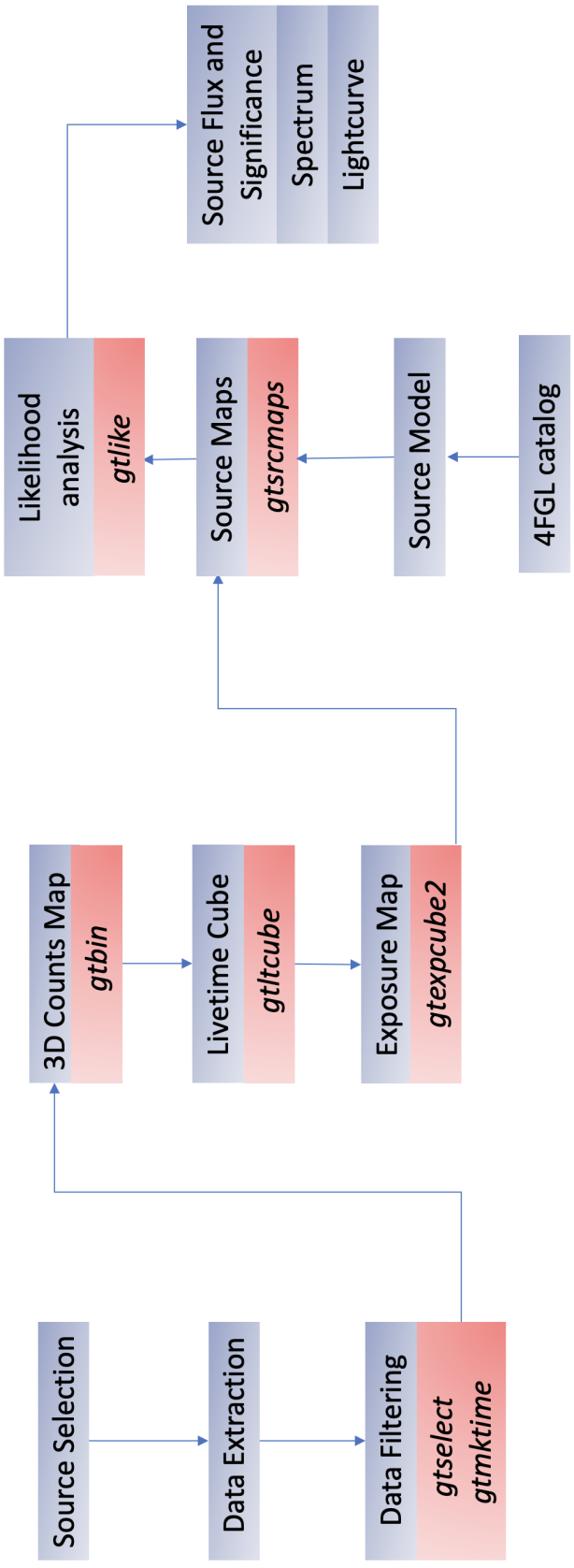

Figure 2.8: A flowchart of the steps involved in the *Fermi* - LAT likelihood analysis also showing, where applicable, the *Fermi* Science Tools routines applied at each step.

2.3.2 Pre-computing the binned response

The next step involves creating a counts map of the RoI summed over photon energies and is implemented with the *gtbin* routine using the CMAP option. A spatial binning of 0.2° pixel^{-1} is chosen and given that the RoI is 30° in diameter, I select the sizes of the x and y axes to be 30/0.2=150 pixels.

The counts map obtained is shown in Figure 2.9 and gives an idea of the source candidates within the RoI. The counts map also acts as a preliminary sanity check to make sure the data query and data selection cuts have been implemented correctly and failure to do so can result in non-circular regions or counts maps containing no events.

Once satisfied that the counts map behaves as expected, the next step is to create a counts cube once again using *gtbin*, this time with the CCUBE option. The choice of energy binning must be sufficiently narrow to prevent loss of accuracy due to rapid variations in the effective area at low energies (see Figure 2.5). At the same time having too many bins could potentially lead to complications at higher energies due to lack of statistics in each individual bin. As a trade-off, my analysis considers eight energy bins per decade in energy. Six snapshots of the counts cube generated, each spanning different energy bins, are shown in Figure 2.10. These highlight that the PSF of the *Fermi*-LAT changes with energy and how different energy cuts can be implemented to localise and investigate different sources within the RoI.

The instrument response of the *Fermi*-LAT also depends on the inclination angle, defined here as the angle between the direction to the source and the instrument z-axis. By extension, the number of photon counts produced by a source is also expected to depend on the time spent by the telescope observing a given inclination angle. In order to expedite the likelihood analysis, the *gtltcube* routine can be applied and this uses the pointing history of the telescope to generate a livetime cube, an array of the accumulated time spent by the instrument as a function of inclination angle during the specified observation period.

Finally, the *gtexpcube2* routine is applied to the livetime cube to generate a binned map of the total exposure, defined as the product of the area and time the instrument observes a

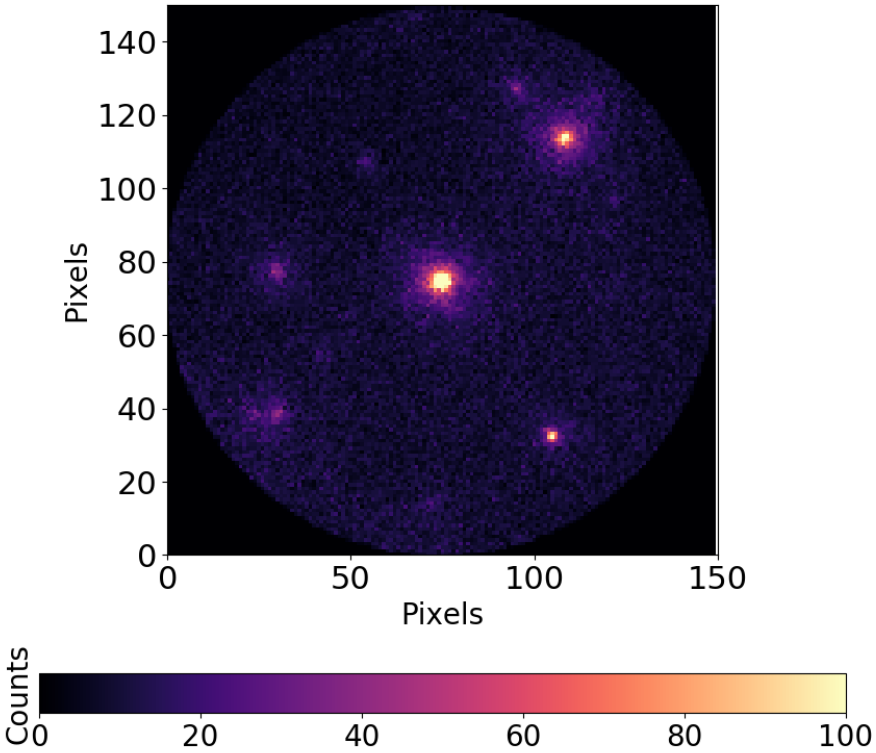

Figure 2.9: A counts map showing the distribution of gamma-ray photons over a RoI of radius 15° centred on 3C 279 for the observation period between August 4, 2008 and August 4, 2009. The colour scale shows the number of photons at each pixel in the counts map.

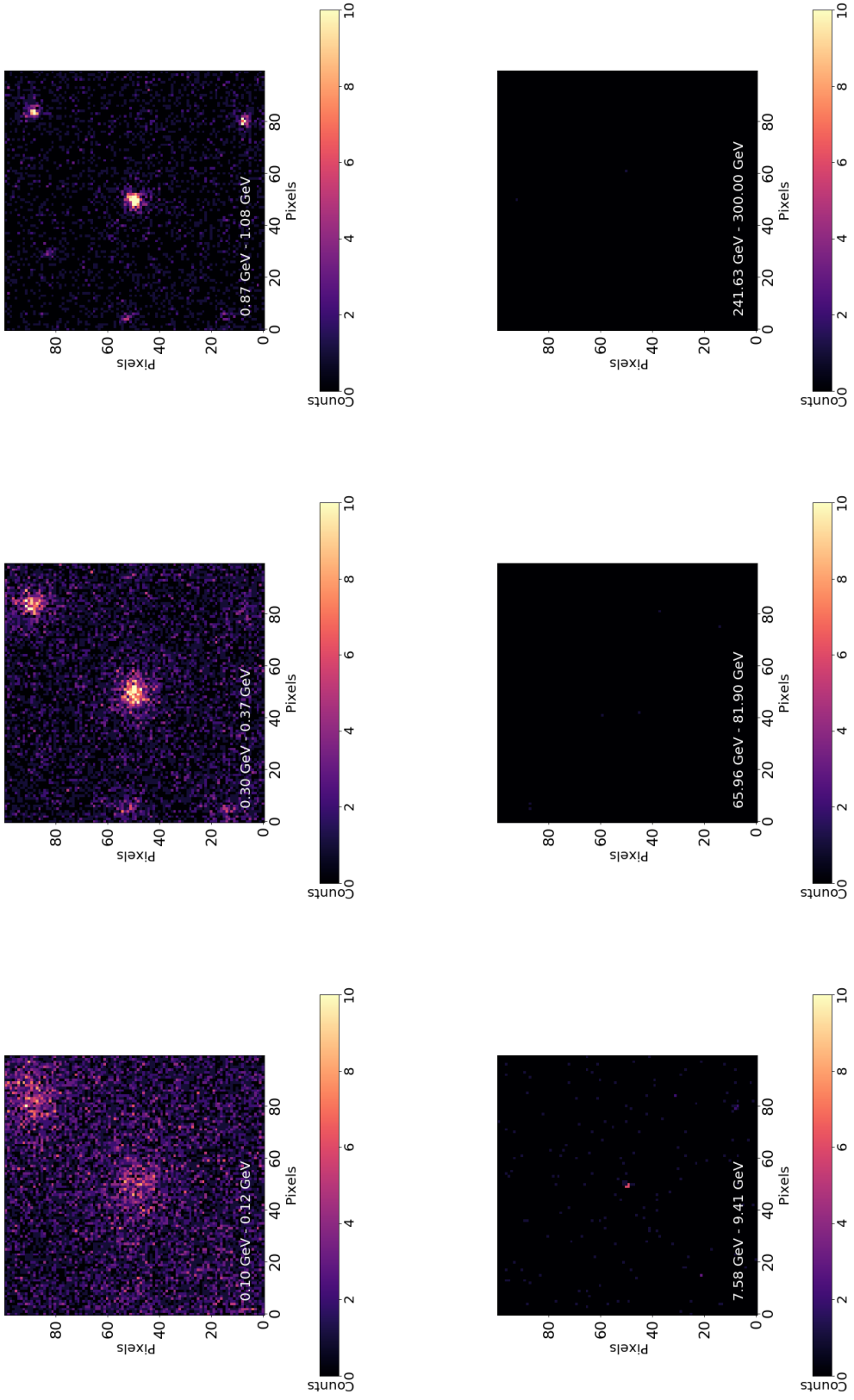

Figure 2.10: Six snapshots of the counts cube showing the distribution of gamma-ray photons in the specified energy intervals over a RoI of radius 15° centred on 3C 279 for the observation period between August 4, 2008 and August 4, 2009. The colour scale shows the number of photons at each pixel in the RoI.

given position, at different energies. The final photon counts produced by a source at any point is given by the integral of the source flux and the value of the exposure map function at that position. Given the large PSF of the *Fermi*-LAT, it is necessary to account for the contributions of sources not included in the counts cube as these could affect the region being investigated. Figure 2.11 shows all sky exposure maps generated for this analysis at three different energies of 100 MeV, 200 MeV and 1 GeV.

2.3.3 Preparing the source model

A source model, in the form of an *XML* file, is required as input for the likelihood analysis. This model contains an initial estimate of the spatial and spectral properties of the each source in the data as well as templates for the isotropic and Galactic diffuse background emission.

The isotropic diffuse emission model appropriate for a 4FGL point source analysis of all *SOURCE* class events striking both the FRONT and BACK of the *Fermi*-LAT is iso_P8R3_SOURCE_V3_v1.txt. This details the contributions of extragalactic diffuse gamma-rays, possible unresolved extragalactic sources, and any residual cosmic ray emission.

The template is derived in the energy range 30 MeV - 1 TeV from a fit to the all sky emission excluding both the Galactic plane and regions surrounding the Celestial poles. This is done in order to reduce any contamination from the Galactic diffuse emission and background gamma-rays from the Earth's limb. A plot showing the differential flux against energy of the isotropic diffuse emission model is shown in Figure 2.12.

The Galactic diffuse emission is modelled using the template gll_iem_v07.fits (The *Fermi*-LAT collaboration (2019b)), shown in Figure 2.12, which gives the background energy flux in the energy range 50 MeV - 81.4 GeV along with the corresponding spatial co-ordinates. This model was developed by the *Fermi*-LAT Collaboration using spectral line surveys of HI and CO (as a tracer to H_2), from which the distribution of interstellar gas in Galactocentric rings was derived.

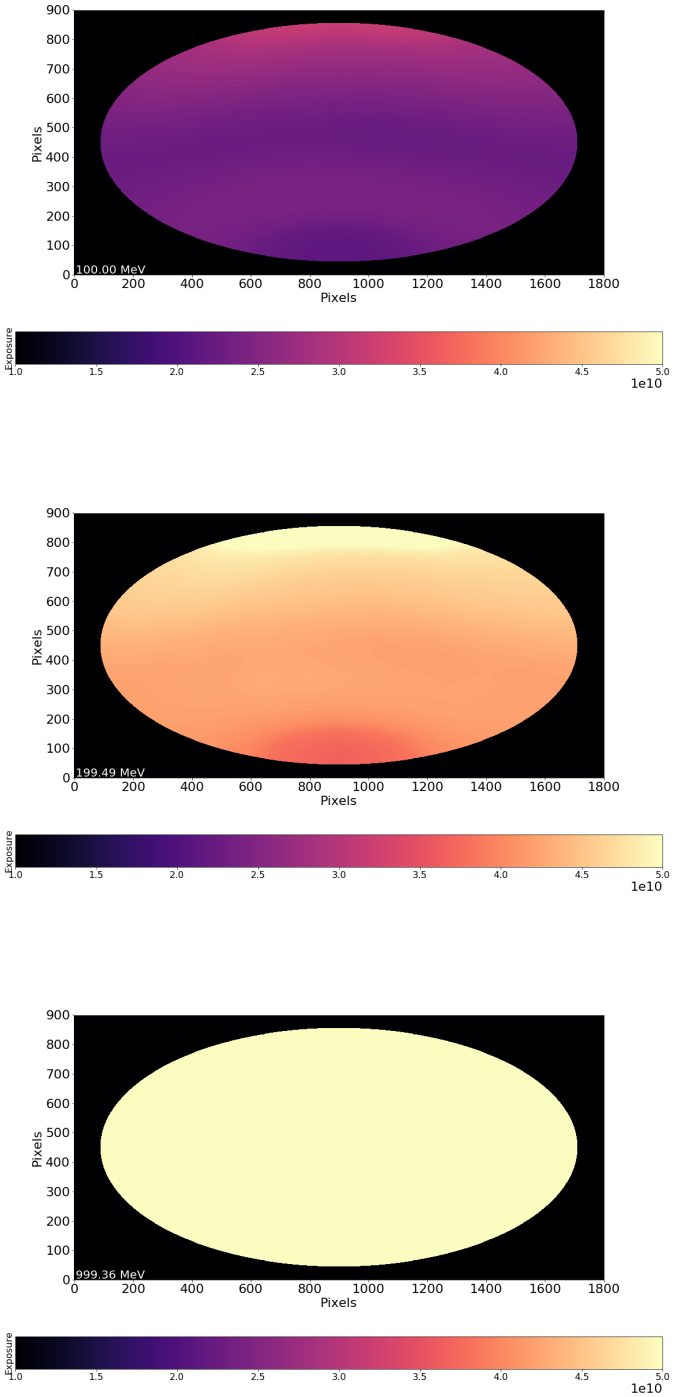

Figure 2.11: Three snapshots of the all sky exposure map at the energies 100 MeV, 200 MeV and 1 GeV during the observation period between August 4, 2008 and August 4, 2009. A spatial binning of 0.2° pixel^{-1} is chosen and given that the observations span the entire sky (360° × 180°), I select the sizes of the x and y axes to be 360/0.2 = 1800 pixels and 180/0.2 = 900 pixels respectively. The colour scale shows the total exposure for each pixel in units of cm^2 s.

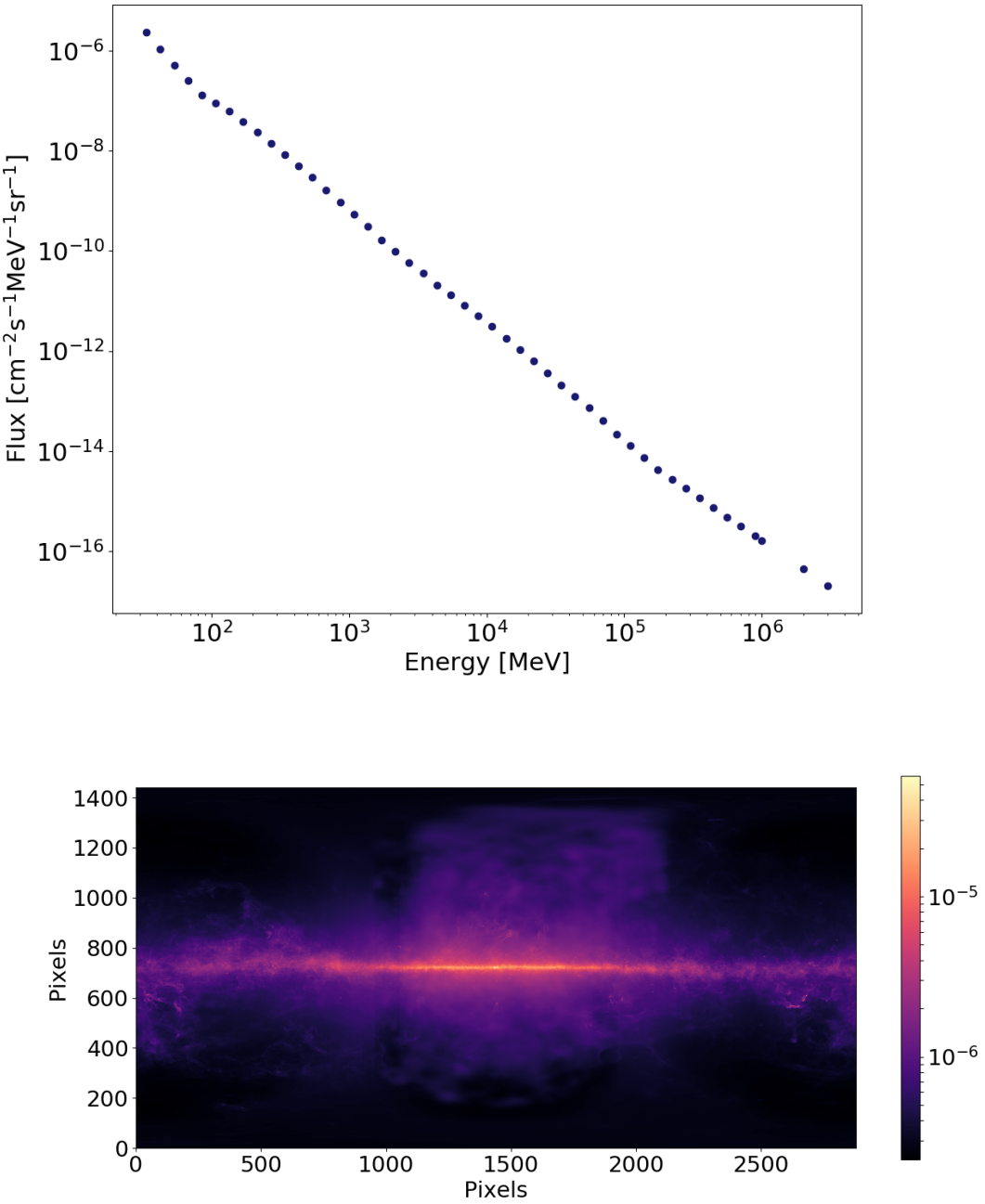

Figure 2.12: Top: The distribution of differential flux against energy of the isotropic diffuse emission model, iso_P8R3_SOURCE_V3_v1.txt, used in the analysis. Bottom: The Galactic diffuse emission model, gll_iem_v07.fits, used in the analysis. The colour scale is a photon flux in units of ph cm^{-2}s^{-1}.

The model describes the gamma-ray emission produced from the interactions between cosmic ray protons with interstellar nuclei, the Bremsstrahlung interaction of cosmic ray electrons with nucleons and the IC scattering of cosmic ray electrons off of interstellar photons. A detailed understanding of the Galactic interstellar emission is beneficial given the lack of statistics associated with gamma-ray observations combined with the limited angular resolution of the instrument and aids in differentiating between the interstellar emission and emission from point sources, especially at low Galactic latitudes.

The normalisation factor of both the isotropic and Galactic diffuse emission models are left free for the fitting procedure. This is necessary because the background templates have been derived using the latest catalog at the time of release and could include sources which have since been resolved when using a non-identical data selection.

I use the 4FGL catalog (The *Fermi*-LAT collaboration (2019a)) to compile a model containing the spatial positions and spectral shapes of all sources within a radius of 20° from the RoI centre. A larger radius of 20° than the RoI radius of 15° is chosen to account for sources lying outside the RoI which might yet contribute photons to the data. While this analysis does not contain any extended sources within the RoI, the contribution from extended sources must also be taken into account, when applicable, and added to the *XML* file*.

Each parameter in the model has a specified range of allowed values and can either be fixed or left free to vary during the fitting procedure. Keeping all spectral parameters i.e. the normalisation and the spectral shapes free for all sources would make it difficult for the fit to converge. It is therefore recommended to only free all spectral parameters for either very bright sources or sources nearby, which I define as being within 5°, of the source being investigated. The normalisation parameter of all remaining sources in the model are left free while their spectral shapes are fixed to the values reported in the 4FGL catalog (The *Fermi*-LAT collaboration (2019a)).

In a binned analysis, the spectrum of each source in the final *XML* model is multiplied by the

*An archive of extended source templates used can be obtained from `https://fermi.gsfc.nasa.gov/ssc/data/access/lat/8yr_catalog/`, accessed on 16/03/2021.

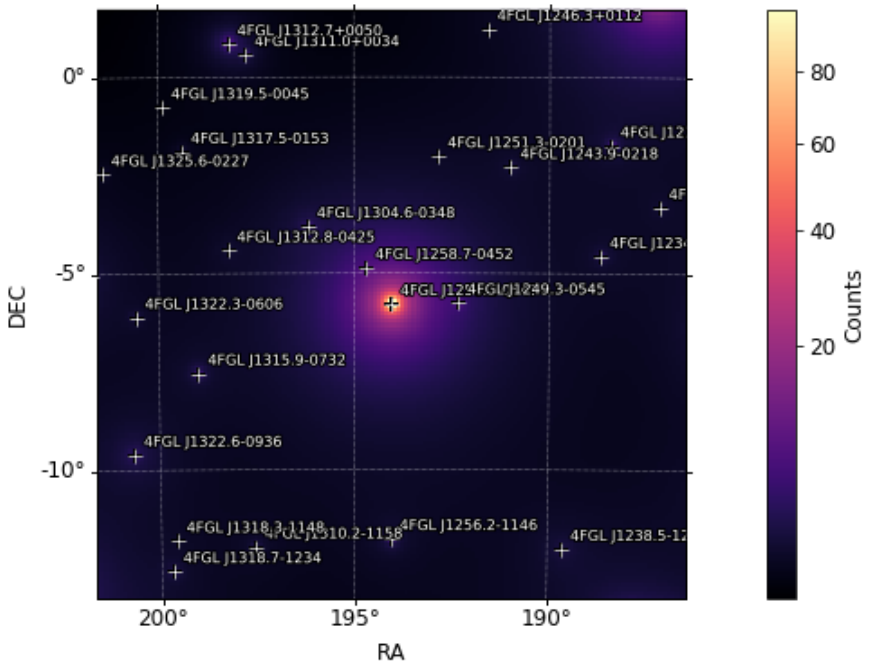

Figure 2.13: Skymap showing the initial modelled distribution of the gamma-ray photons of the analysis over the RoI centred on 3C 279 for the observation period between August 4, 2008 and August 4, 2009. The colour scale corresponds to the number of photons at each pixel in the counts map.

exposure at that particular source position and then convolved with the instrument response PSF for the specific observation using the *gtsrcmaps* tool. This produces a preliminary counts map for all sources in the model binned in space and energy to be used in the likelihood analysis and is shown in Figure 2.13.

2.3.4 The likelihood analysis

The likelihood can be defined as the probability of obtaining the observed data from the given input model of sources over the RoI. The significance of the gamma-ray emission from each source is evaluated using the maximum likelihood test statistic (TS). The TS is defined as (Mattox et al. (1996)):

$$\mathrm{TS} = -2\ln\left(\frac{L_0}{L_1}\right) \tag{2.1}$$

where L_0 is the maximum likelihood of a model without the additional source (i.e. the null hypothesis) and L_1 is the maximum likelihood of a model with the additional source at the specified location.

For a sufficiently large number of counts, the TS is asymptotically distributed as χ^2_n where the degrees of freedom, n, corresponds to the number of free parameters in the additional source component (Cash (1979)). The presence of an additional source will result in a fluctuation from this distribution. A large TS value (typically TS $\geq$ 25) quantifies the presence of an additional source (i.e. the null hypothesis is incorrect). The detection significance of the source in Gaussian sigma, σ, is given as:

$$\sigma = \sqrt{2}\mathrm{erf}^{-1}\left(\chi^2_n(\mathrm{TS})\right), \tag{2.2}$$

where erf (z) is the error function defined as:

$$\mathrm{erf}(z) = \frac{2}{\sqrt{\pi}}\int_0^z e^{-t^2}\,dt. \tag{2.3}$$

If the additional source has one degree of freedom, the significance approximates to $\sigma = \sqrt{\mathrm{TS}}$.

An initial automatic optimisation of the RoI is first applied by iteratively fitting the sources and ensuring all parameters are close to their global likelihood maxima. All sources found to have a TS < 10 (roughly corresponding to a significance of $\sim 3\sigma$) are then removed from the source model. This reduces the noise contribution from sources not producing any gamma rays during the observation period investigated, thereby allowing for a better estimate of the likelihood of the model describing the data.

The *gtfindsrc* routine is then applied to search for any additional point sources present in the data and not accounted for in the model. Any source found to have a TS $\geq$ 10 is permanently added to the model at the position of its highest TS value. This is followed by a re-optimization of the RoI. The model maps generated after each of the previous steps are shown in Figure 2.14.

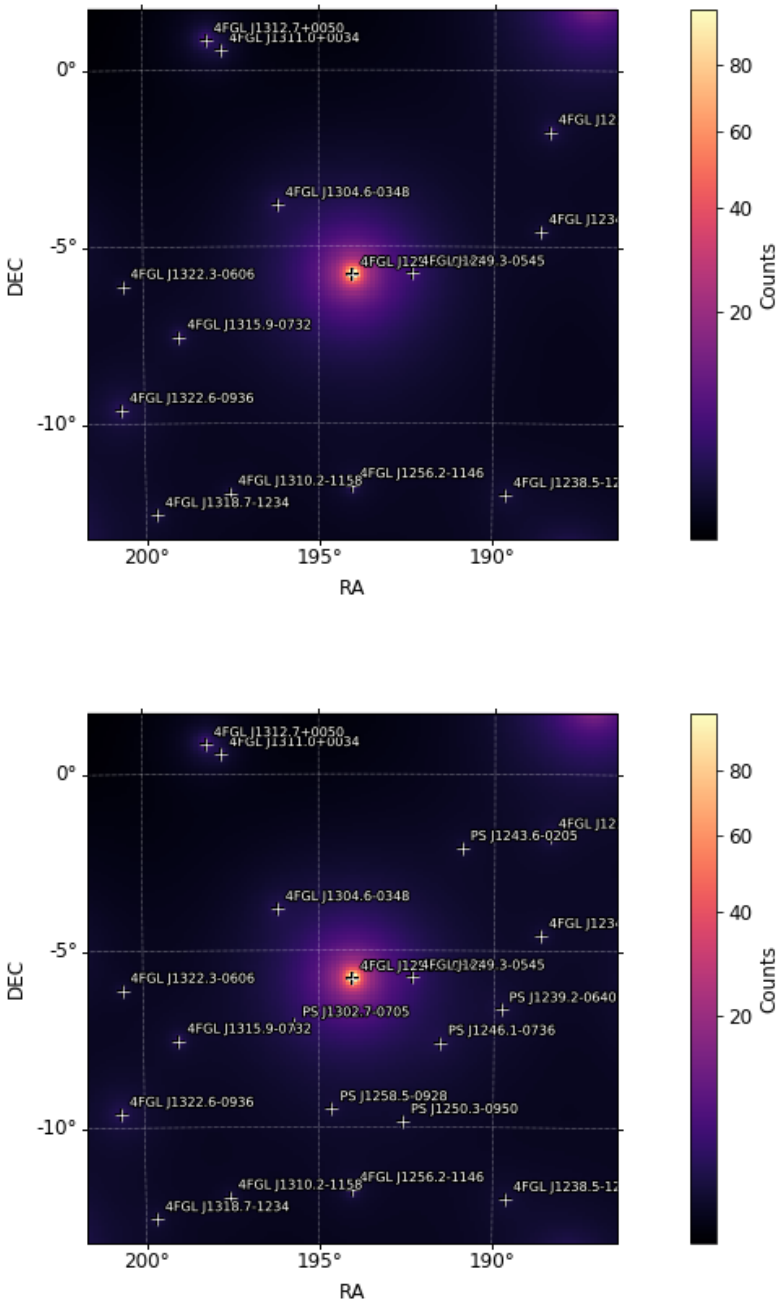

Figure 2.14: Top: Skymap showing the modelled distribution of the gamma-ray photons obtained after removing all sources found to have a TS < 10 from the initial model of the analysis over the RoI centred on 3C 279 for the observation period between August 4, 2008 and August 4, 2009. Bottom: Skymap showing the modelled distribution of the gamma-ray photons obtained after removing all sources found to have a TS < 10 followed by applying the *gtfindsrc* routine and adding sources found to have a TS ≥ 10 to the initial model of the analysis over the RoI centred on 3C 279 for the observation period between August 4, 2008 and August 4, 2009. The colour scales corresponds to the number of photons at each pixel in the counts map.

Table 2.1: The results of the binned likelihood analysis for 3C 279 observed with the *Fermi*-LAT between August 4, 2008 and August 4, 2009 in the energy range 100 MeV-300 GeV. The final two columns list the one year time-averaged flux and the TS values (see equation 2.1) obtained from the likelihood analysis. The redshift was taken from Marziani et al. (1996).

Source	RA [deg]	DEC [deg]	z	E_0 [MeV]	α	β	Flux [10^{-7} photons cm^{-2}s^{-1}]	TS
3C 279	194.04	-5.79	0.5362 ± 0.0004[1]	442.1	2.21 ± 0.15	0.058 ± 0.009	6.11 ± 0.02	24245

A binned likelihood analysis is performed on the source model to obtain the spectral parameters best describing the data during the one year observation period. During the likelihood analysis, 3C 279 was found to be best modelled by a log parabola:

$$\frac{dN}{dE} = N_0 \left(\frac{E}{E_0}\right)^{-\alpha-\beta\ln\left(\frac{E}{E_0}\right)} \tag{2.4}$$

where N_0 is the normalisation in units of photons cm^{-2}s^{-1}MeV^{-1}, E_0 is the pivot energy in MeV, α the spectral index and β the curvature. The best fit spectral parameters for 3C 279 are presented in Table 2.1 along with the one year time-averaged flux and the TS values.

The *residmap* routine can be applied to plot the residuals between the smoothed data and model maps. This method is sensitive to both positive and negative fluctuations making it a useful technique for assessing the goodness-of-fit. Residual maps showing both the excess significance and excess counts obtained during this analysis are shown in Figure 2.15.

No significant residuals are found indicating that all sources in the counts map have been accounted for. If this were not the case, the *XML* file would need to be remodelled with the additional contributions and the analysis repeated until a minimal difference is obtained.

2.3.5 Generating the SED

The spectral energy distribution (SED) of a source in the model can be computed using the *sed* routine. This method, by default, uses the same binning as the underlying analysis and performs independent fits to obtain the flux normalization of the source in each energy bin assuming a power law spectral distribution (see equation 3.9). The spectral index used in

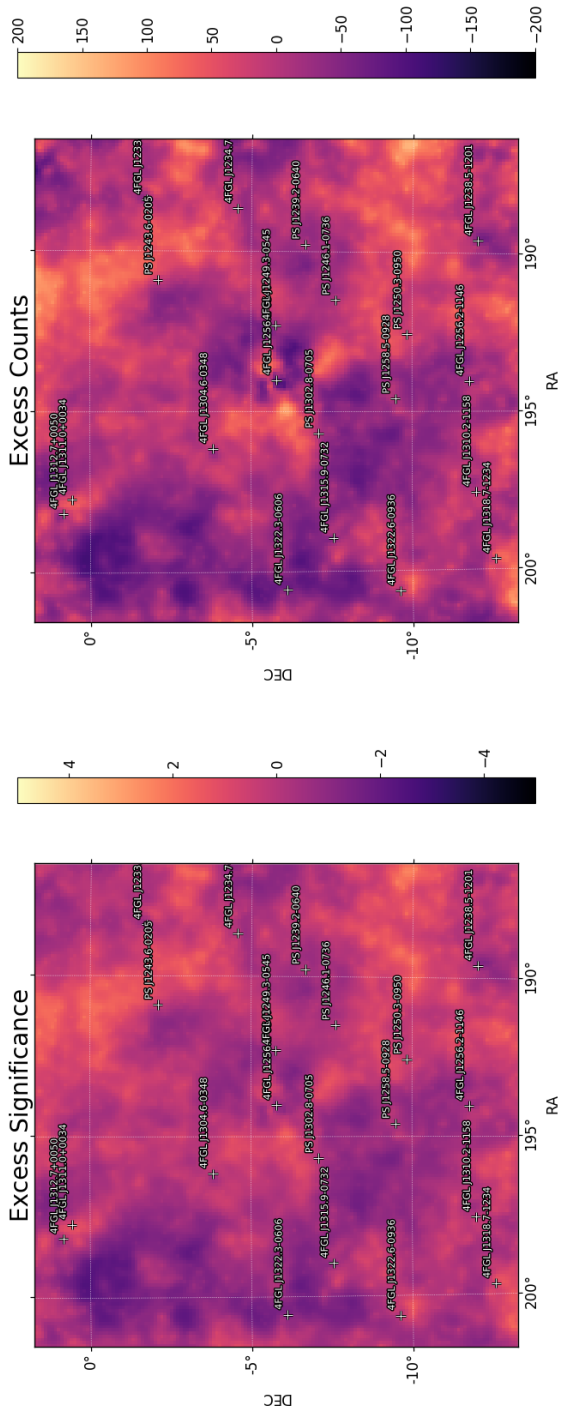

Figure 2.15: Skymaps of the residual significance (left) and the excess photon counts (right) obtained in the analysis over the RoI centred on 3C 279 for the observation period between August 4, 2008 and August 4, 2009. The colour scale on the left plot corresponds to the excess significance of each pixel in the RoI in Gaussian σ. The colour scale on the right plot shows the number of excess photons at each pixel in the RoI.

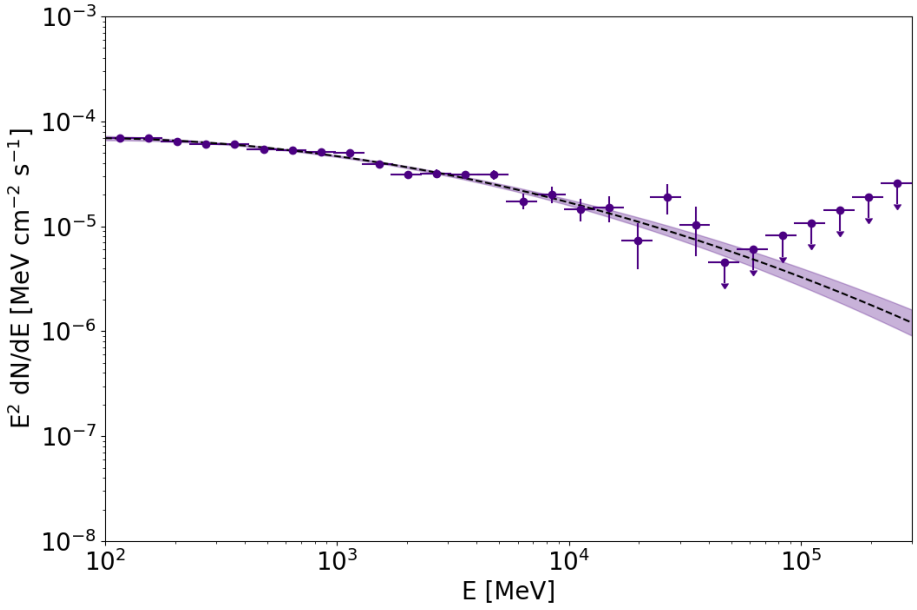

Figure 2.16: The one year averaged *Fermi*-LAT spectrum obtained for 3C 279 in the energy range 100 MeV-300 GeV. The data points are shown as circles along with the corresponding uncertainties. The shaded region represents the best fit interval to the spectra with the spectral parameters and their corresponding uncertainties tabulated in Table 2.1. The data is binned into eight energy bins per decade, with individual bins having a TS < 10 (roughly corresponding to a significance of $\sim 3\sigma$) considered as upper limits.

the fitting can either be set to a fixed value or allowed to vary over the energy range based on the shape of the spectrum in each energy bin.

The spectral shapes of all the background components are, by default, fixed but can also be set free during the fitting procedure. The output contains, for each energy bin, the source flux along with the corresponding uncertainties and upper limits for individual bins having a TS < 10, as well the TS and predicted counts in each bin. The SED obtained for 3C 279 is shown in Figure 2.16.

2.3.6 Gamma-ray Lightcurves

To study the temporal behaviour of the gamma-ray flux, the *Fermi*-LAT data can be binned into a sequence of time intervals with a likelihood routine applied to each bin separately using the *lightcurve* method. This step uses the same data selection criterion and input

model as the baseline analysis and, for each temporal bin, I re-fit the spectral parameters of all sources within 5° of the RoI centre as well as the normalisation factors of the background emission models.

The output file contains the time intervals (in MJD), the corresponding flux measurements along with their associated uncertainties, the TS values for each bin and the spectral parameters (in this case the index α and curvature β) along with their corresponding uncertainties. The resulting lightcurves generated for this one year analysis of 3C 279, binned in weekly intervals are shown in Figure 2.17.

Generating lightcurves for a large data selection and size of RoI can be a time consuming process and a number of options can be used to reduce the computation times required. It is possible to split the analysis of the separate time bins across multiple cores by enabling the *multithread* option. Furthermore, the *use_scaled_srcmap* option can be used to generate, for each time bin, an approximate source map using the source map of the baseline analysis scaled by the relative exposure*.

2.3.7 Extracting VHE photons

It is often useful to identify the highest energy photons associated with the source of interest. For example, measuring the VHE ($E_\gamma \geq 20$ GeV) photon emission can provide a robust method for constraining the location of the emission region (for example Brown (2013), Coogan et al. (2016), Acharyya et al. (2020); see Section 3.5). Furthermore, this method has also proved beneficial in probing the EBL attenuation in high-redshift sources (Armstrong et al. (2017)).

It is crucial to first ensure that the VHE photons being measured are genuinely associated with the source of interest rather than other sources such as the isotropic and Galactic diffuse background emission. This is done using the *gtsrcprob* routine which calculates the probability of each detected photon being associated with a source in the model by

*This option has been found to speed up the computation times by at least a factor of 2 while only resulting in a slight loss of accuracy in model evaluation. For a point source analysis spanning daily to yearly timescales, the loss of accuracy should be < 2%. See `https://fermipy.readthedocs.io/en/latest/advanced/lightcurve.html`, accessed on 14/03/2021.

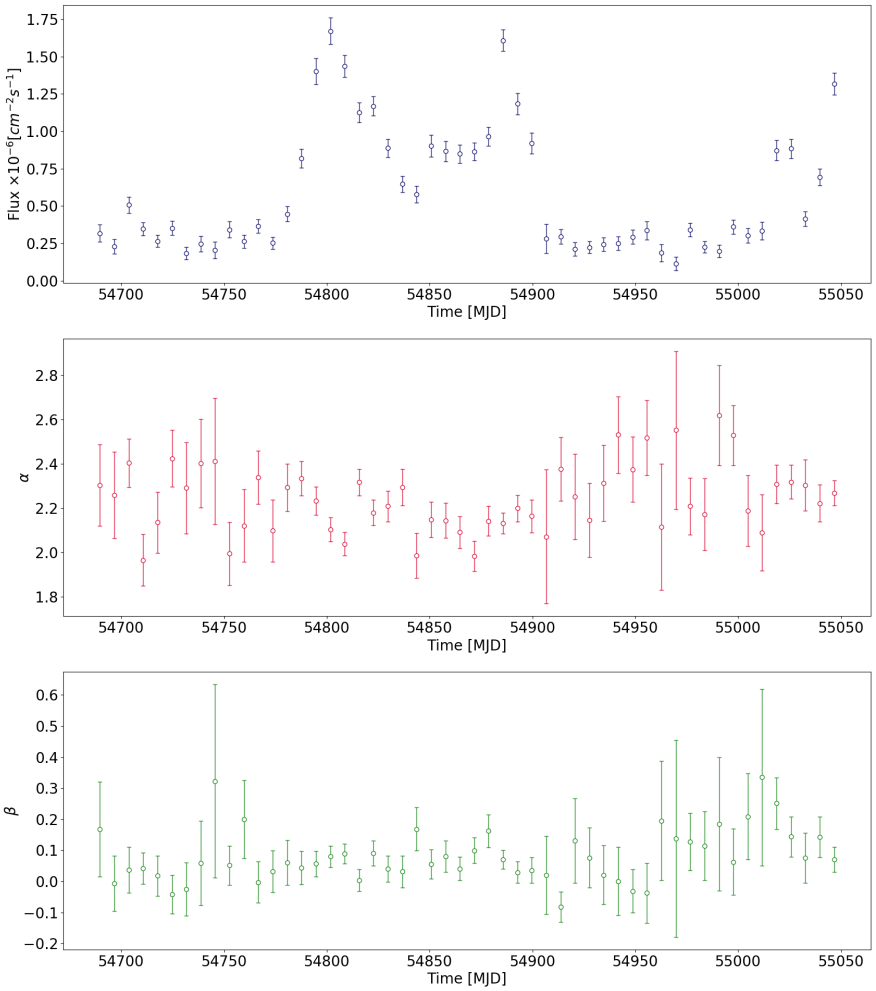

Figure 2.17: Upper panel: The gamma-ray lightcurve for 3C 279 observed between August 4, 2008 and August 4, 2009 binned in weekly periods. Middle panel: The weekly variation of the spectral index, α, during the corresponding interval. Lower panel: The weekly variation of the spectral curvature, β, during the corresponding interval. The errors in all three plots are purely statistical and only data points with TS $\geq$ 10 are shown.

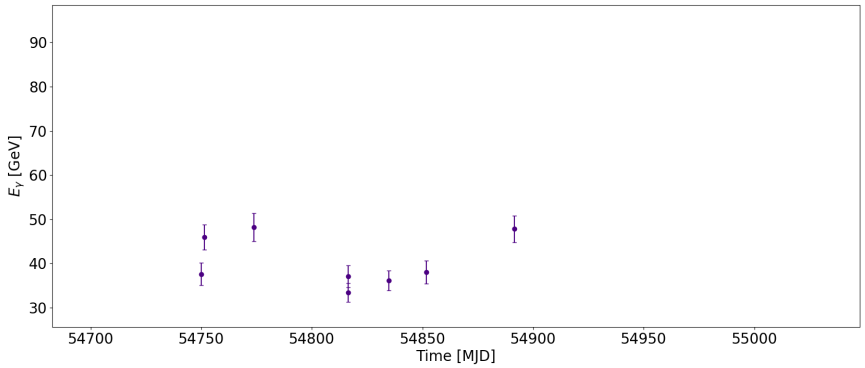

Figure 2.18: The detected energy, E_γ, of the individual high energy photons detected with the *Fermi*-LAT over the one year observation period as a function of time for 3C 279. All energies are in the rest frame of the galaxy. Only photons with energy $E_\gamma \geq 20$ GeV and a probability of $\geq 99\%$ for originating from 3C 279 are shown.

applying a likelihood routine to the convolution of the source model with the instrument response.

Before this step, it is necessary to account for the diffuse components using another *Fermi* science tool *gtdiffrsp* and adding the response to the input data. This tool calculates the integral of the convolution of the diffuse source model and the instrumental response function over solid angle and is computationally quite intensive as the integration is performed, in principle, over the entire sky.

Figure 2.18 shows a lightcurve of the VHE photons emitted from within a radius of 0.1° around 3C 279 and having a $\geq$ 99 % probability of originating from 3C 279 over the one year observation period investigated. A radius of 0.1° is chosen based on the 68 % containment angles for both FRONT and BACK event types in the VHE regime (see Figure 2.3). The uncertainties associated with the photon energies are evaluated using the energy resolution of the *Fermi*-LAT (see Figure 2.6).

2.4 Conclusion

In this chapter, the field of space based gamma-ray astronomy has been introduced. This includes a review of some historical telescopes like *Cos B* and *CGRO* as well as still active

experiments like *INTEGRAL* and *AGILE*. The discussion focuses on a description of the components of each detector, the energy range covered and some of the key scientific outputs at the time of writing.

The second half of the chapter focuses solely on the *Fermi*-LAT beginning with a discussion on the design and methodology of the various components, the algorithms used in event reconstruction as well as background rejection and a summary of the performance and sensitivity in terms of angular and energy resolution.

Finally, the steps involved in a typical data analysis pipeline are discussed in detail. This includes an overview of the initial filtering applied to the data extracted from the server, a step-by-step discussion of the methods used in pre-computing the binned response, and a description of the different components in the source model including the diffuse background models. This is followed by an outline of the steps involved in the likelihood analysis before moving on to more advanced analysis techniques such as generating a gamma-ray lightcurve and extracting the photon information from the data.

The aim of this chapter is to set the scene for Chapter 3, where I conduct a detailed investigation of the nine brightest FSRQs observed with the *Fermi*-LAT, aiming to constrain the size and location of the emission region.

Chapter 3

Locating the gamma-ray emission region in the brightest *Fermi*-LAT Flat Spectrum Radio Quasars

As discussed in Chapter 1, Flat Spectrum Radio Quasars (FSRQs) are a subclass of blazars characterised by strong, broad emission lines (Urry and Padovani (1995))). Being closely oriented with our line of sight, the emission from these objects is highly Doppler-boosted, making them some of the brightest objects in the gamma-ray sky. The close orientation of the jet to the line-of-sight renders the resolution of structures within the jet difficult, and consequently uncovering the location and origin of the emission remains one of the most active areas of research. In this respect, the Large Area Telescope (LAT) on board the *Fermi* satellite (Atwood et al. (2009)), discussed in Chapter 2, has been particularly

important and this chapter presents a study of the location of the emission region in the brightest FSRQs detected with the *Fermi*-LAT.

3.1 Introduction

Localizing the gamma-ray emission is an indirect process and a variety of different methods have been used previously. The emission is assumed to be coming from compact regions, supported by the rapid flux variability found in these objects. Timescales of the order of a few hours have been detected in several FSRQs, for example 3C 454.3 (Abdo et al. (2011)), PKS 1510-089 (Brown (2013), Saito et al. (2013)) and 4C 21.35 (Tanaka et al. (2011)). There is also evidence of timescales as short as a few minutes, as has been reported in the cases of CTA 102 (Shukla et al. (2018)) and 3C 279 (Ackermann et al. (2016)).

Assuming constant jet geometry, the size of the emission region, r, can be used to infer the distance from the supermassive black hole (SMBH), R, using r = ψR, where ψ is the semi-aperture opening angle of the jet (Ghisellini and Tavecchio (2009), Dermer et al. (2009)). This relation has been used to constrain the location of the emission region to be close to the base of the jet. For example, in a study of 3C 454.3, 3C 273 and 4C 21.35 undertaken by Foschini et al. (2011a) using $\sim$ 2 years of *Fermi*-LAT observations, the emission was constrained to be from within the broad line region (BLR) under the assumption that the full width of the jet is responsible for the emission.

Further arguments towards BLR origin are based on evidence of a spectral cut-off at GeV energies. This has been interpreted as a consequence of photon-photon pair production of gamma-rays with the Helium Lyman recombination continuum within the photon-rich BLR environment (Poutanen and Stern (2010), Stern and Poutanen (2014)). However, this interpretation has been questioned by Harris et al. (2012) who found the location of the cut-off inconsistent with the absorption model proposed. A cut-off in the spectrum can also be the consequence of a break in the energy distribution of the emitting electrons (Dermer et al. (2015)).

Other studies suggest the emission originates farther out, on parsec scale distances from the SMBH, and thus within the molecular torus (MT) region. Some of these studies use multi-wavelength observations of a single source, which have revealed that gamma-ray flares are often accompanied by flares at optical or radio wavelengths which are known to be resolved to parsec scale distances from the SMBH (Marscher et al. (2010), Agudo et al. (2011), Jorstad et al. (2013)). For instance, Marscher et al. (2010) studying optical, radio and gamma-ray flares in PKS 1510-089 found a single emission feature to be a superluminal knot outside the BLR. While emission at parsec scales would appear to contradict the short-term variability timescales observed in these objects, the two can be reconciled by assuming localised emission in turbulent cells (Giannios et al. (2009), Giannios (2013)).

The observation of very high energy (VHE) photons ($E_\gamma \geq 20$ GeV) also supports the theory of emission from outside the BLR (Donea and Protheroe (2003), Liu and Bai (2006)). VHE photons would be expected to be severely attenuated by interactions with the photons in the BLR and their detection is difficult to explain if the emission were to originate in regions near the central engine. At the time of writing, 8 FSRQs have been detected at $E_\gamma \geq 100$ GeV, of which 3C 279 (Errando et al. (2008), MAGIC Collaboration et al. (2008)), PKS 1510-089 (Cortina (2012), Abramowski et al. (2013)) and 4C 21.35 (Mose Mariotti (2010), Aleksić et al. (2011)) are included in this study *. In addition, Pacciani et al. (2014), studying high energy flares from a sample of FSRQs using multi-wavelength SED modelling, found the emission to be located significantly outside the BLR.

A possible solution to accommodate both the short variability timescales and VHE photons observed is to abandon the one-zone emission model and invoke the presence of multiple emission regions. Multi-zone emission models have been proposed to interpret the VHE observations of misaligned AGN (for example Lenain et al. (2008), Brown and Adams (2011)) as well as the multi-wavelength spectral distribution of blazars (for example PKS 1510-089 (Nalewajko et al. (2012))). Furthermore, it has been suggested that these multiple simultaneously active emission regions lie at various points throughout the jet, both in the BLR and MT (for example PKS 1510-089 (Brown (2013))). In a study of the absorption

*`http://tevcat.uchicago.edu/`, accessed on 11/06/20.

of VHE photons in the BLR field of FSRQs, Böttcher and Els (2016) suggest that the opacity constraints derived can be circumvented by resorting to multi-zone models. In such a model, the GeV and VHE emission would not be produced co-spatially, with the latter being emitted at a scale of several parsecs from the central engine.

The detection of 4C 21.35 with MAGIC (Aleksić et al. (2011)) has been explained by invoking the presence of axion-like particles (ALPs; Tavecchio et al. (2012)). ALPs (Weinberg (1978)) are light, neutral bosons and have been predicted by the extension of the standard model in particle physics. Gamma-rays produced inside the BLR are assumed to oscillate into ALPs, which do not interact with BLR photons and are therefore not absorbed until they are converted back into photons in magnetic fields outside the BLR (Galanti et al. (2019)). This leads to a considerable fraction of VHE photons escaping absorption inside the BLR. Multiple experiments are in operation to confirm the presence of ALPs (see Graham et al. (2015) for a review).

In this chapter, I investigate the gamma-ray emission from a sample of nine bright FSRQs detected with the *Fermi*-LAT during the first eight years of observations. In particular, I identify periods of high flux with the aim of using the increased photon statistics to constrain the characteristics and location of the emission region under the assumption of a leptonic model for the origin of the gamma-rays. This is followed by a study of the VHE ($E_\gamma \geq 20$ GeV) photon emission from each source. More specifically, I want to:

- identify the shortest variability timescales for the two brightest flare periods in each source and understand the implications on the size and location of the emission region;
- investigate further evidence for either BLR or MT emission in the flare spectra such as a possible spectral cut-off and evidence for energy dependent cooling timescales;
- determine whether the VHE emission observed with the *Fermi*-LAT for the sample is compatible with BLR origin and what the findings tell us about the nature of the emission region(s);

- assess whether there is an overarching trend in the results obtained for the sources and consider how they compare with other studies in the literature.

3.2 Source Selection and Data Reduction

The main goal of this investigation is to locate the origin of the gamma-ray emission in FSRQs. This led to a three step process in the identification of suitable sources, primarily governed by having sufficient photon statistics to allow for a detailed study of the gamma-ray emission. The first step involved surveying the *Fermi*-LAT 8 year catalog of detected sources, the 4FGL catalog (The *Fermi*-LAT collaboration (2019a)), for point sources identified as FSRQs and ordering these by the detection significance of each identification.

It was also desirable to choose from these bright FSRQs sources having flaring episodes with averaged daily fluxes $\geq 10^{-6}$ cm^{-2} s^{-1} within uncertainties of 1σ above 100 MeV as reported in the *Fermi*-LAT list of monitored sources[†]. Finally, it was essential that all the identified sources had known redshifts as this is important for interpretation. The final sample of nine sources chosen for this study is shown in Table 3.1.

The data reduction routine applied is described in detail in Section 2.3. To summarise, I select all *SOURCE* class events from both the FRONT and BACK of the detector observed between modified Julian dates (MJD) 54682.66 and 57604.66. This corresponds to midnight on the August 4, 2008 until midnight on August 4, 2016. I consider the energy range 100 MeV-300 GeV and a region of interest (RoI) with radius 15° centred on each source.

The initial model for each analysis consisted of all sources within 20° of the RoI centre with the spatial positions of each source given by the RA and DEC obtained from the 4FGL catalog (The *Fermi*-LAT collaboration (2019a)). Also included in the model were the most recent templates for the isotropic and Galactic diffuse emission, iso_P8R3_SOURCE_V3_v1.txt and gll_iem_v07.fits respectively (see Section 2.3.3).

The analysis began with an initial automatic optimisation of the RoI by iteratively fitting

[†]`https://fermi.gsfc.nasa.gov/ssc/data/access/lat/msl_lc/`, accessed on 11/03/2021.

the sources. This ensures all parameters are close to their global likelihood maxima. The spectral normalisation of all modelled sources within the RoI were left free as were the normalisation factor of both the isotropic and Galactic diffuse emission templates. Furthermore, the spectral shape parameters of all sources within 5° of the centre of the RoI were left free to vary while those of other sources were fixed to the values reported in the 4FGL catalog (The *Fermi*-LAT collaboration (2019a)).

The *gtfindsrc* routine was then applied to search for any additional point sources present in the model and not included in the 4FGL catalog. No significant additional point sources were detected indicating that all sources in the model had been accounted for. A binned likelihood analysis was performed to obtain the spectral parameters best describing the data during the eight year observation period.

The significance of the gamma-ray emission from each source was evaluated using the maximum likelihood test statistic (TS). The TS is defined as the log likelihood ratio between the maximized likelihoods with and without an additional source, L_1 and L_0 respectively (Mattox et al. (1996)):

$$\mathrm{TS} = -2\ln\left(\frac{L_0}{L_1}\right) \tag{3.1}$$

During the likelihood analysis, eight sources in the sample were found to be best modelled by a log parabola:

$$\frac{dN}{dE} = N_0\left(\frac{E}{E_0}\right)^{-\alpha-\beta\ln\left(\frac{E}{E_0}\right)} \tag{3.2}$$

where N_0 is the normalisation in units of photons $\mathrm{cm}^{-2}\mathrm{s}^{-1}\mathrm{MeV}^{-1}$, E_0 is the pivot energy in MeV, α the spectral index and β the curvature.

The brightest source in the sample, 3C 454.3, was found to be best modelled by a power law with super exponential cut-off:

$$\frac{dN}{dE} = N_0\left(\frac{E}{E_0}\right)^{-\gamma}\exp\left(-\frac{E}{E_{\mathrm{cut}}}\right)^{\alpha} \tag{3.3}$$

where γ and α are index1 and index2 respectively and E_{cut} is the cut-off energy in MeV.

The resulting eight year averaged spectra of all sources are shown in Figure 3.1 with the spectral parameters obtained from the fit tabulated in Table 3.1 along with the observed time-averaged flux and TS values of each source.

3.3 Gamma-ray Lightcurves

To study the temporal behaviour of the gamma-ray flux, the eight year *Fermi*-LAT data were initially binned monthly with a likelihood routine applied to each bin separately using the *lightcurve* method (see Section 2.3.6). The spectral parameters of all sources within 5° of the RoI centre were left free for each bin as were the normalisation factors of the background emission models. The resulting lightcurves are shown in Figure 3.2 along with the corresponding uncertainties. Only time intervals having TS $\geq$ 10 (roughly corresponding to a significance of 3σ) were considered.

In order to pursue an analysis of the location of the emission region, it is necessary to identify periods of flaring in the lightcurves. There is no general consensus on how to define a flaring period (for example Resconi et al. (2009), Meyer et al. (2019)). A study by Nalewajko (2013) defines flares as a contiguous period of time associated with a flux peak having a flux higher than half the peak value of the entire observation. While this approach is intuitive, the identification of the flux peaks considered and, in particular, the treatment of overlapping flare periods is arbitrary.

Meyer et al. (2019) propose a simple two-step procedure based on the Bayesian Block algorithm (Scargle et al. (2013)), an approach designed to find a series of segments in the lightcurves over which the flux measurements are compatible to within observational uncertainties. This method identifies blocks of data points having a flux higher than both the preceding and subsequent blocks and then proceeding downwards in both directions as long as the blocks have successively lower fluxes. This approach allows to objectively split the lightcurves into groups of intervals corresponding to flare and quiescent periods.

My definition of flares is primarily designed to identify the periods of highest flux during the eight year dataset, and I define a flare by combining these two approaches. The method

Table 3.1: List of FSRQs selected for this study along with their right ascensions (RA) and declinations (DEC) in degrees (The *Fermi*-LAT collaboration (2019a)) and redshifts (z; references given below). Also shown are the results of the eight year likelihood analysis in the energy range 100 MeV-300 GeV. All sources, with the exception of 3C 454.3, were found to be best modelled by a log parabola (see equation 3.2) with the spectral parameters being the spectral index (α), spectral curvature (β) and the pivot energy (E_0). 3C 454.3 was found to be best modelled by a power law with a super exponential cut-off (see equation 3.3) having the spectral parameters index1 (γ), index2 (α), pivot energy (E_0) and the cut-off energy ($E_{\rm cut}$). The final two columns list the observed eight year time-averaged flux and the TS values (see equation 3.1) of each source obtained from the likelihood analysis.

Source	RA [deg]	DEC [deg]	z	E_0 [MeV]	α	β	Flux [10^{-7} photons cm^{-2}s^{-1}]	TS
CTA 102	338.15	11.73	1.0320 ± 0.0030[1]	414.1	2.32 ± 0.01	0.078 ± 0.005	4.19 ± 0.04	75211
B2 1520+31	230.55	31.74	1.4886 ± 0.0002[2]	593.4	2.40 ± 0.01	0.059 ± 0.006	3.10 ± 0.03	63775
PKS 1510-089	228.22	-9.11	0.3600 ± 0.0020[3]	743.5	2.39 ± 0.01	0.045 ± 0.003	8.71 ± 0.07	180884
PKS 1502+106	226.10	10.49	1.8381 ± 0.0015[4]	496.7	2.18 ± 0.01	0.075 ± 0.005	3.04 ± 0.03	66529
PKS 1424-41	216.99	-42.11	1.5220 ± 0.0002[5]	677.7	2.12 ± 0.01	0.069 ± 0.003	4.87 ± 0.04	122369
3C 279	194.04	-5.79	0.5362 ± 0.0004[6]	442.1	2.32 ± 0.01	0.049 ± 0.004	5.27 ± 0.04	107214
4C 21.35	186.23	21.38	0.4320 ± 0.0010[7]	393.7	2.31 ± 0.01	0.031 ± 0.004	4.09 ± 0.03	88689
PKS 0454-234	74.26	-23.41	$1.0030 \pm$ NA[8]	477.7	2.12 ± 0.01	0.069 ± 0.005	2.87 ± 0.03	72177

Source	R.A [deg]	DEC [deg]	z	E_0 [MeV]	γ	α	$E_{\rm cut}$ [MeV]	Flux [10^{-7} photons cm^{-2}s^{-1}]	TS
3C 454.3	343.50	16.15	0.8590 ± 0.0001[9]	413.3	1.75 ± 0.01	0.283 ± 0.005	47.91 ± 3.92	15.63 ± 0.38	871437

Redshift references : [1]: Monroe et al. (2016), [2]: Pâris et al. (2014), [3]: Thompson et al. (1990), [4]: Hewett and Wild (2010), [5]: Gaia Collaboration (2018), [6]: Marziani et al. (1996), [7]: Osterbrock and Pogge (1987), [8]: Stickel et al. (1989), [9] Paturel et al. (2002).

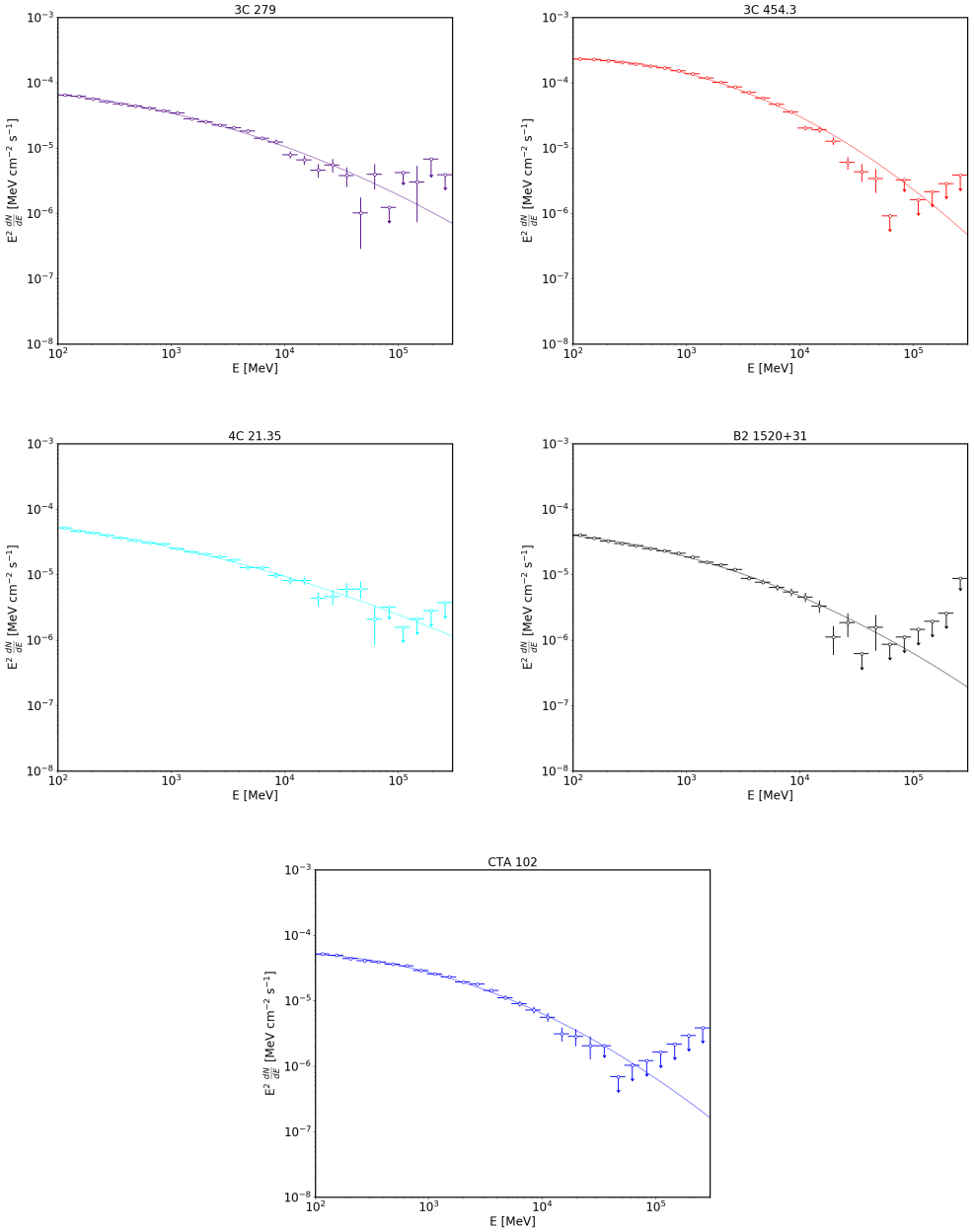

Figure 3.1: **a.** The eight year time-averaged *Fermi*-LAT spectra obtained for 3C 279, 3C 454.3, 4C 21.35, B2 1520+31 and CTA 102 in the energy range 100 MeV-300 GeV, shown in separate plots for clarity. The data points are shown as circles along with the corresponding uncertainties. The curves represent the best fits to the spectra with the spectral parameters for each source tabulated in Table 3.1. The data are binned into eight energy bins per decade, with individual bins having a TS < 10 considered as upper limits.

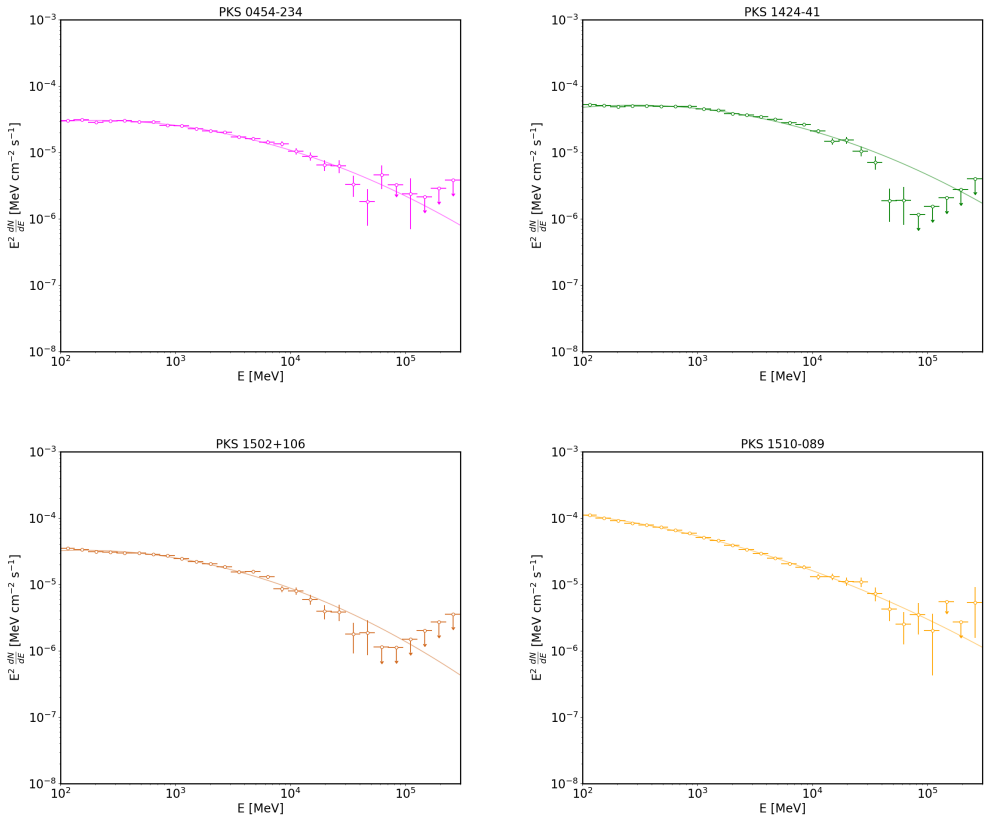

b. The eight year time-averaged *Fermi*-LAT spectra obtained PKS 0454-234, PKS 1424-41, PKS 1502+106 and PKS 1510-089 in the energy range 100 MeV-300 GeV, shown in separate plots for clarity. The data points are shown as circles along with the corresponding uncertainties. The curves represent the best fits to the spectra with the spectral parameters for each source tabulated in Table 3.1. The data are binned into eight energy bins per decade, with individual bins having a TS < 10 considered as upper limits.

identifies local peaks in flux defined as bins having a flux more than both the preceding and succeeding bin. I then keep going in both directions as long as the corresponding bins are successively lower in flux. I then impose the following conditions: (1) The peak of the flare must have a flux greater than twice the average flux during the entire observation period; (2) Each bin in the flare must also have a flux greater than the average flux during the observation period. Once this is no longer satisfied, I extend the final ranges by one time bin on each side to mark the onset and end of the flares.

Also shown in Figure 3.2 are the time periods satisfying my definition of a flare. Although some objects show several flares based on my definition, this study focuses on the two

brightest flares for each object indicated by darker shaded regions. These are likely to provide sufficient statistics to search for the shortest variability timescales and investigate the presence of a spectral cut-off or energy dependence in the cooling timescales during these periods.

For the identified flare periods, I search for variability on shorter timescales by re-analysing the data with finer binning including daily, 6 hour and 3 hour bins which still satisfy the TS $\geq$ 10 criterion. The choice of 3 hour bins as a minimum is motivated by the fact that this is roughly the time taken for the *Fermi*-LAT to complete a full scan of the sky (2 orbits). The resulting 3 hour binned lightcurves for each flare period considered in this study are shown in Appendix A.

3.4 Constraining the size and location of the Emission region

3.4.1 Variability timescales

The observed flux variability can be characterised by calculating the time taken for the flux to increase or decrease by a factor of 2. Known as the doubling or halving timescale, τ, this is defined by:

$$F(t) = F(t_0)2^{\tau^{-1}(t-t_0)} \tag{3.4}$$

where F(t) and F(t_0) are the fluxes at times t and t_0 respectively. A least squares routine was performed to provide the best fit to equation 3.4 for three consecutive flux measurements in the 3 hour binned lightcurves of each flare period. From these, we can calculate the intrinsic timescales, $\tau_{\rm int} = \tau/(1+z)$, where z is the redshift of each source.

The choice of three consecutive observations in the fitting procedure is motivated by it being the minimum number of points required to estimate the variability timescale given the number of free parameters in equation 3.4. As I am going through every single point

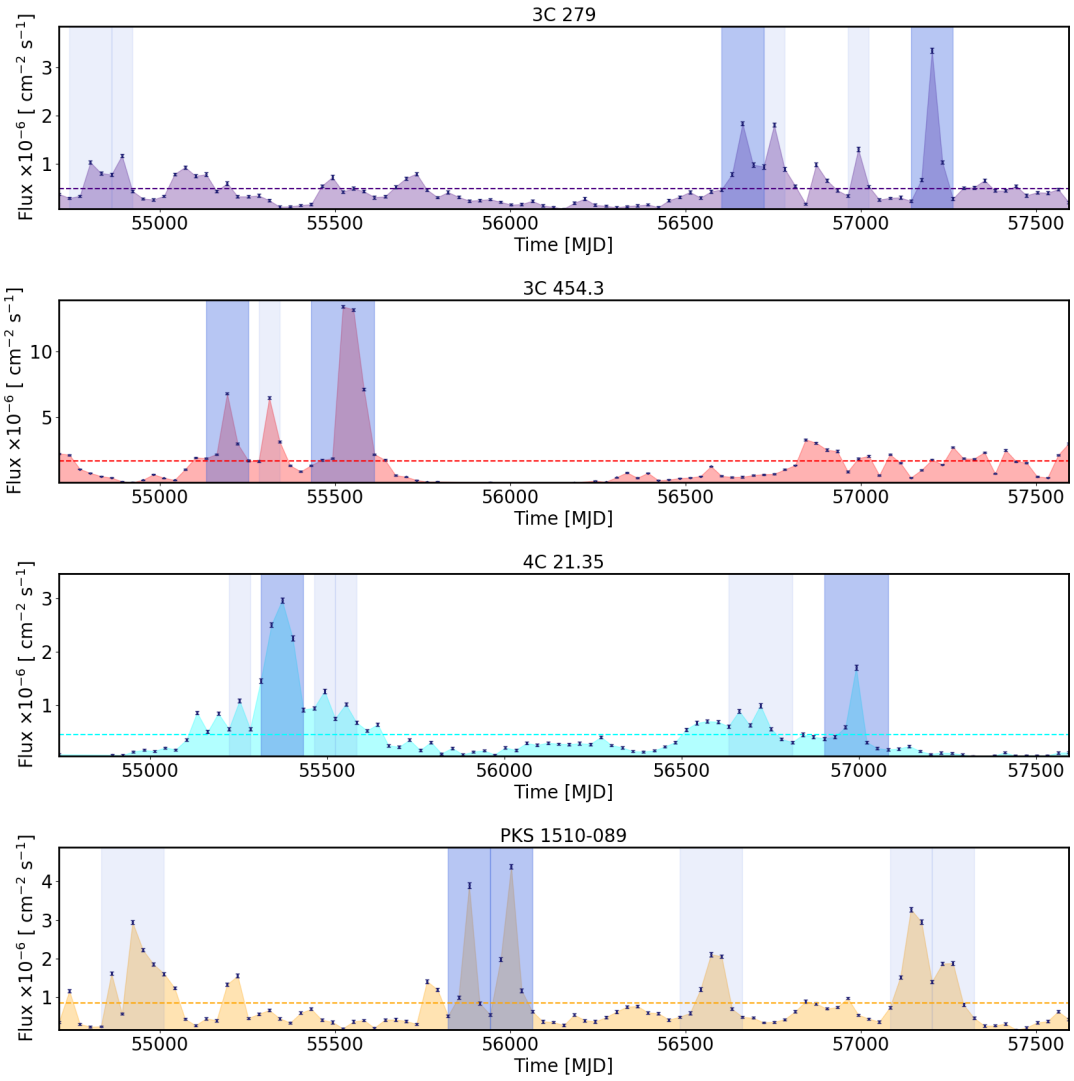

Figure 3.2: **a.** The eight year gamma-ray lightcurves for 3C 279, 3C 454.3, 4C 21.35 and PKS 1510-089 between August 4, 2008 (MJD 54682.66) and August 4, 2016 (MJD 57604.66) binned in monthly periods. The errors are purely statistical and only data points with TS $\geq$ 10 are shown. The horizontal lines indicate the average flux of each source during the entire period. The blue shaded regions indicate periods of flaring activity, with the dark blue shaded regions being the time intervals studied in this investigation.

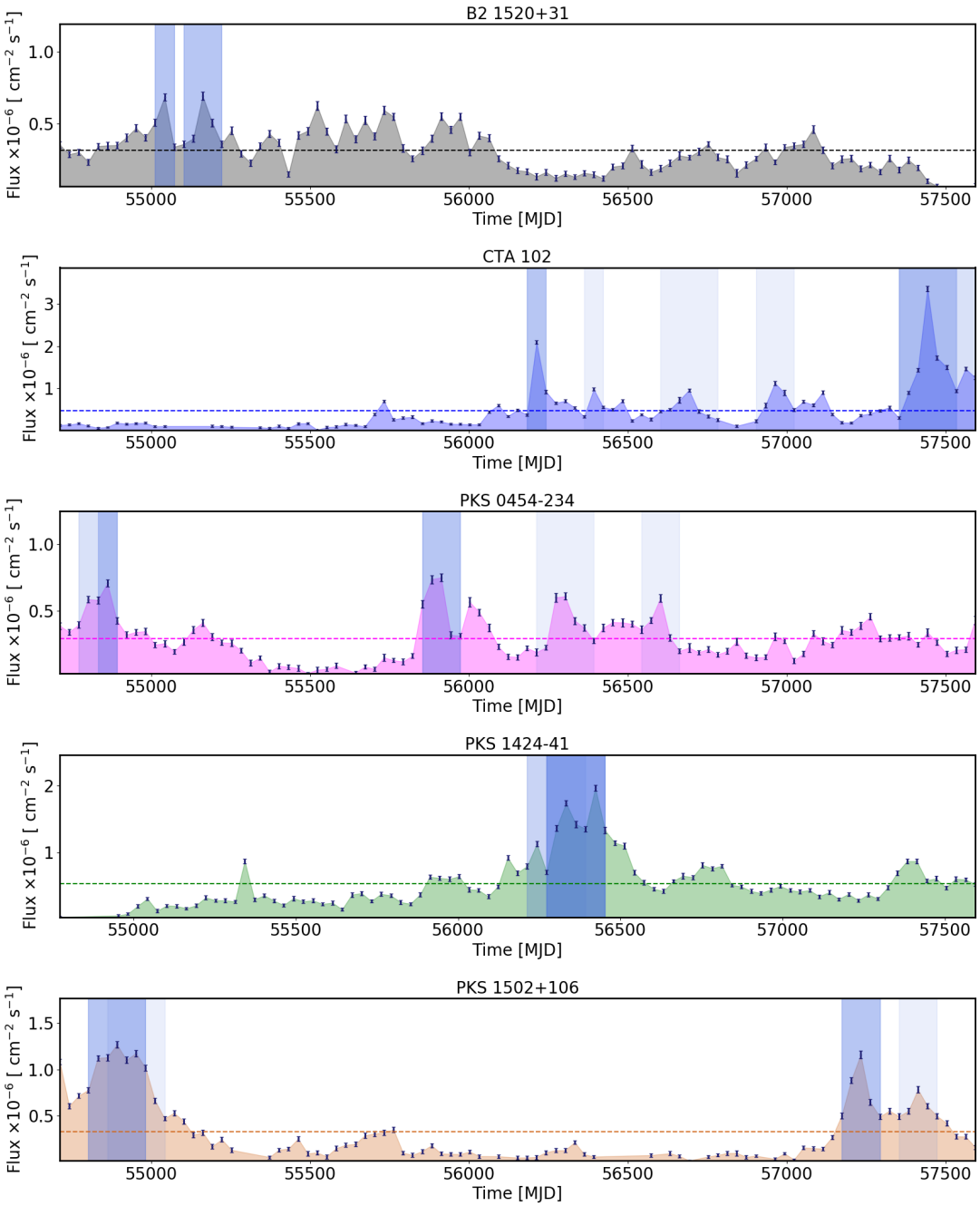

b. The eight year gamma-ray lightcurves for B2 1520+31, CTA 102, PKS 0454-234, PKS 1424-41 and PKS 1502+106 between August 4, 2008 (MJD 54682.66) and August 4, 2016 (MJD 57604.66) binned in monthly periods. The errors are purely statistical, and only data points with TS ≥ 10 are shown. The horizontal lines indicate the average flux of each source during the entire period. The blue shaded regions indicate periods of flaring activity, with the dark blue shaded regions being the time intervals studied in this investigation.

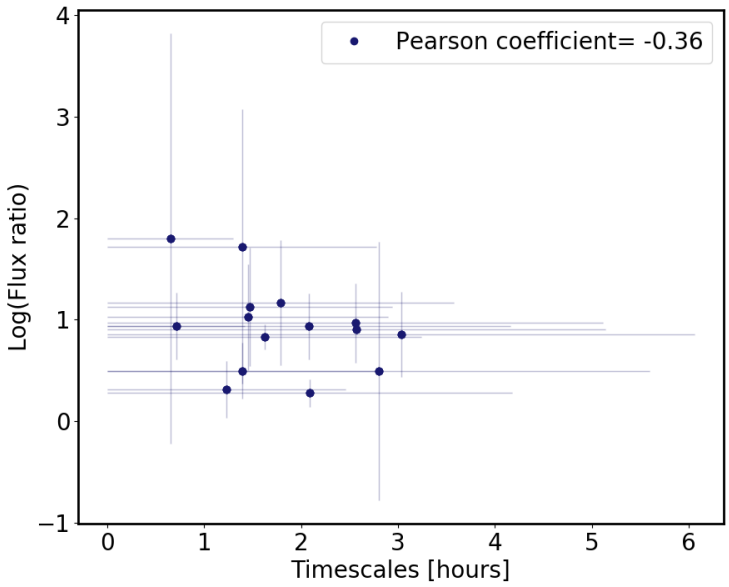

Figure 3.3: The logarithm of the ratio of the fluxes against the rise timescales (i.e. those associated with an event corresponding to an increase in flux) from Table 3.2. A Pearson coefficient of -0.36 indicates mild anti-correlation.

in the lightcurve sequentially, this method should be able to give a good estimate for variability.

However, an important caveat of using equation 3.4 is that it considers flux ratios rather than the flux values, which as seen in Figure 3.3 raises the possibility of the timescales anti-correlating with the logarithm of the ratio of the fluxes for fixed time differences between observations. Nevertheless, the measurement of doubling timescales is common in the study of FSRQs (for example Foschini et al. (2011a), Saito et al. (2013)) and I use the same method for the purposes of comparability. As seen in Section 3.6, the results I obtained are compatible with other studies of the same flares.

The fastest variability timescales having a statistical significance of at least 3σ found for the flares studied are tabulated in Table 3.2. Interestingly, only 3 of the 18 fastest timescales are associated with an event corresponding to a decrease in flux. This could be interpreted as evidence for fast-rise exponential decay (FRED) type flares, resulting from the injection of energetic particles on shorter timescales than the timescales associated with subsequent

cooling processes.

A further caveat when investigating a sample spanning a large range of redshifts, in conjunction with considering a fixed time difference between observations when calculating the variability timescales, is a potential bias towards rapidly varying sources at high redshift. As seen in Table 3.2, the three shortest variability timescales measured are associated with the three farthest FSRQs in the sample, namely B2 1520+31, PKS 1424-41 and PKS 1502+106. This could be a consequence of the Malmquist bias, an effect leading to the preferential detection of intrinsically brighter objects to greater distances. This selection bias affects flux-limited surveys, with AGN sources which are more luminous being detectable to higher redshifts, resulting in a trend of increase in luminosity with redshift as seen for my sample in Figure 3.4.

Since the luminosities strongly correlate with redshift, any correlation between the mass of the SMBH and luminosity would also result in it corellating with redshift too. If the variability timescales scale with the mass of the SMBH, it would also be redshift dependent. Nevertheless, selecting a sample of the brightest sources is common in the study of FSRQs (for example Meyer et al. (2019)) and the choice of sample is motivated by the necessity to have sufficient photon statistics in order to allow for a detailed study of the gamma-ray emission. As seen in Section 3.6, the choice of sample also facilitates comparison with other studies of the same flares in literature.

Using geometric arguments, the intrinsic variability timescales can be used to constrain the size of the emission region:

$$r \leq c\delta\tau_{\mathrm{int}} \tag{3.5}$$

where r is the size of the emission region, c is the speed of light and δ is the Doppler factor of the jet. Wherever possible, I use the measurements of δ from Jorstad et al. (2017) for this calculation. The measurements are based on the finding in Jorstad et al. (2005) that the flux density of majority of the 43 GHz superluminal knots decrease faster than the rate at which the knots expand, implying that the decay is a result of radiative losses instead of

Table 3.2: Summary of the shortest intrinsic variability timescales in hours for each source during the flare periods investigated which have a significance of at least 3σ. The times listed, T_{start} and T_{stop} respectively, are in MJD, with the corresponding fluxes in units of 10^{-6} photons cm^{-2}s^{-1}. The intrinsic variability timescales, τ_{int}, are calculated from the observed characteristic timescales τ (see equation 3.4) with $\tau_{int} = \tau/(1+z)$, where z is the redshift of each source. The last column indicates whether the variability event results from a rise (R) or decay (D) in the flux.

Source	Flare Peak	T_{start} [MJD]	T_{stop} [MJD]	$Flux_{start}$ [10^{-6} photons cm^{-2}s^{-1}]	$Flux_{stop}$ [10^{-6} photons cm^{-2}s^{-1}]	τ_{int} [hours]	Significance σ	Rise/Decay
3C 454.3	Dec 2009	55191.89	55192.02	1.45 ± 0.73	4.48 ± 1.31	1.47 ± 0.32	4.59	R
3C 454.3	Nov 2010	55516.76	55516.89	14.47 ± 1.84	24.68 ± 2.90	2.80 ± 0.39	7.27	R
CTA 102	Sept 2012	56191.76	56191.89	1.10 ± 0.62	3.00 ± 0.83	1.45 ± 0.26	5.55	R
CTA 102	Feb 2016	57439.89	57440.01	17.81 ± 2.09	4.81 ± 0.87	1.09 ± 0.18	6.02	D
B2 1520+31	July 2009	55046.64	55046.77	0.11 ± 0.08	0.65 ± 0.67	0.65 ± 0.11	5.85	R
B2 1520+31	Nov 2009	55146.64	55146.77	0.44 ± 0.24	1.05 ± 0.38	3.03 ± 0.84	3.61	R
PKS 1510-089	Nov 2011	55880.24	55880.37	0.43 ± 0.19	1.39 ± 0.52	1.79 ± 0.27	6.57	R
PKS 1510-089	Feb 2012	55966.24	55966.37	1.33 ± 0.65	7.42 ± 3.66	1.39 ± 0.41	3.40	R
PKS 1502+106	Feb 2009	54876.51	54876.64	2.79 ± 0.75	0.81 ± 0.34	0.86 ± 0.17	5.00	D
PKS 1502+106	July 2015	57216.01	57216.14	0.88 ± 0.28	1.79 ± 0.73	1.23 ± 0.08	14.71	R
PKS 1424-41	Jan 2013	56300.76	56300.89	0.46 ± 0.21	2.82 ± 0.91	0.71 ± 0.22	3.31	R
PKS 1424-41	Apr 2013	56393.64	56393.77	0.55 ± 0.26	1.45 ± 0.43	2.56 ± 0.61	4.21	R
3C 279	Dec 2013	56646.26	56646.39	4.14 ± 1.01	9.09 ± 1.53	2.08 ± 0.17	12.26	R
3C 279	June 2015	57196.99	57197.12	5.54 ± 1.96	2.06 ± 0.72	2.14 ± 0.65	3.28	D
4C 21.35	June 2010	55369.64	55369.76	1.39 ± 0.50	3.41 ± 0.77	2.57 ± 0.83	3.10	R
4C 21.35	Nov 2014	56975.14	56975.26	1.01 ± 0.48	1.74 ± 0.71	2.09 ± 0.15	13.54	R
PKS 0454-234	Jan 2009	54840.89	54841.01	0.69 ± 0.34	1.70 ± 0.54	1.62 ± 0.28	5.72	R
PKS 0454-234	Nov 2011	55896.01	55896.14	0.86 ± 0.44	2.47 ± 0.83	1.39 ± 0.24	5.73	R

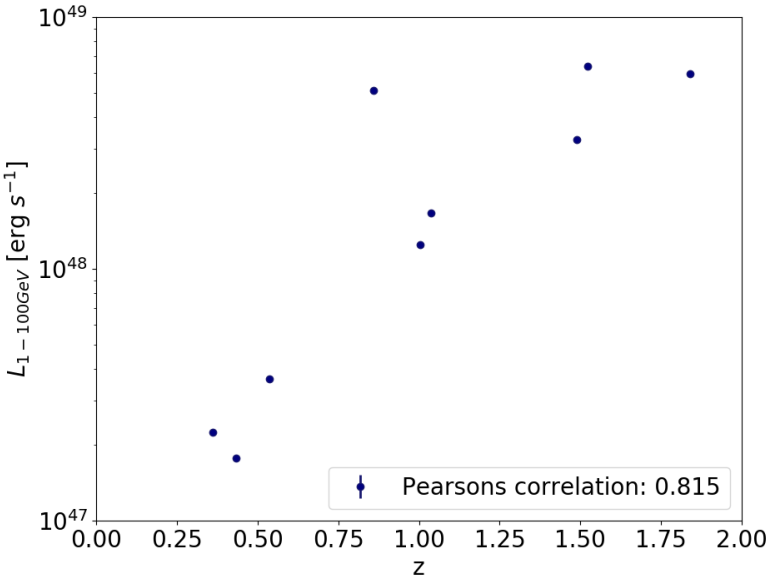

Figure 3.4: The distribution of gamma-ray luminosity against redshift for the sample of FSRQs investigated in this study. A Pearson coefficient of 0.82 indicates strong correlation.

adiabatic cooling. Under this assumption, the value of the Doppler factor , δ, was derived from the observed radio variability timescale, $\tau_{\rm var}$, luminosity distance, d_L and angular size of knot, s, using:

$$\delta = \frac{15.8 s d_L}{\tau_{\rm var}(1+z)} \tag{3.6}$$

If a measurement of δ is not available in literature I use a value of 10, considered typical for these objects (for example Foschini et al. (2011a)). The size of the emission region derived for each of the flares is reported in Table 3.3. Also given for comparison are the Schwarzschild radii for these objects calculated from the mass of the SMBH (Ghisellini et al. (2010)).

The measurement of the size of the emission region also allows for a simple back-of-the-envelope calculation of the energetics of the flare events. I consider the classical shock-in-jet model (for example Marscher and Gear (1985)), which assumes that instabilities in the flow can lead to the formation of an internal shock within the jet. The particles at the shock front

Table 3.3: Results for the size of the emission region, $r_{emission}$, obtained for both flare periods of each source. Also listed are the fastest intrinsic variability timescales, τ_{int}, in hours (see Table 3.2) as well as the average values of the Doppler factors, δ (Jorstad et al. (2017)) (see equation 3.5), used in the calculation. Where a Doppler factor is not available in the literature I use a value of 10, considered typical for these objects (for example Foschini et al. (2011a)). For comparison, the final column shows the Schwarzschild radius, r_s, for each source, calculated from the mass of the SMBH (Ghisellini et al. (2010)).

Source	Flare Peak	δ	τ_{int} [hours]	$r_{emission}$ [10^{13}m]	r_s [10^{13}m]
3C 454.3	Dec 2009	24.4	1.47 ± 0.32	3.87 ± 0.84	0.15
3C 454.3	Nov 2010	24.4	2.80 ± 0.39	7.38 ± 1.03	0.15
CTA 102	Sept 2012	30.5	1.45 ± 0.26	4.78 ± 0.86	0.15
CTA 102	Feb 2016	30.5	1.09 ± 0.18	3.59 ± 0.59	0.15
B2 1520+31	July 2009	10.0	0.65 ± 0.11	0.70 ± 0.12	0.37
B2 1520+31	Nov 2009	10.0	3.03 ± 0.84	3.27 ± 0.91	0.37
PKS 1510-089	Nov 2011	35.3	1.79 ± 0.27	6.82 ± 1.03	0.10
PKS 1510-089	Feb 2012	35.3	1.39 ± 0.41	5.30 ± 1.56	0.10
PKS 1502+106	Feb 2009	10.0	0.86 ± 0.17	0.93 ± 0.18	0.44
PKS 1502+106	July 2015	10.0	1.23 ± 0.08	1.33 ± 0.09	0.44
PKS 1424-41	Jan 2013	10.0	0.71 ± 0.22	0.77 ± 0.24	0.15
PKS 1424-41	Apr 2013	10.0	2.56 ± 0.61	2.76 ± 0.66	0.15
3C 279	Dec 2013	18.3	2.08 ± 0.17	4.11 ± 0.34	0.13
3C 279	June 2015	18.3	2.14 ± 0.65	4.23 ± 1.28	0.13
4C 21.35	June 2010	7.4	2.57 ± 0.83	2.05 ± 0.66	0.09
4C 21.35	Nov 2014	7.4	2.09 ± 0.15	1.67 ± 0.12	0.09
PKS 0454-234	Jan 2009	26.0	1.62 ± 0.28	4.55 ± 0.79	0.37
PKS 0454-234	Nov 2011	26.0	1.39 ± 0.24	3.91 ± 0.67	0.37

get accelerated due to diffuse shock acceleration processes. The cross-sectional radius of the shock, R_{shock}, is given by (Bromberg and Levinson (2009)):

$$R_{shock} = 2.5 \times 10^{-2.5} \left(\frac{L_{jet}}{10^{46} \mathrm{erg/s}} \right) \left(\frac{R_{BLR}}{0.1 \mathrm{pc}} \right)^{-1} \mathrm{pc} \tag{3.7}$$

where R_{BLR} is the radius of the BLR and L_{jet} is the power of the jet and can be approximated as $L_{jet} \sim \frac{L_\gamma}{\eta \Gamma^2}$ (Shukla and Mannheim (2020)), where L_γ is the gamma-ray luminosity, Γ the Lorentz factor of the jet and η the radiative efficiency of the jet, typically taken to be 0.1 (Nemmen et al. (2012)).

Equating the radius of the shock with the size of the emission region, a lower limit of the Lorentz factor can be obtained. For the June 2015 flare for 3C 279, the value of the

Lorentz factor is found to be $\Gamma \sim 65$. Assuming that the Doppler factor $\delta \sim \Gamma \sim 65$ (for example Foschini et al. (2011a), Shukla and Mannheim (2020)), this would give values of δ contrary to that measured in Jorstad et al. (2017), implying that this particular flare is incompatible with a shock-in-jet model and requires other models, for example models invoking magnetic reconnection within the jet (Giannios et al. (2009), Giannios (2013)).

With the size of the emission region accounted for, I then try to constrain its location. A small emission region does not automatically imply emission from near the central engine as over-densities of the plasma can occur throughout the jet, including within the MT. It has been proposed that these result from magnetic reconnection events (Giannios et al. (2009), Giannios (2013)) or the recollimation of the jet (Bromberg and Levinson (2009)).

A first order approximation of the distance of the emission region from the SMBH can be made by assuming a simple one-zone emission model in which the entire width of the jet is responsible for the emission. This assumption is supported by evidence of observed variability correlations at different frequencies (Ulrich et al. (1997)). However, FSRQs have also been known to exhibit orphan flares, for example gamma-ray flares with no counterpart at longer wavelengths (for example MacDonald et al. (2017)). As noted in Romero et al. (2017), while this assumption is an over-simplification of the jet geometry, it does allow for a valid first order approximation to localise the compact emission regions, and is complemented with the other methods discussed in the remainder of this section.

The size of the emission region, r, is then related to the distance of the emission region from the central engine, R, using:

$$r = \psi R \tag{3.8}$$

where ψ is the semi-aperture opening angle of the jet and has typical values between 0.1 - 0.25. (Ghisellini and Tavecchio (2009), Dermer et al. (2009)). The limits obtained are shown in Figure 3.5 which plots the distances of the gamma-ray emission regions from the central engine obtained for the two brightest flares together with the radius of the BLR (R_{BLR}) for each source (Ghisellini et al. (2010), Britto et al. (2015)).

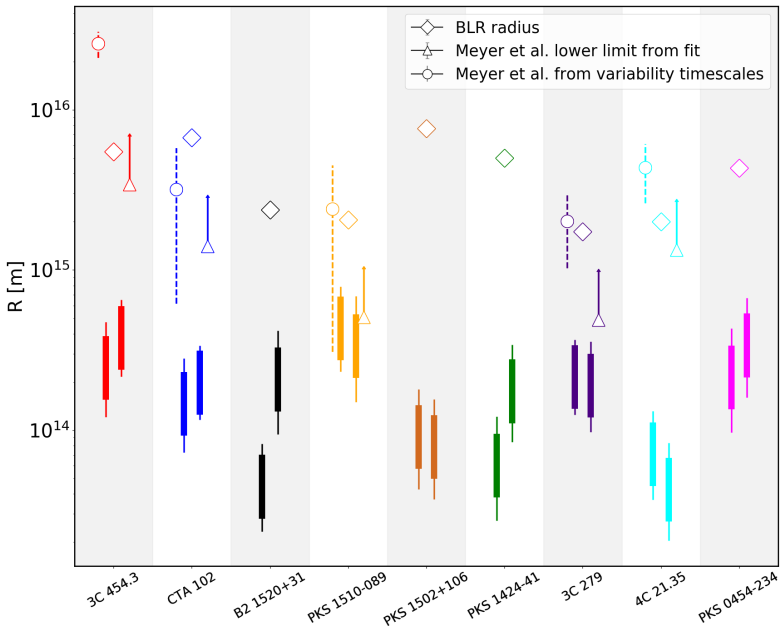

Figure 3.5: Limits on the distance of the gamma-ray emission regions from the central black hole obtained for both flares from each source are shown as solid shaded regions, with the earlier flare on the left. This calculation assumes the entire width of the jet to be responsible for the emission. The circles represent the limits on the corresponding distances calculated by Meyer et al. (2019) using variability considerations under the assumption of a conical jet model. The triangles represent lower limits obtained by Meyer et al. (2019) using fits to the gamma-ray spectra (M. Meyer, private communication). The diamonds represent the radius of the BLR (R_{BLR}) for each source taken from Ghisellini et al. (2010). For sources not reported in Ghisellini et al. (2010), R_{BLR} was calculated using $R_{BLR} = 10^{15} L_{disk,45}^{0.5}$ m from values of $L_{disk,45}$, the disk luminosity in units of 10^{45}erg s^{-1}, reported in Britto et al. (2015).

For comparison, I also show the corresponding distances reported in Meyer et al. (2019) who investigated five of the sample of FSRQs studied here (exact values obtained from M. Meyer, private communication). These distances were obtained using variability timescales (shown as circles) and from fits to the observed gamma-ray spectrum (shown as triangles). In general, I find the emission regions to be closer to the black hole than both sets of results reported in Meyer et al. (2019) and within the BLR for all sources.

3.4.2 Photon-photon pair production

The BLR is a photon-rich environment and the interaction between these photons and gamma-ray photons can lead to photon-photon pair production ($\gamma\gamma \rightarrow e^+e^-$). The MT has a much lower photon density than the BLR, meaning there is less likelihood of pair production in the MT compared to the BLR. Pair production manifests itself as an attenuation of the gamma-ray flux for emission coming from the inner regions of the BLR, whereas emission originating from the MT is not expected to have this spectral feature (Donea and Protheroe (2003), Liu and Bai (2006)).

Emission originating from the BLR would therefore be expected, in general, to be better described by a model with a cut-off (such as a log parabola) rather than a power law. It should be noted that the presence of a cut-off in the spectrum does not automatically imply BLR origin of emission; it can also be the consequence of a break in the energy distribution of the emitting electrons (Dermer et al. (2015)).

To search for the presence of a cut-off, each flare period was re-analysed in daily bins using the routine outlined in Section 3.2. This helped improve statistics at the high energy (1-300 GeV) end of the spectrum. In addition to a log parabolic model (see equation 3.2), I also fitted the spectra during the flare periods with a simple power law, defined as:

$$\frac{dN}{dE} = N_0 \left(\frac{E}{E_0}\right)^{-\gamma} \tag{3.9}$$

where γ is the spectral index, E_0 is the pivot energy in MeV and N_0 is the normalisation in units of photons $\mathrm{cm}^{-2}\mathrm{s}^{-1}\mathrm{MeV}^{-1}$.

To compare the fits provided by the two models, I performed an Akaike Information Criterion (AIC) test (Akaike (1974)) to determine which model fits the data better. The AIC of a model s is given by:

$$\mathrm{AIC}_s = -2\ln L_s + 2k_{f_s} \tag{3.10}$$

where L_s is the likelihood of the model s given the data and k_{fs} is the number of free parameters in the model.

In order to compare two models s and s', I use the difference in AIC values:

$$\Delta \mathrm{AIC}_{s,s'} = \mathrm{AIC}_s - \mathrm{AIC}_{s'} \tag{3.11}$$

which estimates how much more model s diverges from the true distribution than model s', also known as the relative Kullback-Leibler information quantities of the two models (Burnham and Anderson (2001), Harris et al. (2012)). Another way of interpreting this is to consider how much data would be lost by modelling the data by model s instead of model s'. This method is true for both nested and non-nested models (Findley et al. (1998)); for example, a power law is nested in a log parabola since every parameter in a power law is also present in a log parabola.

A log parabolic model has one extra free parameter relative to a power law model and an AIC test also balances the systematic error in a model with fewer parameters with the random errors of a model having more parameters (Bozdogan (1987)). A lower AIC means a better description of the data. An AIC difference of greater than 2 between two models means that the model with the higher AIC is significantly worse than the model with the lower AIC value (Lewis et al. (2011)). The AIC differences between the log parabolic and power law models found for each flare investigated in this work are tabulated in Table 3.4.

Two of the sources, 3C 454.3 and CTA 102, are found to favour a log parabola during both flares studied, suggesting emission from the BLR. Three further sources, namely 3C 279, 4C 21.35 and PKS 1510-089, are seen to favour a log parabola during one flare but the results are inconclusive during the other. The results for the remaining four sources are inconclusive during either flare. This broadly agrees with the results of Costamante et al. (2018), who investigated the presence of a cut-off in the spectra for a sample of 106 FSRQs with the highest significance in the Third *Fermi*-LAT catalog (Ackermann et al. (2015)) including all nine sources studied in this work. Evidence was found for a cut-off in 1/3 of the sources, and it was concluded that the emission in the sample originated in regions outside the BLR.

Table 3.4: Summary of the mean difference in AIC values (see equations 3.10 and 3.11) between a log parabola and power law model during the flare periods from each source. Also shown is the model the flare spectra prefer, if any; this was determined using the mean difference in AIC values, whereby a difference of greater than 2 between two models indicates that the model with the higher AIC is significantly worse than that with the lower AIC value (Lewis et al. (2011)).

Source	Flare Peak	Model Preferred	Δ_{AIC}
3C 454.3	Dec 2009	Log parabola	-6.10
3C 454.3	Nov 2010	Log parabola	-39.45
CTA 102	Sept 2012	Log parabola	-2.51
CTA 102	Feb 2016	Log parabola	-2.22
B2 1520+31	July 2009	Neither	-0.57
B2 1520+31	Nov 2009	Neither	1.09
PKS 1510-089	Nov 2011	Neither	-0.05
PKS 1510-089	Feb 2012	Log parabola	-2.28
PKS 1502+106	Feb 2009	Neither	-1.45
PKS 1502+106	July 2015	Neither	-0.40
PKS 1424-41	Jan 2013	Neither	-0.65
PKS 1424-41	Apr 2013	Neither	-0.47
3C 279	Dec 2013	Neither	-1.64
3C 279	June 2015	Log parabola	-6.01
4C 21.35	June 2010	Log parabola	-2.03
4C 21.35	Nov 2014	Neither	0.51
PKS 0454-234	Jan 2009	Neither	-1.97
PKS 0454-234	Nov 2011	Neither	-0.92

Figure 3.6 shows two representative sets of plots for 3C 454.3 (December 2009) and PKS 1502+106 (July 2015). The top plots show the evolution of daily flux during the course of the flares. 3C 454.3 is seen to strongly favour a log parabolic model during this outburst, which is also in accordance with the negative mean AIC value found. PKS 1502+106 is also observed to favour a curved spectrum during some days of the flare period but this behaviour is not consistent, resulting in neither model being favoured ultimately. I address the exact nature and implications of any cut-off on the VHE emission later on in Section 3.5.

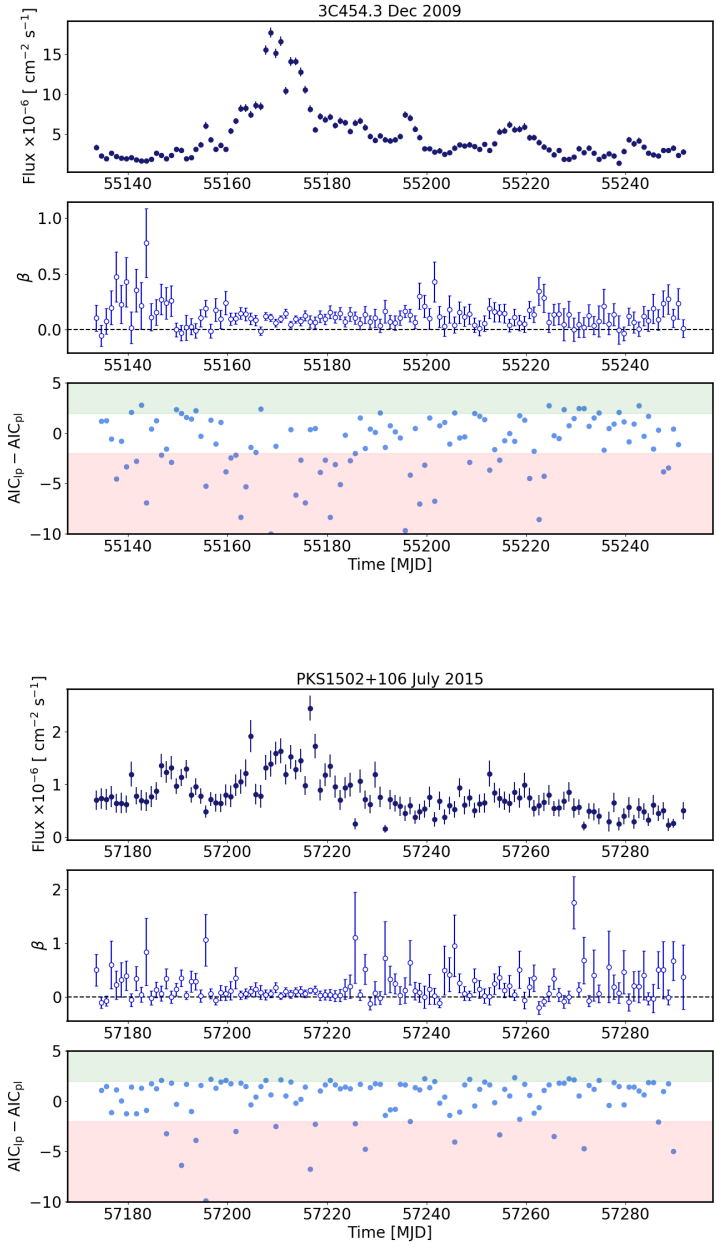

Figure 3.6: Upper panels: Daily evolution of flux for 3C 454.3 during its December 2009 flare (top) and PKS 1502+106 during its July 2015 flare (bottom). Middle panels: The daily variation of the spectral parameter β during the corresponding flare periods. The dashed horizontal line is at $\beta = 0$. Lower panels: Difference in AIC values between the log parabola and power law fits to spectra observed during the flare in daily intervals. The points in the red shaded region represent daily intervals better modelled with a log parabola over a power law. The points in the green shaded region represent daily intervals favouring a power law over a log parabola. Points between the shaded regions represent daily intervals showing no significant deviation between the two models.

3.4.3 Energy dependent cooling

Another key difference between BLR and MT emission is the energy of the seed photons in these regions. The photons in the BLR, being ultraviolet photons, are typically a factor $\sim$ 100 more energetic than the infrared photons present in the MT. Dotson et al. (2012) found that Inverse Compton (IC) scattering takes place in the Klein-Nishina regime when the emission region is located inside the BLR, and in the Thomson regime for emission from farther out within the MT.

This difference results in energy-independent electron cooling times for emission from the BLR as opposed to energy-dependent cooling timescales for regions within the MT. Cooling times are shorter at higher energies, such that emission from the MT would be expected to have, in general, a time-lag on timescales of a few hours between the cooling of the MeV and GeV components of the flare.

To investigate this, I re-analysed the flare periods in two distinct energy ranges: 0.1 - 1 GeV (low energy) and 1 - 300 GeV (high energy), binned in six hourly intervals using the procedure outlined in Section 3.2. Six hour bins were chosen as a compromise to allow for sufficient events for analysis (especially at high energies) while still enabling the detection of short timescale variability. The resulting high- and low-energy lightcurves are shown in Appendix B.

Local cross-correlation functions (LCCFs; Welsh (1999)) were then applied to the high- and low-energy lightcurves to search for correlations in the data. The use of LCCFs was motivated by the fact that this technique is independent of differences in sampling rates of the two lightcurves. Unlike Discrete Correlation Functions (DCFs; Edelson and Krolik (1988)), LCCFs are intrinsically bound in the interval [-1,1] and have also been found to be more efficient than DCFs in the study of correlations (Max-Moerbeck et al. (2014b)). There were not sufficient statistics to enable a LCCF analysis for all flares: this was the case for both the flares studied from B2 1520+31, PKS 0454-234 and PKS 1424-41, and the November 2014 flare from 4C 21.35. Furthermore, the LCCF for the December 2013 flare from 3C 279 did not exhibit a clear peak making it difficult to draw any conclusions.

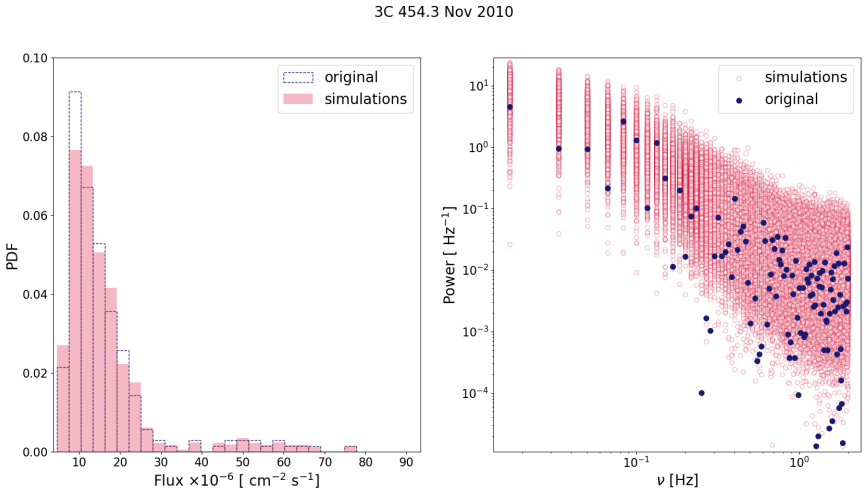

Figure 3.7: Left : A comparison between the PDF histograms of the original lightcurve (in blue) and the lightcurves generated from 1000 simulations (in red). Right : Periodograms of the original lightcurve (in blue) and the lightcurves generated from 1000 simulations (in red). The final two columns in Table 3.5 list the spectral slopes, β where the power spectral density PSD $\propto \nu^{-\beta}$, of the original lightcurves and the mean and 95% confidence intervals of the simulated lightcurves respectively.

The LCCFs obtained from flares of the remaining sources are shown in Figure 3.8. Also shown is the peak of the LCCFs along with the corresponding uncertainties, both derived from Gaussian fits. While the peaks of the Gaussian fits give a first order determination of the uncertainty, these do not account for the effects of correlated red-noise between the datasets (Uttley et al. (2003)).

In order to provide a better estimate of the significance of the observed peaks, Monte Carlo simulations were performed to generate 1000 artificial low energy lightcurves matching the probability distribution function (PDF) and power spectral density (PSD) of the observations using the method outlined in Emmanoulopoulos et al. (2013)*. Figure 3.7 shows a representative plot of the PDF and PSD obtained from both the original and 1000 simulated lightcurves of the November 2010 flare of 3C 454.3.

Each simulated lightcurve was cross-correlated with the corresponding observed high energy lightcurves and the 68%, 95% and 99% confidence intervals obtained are shown in

*The code was developed from Connolly, S. D., 2016, Astrophysics Source Code Library, record ascl:1602.012. See `https://github.com/samconnolly/DELightcurveSimulation`, accessed on 11/06/20.

Figure 3.8 with the results summarised in Table 3.5. With the exception of the December 2009 flare from 3C 454.3, the February 2009 flare from PKS 1502+106 and the February 2012 flare of PKS 1510-089, all correlations are found to have a significance of ≥ 95%.

A peak at 0 indicates an absence of time-lag implying BLR origin of the gamma-ray emission. This is found to be compatible with observations from the June 2015 flare from 3C 279, the November 2010 flare of 3C 454.3, the February 2016 flare of CTA 102 and the July 2015 flare from PKS 1502+106. A positive time-lag on the other hand implies that the low energy flux is delayed with respect to the high energy flux. Under the assumption that the flux increase in both energy bands occurs at the same time, this points towards MT origin of emission and is seen for both flares from PKS 1510-089, the December 2009 flare from 3C 454.3 and the February 2009 flare from PKS 1502+106.

Two flares, namely the June 2010 flare from 4C 21.35 and the September 2012 flare from CTA 102, show evidence of a negative temporal lag indicating that the changes to the low energy flux precede any changes to the high energy flux. While a negative temporal lag does not constrain the location of the emission to either the BLR or MT, it can be interpreted as evidence indicating the MeV and GeV components of the flare have different origin. Evidence of a negative time lag between the high- and low-energy lightcurves in FSRQs has also been reported in other studies (for example Brown (2013), Cohen et al. (2014)).

3.5 VHE Emission

I now investigate the very high energy (VHE) photon emission from the sample of FSRQs and discuss its implications on the location of the emission region. For this study, VHE photons are defined as photons having an energy $E_\gamma \geq 20$ GeV in the rest frame of the source. The observation of VHE photons is generally difficult to explain if the emission is assumed to be coming from the inner regions of the BLR as photon-photon pair production would make the escape of the high energy photons less probable (Donea and Protheroe (2003), Liu et al. (2008), Böttcher et al. (2009)).

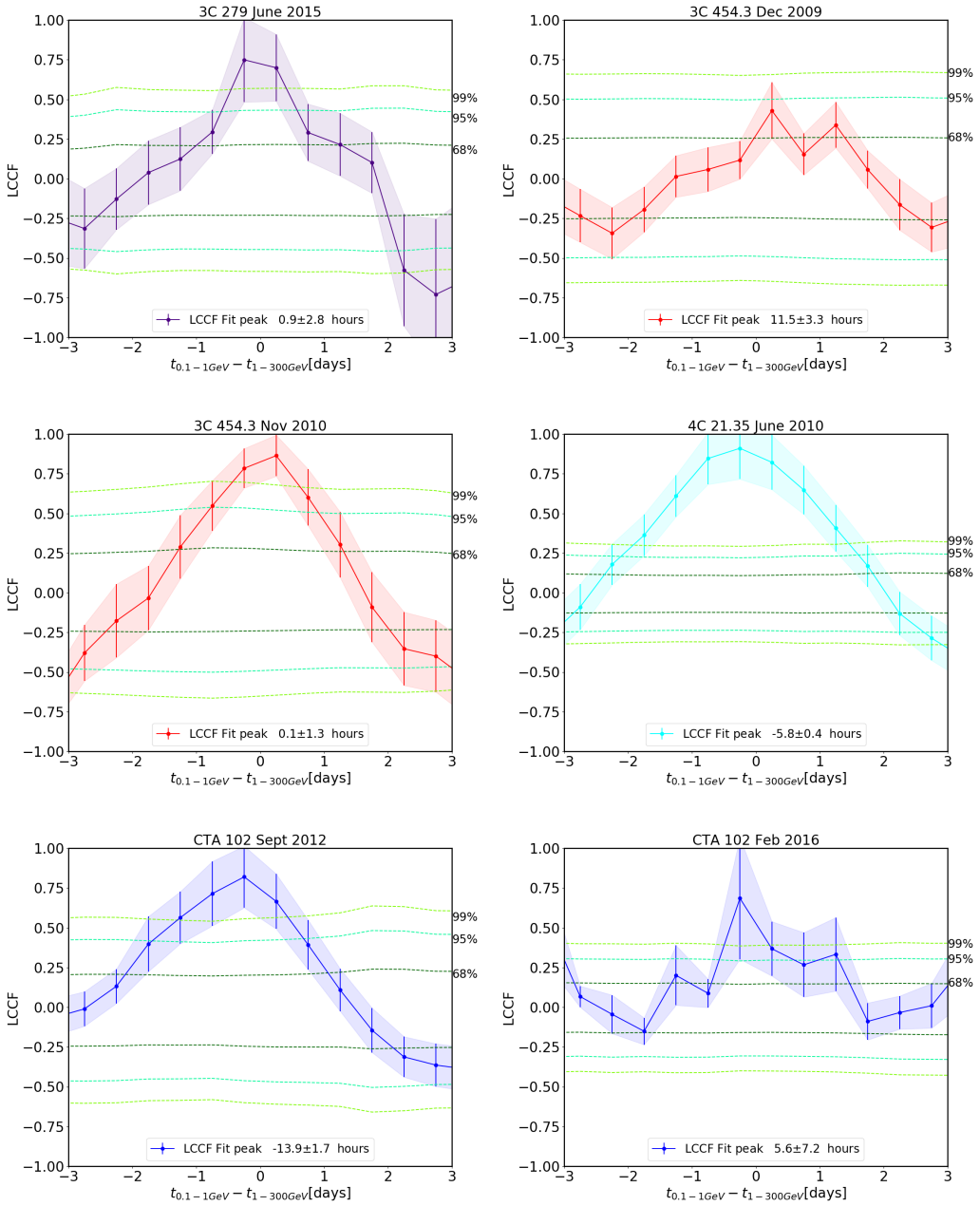

Figure 3.8: **a.** Local cross-correlation functions (LCCFs) calculated between the 0.1 - 1 GeV and the 1 - 300 GeV lightcurves during the flare periods. (The lightcurves, binned in six hour intervals, shown in Appendix B.) The shaded regions indicate the error bounds of the LCCFs. The LCCFs have been fitted with a Gaussian with the time corresponding to the peak of the fit and the associated uncertainty shown in the legend. The green lines represent the 68%, 95% and 99% confidence intervals (from darker to lighter shades) derived from Monte Carlo simulations.

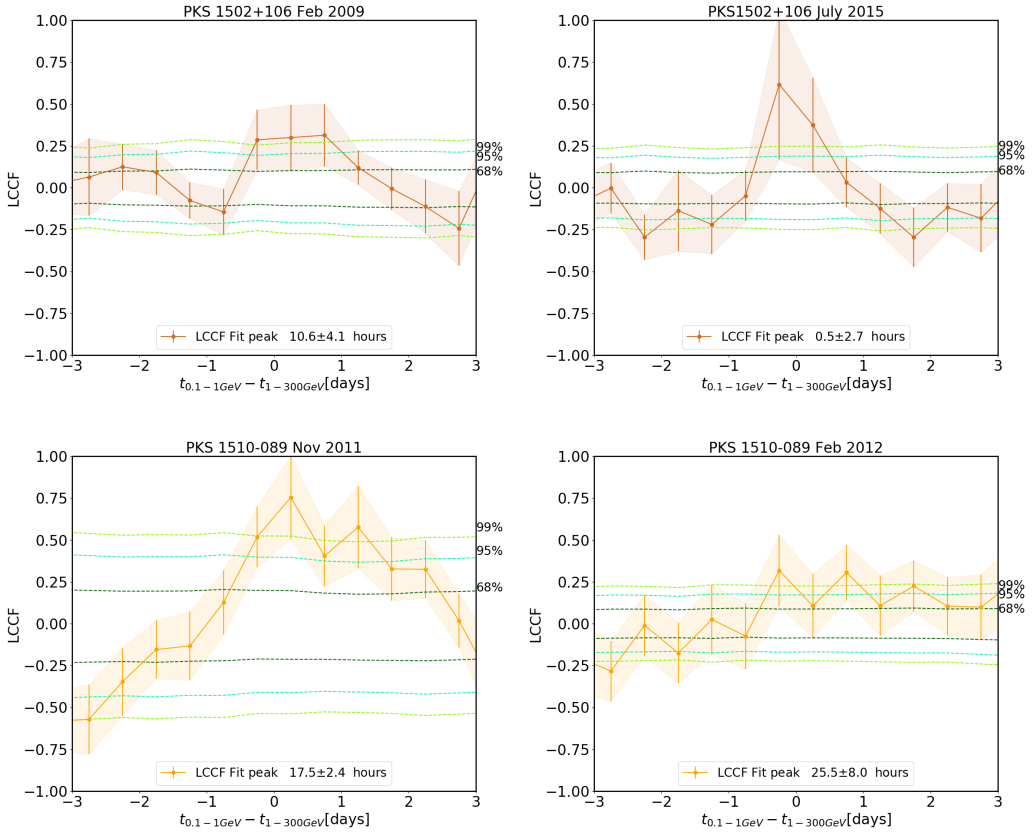

b. Local cross-correlation functions (LCCFs) calculated between the 0.1 - 1 GeV and the 1 - 300 GeV lightcurves during the flare periods. (The lightcurves, binned in six hour intervals, shown in Appendix B.) The shaded regions indicate the error bounds of the LCCFs. The LCCFs have been fitted with a Gaussian with the time corresponding to the peak of the fit and the associated uncertainty shown in the legend. The green lines represent the 68%, 95% and 99% confidence intervals (from darker to lighter shades) derived from Monte Carlo simulations.

As a first step, I performed a binned maximum likelihood analysis on the entire eight year data set in the 20 GeV-300 GeV, 50 GeV-300 GeV and 100 GeV-300 GeV energy ranges, using the point source and diffuse emission models outlined in Section 3.2. The positions and spectral definitions of all sources in the RoI were once again taken from the 4FGL catalog (The *Fermi*-LAT collaboration (2019a)).

The resulting flux values and test statistic of sources having a TS $\geq$ 10 for the different energy ranges are listed in Table 3.6. As expected, both flux and detection significance decrease with increasing threshold energy. Two of the three sources found to have a TS $\geq$ 10 above 100 GeV are among the FSRQs detected with ground-based instruments: PKS

Table 3.5: Results of the LCCF study between the 0.1 - 1 GeV and the 1 - 300 GeV lightcurves during the flare periods. This includes the times corresponding to the peaks of the Gaussian fit along with the associated uncertainties and their significance in percentile derived from Monte Carlo simulations. The final two columns list the spectral slopes, β where the power spectral density PSD $\propto \nu^{-\beta}$, of the original lightcurves and the mean and 95% confidence intervals of the simulated lightcurves respectively.

Source	Flare Peak	LCCF Peak	Timelag [hours]	Significance [%]	β_{original}	$\beta_{\text{simulations}}$
3C 454.3	Dec 2009	0.4±0.2	11.5±3.3	≥68	1.05 ± 0.01	1.11 ± 0.20
3C 454.3	Nov 2010	0.9±0.1	0.1±1.3	≥99	1.22 ± 0.01	1.27 ± 0.28
CTA 102	Sept 2012	0.8±0.2	-13.9±1.7	≥99	0.67 ± 0.03	0.73 ± 0.36
CTA 102	Feb 2016	0.7±0.4	5.6±7.2	≥95	1.28 ± 0.02	1.32 ± 0.31
PKS 1510-089	Nov 2011	0.8±0.2	17.5±2.4	≥99	0.71 ± 0.01	0.74 ± 0.22
PKS 1510-089	Feb 2012	0.3±0.2	25.5±8.0	≥68	1.05 ± 0.01	1.01 ± 0.17
PKS 1502+106	Feb 2009	0.3±0.2	10.6±4.1	≥68	1.13 ± 0.02	1.20 ± 0.28
PKS 1502+106	July 2015	0.6±0.4	0.5±2.7	≥95	0.86 ± 0.01	0.75 ± 0.19
3C 279	June 2015	0.7±0.3	0.9±2.8	≥99	0.76 ± 0.01	0.77 ± 0.16
4C 21.35	June 2010	0.9±0.2	-5.8±0.4	≥99	0.97 ± 0.02	1.08 ± 0.25

1510-089 (Abramowski et al. (2013)) and 3C 279 (Errando et al. (2008)). PKS 0454-234, while not yet detected with current ground-based instruments, is an interesting candidate for such observations.

To check that the VHE photon emission is associated with the source, I used the *Fermi* science tool *gtsrcprob* (see Section 2.3.7), which calculates the probability of each photon being associated with a source in the RoI. Before this step, it was necessary to account for the diffuse components using another *Fermi* science tool *gtdiffrsp* and adding the response to the input data. I restrict myself to a radius of 0.1° around each source and consider only photons having a ≥ 99 % probability of originating from the sources.

Figure 3.9 shows the lightcurves of the VHE photons emitted by the sample over the entire eight year observation period with the time periods satisfying my definition of flares (see Section 3.3) again shown as shaded regions. In most cases, the VHE photon emission is seen to occur during the flare events.

There are instances (for example PKS 0454-234) in which there is VHE photon emission outside the flare periods. As discussed later, this could indicate that the VHE photons are emitted from a different location than the lower energy emission studied previously, but at the very least shows that GeV flares are not necessarily a predictor of VHE emission,

and vice versa. This reinforces the requirement for comprehensive sky surveys in the VHE regime (Hassan et al. (2017b); see Chapter 5).

As discussed in Section 3.4.2, emission coming from the BLR is expected to have an intrinsic cut-off due to photon-photon pair production. I now attempt to quantify the nature of this cut-off and study its implications for the location of the emission region. The *Fermi* science tool *gtobssim* is used to simulate observations for the sample of FSRQs taking into account IRFs and the spacecraft pointing history.

This routine allows the simulation of observations from both point and diffuse sources within a selected RoI having a specified spectral shape. In addition to evaluating actual data, this method is also useful in planning observation proposals. The *gtobssim* tool requires the spacecraft pointing history and livetime cube files as well as a source model *XML* file containing information, such as the integral flux, spectral shape, energy range and spatial position of the source. Furthermore, more than one source may be simulated at any given time with the list of sources to be simulated provided as a separate input.

The simulations assume intrinsic absorption due to BLR photons and the energies of the simulated photons, when compared to the energies of the observed photons, should reveal whether this assumption is correct and if the observed VHE photons are indeed compatible with BLR origin. I specify the energy distribution for my simulations by starting with the eight year time-averaged spectra obtained in Section 3.2 and concentrate on the energy range 20 GeV-300 GeV.

Attenuation due to the Extragalactic Background Light (EBL) is also accounted for; I use the EBL opacities, τ, stated in the Domínguez et al. (2011) model in this study to calculate the likely attenuation. This model has been found to be compatible with the upper limits from gamma-ray astronomy (for example Mazin and Raue (2007), MAGIC Collaboration et al. (2008)).

The intrinsic absorption due to photons present in the BLR is accounted for by choosing a number of cut-off energies, $E_{\rm cut}$, evenly spaced in the interval 10 GeV-30 GeV. The

resultant differential flux used for simulations is given by:

$$\frac{dN}{dE} = N_0 \left(\frac{E}{E_0}\right)^{-\alpha-\beta\ln\left(\frac{E}{E_0}\right)} e^{-\tau} e^{-\left(\frac{E}{E_{\rm cut}}\right)} \tag{3.12}$$

where once again E_0 is the pivot energy in MeV, N_0 is the normalisation in units of photons $\mathrm{cm}^{-2}\mathrm{s}^{-1}\mathrm{MeV}^{-1}$ and α and β the spectral index and curvature respectively.

Using 1000 simulations for each source with different seed variables, the energy distribution of the most energetic photons simulated was determined. These are shown in Figure 3.10, where I plot the 1σ and 2σ confidence intervals as a function of the different cut-off energies used in the simulations. Also shown is the energy of highest energy photon observed with the *Fermi*-LAT during the eight year period for each source with its corresponding uncertainty.

The cut-off energy range which best agrees with the observation was then determined and compared to the expected onset of the intrinsic cut-off due to interaction with Lyman alpha photons in the BLR ($E_{\mathrm{Ly}\alpha} = \frac{25}{1+z}$ GeV for a source at redshift z (Pacciani et al. (2014))). In the case where the observed and expected photon energies are compatible, the VHE photon emission observed with the *Fermi*-LAT is compatible with BLR origin; this is the case for for 3C 279, 3C 454.3 and 4C 21.35. However, for the other 6 sources, the VHE emission is constrained to parsec scale distances from the central engine, i.e. within the MT.

3.6 Discussion

3.6.1 Individual Sources

In order to draw conclusions regarding the location of the emission region, I now combine the findings from the methods discussed in the previous two sections and study their implications for each source individually. The results are summarised in Table 3.7.

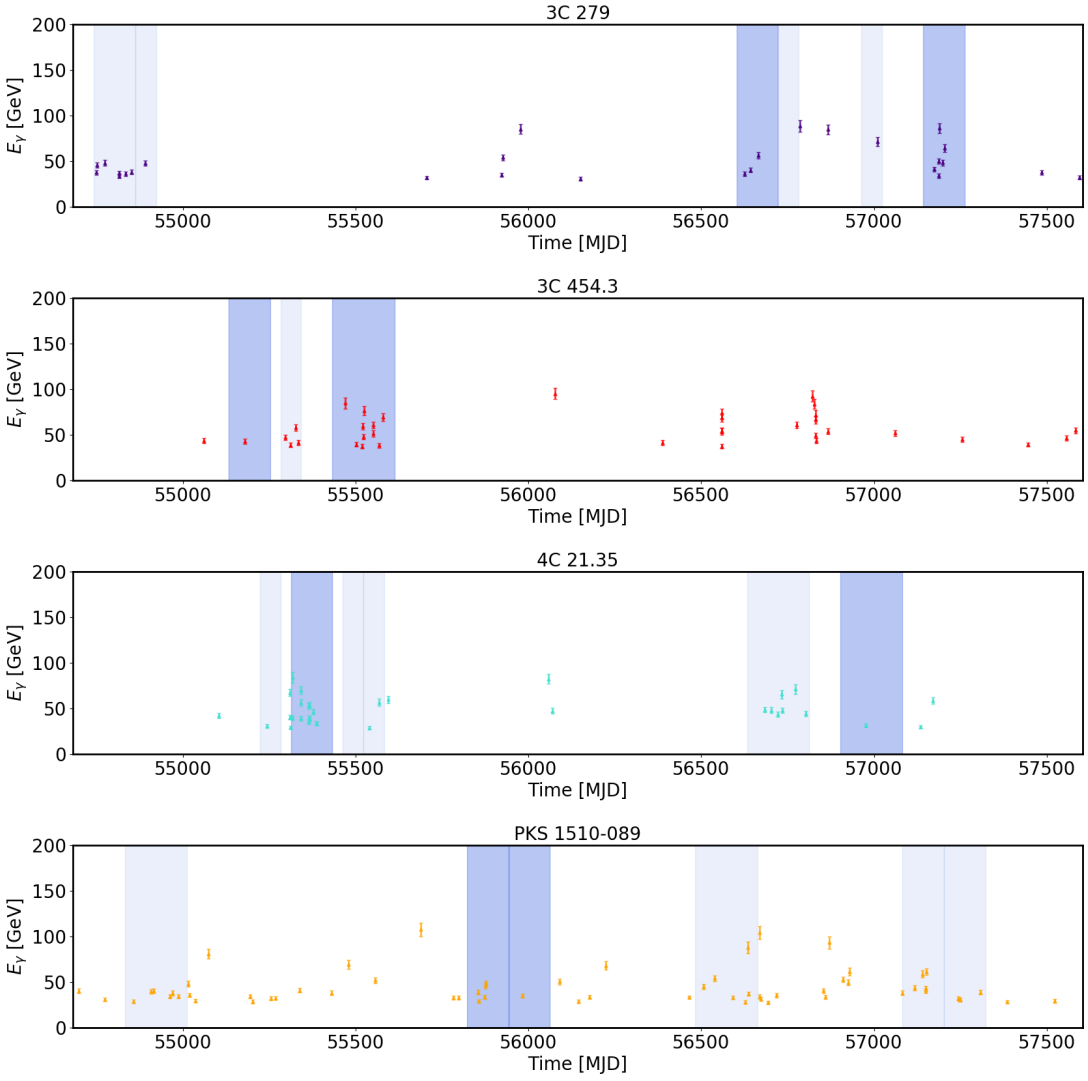

Figure 3.9: **a.** The detected energy, E_γ, of the individual high energy photons detected with the *Fermi*-LAT over the entire eight year observation period as a function of time for 3C 279, 3C 454.3, 4C 21.35 and PKS 1510-089. All energies are in the rest frame of the galaxy. Only photons with energy $E_\gamma \geq 20$ GeV and a probability of $\geq 99\%$ for originating from each source are shown. Also shown as blue shaded regions are the time intervals which satisfy my definition of a flare period (see Section 3.3), with the darker shaded regions being the time intervals studied in this investigation.

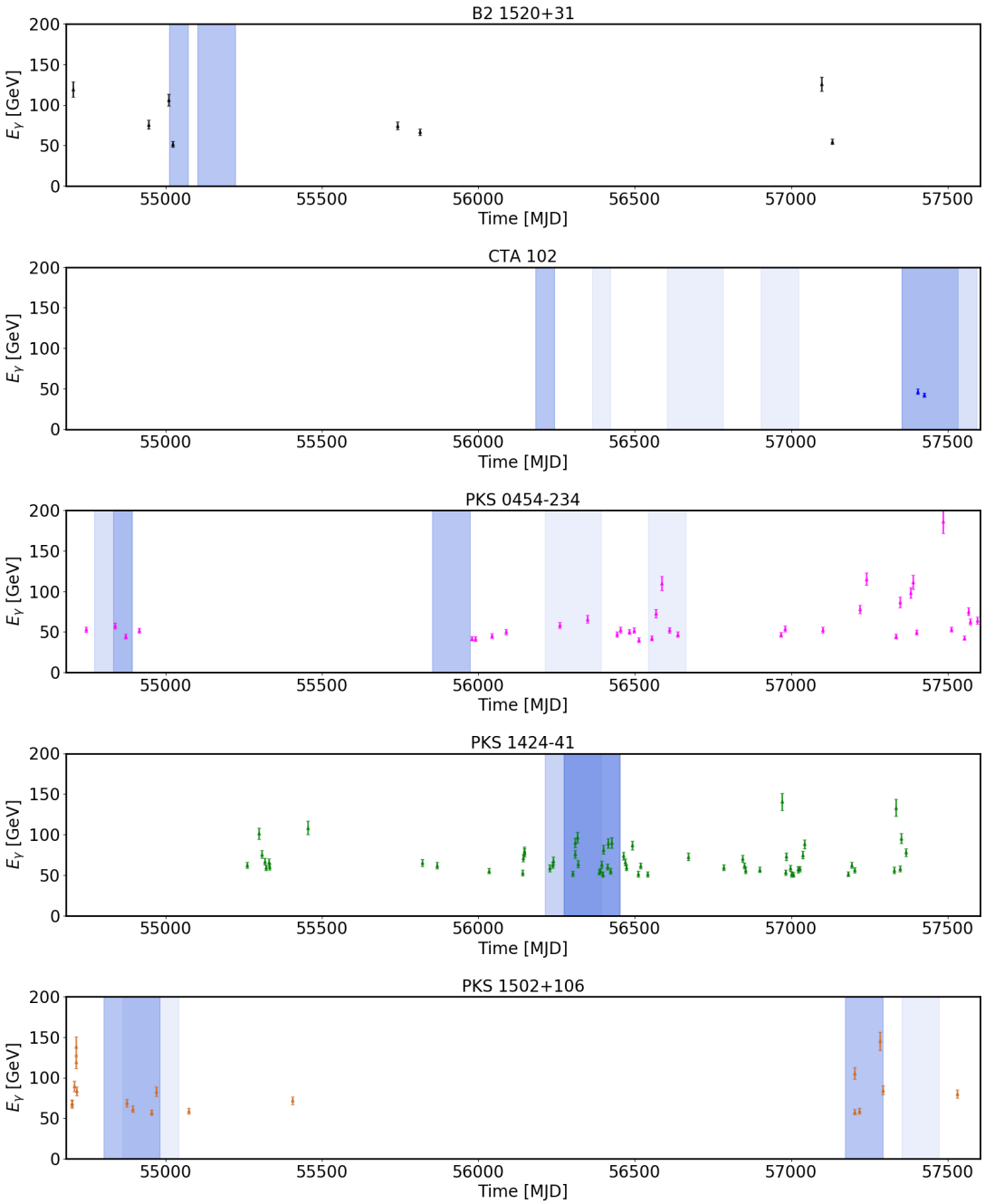

b. The detected energy, E_γ, of the individual high energy photons detected with the *Fermi*-LAT over the entire eight year observation period as a function of time for B2 1520+31, CTA 102, PKS 0454-234, PKS 1424-41 and PKS 1502+106. All energies are in the rest frame of the galaxy. Only photons with energy $E_\gamma \geq 20$ GeV and a probability of $\geq 99\%$ for originating from each source are shown. Also shown as blue shaded regions are the time intervals which satisfy my definition of a flare period (see Section 3.3), with the darker shaded regions being the time intervals studied in this investigation.

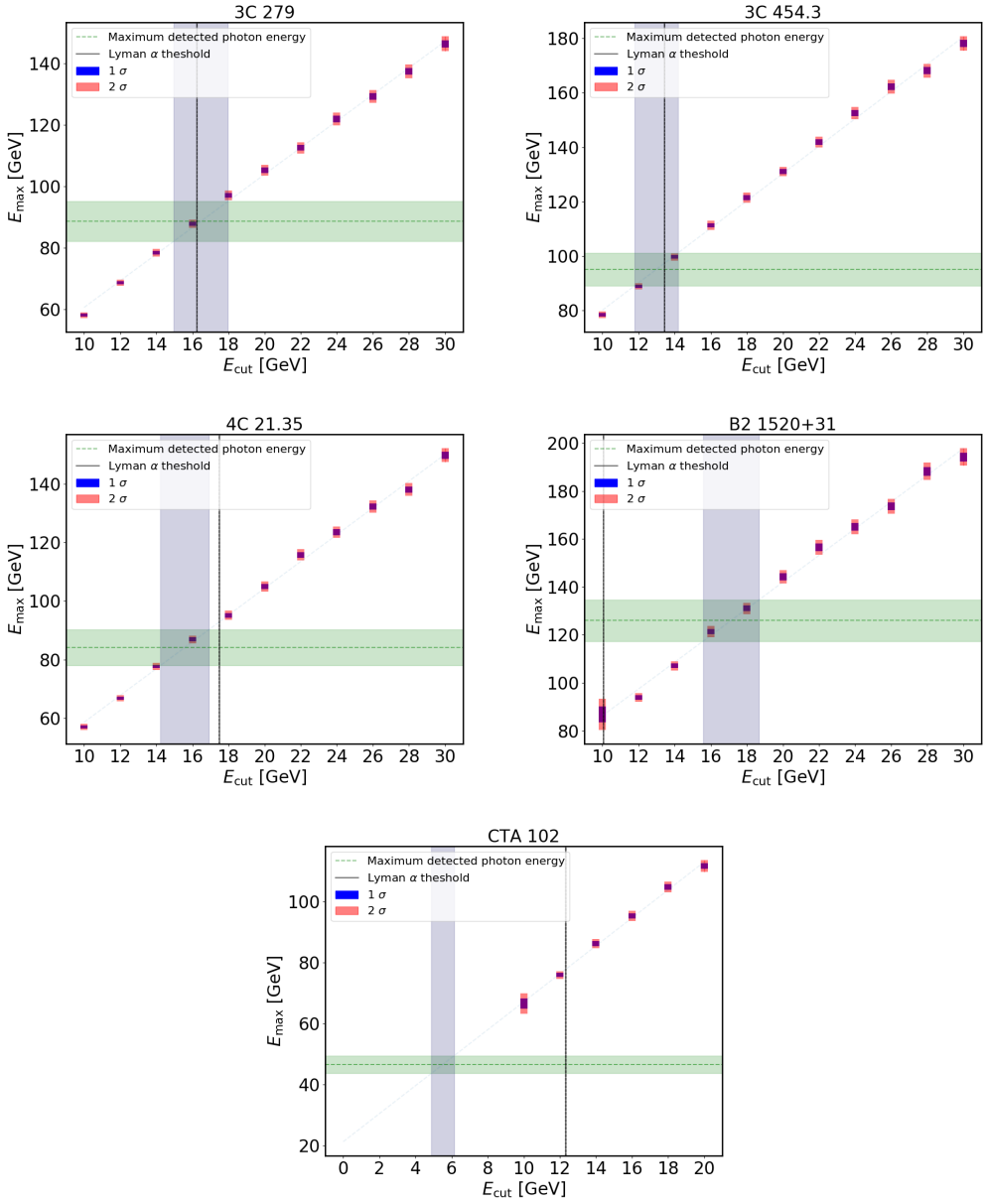

Figure 3.10: **a.** The plots show the energy distributions of the most energetic photons, E_{max}, obtained from Monte Carlo simulations as a function of the cut-off energy, E_{cut}, used in the simulations (see equation 3.12) for 3C 279, 3C 454.3, 4C 21.35, B2 1520+31 and CTA 102. The blue and red shaded regions represent the 1σ and 2σ confidence intervals respectively. The green dashed line is the energy of highest energy photon observed with the *Fermi*-LAT during the eight year observation period for each source along with the corresponding uncertainty. The cut-off energy range which best agrees with the observations is shown as the vertical blue shaded region. For comparison, the black vertical line is the expected intrinsic cut-off energy due to interaction with Lyman alpha photons calculated as $E_{\mathrm{Ly}\alpha} = \frac{25}{1+z}$ GeV where z is the redshift of the source.

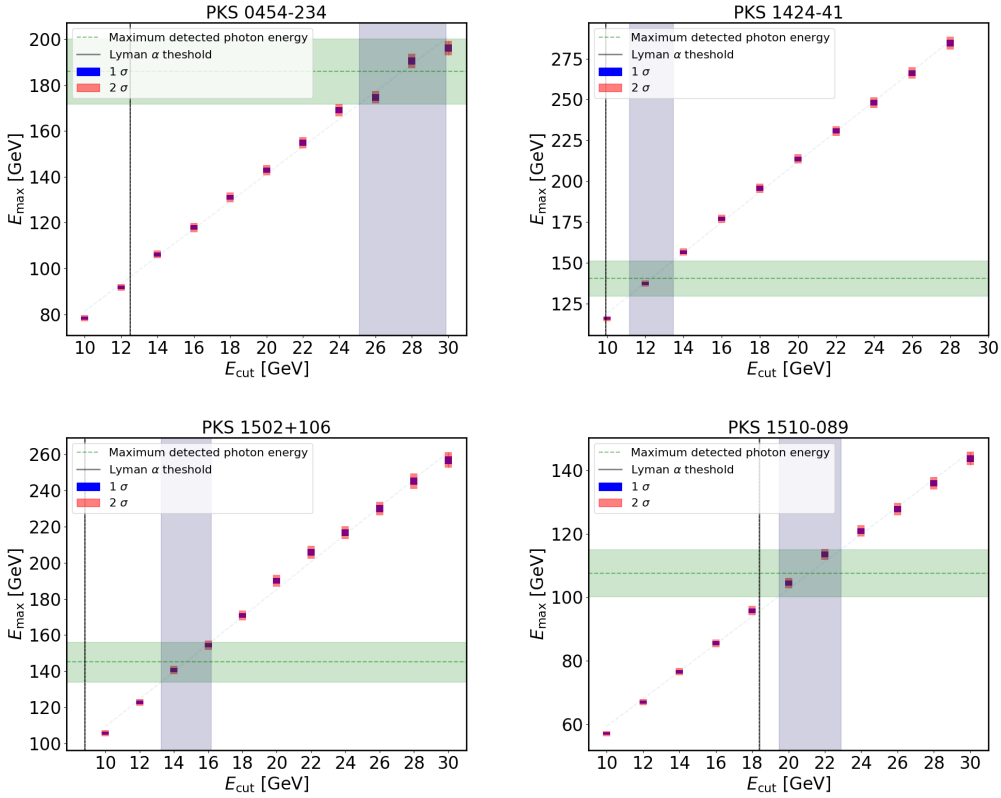

b. The plots show the energy distributions of the most energetic photons, $E_{\max}$, obtained from Monte Carlo simulations as a function of the cut-off energy, $E_{\rm cut}$, used in the simulations (see equation 3.12) for PKS 0454-234, PKS 1424-41, PKS 1502+106 and PKS 1510-089. The blue and red shaded regions represent the 1σ and 2σ confidence intervals respectively. The green dashed line is the energy of highest energy photon observed with the *Fermi*-LAT during the eight year observation period for each source along with the corresponding uncertainty. The cut-off energy range which best agrees with the observations is shown as the vertical blue shaded region. For comparison, the black vertical line is the expected intrinsic cut-off energy due to interaction with Lyman alpha photons calculated as $E_{{\rm Ly}\alpha} = \frac{25}{1+z}$ GeV where z is the redshift of the source.

Table 3.6: The average flux and test statistic (TS) values (see equation 3.1) obtained from a likelihood analysis of the eight year (MJD 54682.66 - MJD 57604.66) *Fermi*-LAT observations of each source above an energy threshold of $E_\gamma \geq 20$ GeV, $E_\gamma \geq 50$ GeV and $E_\gamma \geq 100$ GeV respectively. Only sources having a TS ≥ 10 in each energy range are shown.

Source	Flux [10^{-6} photons cm^{-2} s^{-1}]	TS
	20 GeV-300 GeV	
3C 454.3	5.71 ± 0.86	536
CTA 102	0.76 ± 0.32	89
B2 1520+31	1.42 ± 0.41	85
PKS 1510-089	11.47 ± 1.51	820
PKS 1502+106	2.77 ± 1.38	213
PKS 1424-41	7.85 ± 0.89	837
3C 279	5.97 ± 1.18	386
4C 21.35	6.89 ± 1.13	501
PKS 0454-234	6.26 ± 1.05	504
	50 GeV-300 GeV	
3C 454.3	0.52 ± 0.35	25
PKS 1510-089	4.42 ± 1.35	119
PKS 1424-41	0.42 ± 0.20	39
3C 279	2.31 ± 0.95	65
4C 21.35	1.19 ± 0.54	69
PKS 0454-234	2.14 ± 0.79	84
	100 GeV-300 GeV	
PKS 1510-089	2.42 ± 1.18	39
3C 279	1.28 ± 1.02	16
PKS 0454-234	0.39 ± 0.29	22

3.6.1.1 3C 454.3

The variability timescales for 3C 454.3, the brightest of the sources, predict a compact emission region of size $(3.87 \pm 0.84) \times 10^{13}$ m for the December 2009 flare and $(7.38 \pm 1.03) \times 10^{13}$ m for the November 2010 flare. Both of these are compatible with emission from the inner regions of the BLR in a simple one-zone model. This conclusion is reinforced by evidence that the spectra of both flares favour a log parabolic model over a power law, particularly in the case of the November 2010 flare.

The bright November 2010 flare also provides sufficient statistics for a LCCF to be obtained; this shows no evidence for a time-lag between the high- and low-energy emission, again

Table 3.7: Summary of the results from the different methods used to constrain the location of the emission region for both flare periods from each source investigated in this work. These methods are the measurement of the shortest variability timescales for the flare periods, the search for evidence of a cut-off in the flare spectra and an investigation into energy dependence in cooling timescales. The final column lists whether the VHE ($E_\gamma \geq 20$ GeV) photon emission observed with the *Fermi*-LAT is compatible with BLR origin. Inconclusive results are due to the flare spectra favouring neither a power law nor a log parabolic model or due to the lack of statistics at high energies preventing obtainment of LCCFs. Multi-zone indicates evidence of multiple emission regions but no physical constraints on the location.

Source	Sizes of emission region from variability timescales[10^{13}m]* Flare 1, Flare 2	Spectral cut-off Flare 1, Flare 2	Energy dependent cooling Flare 1, Flare 2	VHE photons from BLR
3C 454.3	3.87 ± 0.84, 7.38 ± 1.03	BLR, BLR	MT, BLR	Compatible
CTA 102	4.78 ± 0.86, 3.59 ± 0.59	BLR, BLR	Multi-zone, BLR	Incompatible
B2 1520+31	0.70 ± 0.12, 3.27 ± 0.91	Inconclusive, Inconclusive	Inconclusive, Inconclusive	Incompatible
PKS 1510-089	6.82 ± 1.03, 5.30 ± 1.56	Inconclusive, BLR	MT, MT	Incompatible
PKS 1502+106	0.93 ± 0.18, 1.33 ± 0.09	Inconclusive, Inconclusive	MT, BLR	Incompatible
PKS 1424-41	0.77 ± 0.24, 2.76 ± 0.66	Inconclusive, Inconclusive	Inconclusive, Inconclusive	Incompatible
3C 279	4.11 ± 0.34, 4.23 ± 1.28	Inconclusive, BLR	Inconclusive, BLR	Compatible
4C 21.35	2.05 ± 0.66, 1.67 ± 0.12	BLR, Inconclusive	Multi-zone, Inconclusive	Compatible
PKS 0454-234	4.55 ± 0.79, 3.91 ± 0.67	Inconclusive, Inconclusive	Inconclusive, Inconclusive	Incompatible

* The variability timescales imply extremely compact emission regions. Assuming the entire width of the jet to be responsible for the emission, all timescales are compatible with BLR origin of emission.

supporting a BLR origin of the emission. However, the LCCF for the December 2009 flare indicates the low energy flux is delayed with respect to the high energy flux with evidence of a time-lag of 11.5 ± 3.3 hours. Assuming the flux increase in both bands takes place at the same time, this favours emission from the MT.

As seen in Figure 3.9, both flare periods studied in this work are observed to be accompanied by the emission of VHE ($E_\gamma \geq 20$ GeV) photons. The most energetic photon from this source, with energy 95.1 ± 6.1 GeV, was emitted on MJD 56076.89 and is outside of the flare periods studied here. Monte Carlo simulations when compared to the energy of this photon show that the cut-off energy that best agrees with the observations is 13.0 ± 1.2 GeV, which is compatible with the expected cut-off of 13.441 ± 0.001 GeV due to interaction with Lyman alpha photons in the BLR. 3C 454.3 has not been detected in the energy range $E_\gamma \geq 100$ GeV with ground-based gamma-ray telescopes and an analysis of the *Fermi*-LAT data over the entire observation period also found no significant emission in this energy range.

The November 2010 flare was studied in Foschini et al. (2011a) and the 2 – 3 hour intrinsic variability timescales reported is compatible with the 2.80 ± 0.39 hours result for the same flare observed in this investigation. It should also be noted that the Foschini et al. (2011a) calculation requires the successive measurements to have a difference in flux significant at at least 3σ. A separate investigation of 3C 454.3 from August 2008 to January 2010 by Tavecchio et al. (2010) also found variability timescales of a few hours and constrained the size of the emission region to $R < 3.5\times10^{13}(\delta)/10\,\mathrm{m} = 8.54\times10^{13}$ m for $\delta = 24.4$ (Jorstad et al. (2017)), a factor ~ 1.8 times larger than the upper limits obtained in this study. Both investigations conclude that the emission region is within the BLR. The same conclusion is also reached in a study of the November 2010 flare by Vercellone et al. (2011).

Combining the results of my analyses, I conclude that the gamma-ray emission in 3C 454.3 predominantly comes from regions within the BLR. However, the December 2009 flare exhibits energy dependence of the cooling timescales, suggesting the possibility of multiple simultaneously active emission regions both within the BLR and the MT. This agrees with the findings of the multi-wavelength study of the same flare by Pacciani et al.

(2010) who concluded that explaining the gamma-ray observations corresponding to the peak of the flare requires models more elaborate than a simple one-zone emission model. An investigation of the June 2014 flare from 3C 454.3 by Coogan et al. (2016) also suggests the presence of multiple emission regions and constrains the location of the emission to be outside the BLR. As seen in Table 3.7, the possibility of multiple simultaneously active emission regions is not a property unique to 3C 454.3 but a general feature found in my sample.

3.6.1.2 CTA 102

The September 2012 flare from CTA 102 shows a shortest variability timescale of 1.45 ± 0.26 hours while the February 2016 flare shows an even shorter timescale of 1.09 ± 0.18 hours. Both of these imply an extremely compact emission region which, assuming the entire width of the jet to be responsible for the emission, are both compatible with emission from near the central engine. The spectra from both flares studied also favour a log parabola over a power law, which in principle reinforces the theory of BLR origin of the emission.

The peak of the Gaussian fit to the LCCF obtained for the February 2016 flare is compatible with an absence of a time-lag and further evidence of emission from within the BLR. The LCCF for the September 2012 flare shows evidence of a lag at -13.9 ± 1.7 hours, which indicates that the variations in low energy flux precede any changes to the high energy flux. This can be interpreted as evidence of multiple emission regions, with the MeV and GeV components having different origins for this particular flare.

Only two VHE photons are seen during the entire observation period, both of which coincide with the February 2016 flare. The most energetic of these photons, observed on MJD 57404.15, has an energy 46.5 ± 2.9 GeV. Monte Carlo simulations indicate this photon best agrees with a cut-off at 5.5 ± 0.6 GeV as opposed to the 12.32 ± 0.02 GeV expected from Lyman alpha photon interaction.

A possible explanation for the unusually low cut-off observed in the spectrum is the

absorption of gamma-rays due to pair production on Helium II recombination continuum photons (Poutanen and Stern (2010)). This would indicate the emission originates deep inside the BLR, within a light-year from the SMBH. Sahakyan (2020) also report evidence of a spectral cut-off in the energy range 9 - 16 GeV from *Fermi*-LAT observations of CTA 102 between January 2016 and April 2018. The feature is stated to be likely due to an intrinsic break in the energy distribution of the emitting particles and the observations were found incompatible with BLR origin of emission.

Zacharias et al. (2017) explain the evolution of CTA 102 from late 2016 to early 2017 as being a result of the addition of a large amount of mass to the jet over a period of a few months, with the subsequent drop in the light curve due to ablation of the material. From modelling the spectrum, a strong constraint on the maximum electron Lorentz factor is derived which also forces a cut-off of the IC component to be fixed at $\sim$ 20 GeV. This is an upper limit of the maximum photon energy achievable without taking EBL absorption into consideration. For comparison, my Monte Carlo simulations are compatible with an expected spectral cut-off at 6.09 $\pm$ 0.60 GeV when EBL absorption is not taken into account, which is not compatible with the result of Zacharias et al. (2017).

In conclusion, I find evidence indicating the gamma-ray emission in CTA 102 is produced in multiple compact emission regions, some of which may be deep inside the BLR.

3.6.1.3 B2 1520+31

B2 1520+31 shows a fastest flux doubling time of 0.65 $\pm$ 0.11 hours from the July 2009 flare, the shortest variability timescale obtained from all the flares studied in this investigation and implying an extremely compact emission region of size $(0.70 \pm 0.12) \times 10^{13}$ m for this particular flare. The November 2009 flare has a variability timescale of 3.03 $\pm$ 0.84 hours corresponding to an emission region of size $(3.27 \pm 0.91) \times 10^{13}$ m. These two timescales were observed in flux measurements $\sim$ 100 days apart and if the two flares had their origin in a single event, this would suggest the emission region is expanding with a velocity of $(2.97 \pm 0.97) \times 10^{6}$ ms^{-1} $\approx$ 0.01 c.

The spectra of both the flares studied show no strong preference for either a power law or a log parabolic model, making the search for a spectral cut-off inconclusive. The study of energy dependence in cooling timescales was also found to be inconclusive, due to a lack of photon statistics preventing analysis using LCCFs. A total of 8 VHE photons were observed over the entire eight year observation of which 2 coincide with the July 2009 flare. The most energetic of these photons, having energy 126.04 ± 8.66 GeV, was observed on MJD 57095.99, outside the time intervals corresponding to a flaring period.

Monte Carlo simulations indicate that a cut-off energy at 17.1 ± 1.6 GeV best agrees with the energy of this photon. This is considerably higher than the 10.040 ± 0.001 GeV expected due to Lyman alpha absorption and indicates that the VHE photon emission is not compatible with BLR origin. Pacciani et al. (2014) investigated a high energy flaring period of B2 1520+31 from April 2009. Interpolating the work of Liu and Bai (2006), the optical depth, $\tau_{\gamma\gamma}$, was calculated for the BLR region. The optical depth for gamma-rays emitted at the midpoint of the spherical BLR shell was found to be $\tau_{\gamma\gamma} = 1.4$ at 35 GeV and $\tau_{\gamma\gamma} = 2.0$ at 50 GeV. This further implies the VHE photons observed are likely produced at large distances from the SMBH.

The evidence from the flare variability studies, put together, suggests the gamma-ray flares are being produced in a very small emission region, which could be within the BLR. However, there is no further evidence to suggest BLR origin of emission since investigations of both a cut-off in the flare spectra and energy dependence of cooling timescales proved inconclusive. Furthermore, the VHE photon emission observed with the *Fermi*-LAT strongly disfavours BLR origin for these photons.

3.6.1.4 PKS 1510-089

The November 2011 flare for PKS 1510-089 was found to have a fastest variability timescale of 1.79 ± 0.27 hours while the February 2012 flare has a shortest timescale of 1.39 ± 0.41 hours. Assuming the entire width of the jet to be responsible for the emission, this would indicate emission from within the BLR. This possibility is supported by the spectrum of

the February 2012 flare favouring a log parabolic model over a power law, although the November 2011 flare favours neither model significantly.

An investigation into the energy dependence of the cooling timescales shows evidence that both flares exhibit a positive time-lag between the high- and low-energy emission. Under the assumption that the flux increase in both energy bands occurs simultaneously, this in turn indicates emission from the MT. Furthermore, the VHE photons observed with the *Fermi*-LAT predict an expected cut-off energy of 21.2 ± 1.7 GeV, which is higher than the 18.38 ± 0.03 GeV cut-off expected for BLR origin emission. There is also substantial VHE photon emission outside the flare periods including the most energetic photon, of energy 107.6 ± 7.4 GeV, observed on MJD 55687.83. Indeed, PKS 1510-089 has been detected at $E_\gamma \geq 100$ GeV with the H.E.S.S. telescopes (Abramowski et al. (2013)), which would also indicate emission farther from the black hole.

An investigation of the first 3.75 years of *Fermi*-LAT data for PKS 1510-089 by Brown (2013) includes the November 2011 flare studied here and reports an even shorter variability timescale of 1.21 ± 0.15 hours by applying equation 3.4 directly to two consecutive flux measurements satisfying TS ≥ 10, rather than the three consecutive time bins I have used. From spectral and variability studies, it was concluded that the jet was capable of simultaneously producing rapid variability gamma-ray emission at various points along the entire jet from the BLR to the MT. Both my study and that of Brown (2013) agree on the lack of a trend between GeV flux and emission of VHE photons, which can be interpreted as further evidence of multiple emission zones with the VHE emission thought to be produced farther out in the MT.

A study of the *Fermi*-LAT data from September to December 2011 by Saito et al. (2013) found similar results and conclusions to Brown (2013) and also reported observed doubling timescales of $\sim$ 1 hour. Assuming a generic Doppler factor $\delta = 20$, the emission region was constrained to be of size 1.5×10^{13} m which is smaller than the upper limit of $(6.82 \pm 1.03) \times 10^{13}$ m obtained in this work using $\delta = 35.3$ (Jorstad et al. (2017)) from optical data. The emission region was thought to be located within the BLR while any VHE emission, if detected, was argued to be produced further from the central engine. A

similar conclusion was reached by Barnacka et al. (2014) who use a two-zone model to reproduce the VHE emission observed with the H.E.S.S. telescopes in March 2009. In their model the bulk of the GeV emission is found to be coming from within the BLR, while the VHE emission results from the Comptonization of IR photons from the MT. My results support this hypothesis.

3.6.1.5 PKS 1502+106

The shortest variability timescale from the February 2009 flare of PKS 1502+106 is 0.86 ± 0.17 hours, one of only three sub-hour timescales discovered among the flares investigated. Based on this timescale, the size of the emission region is constrained to be (0.93 ± 0.18) $\times 10^{13}$ m. The July 2015 flare also shows hour scale variability, with a shortest variability timescale of 1.23 ± 0.08 hours implying an emission region of size (1.33 ± 0.09) $\times 10^{13}$ m.

The spectra for both flares were found to favour neither a power law nor a log parabolic model, so there is no evidence for a cut-off in the spectrum. The results of the LCCF study are mixed; emission from the July 2015 flare supports the premise of BLR origin with evidence for a correlation peak at 0.5 ± 2.7 hours, but the more rapid February 2009 flare shows a correlation peak at 10.6 ± 4.1 hours, which is instead compatible with emission from within the MT.

Both the flare periods studied coincide with VHE photon emission, including the most energetic photon which has an energy 145.11 ± 11.09 GeV and was observed on MJD 57283.92 (during the July 2015 flare). Monte Carlo simulations reveal that a cut-off energy of 14.7 ± 1.5 GeV best agrees with this observation, which is higher than the expected cut-off of 8.803 ± 0.005 GeV due to Lyman alpha absorption of BLR photons. This implies that the VHE photon emission observed with the *Fermi*-LAT is not compatible with the BLR and might indicate the presence of multiple emission regions.

The complex nature of my findings agrees with the results of Abdo et al. (2010d), whose study of *Fermi*-LAT observations from PKS 1502+106 between August - December 2008 concluded that the gamma-ray emission was produced by External Compton (EC) scattering

of BLR photons. Using the flux increase between August 5 and 6, the maximum size of the emission region was constrained to be $R \leq 6.8 \times 10^{13}$ m which is a factor ~ 6 bigger than my findings. The level of correlations found between gamma-ray, X-ray, optical and UV data during the flare and post-outburst periods, supported the conclusion that this source is likely to be at the border between BLR dissipated FSRQs and MT dissipated FSRQs. Abdo et al. (2010d) also suggest the large gamma-ray dominance over other wavelengths observed during the outburst is difficult to explain with a single-zone emission model.

An investigation by Max-Moerbeck et al. (2014a), using the first three years of *Fermi*-LAT data cross-correlated with radio data, found PKS 1502+106 as one of only three sources to show a correlation at larger than 2.25σ. The radio variations were found to lag the gamma-ray variations, indicating the gamma-ray emission originates upstream of the radio emission at a distance of 22 ± 15 pc from the central engine, which is beyond the BLR for a conical jet model.

In conclusion, this study finds PKS 1502+106 to be another example of an FSRQ with multiple simultaneously active emission regions. There is evidence of BLR emission from the short variability timescales, while the study of energy dependent cooling timescales yields different results for the two flare periods. However, the VHE photons observed with the *Fermi*-LAT are clearly not compatible with a BLR origin for the emission.

3.6.1.6 PKS 1424-41

The observed variability timescales of the January 2013 flare from PKS 1424-41 indicate a gamma-ray emission region of size $(0.77 \pm 0.24) \times 10^{13}$ m. The April 2013 flare from this source was found to have a larger emission region of size $(2.76 \pm 0.66) \times 10^{13}$ m. However, in neither flare is one spectral model favoured over another, and a lack of statistics at high energies made the study of energy dependent cooling inconclusive. Monte Carlo simulations show that the most energetic photon observed with the *Fermi*-LAT, having energy 140.5 ± 10.7 GeV and observed on MJD 56970.42, outside the flare periods I have studied, is compatible with a cut-off energy of 12.3 ± 1.2 GeV. This is just incompatible

with the energy cut-off expected due to BLR emission of 9.920 ± 0.001 GeV.

A multi-wavelength study of the April 2013 flare by Tavecchio et al. (2013) found the emission region to be located outside the BLR. Interpreting the SED using a one-zone leptonic model, the emission region was constrained to a distance of 5×10^{16} m from the central engine. Emission regions within the MT can also be reconciled with the short variability timescales observed in this study if one assumes the existence of compact emission regions throughout the jet. It has been proposed that these result from magnetic reconnection events (Giannios et al. (2009), Giannios (2013)) or the recollimation of the jet (Bromberg and Levinson (2009)).

The gamma-ray observations corresponding to the January 2013 flare period investigated in this work were claimed to be coincident with the petaelectronvolt (PeV; 1 PeV = 10^6 GeV) neutrino *cascade* event IC 35 detected by the IceCube collaboration (Kadler et al. (2016)), interpreted as evidence for hadronic emission from this object. IceCube events are classified depending on the pattern of the light seen in the detector array. *Track* events result from a high energy muon travelling a large distance, forming a visible track in the detector, and have an angular resolution of $\leq 1^\circ$. *Cascade* events, such as IC 35, are due to particle showers resulting from neutrino interactions and can be resolved to $\sim 15^\circ$(Aartsen et al. (2014)). The larger positional uncertainty for the cascade event raises the possibility of chance spatial coincidences between astrophysical neutrinos and potential astrophysical sources.

The IC 35 neutrino event that Kadler et al. (2016) claimed to associated with the gamma-ray flare studied in this work was centered on the coordinates RA = 208.4° and DEC = -55.8° with a median positional uncertainty of $R_{50} = 15.9^\circ$. As such, there is an angular separation of $\theta = 14.8^\circ$ between PKS 1424-41 and the neutrino *cascade* event. A Monte Carlo study of IceCube *track* neutrino candidates, revealed that a single neutrino event within 1° of a gamma-ray source is consistent with chance coincidence (Brown et al. (2015)). Finally, I note that the January 2013 flare period also included the emission of 8 VHE photons but that there was no reported detection of neutrino events at those exact time intervals.

Nonetheless, a hadronic component to the emission might explain why the leptonic approaches used throughout this study to determine the location of the emission region from the flares have proved inconclusive.

The results of my investigations, put together, implies an extremely compact gamma-ray emission region. There is no direct evidence to suggest BLR origin as investigations into the presence of a cut-off in the spectrum and the energy dependence of the cooling timescales proved inconclusive for both flare periods studied. The VHE photon emission observed with the *Fermi*-LAT is incompatible with BLR origin and indicates emission from within the MT.

3.6.1.7 3C 279

3C 279 shows a shortest variability timescale of 2.08 ± 0.17 hours during the December 2013 flare and 2.14 ± 0.65 hours for the June 2015 flare. While the December 2013 flare favours neither model, the spectrum of the June 2015 flare strongly favours a log parabola over a power law and is therefore compatible with an emission region inside the BLR. Further evidence towards BLR origin of emission is provided by the LCCF study of the June 2015 flare showing a lag of 0.9 ± 2.8 hours, indicating no energy dependence in cooling timescales. The LCCF study of the December 2013 flare was inconclusive due to a lack of photon statistics.

During the flare periods studied, 19 VHE photons were observed with the *Fermi*-LAT. However, the maximum observed photon energy, 88.6 ± 6.5 GeV, was observed on MJD 56785.70, just outside the period of the December 2013 flare. Monte Carlo simulations suggest that this corresponds to a cut-off energy of 16.5 ± 1.5 GeV, which is compatible with the expected cut-off energy of 16.234 ± 0.004 GeV due to interaction with Lyman alpha photons and indicates the VHE emission is also compatible with BLR origin.

A study of the December 2013 flare by Hayashida et al. (2015), based on broadband spectral modelling, found the shortest variability timescales to be $\sim$ 2 hours which agrees well with my result and also places the emission region within the radius of the BLR. Rani

et al. (2018) studied the flaring activity of 3C 279 between November 2013 - August 2014 and found six bright flares superimposed on the long term outburst. The first three of these correspond to the December 2013 flare studied in this investigation. This flare was accompanied by the ejection of a new VLBI component, and the 43 GHz core beyond the BLR is suggested as the potential source of the gamma-ray emission.

The June 2015 flare was studied by Ackermann et al. (2016) and a flux doubling time of less than 5 minutes on top of the long term evolution of the event has been reported. These extremely short timescales constrain the emission region to a size of $R \leq 10^{-4}(\delta/50)$ pc = 1.13×10^{12} m for $\delta = 18.3$ (Jorstad et al. (2017)).

A separate investigation of the June 2015 flare was undertaken in the $E_\gamma \geq 100$ GeV domain with H.E.S.S. (H. E. S. S. Collaboration et al. (2019)). Using a combined fit of the *Fermi*-LAT data and H.E.S.S. data to find constraints on the absorption of gamma-rays, the emission region was found to be at a distance $r \geq 1.7 \times 10^{15}$ m from the SMBH and beyond the BLR. The minute scale variability was attributed to small turbulent cells (Giannios (2013)) rather than an emission region encompassing the entire width of the jet.

The H. E. S. S. Collaboration et al. (2019) study used EBL optical depths from the Franceschini et al. (2008) model and adopted a detailed study of the BLR absorption by considering different geometries in order to extrapolate the *Fermi*-LAT data beyond 10 GeV. Nonetheless, the extrapolation under-predicts the H.E.S.S. flux at the highest energies by an order of magnitude, and indeed no one-zone model was able to fully describe the multi-wavelength behaviour during the June 2015 flare.

In conclusion, while the results from the December 2013 flare are inconclusive, the results from the June 2015 flare support a BLR origin for the gamma-ray emission. The VHE emission observed more generally from this source with the *Fermi*-LAT is also found to be compatible with a BLR origin. While the presence of multiple emission regions seen in other sources has been suggested (Rani et al. (2018)), this study finds no direct evidence for emission from beyond the BLR.

3.6.1.8 4C 21.35

The variability timescales of 4C 21.35 (also known as PKS 1222+216) are indicative of an emission region of size (2.05 ± 0.66) × 10^{13} m for the June 2010 flare and (1.67 ± 0.12) × 10^{13} m for the November 2014 flare. Under the simple one-zone model assumption, both of these indicate emission from within the BLR. In terms of the spectral shape, the November 2014 flare favours neither model, but the June 2010 flare is better fitted by a log parabola than a power law which, in principle, is further evidence for BLR origin of the emission.

The June 2010 flare shows evidence of a LCCF peak at -5.8 ± 0.4 hours, indicating that changes to the low energy component of the emission precedes changes to the high energy component. This suggests that, similarly to the case of CTA 102, the MeV and GeV components of this particular flare have different origins and may be interpreted as evidence for multiple emission regions. The November 2014 flare did not have enough photon statistics to allow the study of energy dependence in cooling timescales using LCCFs.

The most energetic VHE photon was observed at an energy of 84.1 ± 6.2 GeV on MJD 55317.89 (during the June 2010 flare). Monte Carlo simulations show that this is indicative of a cut-off energy of 15.6 ± 1.4 GeV, which is lower than the expected cut-off at 17.48 ± 0.01 GeV due to interaction with Lyman alpha photons within the BLR. This implies the high energy photon emission observed with the *Fermi*-LAT is, in principle, compatible with BLR origin.

The June 2010 flare of 4C 21.35 investigated in this work was detected with MAGIC (Aleksić et al. (2011)) in the energy range 70 GeV ≤ E_γ ≤ 400 GeV. This spectrum was found to be well described with a hard power law and also, unlike the H.E.S.S. 3C 279 spectrum (H. E. S. S. Collaboration et al. (2019)), to connect smoothly with the *Fermi*-LAT spectrum (Tanaka et al. (2011)), suggesting a common origin for the emission. The observed flux doubling times of 10 minutes also constrained the size of the emission region to R ≤ 2.5(δ/10) × 10^{12} m = 1.85 × 10^{12} m for δ = 7.4 (Jorstad et al. (2017)).

Assuming a standard one-zone model, this would imply an emission region well within the BLR. However, the dense photon fields in the BLR would lead to high opacity for the gamma-rays detected with MAGIC due to photon-photon pair production (see Section 3.4.2).

This contradiction is addressed in Tavecchio et al. (2011) who examine whether a one-zone model is a viable solution to reproduce the observed spectral energy distribution and variability of 4C 21.35 from the MAGIC detection. Three different models are used: i) a simple one-zone model outside the BLR, ii) a two-zone model with the emission region predominantly located outside the BLR and iii) a two-zone model with the emission regions inside the BLR. The two-zone models are found to be energetically less demanding than the single zone model and the results are compatible with a scenario in which the jet undergoes recollimation at large distances from the SMBH.

The results of my investigations for 4C 21.35, together with evidence from other work, again suggests that gamma-ray emission results from multiple compact regions along the relativistic jet.

3.6.1.9 PKS 0454-234

PKS 0454-234 is seen to have a shortest variability timescale of 1.62 ± 0.28 hours for the January 2009 flare and 1.39 ± 0.24 hours during the November 2011 flare. Both timescales indicate emission from extremely compact regions in the jet of size (4.55 ± 0.79) × 10^{13} m and (3.91 ± 0.67) × 10^{13} m respectively. However, a search for evidence of a possible cut-off in the spectrum for both flares proved inconclusive. This was also the case for the investigation into the energy dependence in cooling timescales, due to the large uncertainties in flux.

While the flare intervals studied are both accompanied by VHE emission, the most energetic VHE photon (E_γ = 185.9 ± 14.2 GeV) was observed on MJD 57486.05, when there is no evidence for any flaring activity at lower energies. An energy cut-off at 27.5 ± 2.4 GeV best agrees with this observation; this is significantly higher than the 12.5 GeV expected

for this source due to interaction with Lyman alpha photons and suggests emission from beyond the BLR.

Interpolating the work of Liu and Bai (2006), who investigated a period of VHE activity of PKS 0454-234 from November - December 2012, the optical depth, $\tau_{\gamma\gamma}$, for gamma-rays emitted at the midpoint of the spherical BLR shell is $\tau_{\gamma\gamma} = 0.9$ at 35 GeV and $\tau_{\gamma\gamma} = 1.3$ at 50 GeV. I find a significant detection (TS = 84) of this object at $E_\gamma > 50$ GeV combining all 8 years of *Fermi*-LAT data (Table 3.6), suggesting that there is emission originating from beyond the BLR. This agrees with the findings of Pacciani et al. (2014) who report that the shape of the SED for PKS 0454-234, in particular the large separation between the IC peak and the synchrotron peak, suggests the VHE emission is likely to be coming from large distances from the SMBH.

Thus, while the rapid variability from this object suggests that emission could originate within the BLR, there is no supporting evidence for this contention from the spectral shape or from a LCCF analysis. The evidence from the VHE emission, which is seen both during the flares studied and outside flare events, is strongly suggestive of emission originating outside the BLR. The observed high energy photon emission makes PKS 0454-234 an interesting candidate for follow-up observations with IACTs, particularly as it is one of only three objects to show evidence (at the $\sim 4\sigma$ level) for emission above 100 GeV in the *Fermi*-LAT dataset I analysed. The other two objects showing such evidence (PKS 1510-089 and 3C 279) have already been detected with IACTs.

3.6.2 Overview and Implications

A detailed analysis of the two brightest flares from the sample of nine FSRQs has revealed flux variability timescales of the order of a few hours, indicating gamma-ray emission from extremely compact regions. Within the context of a simple one-zone model, these timescales are compatible with emission regions within the BLR. However, other evidence reveals a more complex picture.

The search for presence of a spectral cut-off shows evidence that 7 of the 18 flares studied

favour a log parabolic model over a power law; this can be interpreted as evidence of BLR origin of emission for these flares. The remaining flares were found to favour neither model over the other, which could indicate emission either from within the BLR or beyond it.

A study of energy dependence in cooling timescales shows evidence of achromatic cooling in 4 flares, indicating BLR origin of emission, while a further 6 flares revealed the presence of a time-lag between the MeV and GeV components of the emission which can be interpreted as evidence of multiple emission regions. Of these, 4 flares (including both those from PKS 1510-089) showed evidence of a positive time-lag between the high- and low- energy flux suggesting emission from regions within the MT, and 2 showed a negative time-lag, which may be indicative of multi-zone emission.

Finally, through Monte Carlo simulations it is shown that the $E_\gamma \geq 20$ GeV photon emission observed with the *Fermi*-LAT from most sources (the exceptions being for 3C 279, 3C 454.3 and 4C 21.35) is incompatible with BLR origin. This implies emission regions within the MT at parsec scale distances from the central engine, and the lack of correlation between the observed GeV flare intervals and VHE photon emission detected in some sources (for example PKS 0454-234) can be interpreted as evidence of multiple emission regions.

The results of the investigations presented in this work lead to the natural conclusion that a more complex emission model than a simple one-zone leptonic model is required. As seen in Table 3.7, there is evidence to suggest the presence of multiple simultaneously active emission regions both within the BLR and the MT, in most individual sources even during the same flaring episode.

In the context of the sources studied in this work, multi-zone emission has been suggested in previous investigations (for example PKS 1510-089 (Nalewajko et al. (2012), Brown (2013)), 3C 454.3 (Coogan et al. (2016), Finke (2018)), 3C 279 (Rani et al. (2018)) and 4C 21.35 (Foschini et al. (2011b)). The existence of multiple extremely compact and simultaneously active emission regions is seemingly a characteristic feature found in gamma-ray observations of the brightest FSRQs.

3.7 Conclusion

This chapter describes a temporal and spectral analysis of the gamma-ray emission from a sample of nine bright FSRQs observed with the *Fermi*-LAT over the first eight years of its operation. I consider photons detected in the energy range 100 MeV-300 GeV in the time interval MJD 54682.66 - MJD 57604.66 which corresponds to midnight on the August 4, 2008 until midnight on August 4, 2016. During this period each source was observed to have several intervals satisfying my definition of a flare (see Section 3.3). The two brightest flares from each source were investigated in detail in order to draw conclusions regarding the size and location of the emission region.

These bright flares provided sufficient statistics to allow for re-analysis in daily, 6 hourly and 3 hourly intervals while still satisfying the TS $\geq$ 10 criterion for each bin. The 3 hour binned lightcurves revealed variability in timescales of a few hours, with the shortest flux doubling time obtained being 0.65 $\pm$ 0.11 hours from the July 2009 flare of B2 1520+31. These short timescales imply an extremely compact emission region of the order of 10^{13} m for each source. While it should be noted that emission regions within the MT can also be reconciled with the short variability timescales observed in this study, for instance those resulting from magnetic reconnection events (Giannios et al. (2009), Giannios (2013)) or the recollimation of the jet (Bromberg and Levinson (2009)), if one assumes that the entire width of the jet is responsible for the emission, the timescales indicate BLR origin.

The flare periods were then studied in more detail to search for the presence of a cut-off in the spectrum which can be interpreted as a consequence of photon-photon pair production within the BLR. An AIC test was undertaken to determine which of a power law and a log parabolic model provided a better fit to the data. This study finds evidence for a spectral cut-off in 7 of the 18 flares investigated, supporting a BLR origin for the emission during these events. No conclusive evidence for a cut-off was found for the other 11 flares.

This was followed by an investigation into the energy dependence in cooling timescales by applying LCCFs to search for correlations between the high energy (1 - 300 GeV) and low

energy (0.1 - 1 GeV) flux. 4 flares were found to have a LCCF compatible with a peak at 0, indicating no energy dependence and implying a BLR origin for the emission. A further 6 flares show evidence of a time-lag between the MeV and GeV components of the emission which can be interpreted as indicating the presence of multiple emission regions. Among these, 4 flares have a positive time-lag between the high- and low- energy flux suggesting emission regions within the MT and 2 showed evidence for a negative time-lag. The results of the remaining flares were found to be inconclusive, with the lack of photon statistics preventing the calculation of LCCFs.

The final investigation considered VHE ($E_\gamma \geq 20$ GeV) photon emission from the sample of FSRQs. A likelihood analysis of all photons in the energy range 20 - 300 GeV over the entire eight year observation period revealed significant emission from all sources at a confidence level of $> 5\sigma$. This was followed by a closer inspection of the individual photons observed. Monte Carlo simulations were used to compare the most energetic photon observed with the *Fermi*-LAT for each source to the expected photon energy distribution assuming BLR origin of emission. Only three of the sources, 3C 279, 3C 454.3 and 4C 21.35, are found to have VHE photon emission compatible with the expected BLR Lyman alpha photon interaction suggesting that the VHE emission in the other sources is being produced in emission regions within the MT.

The apparent contradictions regarding the origin of the gamma-ray emission found in the sample can be reconciled by invoking the presence of multiple simultaneously active emission regions both within the BLR and the MT.

Future study of the gamma-ray emission from FSRQs as well as other sources in the VHE energy range is expected to improve with the construction of the Cherenkov Telescope Array (CTA; Acharya et al. (2013); Cherenkov Telescope Array Consortium et al. (2019); see Section 4.4). The CTA is expected to provide unprecedented insight over a wide energy range of 20 GeV-300 TeV and improve on the sensitivity of current ground-based telescopes by more than an order of magnitude. The CTA will comprise two observatories in order to provide a full-sky coverage. The Northern array will be located in La Palma (Spain) and the Southern array will be located at Paranal (Chile).

The results of my simulations presented in Section 5.4 (see Table 5.2) indicate that 7 of the 9 sources investigated in this chapter should be detectable with the CTA in just 5 hours of observation with the exceptions being B2 1520+31 and PKS 1502+106. The enhanced sensitivity should provide improved statistics to make even stronger conclusions regarding the nature of the emission regions.

In particular, it will be fascinating to have an improved understanding of the dominant factors responsible for the origin of the emission as well as possible reasons for the changeable location within the context of the multi-zone emission model. Furthermore, the lack of correlations between the VHE photon emission and the GeV flares seen in some sources (for example PKS 0454-234) underlines the importance of survey, as opposed to targeted, observations of FSRQs with IACTs.

Chapter 4

Ground-based gamma-ray astronomy

Despite the remarkable success of the *Fermi* mission, an important disadvantage of space based gamma-ray astronomy is the smaller effective area of telescopes, leading to a reduced sensitivity at the highest energies. Furthermore, current space based detectors also lack the instantaneous sensitivity required to finely probe the underlying physics of the emission phenomena. While it is conceivable to launch a space satellite with a very large detector, as things stand such an undertaking would be far too expensive to make it practical. Fortunately, a pair production mechanism similar to that found in the *Fermi*-LAT detector already exists all around us.

As discussed in Section 1.3.2.1, a gamma-ray entering the Earth's atmosphere undergoes electron positron pair production and ultimately gives rise to electromagnetic air showers. The Cherenkov light produced in these showers can be observed by ground-based instru-

ments. This chapter begins with a description of the mechanisms involved in the production of the air showers before proceeding to a discussion on Cherenkov radiation and the current generation imaging atmospheric Cherenkov telescopes (IACTs). I conclude by introducing the Cherenkov Telescope Array (CTA), the next generation ground-based observatory for gamma-ray astronomy.

4.1 Air showers

High energy photons entering the Earth's atmosphere interact with the Coulomb field of atmospheric nuclei to produce an electron positron pair. These particles can themselves interact with the nuclei and emit Bremsstrahlung radiation, which can further pair produce, leading to a cascade of secondary particles. The cascade continues as long as the resulting particles have an energy greater than the critical energy required for pair production, $E_{\rm c} = 2m_e = 1.02$ MeV where m_e is the rest mass of an electron. This results in electromagnetic air showers as illustrated in Figure 4.1.

The propagation of an air shower can be understood using the basic model proposed by Bethe and Heitler (Heitler (1954); Matthews (2005)). This simplified model relies on the assumptions that only Bremsstrahlung and pair production interactions take place and the energy is divided equally between the particles produced at each stage of interaction. Therefore, the number of shower particles (electrons, positrons and photons) involved at each interaction doubles, meaning that after a distance nR, where R is the radiation length, the number of particles will be 2^n.

Since the energy is divided equally, each particle will have an energy $E_0/2^n$ where E_0 is the energy of the primary gamma-ray photon. The process continues until the energy of each particle drops below E_c at which point the rate of production of new particles falls drastically. The number of particles at shower maximum is therefore $N_{\rm max} = 2^{n_{\rm max}} = E_0/E_c$ and occurs after a distance:

$$d = n_{\rm max} R = \frac{\ln E_0/E_c}{\ln 2} R. \tag{4.1}$$

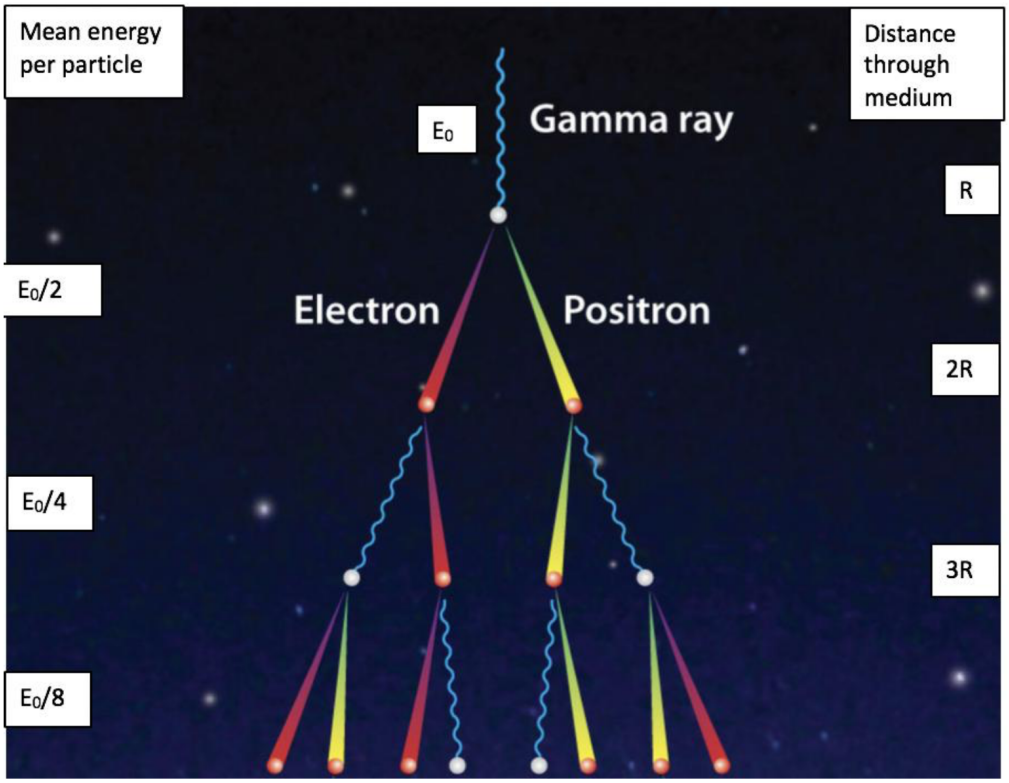

Figure 4.1: An illustration of an electromagnetic air shower induced by a primary gamma-ray photon having energy E_0 and radiation length R. Adapted from Longair (2011).

Hadronic particles, for example cosmic rays, also interact with atomic nuclei and produce similar air showers on entering the Earth's atmosphere. These interactions are more common than gamma-ray induced showers and involve the production of secondary particles like electrons, positrons, pions, muons and kaons. The neutral pions decay into a pair of gamma-ray photons and initiate an electromagnetic shower as discussed previously. Cosmic ray air showers, in general, have a larger transverse momentum and, as seen in Figure 4.2, the resulting particles are more spread out than those produced from gamma-rays.

Another potential source of electromagnetic air showers are cosmic ray electrons (Earl (1961), Meyer and Vogt (1961)). Electrons are primarily produced as secondary particles from high energy collisions between cosmic rays with the interstellar medium. Both air showers produced by cosmic ray electrons and showers initiated by gamma-rays are pure electromagnetic showers, making them difficult to distinguish using current ground-based instruments (Grieder (2010)).

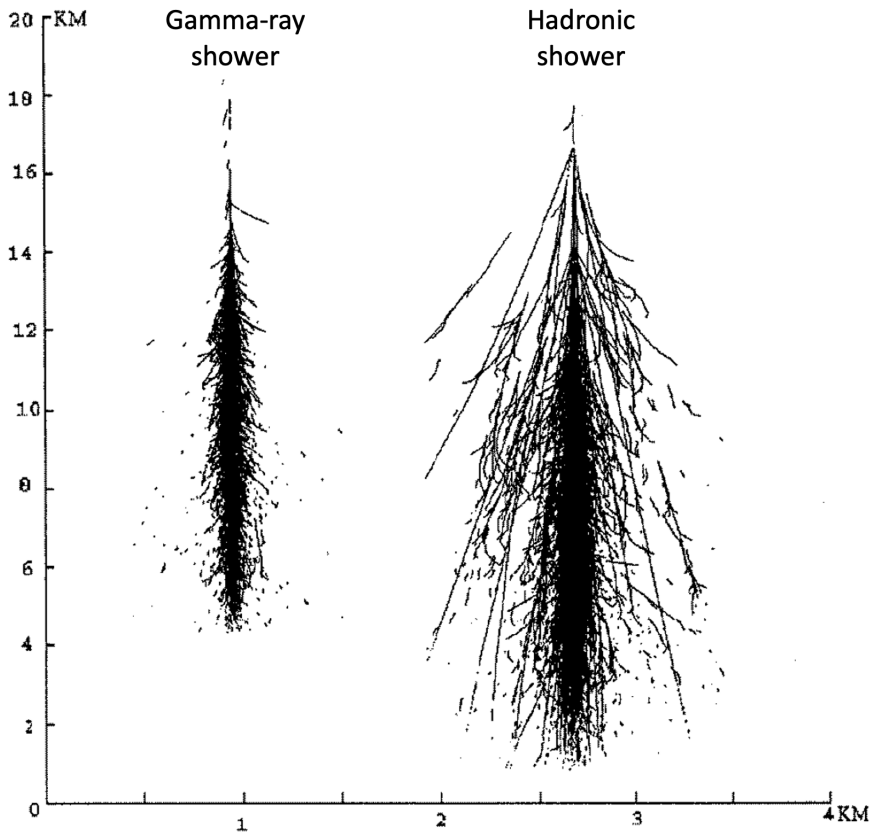

Figure 4.2: A comparison of Monte Carlo simulations for the development of a 300 GeV gamma-ray shower (left) and a 900 GeV hadronic shower (right). The horizontal scale has been exaggerated for clarity of illustration. Adapted from Fegan (1997).

4.2 Cherenkov Radiation

A charged particle, for example an electron or positron formed during an air shower, moving through a medium, for example the Earth's atmosphere, at a velocity greater than the phase velocity of light in that medium forms a shock wave and emits a pulse of Cherenkov radiation.

As shown in Figure 4.3, the Cherenkov radiation propagates outward, generating a cone of constructive interference governed by the Huygens principle. The entire process is analogous to a sonic boom generated when an object travels through air at a velocity faster than the speed of sound in air.

The direction of propagation of the Cherenkov radiation wavefront is determined by the

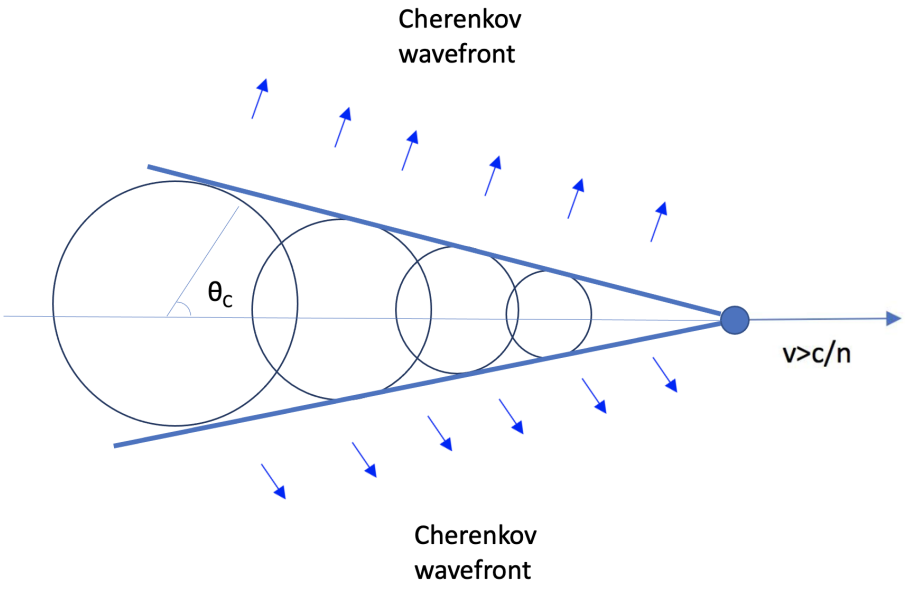

Figure 4.3: An illustration of the Huygens construction for determining the direction of propagation of the Cherenkov radiation wavefront.

opening angle, θ_C, and depends on both the velocity of the charged particle, v, as well as the refractive index of light in the medium, n, such that:

$$\cos\theta_C = \frac{1}{n\beta} \tag{4.2}$$

where $\beta = v/c$. For Cherenkov radiation to be emitted, the velocity of the particle must be larger than the phase velocity of light in the medium, $v > c/n$.

Since the refractive index of air decreases with altitude, as the density of air decreases, the opening angle increases downwards but is always less than $\sim 1.4°$. Figure 4.4 shows the evolution of the opening angle and radius of the resulting cone with altitude. This variation results in the Cherenkov light being focused as a ring around the shower axis having a typical radius of $\sim$ 120 m, although there may be further spread due to the Coulomb scattering of the electron positron pairs.

Figure 4.5 compares the distributions of the Cherenkov emission at ground level produced by a 300 GeV gamma-ray photon and a 1 TeV proton. The proton shower has a more complex distribution with small sub-clusters produced by secondary electromagnetic showers and

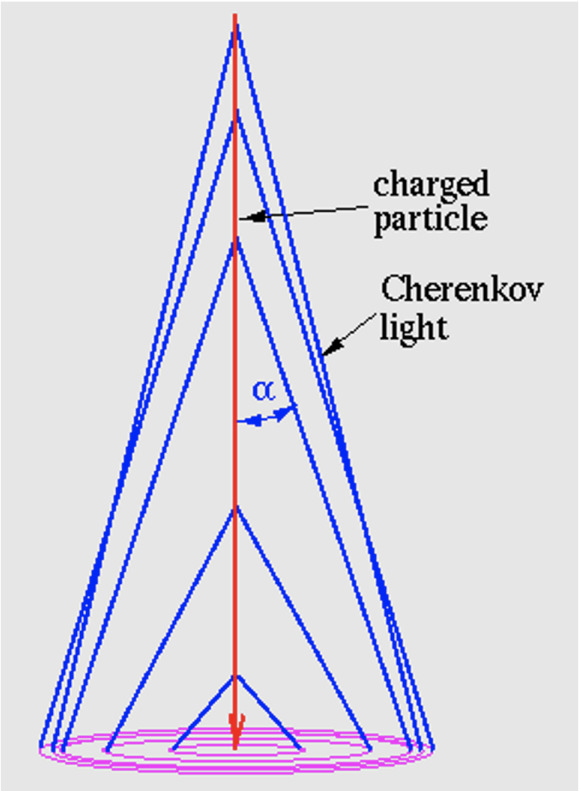

Figure 4.4: An illustration of the evolution of the opening angle, α, and radius of the resulting cone of Cherenkov radiation with altitude. Credit: K. Bernlöhr, MPIK Heidelberg. (`https://www.mpi-hd.mpg.de/hfm/CosmicRay/ChLight/Cherenkov.html`, accessed on 22/01/2021).

rings generated from muon showers. This difference in the distributions can be used to reject background cosmic-ray events with stereoscopic systems i.e. several telescopes viewing the same shower from different angles.

The number of Cherenkov photons emitted by a charged particle at a given wavelength, λ, and path length, x, is given by the Frank-Tamm formula (Tamm and Frank (1937)):

$$\frac{d^2N}{dxd\lambda} \propto \frac{1}{\lambda^2}, \tag{4.3}$$

indicating a preference for shorter wavelengths. As a result of atmospheric absorption, the Cherenkov radiation is found to peak in the blue/UV regime at typical wavelengths of $\sim$ 400 nm.

The Frank-Tamm relation was derived under the assumption that an electron is moving an

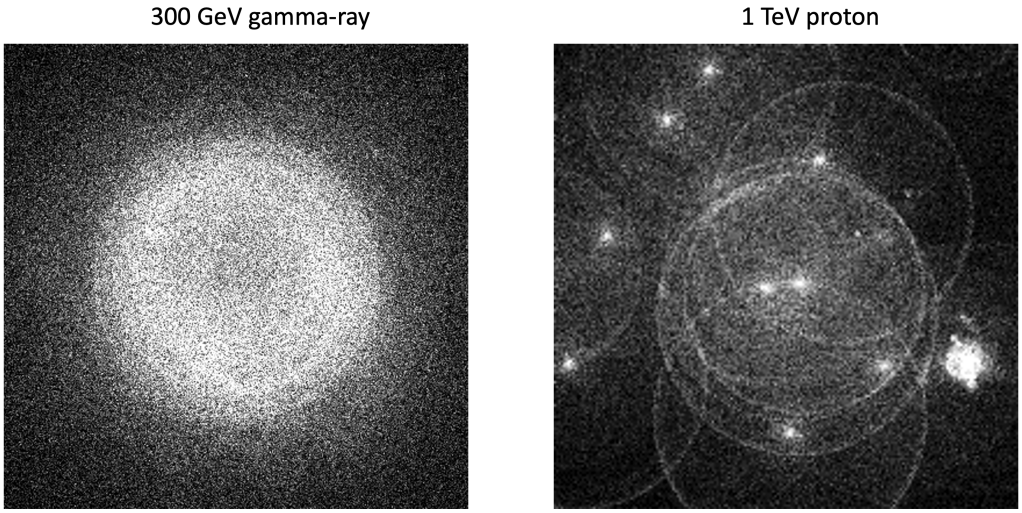

Figure 4.5: The lateral distributions of the Cherenkov light generated from an air shower initiated by a 300 GeV gamma-ray photon (left) and a 1 TeV proton (right) as seen from ground level. The area displayed covers 400 × 400 m^2 with the shower core at the centre. Credit: K. Bernlöhr, MPIK Heidelberg. (`https://www.mpi-hd.mpg.de/hfm/CosmicRay/ChLight/Cherenkov.html`, accessed on 22/01/2021).

infinite distance in a perfectly isotropic dielectric medium at a constant velocity, as shown in Figure 4.6. The electric field of the electron distorts the nearby atoms of the medium. These atoms are momentarily transformed into electric dipoles aligned with respect to the electric field of the electron.

If the electron was moving at a non-relativistic velocity, the polarisation would be completely symmetric and no net field would be produced by the medium. However, if instead, the velocity of the electron was faster than the phase velocity of light in the medium, an asymmetry would be formed along the trajectory of the electron and result in a net dipole field, causing parts of the polarised medium to release small bursts of electromagnetic radiation.

4.3 Current generation IACTs

The Cherenkov radiation produced in air showers can be observed using IACTs. In principle, the method involves a telescope with a large collection area focusing these pulses onto a camera, traditionally composed of photomultiplier tubes (PMTs), and capable of

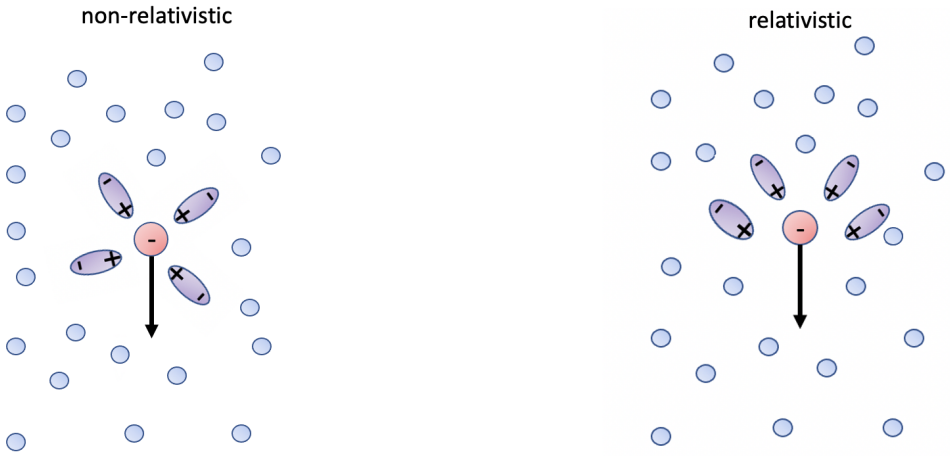

Figure 4.6: The polarisation produced in the dielectric medium due to the presence of the electron, for the cases of a non-relativistic (left) and relativistic (right) electron respectively.

very fast image capturing. The three main experiments involving current generation IACTs, namely MAGIC, H.E.S.S. and VERITAS, are shown in Figure 4.7.

4.3.1 MAGIC

The Major Atmospheric Gamma-ray Imaging Cherenkov (MAGIC) telescopes are located at the Roque de los Muchachos Observatory in La Palma, Spain. At an altitude of 2200 m above sea level, it comprises two IACTs, each 17 m in diameter, separated by 85 m. MAGIC is sensitive to gamma-rays in the energy range 25 GeV - 30 TeV, and is the most sensitive currently generation IACT at $E_\gamma \leq 100$ GeV. This is a result of having a large total mirror surface area of 236 m^2 which made it, prior to the construction of H.E.S.S. II, also the biggest IACT.

Particular highlights among the investigations performed with MAGIC relevant to my thesis are the detection of 3C 279 (MAGIC Collaboration et al. (2008)) and 4C 21.35 (Aleksić et al. (2011)) in the energy range 70 GeV $\leq E_\gamma \leq$ 400 GeV. Another major discovery with MAGIC was the observation of rapid variability from the radio galaxy IC 310 located at the outskirts of the Perseus cluster which constrained the emission region to be smaller than 20 % of the gravitational radius of its central SMBH (Aleksić et al. (2014)).

Figure 4.7: Top: The MAGIC II (left) and MAGIC I (right) telescopes. Credit: Derek Strom, Giovanni Ceribella and the MAGIC Collaboration (https://www.sense-pro.org/portraits/experiments/magic, accessed on 28/08/2020). Middle: The large central H.E.S.S. telescope along with two smaller telescopes. Credit: MPIK (https://www.mpi-hd.mpg.de/hfm/HESS, accessed on 28/08/2020). Bottom: The VERITAS gamma-ray telescope located in the Santa Rita Mountains, Arizona. Credit: VERITAS (https://scitechdaily.com, accessed on 28/08/2020).

4.3.2 H.E.S.S.

The High Energy Stereoscopic System (H.E.S.S. after Victor F. Hess, Nobel laureate who first observed cosmic rays) located at the Khomas Highlands in Namibia, is formed of 5 IACTs at an altitude of 1800 m above sea level. The observatory comprises four 12 m telescopes forming a perfect square of side 120 m with a larger 28 m telescope at its centre. It is sensitive to gamma-rays in the energy range 30 GeV - 100 TeV.

The Galactic survey performed with H.E.S.S. (H. E. S. S. Collaboration et al. (2018)) has detected 78 sources in the VHE regime. Furthermore, deep gamma-ray observations performed with H.E.S.S. showed evidence of the SMBH at the centre of the Milky Way being a potential source of PeV cosmic rays (HESS Collaboration et al. (2016)). Finally, among the FSRQs investigated in this thesis, observations made with H.E.S.S. have detected PKS 1510-089 (Abramowski et al. (2013)) and 3C 279 (H. E. S. S. Collaboration et al. (2019)) in the energy range $E_\gamma \geq 100$ GeV.

4.3.3 VERITAS

Located on Mount Hopkins in Arizona, USA, the Very Energetic Radiation Imaging Telescope Array System (VERITAS) is an array of four 10 m IACTs sensitive to photons in the energy range 50 GeV - 50 TeV. The telescopes, at an altitude of 1268 m above sea level, are arranged in a diamond-shaped distribution separated by a baseline of $\sim$ 100 m. Due to its being able to collect scientific data even under conditions of partial moonlight, VERITAS has on average, a 40% increase in data yield (Daniel (2020)).

Since it began operations in September 2007, observations with VERITAS have led to the detection of VHE emission from 31 BL Lac objects, the first of which were the discoveries of W Comae and 1ES 1218+304 in the same field (Acciari et al. (2008), Acciari et al. (2009b)), 3 FSRQs (for example 4C 21.35 (Holder (2014))) and 3 radio galaxies (for example M87 (Acciari et al. (2009a)))*. Moreover, the discovery of the starburst galaxy

* `http://tevcat.uchicago.edu/`, accessed on 29/04/21 and Benbow (2019).

M82 (VERITAS Collaboration et al. (2009)) provided evidence of supernovae from massive stars being a dominant accelerator for cosmic ray particles.

4.4 The Cherenkov Telescope Array

Building on the success of current ground-based experiments, the Cherenkov Telescope array (CTA) represents the next generation observatory in ground-based gamma-ray astronomy. Driven by the engagement of the CTA Consortium, comprising more than 1500 members from institutions in 31 different countries, the CTA will operate as an open observatory potentially capable of achieving unprecedented scientific goals.

4.4.1 Layout

The CTA will consist of arrays of 50 - 100 IACTs on two different sites, one in each hemisphere, aiming to provide full sky coverage with enhanced sensitivity and improved angular and energy resolution. The northern array, CTA N, will be located at the Roque de los Muchachos Observatory in La Palma, Spain, close to the site which currently hosts the MAGIC telescopes. The southern array, CTA S, will be located in the Atacama Desert, Chile, less than 10 km away from the Paranal Observatory operated by the European Southern Observatory (ESO).

As a trade-off between achieving peak performance over a wide range of energy and costs of construction, the CTA will comprise different sized telescopes:

Small-Sized Telescopes (SSTs)

At energies beyond a few TeV, air showers are capable of producing a large number of Cherenkov photons spread over a large area. In order to maximise the detection of these photons, the CTA is expected to have 70 Small-Sized Telescopes (SSTs) having ~ 8 m^2 collection area well spread out at distances of 200 m to 400 m between them. The SSTs will be present only in the southern site and will achieve full system sensitivity in the energy range 5 TeV - 300 TeV.

Medium-Sized Telescopes (MSTs)

The Medium-Sized Telescopes (MSTs) represent the "workhorses" of the CTA and are most optimised to an energy range between 150 GeV - 5 TeV. Each telescope, similar in design to H.E.S.S. and VERITAS, will be ~ 12 m in diameter and spread out over an area of 5×10^5 m^2 across both the northern and southern sites. The larger area covered will provide greater sensitivity and help build on the knowledge already gained in this energy regime from other ground-based experiments.

Schwarzschild-Couder Telescopes (SCTs)

The Schwarzschild-Couder Telescopes (SCTs) are a proposed dual-mirrored alternative version of the MSTs also achieving full system sensitivity in the energy range between 150 GeV - 5 TeV. The dual-mirror optical system is designed to focus the photons better and obtain a more detailed image, helping in the detection of faint sources. The prototype Schwarzschild-Couder Telescope (pSCT) was inaugurated at the Whipple Observatory, Arizona in January 2019.

Large-Sized Telescopes (LSTs)

The CTA will comprise four Large-Sized Telescopes (LSTs), ~ 23 m in diameter, spread over both the northern and southern sites and most optimised to the energy range between 20 GeV - 150 GeV. At these energies, the air showers produce lower densities of Cherenkov photons, typically contained within a ring of radius ~ 100 m which are relatively faint, requiring larger mirrors in order to image them.

CTA N will focus on the lower and middle energy ranges roughly between 20 GeV - 20 TeV and is planned to host 4 LSTs, 15 MSTs and no SSTs. CTA S, on the other hand, should be sensitive to photons between 20 GeV - 300 TeV, the full energy range of the CTA. The full array will consist of 4 LSTs, 25 MSTs and 70 SSTs. The proposed layouts of the full northern and southern baseline arrays are shown in Figure 4.8.

It should be noted that Figure 4.8 is based on the expected layout of the full CTA baseline array. The initial construction phase of the CTA, referred to as the alpha configuration, will consist of 4 LSTs and 9 MSTs for the Northern array and 14 MSTs and 37 SSTs for the

Southern array. The full array, referred to as the omega configuration, will be completed in a later phase of construction subject to the availability of funds.

The performance of an IACT array can be estimated through detailed Monte Carlo simulations (for example Bernlöhr et al. (2013)) and depends on parameters related to both the design of the telescopes and the arrangement of the telescopes on the ground. A detailed study of optimal and cost-effective telescope layouts required to maximise performance over a wide range of energies is given in Acharyya et al. (2019).

At the low energy regime, for example, the performance of the CTA will be dominated by the LSTs since these telescopes are capable of detecting faint low energy showers due to their larger reflecting surfaces. For LSTs, a further consideration is the cost of the dish structures and it is expected that the CTA Northern site will consist of a square array of 4 LSTs, both for the full baseline array as well as the initial alpha phase of construction.

Furthermore, the telescopes should be optimally spaced as, for example, having too-large separations will result in fewer showers being simultaneously detected by all four telescopes, and have an adverse effect on the cosmic-ray background rejection. The size of the lightpool generated on the ground increases with energy and also impacts the layout. At energies $\sim$ 30 GeV, the Cherenkov light is contained within a typical radius of $\sim$ 120 m (Hassan et al. (2017a)). Acharyya et al. (2019) find an inter-telescope spacing of between 100 m to 150 m between the LSTs provides a good trade-off between having sufficient images for each air shower and a reasonable collection area, resulting in optimal sensitivity.

On the other hand, for energies in the TeV regime, the performance of the CTA will be limited by the number of gamma-ray showers detected. Having multiple SSTs up to large distances from the centre of the array increases the effective collection area and allows to observe multiple sources with sufficient statistics, even for reduced observing times (Colin and LeBohec (2009)). Furthermore, at these energies the cosmic-ray background can be rejected almost entirely and an inter-telescope spacing of 190 m to 300 m between the SSTs was found to provide optimal performance (Acharyya et al. (2019)).

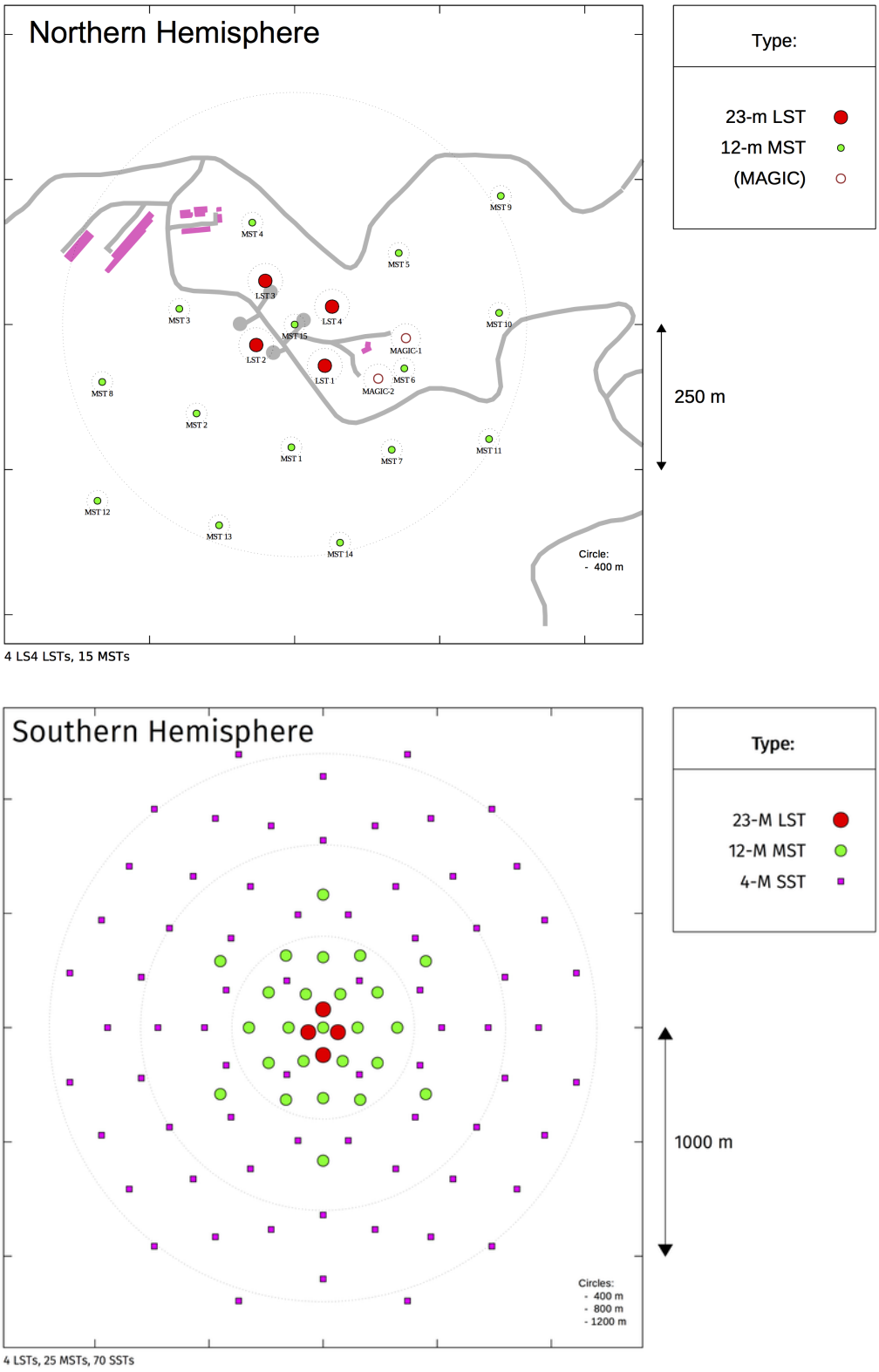

Figure 4.8: The proposed layout of both the CTA northern and southern arrays. Credit: the CTA consortium, see `https://www.cta-observatory.org/about/how-cta-works/array-layouts/`, accessed on 21/09/2020.

4.4.2 Performance and Sensitivity

It is expected that the CTA will improve upon the sensitivity of current generation IACTs by at least an order of magnitude. This can be achieved with the help of improved background rejection techniques, an increase in collection area and enhanced angular and energy resolution.

The Cherenkov photons are collected by mirrors and then focused on a camera capable of imaging the air showers and reconstructing the direction and energy of the primary gamma-ray photon. Traditionally, the reflecting surface of IACTs comprises a Davies-Cotton design (Davies and Cotton (1957)) with the camera located in the focal plane. The extremely short timescales of Cherenkov flashes (typically of the order of a ns) mandate that the camera must have fast electronics and as a result sensors like charge-coupled devices are disfavoured. Instead cameras are based on photomultiplier tubes (PMTs) or more recently silicon photomultipliers; these transform the incoming photons into electrical pulses which are processed and stored by a readout system.

The improved sensitivity with the CTA will be a result of the large number of telescopes observing each event and the increased collection area. Traditionally, shower images are parameterised in terms of second order moments using Hillas parameters (see Appendix C). Having multiple points of view of the same event will aid in determining the origin of the shower. Furthermore, having a large number of telescopes will also lead to the collection of a larger percentage of the Cherenkov radiation, resulting in enhanced energy reconstruction.

The expected performance of the CTA is estimated through detailed Monte Carlo simulations of several key parameters such as the minimum detectable flux, field of view and angular and energy resolution. These parameters are also strongly linked to the proposed layout of both arrays (see Acharyya et al. (2019) for a detailed study of optimal layout). The simulations generate large scale productions (*prod*) and IRFs released by the CTA Analysis and Simulation Working Group (ASWG) are periodically updated to reflect an improved understanding of the CTA layout and can be used, as in Chapter 5, to study the

scientific potential of the CTA.

For the purpose of this thesis, I use the latest *prod3b-v2* IRF release [†]. Response functions have been provided for observation times of 30 mins, 5 hours and 50 hours using both arrays at zenith angles of 20°, 40° and 60° respectively. The production focused on the optimisation of flux sensitivity, so the results do not as yet reflect the final performance of the CTA in terms of angular and energy resolution. Furthermore, the simulations assume nominal telescope pointing i.e. all the telescopes in the array are pointed parallel to each other. A performance evaluation for divergent pointing modes is currently under production.

Figure 4.9 shows a comparison between the expected sensitivity with the CTA and existing gamma-ray experiments. As seen in Figure 4.9, the observable energy range with the CTA should extend from below 100 GeV to beyond 100 TeV, spanning more than four decades in energy. The improved sensitivity will help, among others, in the study of faint sources already observed with the *Fermi*-LAT, the discovery of potentially new source populations at high energies and to discriminate between different hypotheses for gamma-ray emission.

Figure 4.10 shows a plot of the angular resolution, defined as the angle containing 68 % of the gamma-ray photons, of the southern array as a function of the reconstructed energy. The CTA is expected to achieve an angular resolution of below 0.05° at TeV energies and, as can be seen, will be a considerable improvement on current generation experiments.

Furthermore, as seen in Figure 4.10, the enhanced angular resolution will also be complemented with an increase in effective collection area. Figure 4.11 shows a comparison between the sensitivity of the CTA and the *Fermi*-LAT as a function of observing timescales. It can be seen that the CTA will be many orders of magnitude more sensitive than the *Fermi*-LAT for variability ranging from minutes to monthly timescales, with the two sensitivities only being comparable for time periods of almost a decade, roughly the entire mission time of the *Fermi*-LAT at the time of writing.

[†] see `https://forge.in2p3.fr/projects/cta_analysis-and-simulations/wiki/Prod3b_based_instrument_response_functions` for the IRF productions, accessed on 21/09/20.

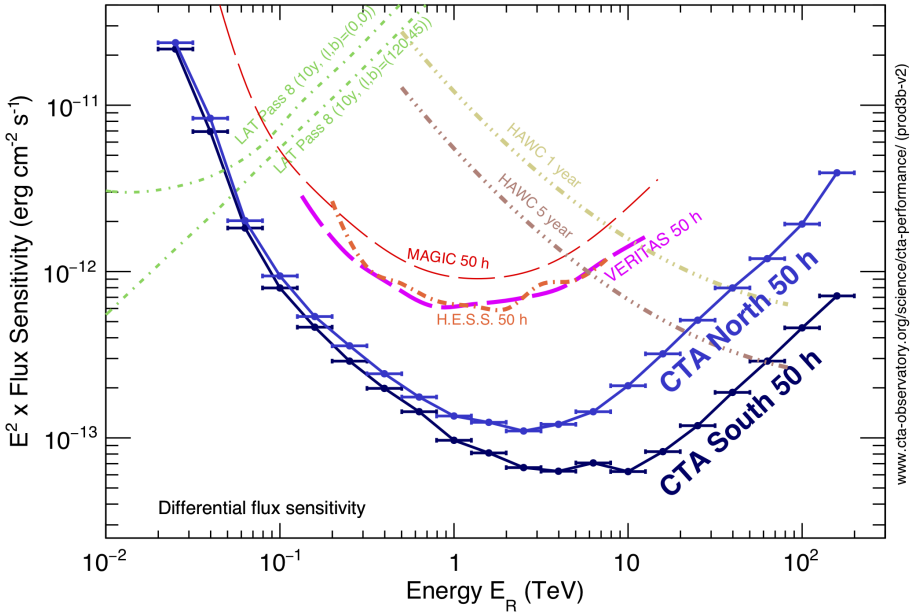

Figure 4.9: The expected differential flux sensitivity as a function of energy for 5σ detections in 50 hour observations with CTA N and CTA S. The plots are generated assuming a binning of five evenly spaced logarithmic bins per decade in energy. Also shown are the corresponding curves for MAGIC, H.E.S.S. and VERITAS as well as the results for 10 year observations with the *Fermi*-LAT and 1 year and 5 year observations using HAWC. The *Fermi*-LAT and HAWC results have both been scaled by a factor of 1.2 to account for different energy binning. Credit: the CTA consortium. The CTA curves represent the performance at the time of writing; for the latest performance plots see `https://www.cta-observatory.org/science/cta-performance`, accessed on 21/09/2020.

4.4.3 Key Science Projects

In order to make the most of the enhanced performance and sensitivity, the CTA Consortium has compiled a dedicated list of Key Science Projects (KSPs) which will take up roughly 40% of the observing time of the CTA over the first ten years of its operation. Some of the science cases considered are described briefly in the rest of this chapter and a comprehensive discussion on each can be found in Acharya et al. (2013) and Cherenkov Telescope Array Consortium et al. (2019).

The Extragalactic Survey

The CTA is expected to carry out a blind survey of 25% of the extragalactic sky at

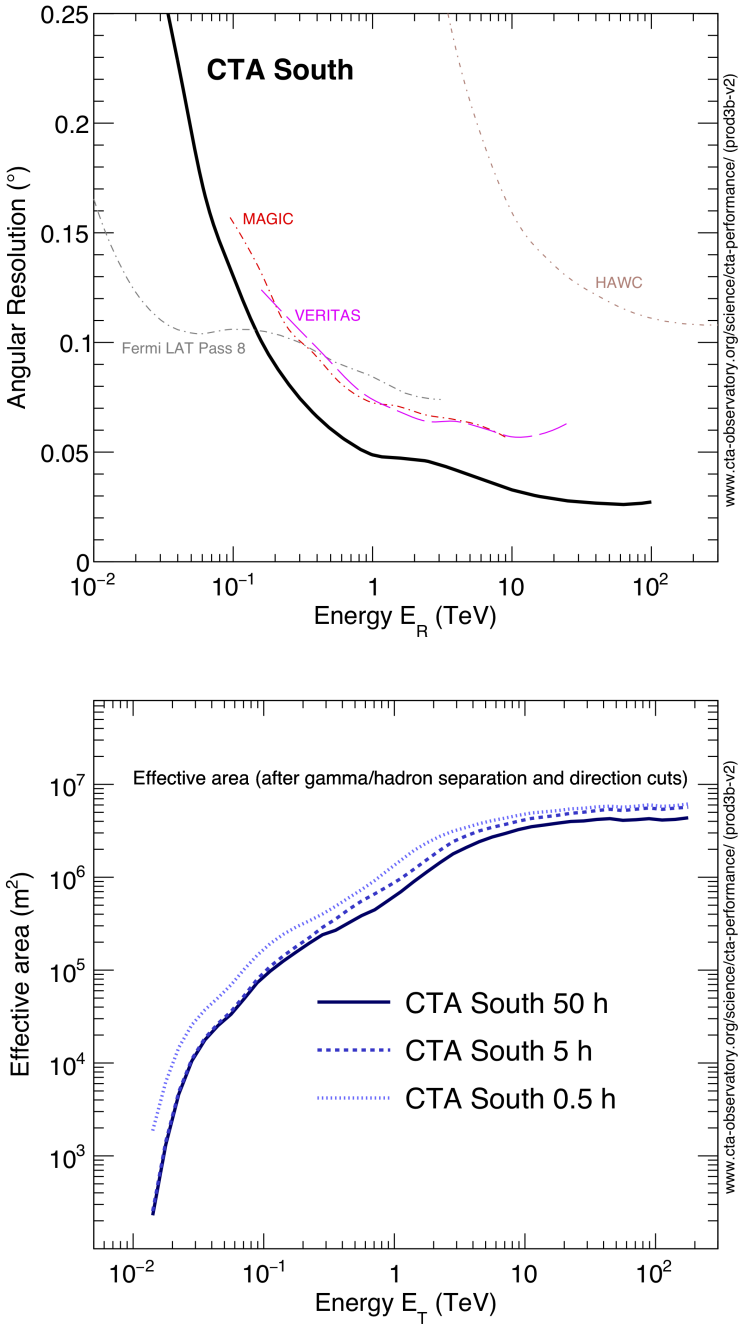

Figure 4.10: Top: The angular resolution, defined as the angle within which 68 % of the reconstructed gamma-ray photons are confined, for CTA S. Also shown for comparison are the corresponding curves for the *Fermi*-LAT, HAWC, MAGIC and VERITAS. Bottom: The effective collection area for gamma-rays from point sources as a function of energy optimised for 30 min, 5 hour and 50 hour observations with CTA S. Cuts have been applied to account for gamma-ray hadron separation and also in the direction of the reconstructed events. Credit: the CTA consortium. The CTA curves represent the performance at the time of writing; for the latest performance plots see `https://www.cta-observatory.org/science/cta-performance`, accessed on 25/09/2020.

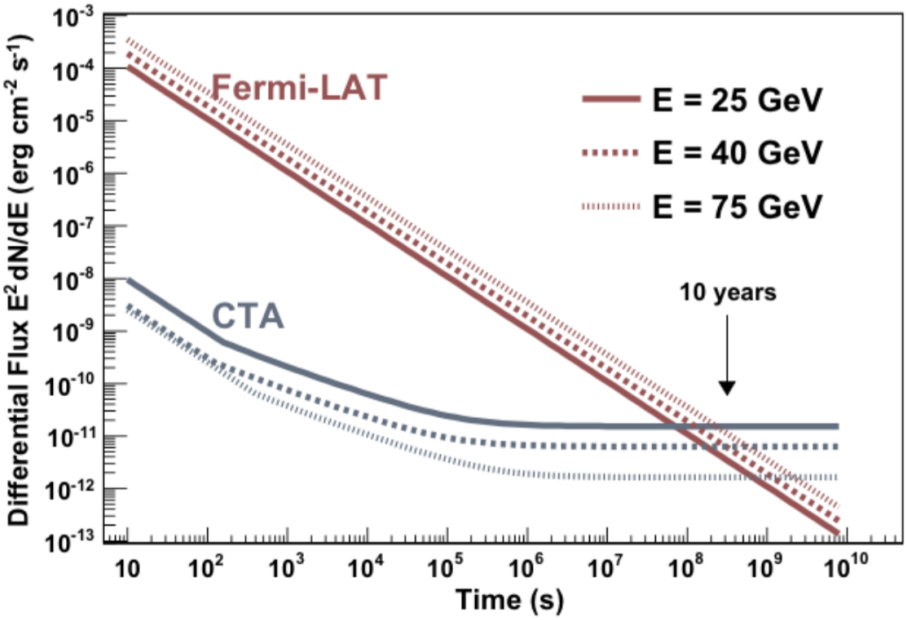

Figure 4.11: A comparison of the differential flux sensitivities of the CTA and the *Fermi*-LAT as a function of observing time. It should be noted that this plot was obtained for *PASS* 6 *Fermi*-LAT IRFs and early models of the CTA. Credit: Funk et al. (2013).

high energies. Current generation IACTs have detected over 60 extragalactic sources, the majority of which are BL Lac objects*. However, this sample is strongly biased since most observations were triggered by high flux measurements at lower energies in the optical, X-ray and gamma-ray regimes and roughly half these alerts took place when the sources themselves were undergoing flaring activity (Acharya et al. (2013); Cherenkov Telescope Array Consortium et al. (2019)). Chapter 5 presents a detailed investigation of the extragalactic source populations that should be detectable with the CTA.

Galactic Plane Survey

The Galactic Plane Survey (GPS), potentially the most exciting endeavour with the CTA, will study the entire Galactic plane using both the northern and southern arrays. It will help to investigate both known targets and also reveal new populations of promising VHE gamma-ray sources including supernova remnants (SNRs), pulsars and other binary systems. Furthermore, the properties of the diffuse gamma-ray emission from the Galactic

*`http://tevcat.uchicago.edu/`, accessed on 11/01/21.

plane can be investigated in detail and the large legacy data sets generated will inform astronomical studies of the future.

Galactic Centre

The study of the Galactic Centre with the CTA aims for a deep exposure of the innermost regions of our Galaxy along with a comprehensive survey of places not previously investigated with existing IACTs at high latitudes extending to the outer edge of the optical Bulge. This region includes a number of possible VHE emitters including the SMBH at the Galactic Centre, dense molecular clouds, active star formation regions (SFRs), multiple pulsars and SNRs and the large outflows known as the *Fermi bubbles*.

LMC Survey

The Large Magellanic Cloud (LMC) is one of the nearest and most active star forming galaxies and contains a number of potential gamma-ray sources. These include multiple SNRs (including SN1987A; the nearest in recent memory), the very active SFR 30 Doradus and numerous bubbles (including 30 Dor C). Deep surveys of the LMC will involve population studies of SNRs and pulsars, investigations into cosmic ray propagation, as well as searches for dark matter signals.

Transients

Transients are populations of astronomical sources both inside and beyond our Galaxy which exhibit extreme flaring activity across the entire electromagnetic spectrum ranging from timescales of a few milliseconds to those spanning many years. A source of gamma-ray emission, Transients are thought to be associated with relativistic emission from compact objects such as neutron stars.

The enhanced sensitivity provided with the CTA will allow for the study of the extremely short timescale variability associated with such phenomena. In addition, the relatively large field of view will help to both detect transient events, as well as conduct follow-up observations based on alerts from monitoring instruments.

This includes the study of high-energy neutrino events. Follow-up investigations of neutrino

alerts from IceCube have been conducted in the VHE regime (for example TXS 0506+056 with VERITAS (Abeysekara et al. (2018))) and the CTA will provide further insight regarding their origin. Transients are also potential sources of gravitational waves, as directly detected for the first time from a binary black hole merger (Abbott et al. (2016a), Abbott et al. (2016b)).

Cosmic Ray PeVatrons

The study of cosmic ray particles is intrinsically linked to that of gamma-ray astronomy because cosmic rays can also produce VHE gamma-rays via the decay of neutral pions. The cosmic ray PeVatron study with the CTA will aim to study the mechanisms of cosmic ray acceleration up to energies of the order of $\sim$ PeV by focusing on sources which exhibit comparatively harder spectra (with typical spectral indices ≤ 2).

Star Forming Systems

CTA observations of star forming systems will investigate whether there is a connection between high energy particles and star formation processes. This includes the study of massive stellar clusters within our Galaxy, in nearby star forming galaxies like the LMC and Andromeda, as well as starburst galaxies having high supernova rates.

Active Galactic Nuclei

AGN already account for roughly 40% of the gamma-ray sources detected with current generation IACTs. Once the CTA is in full operation, the number of detections is expected to increase by at least a factor of four, especially for sources at high redshift. A comprehensive measurement of the gamma-ray emission from AGN would, among other things, improve our understanding of the acceleration processes taking place near the SMBH, complement the study of the origin of cosmic rays, open a window for the study of ALPs, and help compute the attenuation due to the EBL.

Clusters of Galaxies

Clusters of Galaxies are among the most massive gravitationally bound systems in the Universe and are believed to harbour cosmic ray particles. The CTA, through the search

for a first detection of the diffuse gamma-ray emission, will aim to establish if there is indeed any evidence for proton acceleration in these environments.

4.5 Conclusion

In this chapter, the field of ground-based gamma-ray astronomy has been introduced. This includes a discussion of the underlying physics of the production and propagation of air showers. A simplified model has been assumed to derive expressions for the location and number of secondary particles produced at shower maximum. Furthermore, a distinction has been made between air showers produced by gamma-ray photons and those induced by hadronic interactions, for example from the cosmic ray background.

The emission of Cherenkov radiation has been discussed with an emphasis on the evolution of the opening angle with altitude. This is followed by a review of current generation IACTs, namely MAGIC, H.E.S.S. and VERITAS focusing on the location and layout, performance and a mention of some of the key scientific outputs at the time of writing.

The second half of the chapter focuses on the CTA with a discussion of the proposed layout of both the northern and southern array. This is followed with an overview of the expected performance and sensitivity as obtained from Monte Carlo simulations. Finally, each of the key scientific cases to be potentially investigated with the CTA have been summarised. The scientific potential is investigated further in Chapter 5 where the expected telescope response is used for a detailed study of the extragalactic source populations that will be detectable with the CTA.

Chapter 5

Extragalactic source population studies for the CTA

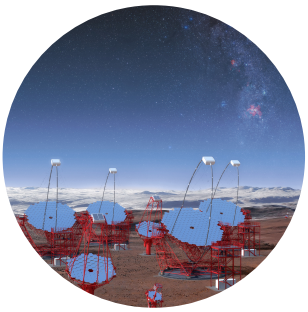

The Cherenkov Telescope Array (CTA; see Section 4.4) is the next generation observatory in ground-based gamma-ray astronomy. While benefiting from the extensive knowledge gained from current generation IACTs (see Section 4.3), the CTA is designed to improve upon their sensitivity by an order of magnitude. The CTA is also expected to achieve unprecedented angular and energy resolution and have a much wider field of view than current ground-based experiments.

These advancements, put together, will enable scientists to conduct large scale surveys of the sky in the VHE regime and generate legacy datasets hugely beneficial to the broader astronomical community. In this chapter, I conduct a detailed study of the CTA's ability

to observe extragalactic AGN, and highlight how these investigations will enhance our understanding of the Universe at the highest energies.

I begin with a discussion of the motivations behind the extragalactic survey within the framework of the CTA KSP (see Section 4.4.3) before introducing the source sample and extrapolation schemes used in this investigation. The steps of the analysis chain are described in detail and major results are presented for each configuration simulated. Finally, using the results of my analysis, I derive the VHE blazar luminosity function (LF), a question of fundamental importance in gamma-ray astronomy.

5.1 The Extragalactic Survey

The extragalactic survey KSP will comprise a blind survey of 25% of the extragalactic sky, and is aimed at producing an unbiased source catalogue in the VHE regime (Acharya et al. (2013); Cherenkov Telescope Array Consortium et al. (2019)). Current generation IACTs have detected over 60 extragalactic sources, the majority of which are BL Lac objects*. However, this sample is strongly biased since most observations were triggered by high flux measurements at lower energies in the optical, X-ray and gamma-ray regimes and roughly half these alerts took place when the sources themselves were undergoing flaring activity (Acharya et al. (2013); Cherenkov Telescope Array Consortium et al. (2019)).

The CTA is expected to increase the number of blazars detectable in their average state while also potentially discovering new source populations previously unseen at the highest energies. The resulting catalogue will form one of the main legacy datasets of the CTA and will greatly benefit the entire astronomical community. It is also expected to:

- provide an unbiased estimate of the yet-to-be-determined LF for AGN in the VHE regime (see Section 5.5),
- potentially discover extreme blazar sources peaking at energies $E_\gamma \geq 100$ GeV, as well as previously undetected VHE source classes (for example Seyfert galaxies),

*`http://tevcat.uchicago.edu/`, accessed on 11/01/21.

- detect rapid flares not observable in short timescales with *Fermi*-LAT and current IACTs,
- detect dark sources having no known astrophysical counterpart (for example Aharonian et al. (2008b)), potentially evidence of dark matter annihilation (see Acharyya et al. (2021) for an assessment of the CTA's potential for dark matter investigations around the Galactic centre).

In order to provide uniform coverage of the entire sky, the extragalactic survey has been proposed to be completed using both the northern and southern arrays within the first three years of the CTA's operation. The final catalogue will contain, for each source, the significance of detection, the differential energy spectrum, spatial and spectral parameters, integral flux and any associations with known objects. Moreover, it will also have information on the time periods in which the observations were obtained as well as the intervals corresponding to flares (if any). The survey will be accompanied by extensive multi-wavelength studies including simultaneous optical and radio observations, *Fermi*-LAT data analysis, and Target of Opportunity (ToO) studies in the X-ray regime.

This chapter presents an investigation of the extragalactic source population accessible to the CTA based on the anticipated performance of both observing arrays. The results, among other things, will:

- show the impact of the CTA on AGN population studies,
- present a list of promising sources of each AGN class (for example BL Lacs, FSRQs, radio galaxies etc.),
- discuss the observation times required to study these objects,
- estimate how accurately the CTA will reconstruct the VHE LF within the context of the extragalactic survey.

5.2 Methodology

5.2.1 Source sample

As described in Section 2.2, the *Fermi*-LAT (Atwood et al. (2009)) scans the entire sky every three hours with excellent sensitivity and angular resolution. The 4FGL catalog (The *Fermi*-LAT collaboration (2019a)) contains a list of gamma-ray sources observed during its first eight years of operation in the energy range from 50 MeV - 1 TeV. Having a total of 5064 sources above a significance of 4σ, the catalog is the deepest in this energy range to date. A large majority of these sources (over $\sim$ 60 %) are AGN, including 3137 blazars (further categorised as 1131 BL Lacs, 694 FSRQs and 1312 blazar candidates of unknown types (BCUs)).

With the energy threshold of the CTA expected to be $\sim$ 20 GeV, the 4FGL provides one of the best available lists of targets for the survey and allows for a realistic forecast of the AGN population accessible to the CTA when in operation. An incremental version of the 4FGL catalog, 4FGL Data Release 2 (4FGL-DR2; Ballet et al. (2020)) was released during the production of the simulations. This catalog is based on the first ten years of *Fermi*-LAT observations and will be used in future simulations.

An accurate measurement of redshift is required for the extrapolation schemes used in the analysis. The sample used in this investigation consists of extragalactic sources from the 4FGL catalog having a known spectroscopic redshift*. Figure 5.1 shows a skymap of the final sample of 1551 AGN used in this investigation and Figure 5.2 plots the redshift distributions for the different classes of AGN.

5.2.2 Extrapolation scheme

The 4FGL catalog provides the spectral parameters of sources in the energy range from 50 MeV - 1 TeV. In order to use this information to investigate the prospects of detection

*The redshifts were compiled from literature by P. Goldoni and T. Hassan. See `https://zenodo.org/record/4721386`, last accessed: 25/05/2021.

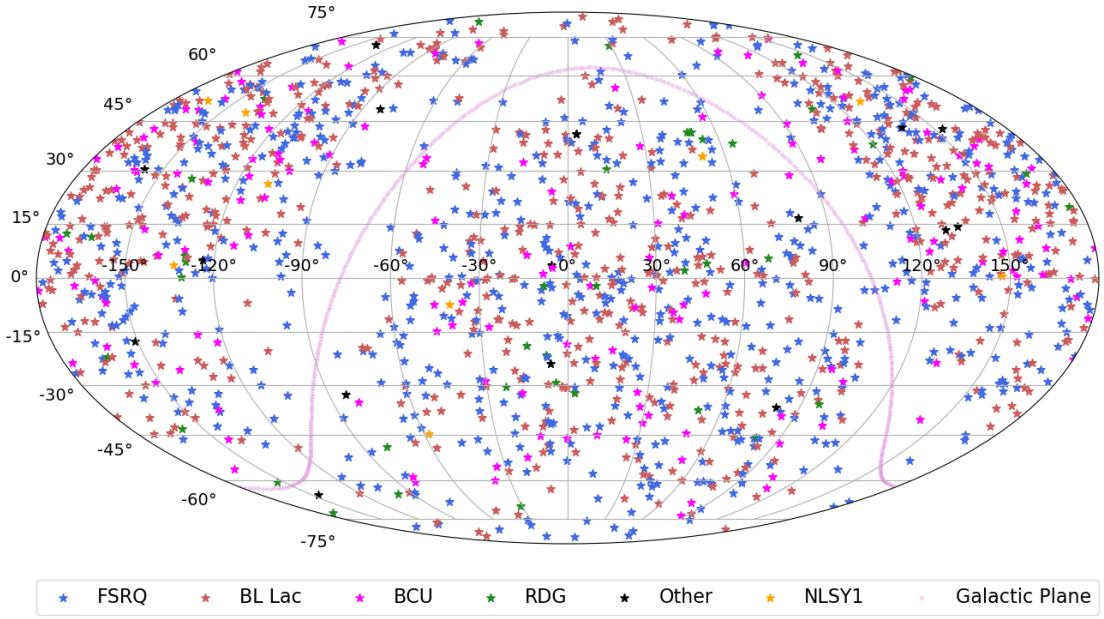

Figure 5.1: A skymap, in celestial co-ordinates, of the 4FGL extragalactic sources of known redshift investigated in this study shown for each class, namely, Flat Spectrum Radio Quasars (FSRQ), BL Lacs, blazar candidates of unknown types (BCU), radio galaxies (RDG), Narrow-Line Seyfert 1 galaxies (NLSY1) and Other which includes Seyfert galaxies, compact steep spectrum quasars, soft spectrum radio quasars and other non-blazar active galaxies. The curve represents the Galactic Plane.

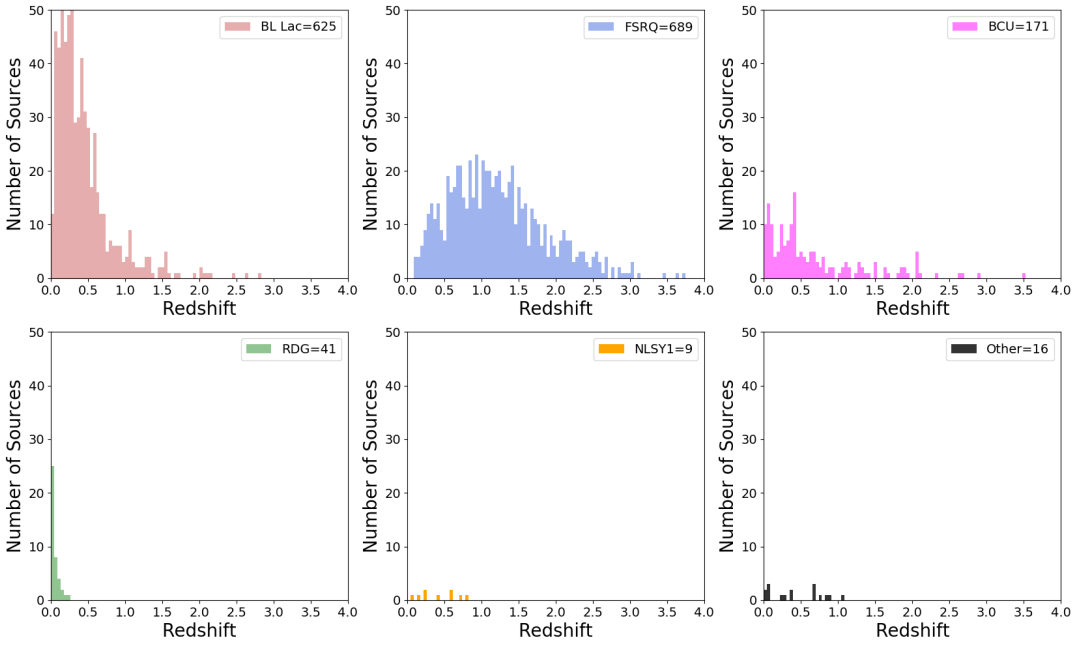

Figure 5.2: The distribution of known spectroscopic redshifts of the 4FGL extragalactic sources investigated in this study for each class of AGN (total number of sources of each type shown in legend). Other includes Seyfert galaxies, compact steep spectrum quasars, soft spectrum radio quasars and other non-blazar active galaxies.

with the CTA, which is sensitive to energies well beyond 1 TeV, the spectra must be carefully extrapolated to higher energies.

During the extrapolation, it is important to take into account the attenuation in the flux resulting from the interaction of the gamma-rays with the photons from the EBL (see Section 1.3.2.2) due to photon-photon pair production. The level of attenuation depends on both the energy of the gamma-ray photon and the distance to the source, hence the requirement for an accurate measurement of redshift. As with the investigation presented in Chapter 3, I use the values of τ (E,z) stated in Domínguez et al. (2011) to calculate the likely attenuation of the spectra from the extragalactic sources (see Figure 1.4).

There is no general consensus on how to extrapolate the *Fermi*-LAT spectra to the VHE regime (for example Hassan et al. (2017b)). For the purpose of this chapter, I consider the following functions to model the extrapolated spectrum:

- Power law + EBL attenuation

$$\frac{dN}{dE} = N_0 \left(\frac{E}{E_0}\right)^{-\gamma} e^{-\tau(E,z)} \tag{5.1}$$

  where γ is the spectral index, E_0 is the pivot energy in MeV and N_0 is the normalisation in units of photons $\mathrm{cm}^{-2}\mathrm{s}^{-1}\mathrm{MeV}^{-1}$.

- Log Parabola + EBL attenuation

$$\frac{dN}{dE} = N_0 \left(\frac{E}{E_0}\right)^{-\alpha-\beta\ln\left(\frac{E}{E_0}\right)} e^{-\tau(E,z)} \tag{5.2}$$

  where α is the spectral index, β the spectral curvature, E_0 the pivot energy in MeV and N_0 the normalisation in units of photons $\mathrm{cm}^{-2}\mathrm{s}^{-1}\mathrm{MeV}^{-1}$.

The assumption regarding the power law spectral behavior of AGN in the VHE regime is motivated by 18 sources in the sample observed to have a power law spectrum when detected with current generation IACTs*. The log parabolic extrapolation scheme is motivated by the *Fermi*-LAT spectra of 320 sources in the sample reported to favour a log parabolic model over a power law at a confidence level of $\geq 3\sigma$ (The *Fermi*-LAT collaboration (2019a)).

It should be noted that given the lack of detailed understanding of the emission mechanisms in AGN, especially in the VHE regime, no chosen extrapolation scheme will be absolute at this stage. For example, Romano et al. (2018) in an investigation of the detection prospects of Narrow-Line Seyfert 1 galaxies account for the intrinsic absorption due to photons present in the BLR by including an additional cut-off at 30 GeV in the power law extrapolated spectra (see equation 3.12). Further investigations to statistically evaluate the most appropriate extrapolation scheme for the final publication based on current VHE detections are ongoing.

*This was obtained from gamma-cat, an open data collection and source catalog for gamma-ray astronomy (`https://github.com/gammapy/gamma-cat`, last accessed: 07/04/2021). The repository itself was last updated on 07/07/2018.

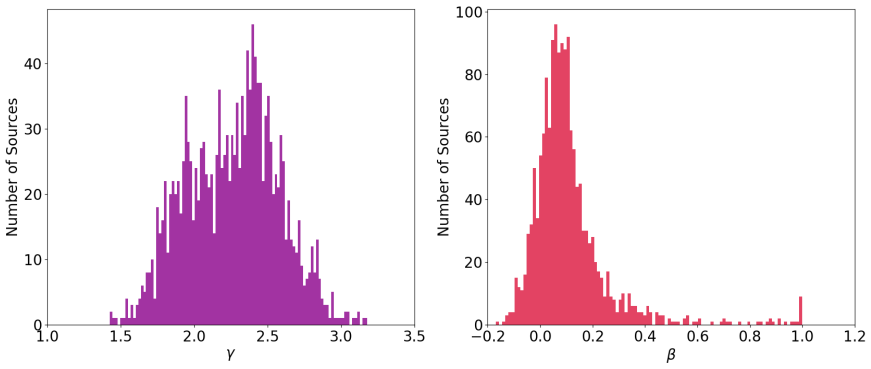

Figure 5.3: The distributions of the spectral index, γ, and curvature, β, for the 4FGL extragalactic sources considered in this investigation.

The distributions of the spectral index, γ, and curvature, β, are shown in Figure 5.3. Figure 5.4 shows the final spectra obtained under the power law and log parabolic extrapolation schemes for all sources investigated. These are used as input for the simulations.

5.3 Data analysis pipeline

The results presented in this chapter were obtained from simulations using *ctools* (Knödlseder et al. (2016)), a software package developed for the scientific analysis of CTA data as well as data from current generation IACTs. *Ctools* is built within the framework of *GammaLib*, a generic library written in *C++* which supports the analysis of gamma-ray event data.

A typical *ctools* analysis is based on a number of independent, well-defined steps combined into a customised data analysis pipeline depending on the goals of the analysis. The framework is similar to that of *ftools* (Pence et al. (1993)), a collection of analysis packages commonly used in X-ray astronomy, and similar to the methods used in the analysis of *Fermi*-LAT and *INTEGRAL* data.

Each step can be run from the command line or, as is more common when handling large datasets, using python scripts. Python scripts allow for the transfer of information from one step to another without the need of storing the intermediate results and thereby reducing the amount of memory consumption. Also included in the package is the calibration database

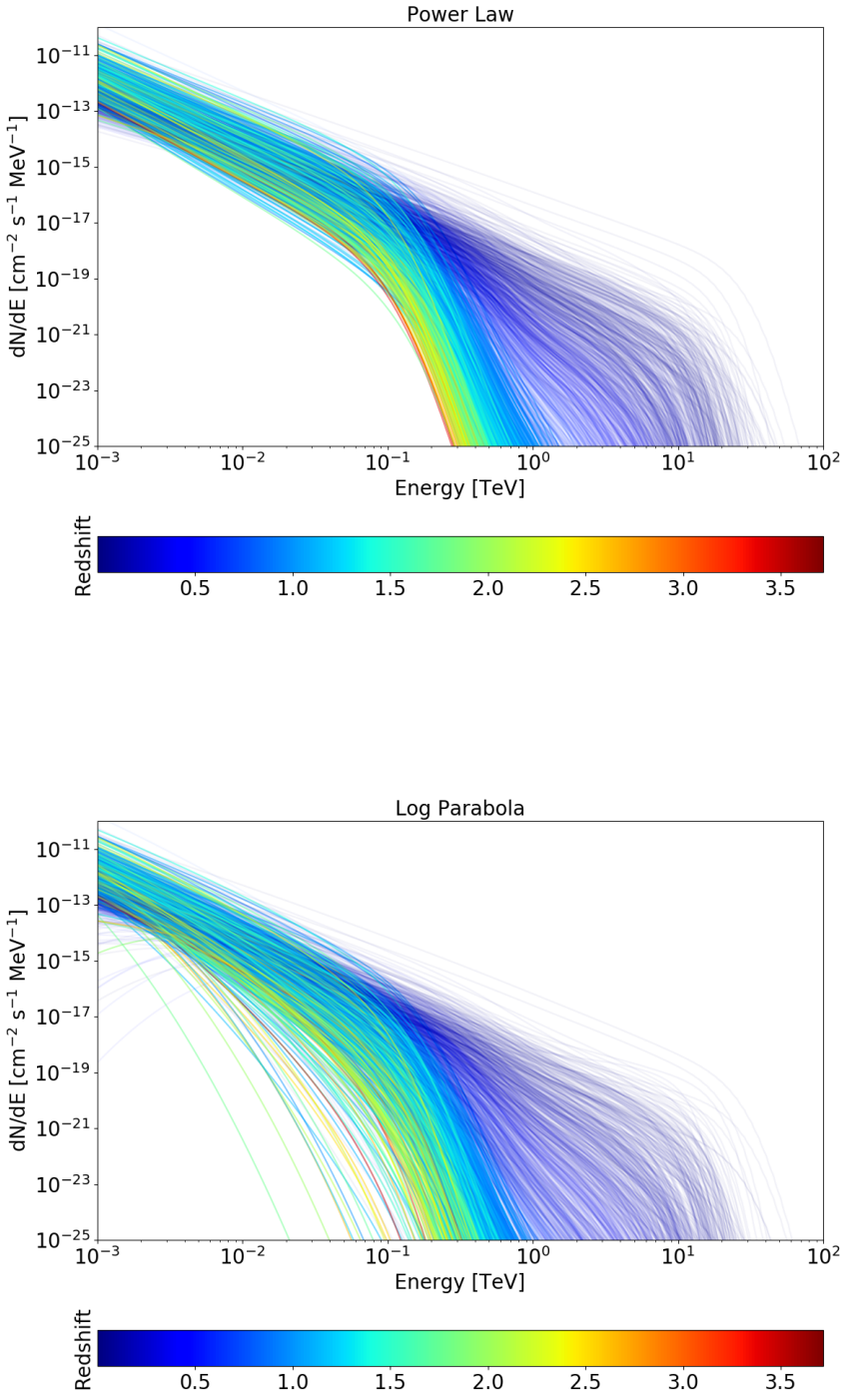

Figure 5.4: The extrapolated spectra obtained for both power law (top) and log parabolic (bottom) functions for all sources simulated in this investigation. This includes the attenuation due to EBL (using the Domínguez et al. (2011) model). The colourbar shows to the redshift of each source.

containing the IRFs labelled by the array and observation times considered. The final results are produced in *FITS* format and the output can be visualised using the *matplotlib* module in python (Hunter (2007)).

The following section describes the steps involved in a typical *ctools* simulation and likelihood analysis using the example of 3C 279, one of the FSRQs investigated in Chapter 3. The steps are summarised in Figure 5.5 and a more detailed description can be found in the online documentation *. Throughout all the analysis presented in this thesis, I use the *ctools* version 1.7.3 in conjunction with the *prod3b-v2* IRFs.

5.3.1 Simulating event data

The first step in the analysis involves simulating a list of source and background events based on an input model and specified instrument response. This is performed using the *ctobssim* tool and the inputs required are the pointing direction, radius of region of interest (RoI), the time and energy intervals considered and the instrument response. The results presented in this work are obtained for observation times of 5 and 20 hours. A random number generator is used to simulate multiple independent samples each using different seed parameters. All the results presented in this investigation consider 100 independent instances of each simulation.

A source model, in the form of an *XML* file, is required as input for the simulation and likelihood analysis. This model contains an initial estimate of the spatial and spectral properties of each source as well as a template for the instrumental background model. The spectral shape of each source is modelled as either the extrapolated power law or log parabolic model derived in Section 5.2.2. The values of the normalisation and the spectral shape parameters of each source are left free during the fitting procedure. The spatial position of each source is fixed to the positional co-ordinates reported in the 4FGL catalog (The *Fermi*-LAT collaboration (2019a)).

The instrumental background model, CTAIrfBackground, is a template of the predicted

*`http://cta.irap.omp.eu/ctools/users`, accessed on 01/03/2021.

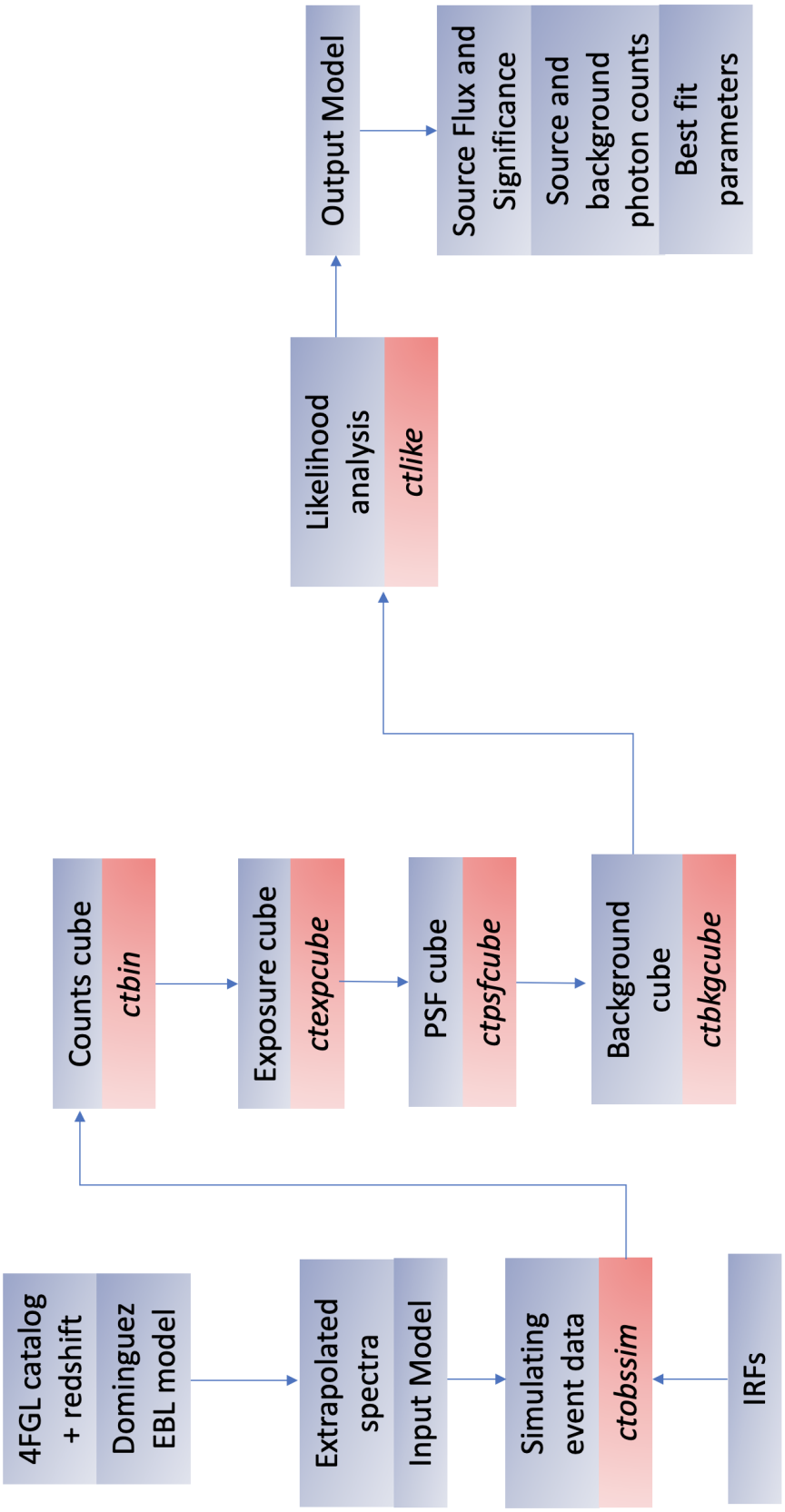

Figure 5.5: A flowchart of the steps involved in the CTA simulation and likelihood analysis also showing, where applicable, the *ctools* routines applied at each step.

background rate, in units of $\mathrm{MeV}^{-1}\mathrm{s}^{-1}\mathrm{sr}^{-1}$, as a function of the position in the field of view and measured energy and is based on the IRFs used for each source. The energy dependence is multiplied by a power law initially defined to represent a constant value of 1 but kept free to accommodate uncertainties in the background information provided.

The IRFs are released by the CTA Analysis and Simulation Working Group (ASWG) and are periodically updated to reflect new Monte Carlo (MC) productions based on an improved understanding of the CTA layout. The simulations presented in this chapter are based on the *prod3b-v2* IRF release [†] which includes the 20°, 40° and 60° zenith angle full array response for observation times of 30 mins, 5 hours and 50 hours with both the northern and southern arrays. The specific IRF used for each source, shown for CTA N and CTA S in Figure 5.6 and Figure 5.7 respectively, is dependent on the observing array being considered as follows:

- 20° IRFs for sources culminating between 0° and 25° from zenith,
- 40° IRFs for sources culminating between 25° and 45° from zenith,
- 60° IRFs for sources culminating between 45° and 65° from zenith,
- sources not culminating in these intervals are not simulated. By imposing this condition, I do not exclude any source from the sample for both observing arrays put together.

It should be noted that the *prod3b-v2* IRF release focused on the optimisation of flux sensitivity, so the results do not as yet reflect the final performance of the CTA in terms of angular and energy resolution. Furthermore, the simulations assume nominal telescope pointing i.e. all the telescopes in the array are pointed parallel to each other. A performance evaluation for divergent pointing modes is currently under production.

The IRF appropriate for the analysis of 3C 279 for an observation period of 20 hours with CTA S is *South_z20_50h* and the corresponding integrated background rate as a function

[†] `https://forge.in2p3.fr/projects/cta_analysis-and-simulations/wiki/Prod3b_based_instrument_response_functions`, accessed on 01/03/2021.

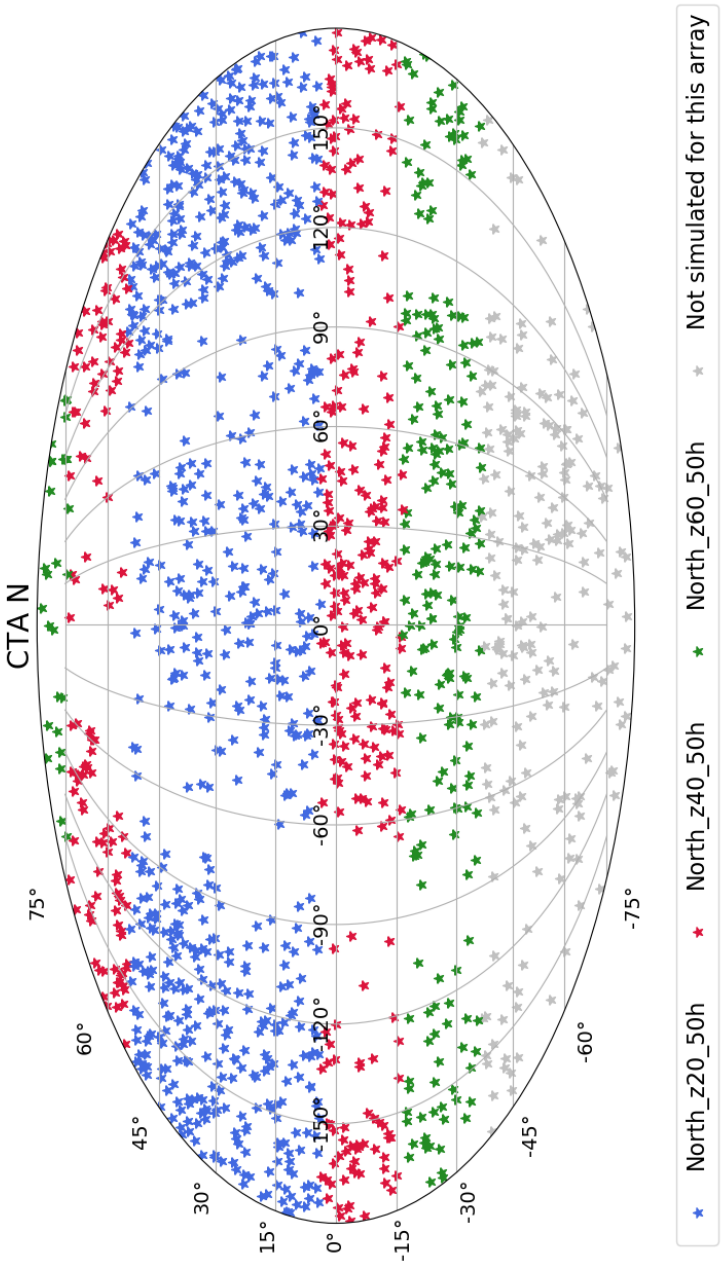

Figure 5.6: A skymap, in celestial co-ordinates, of the IRFs used for 20 hour northern array simulations of all sources in the sample.

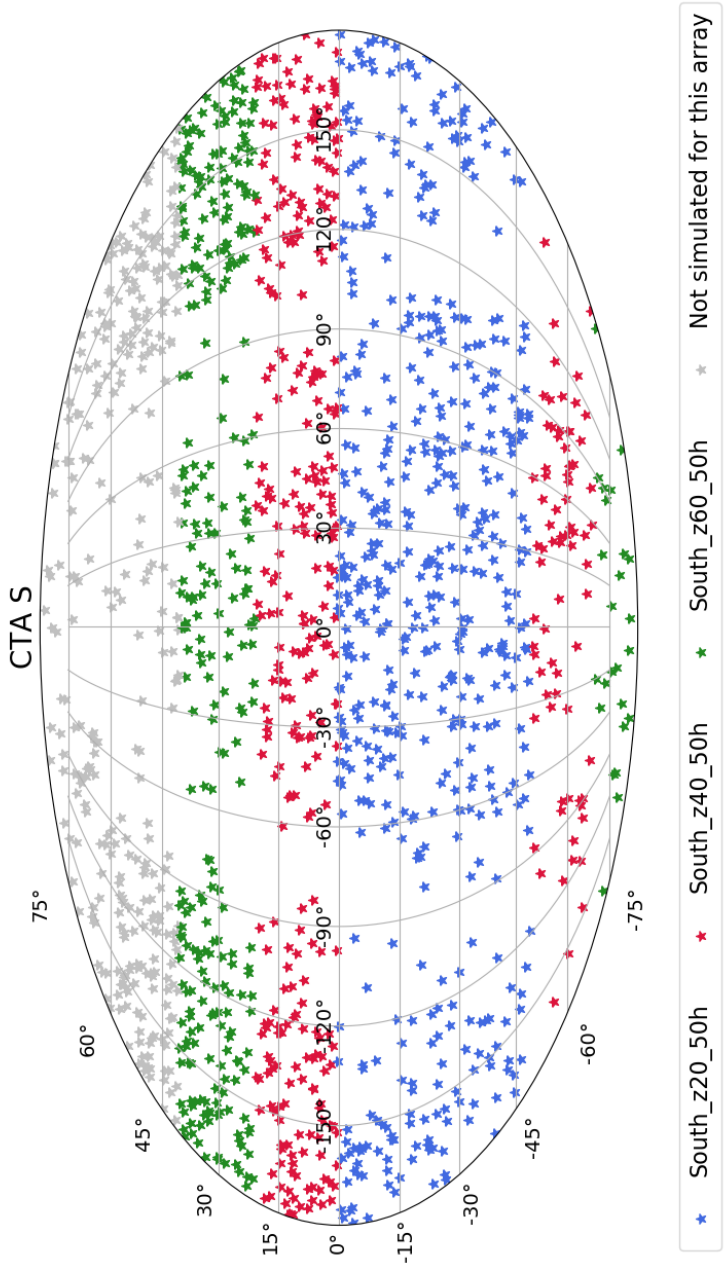

Figure 5.7: A skymap, in celestial co-ordinates, of the IRFs used for 20 hour southern array simulations of all sources in the sample.

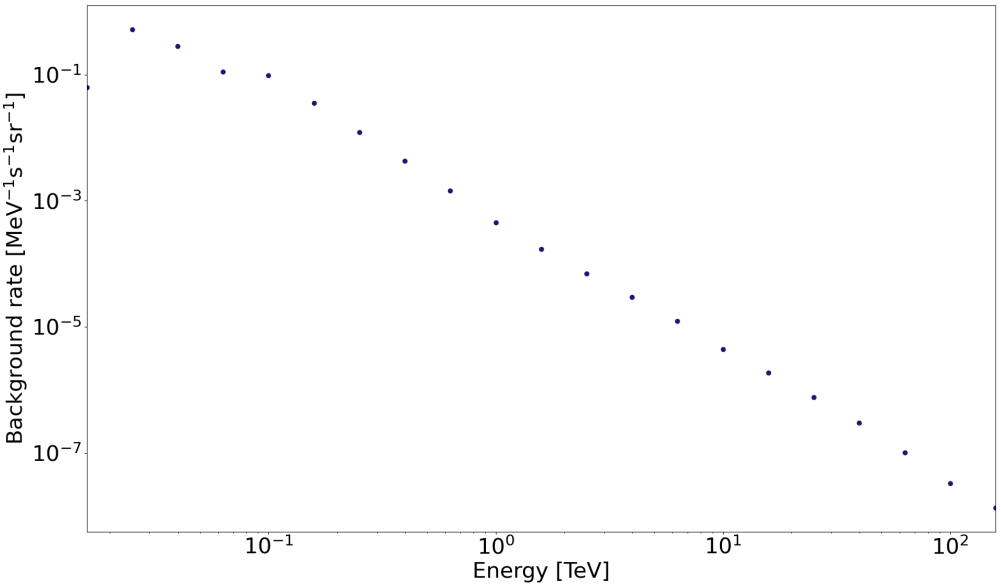

Figure 5.8: The distribution of the integrated background rate against energy of the *South_z20_50h* IRF, used in the simulation of 3C 279 for an observation period of 20 hours with CTA S. The feature observed at ~ 100 GeV corresponds to where the MSTs start detecting events.

of energy is shown in Figure 5.8. This estimate only includes contributions from simulated hadronic and electron air shower events that pass selection cuts optimised for the different observing times.

In this investigation, I consider a RoI of radius 3°. This choice is based on the anticipated off-axis sensitivity of the CTA. Above 100 GeV, the radius of the RoI within which the sensitivity is still within a factor of 2 of the sensitivity at the centre is ~ 3°. No further sources except for the source of interest and the instrumental background are included in each event simulation.

The six energy thresholds considered for simulations involving the 20° IRFs are 30 GeV, 50 GeV, 100 GeV, 300 GeV, 500 GeV and 1 TeV. The IRFs generated for 40° and 60° zenith angles have a lower energy limit of ~ 67 GeV and the corresponding simulations only consider four different energy thresholds, at 100 GeV, 300 GeV, 500 GeV and 1 TeV. The upper energy limit of the simulated events in all cases is fixed at 200 TeV. Energy dispersion is not considered at this stage since both my test simulations and those

undertaken by Romano et al. (2018) showed that it increased computation times by a factor of ~ 10 without bringing any noticeable change in the results.

5.3.2 Pre-computing the binned response

The *ctobssim* tool outputs a *FITS* file containing a list of events and good time intervals (GTIs), defined here as contiguous time periods for which the recorded events can be used for scientific analysis. A counts map obtained during an instance of simulation of 3C 279 for an observation period of 20 hours with CTA S at an energy threshold of 100 GeV is shown in Figure 5.9. A spatial binning of 0.02° pixel^{-1} is chosen and given that the RoI is 6° in diameter, I select the sizes of the x and y axes to be 6/0.02=300 pixels.

The event data are then binned into a counts cube, a 3-dimensional data cube spanning the spatial co-ordinates and reconstructed energy in logarithmically spaced intervals. The *ctbin* tool is used to create a counts cube *FITS* file containing the photon counts, energy bounds and GTIs of all events in the counts cube.

Following the standard rules implemented in CTA performance evaluation*, I divide the energy range into 5 logarithmic bins per decade in energy. Four snapshots of the counts cube generated during an instance of simulation of 3C 279, spanning the first four energy bins and covering an energy range 100 GeV - 670 GeV, are shown in Figure 5.10.

In order to expedite the fitting procedure, the next step is to pre-compute the instrument response from the counts cube. This involves creating an exposure cube, a point spread function (PSF) cube and a background cube.

The exposure cube is a 3-dimensional data cube containing the exposure, defined as the sum of the effective area multiplied by the livetime of the observations, as a function of sky direction and energy. Mathematically, the exposure function, $X(p, E)$, is given by:

$$X(p, E) = \sum_i A_{\mathrm{eff},i}(p, E) \times \tau_i \tag{5.3}$$

where $A_{\mathrm{eff},i}(p, E)$ is the effective area for observation i having photon arrival direction p, energy E and an observation lifetime τ_i. This computation is performed using the

*`https://www.cta-observatory.org/science/cta-performance`, accessed on 02/04/2021.

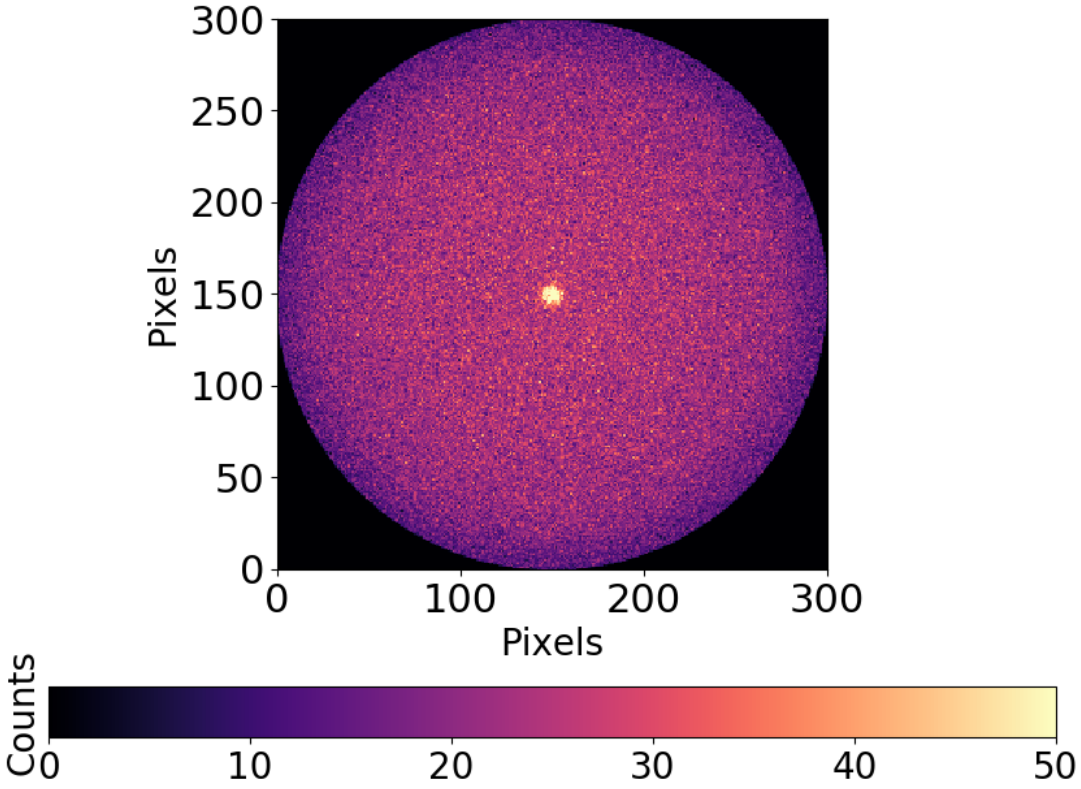

Figure 5.9: A counts map showing the distribution of gamma-ray photons in the energy range 100 GeV - 200 TeV over a RoI of radius 3° centred on 3C 279 for an observation period of 20 hours with CTA S. The colour scale shows the number of photons at each pixel in the counts map.

ctexpcube tool and results in another *FITS* file containing three extensions, namely the exposure values (in units of cm^2 s), energy intervals and GTIs of all observations in the exposure cube. Four snapshots of the exposure cube generated during an instance of simulation of 3C 279, spanning the first four energy bins and covering an energy range 100 GeV - 670 GeV, are shown in Figure 5.11.

The *ctpsfcube* tool is then used to generate a PSF cube, a 4-dimensional cube spanning the spatial co-ordinates, photon energy and the off-set angle between the true and measured arrival directions of the photon. The PSF cube values are defined as:

$$PSF(\delta|p,E) = \frac{\sum_i PSF_i(p'|p,E) \times A_{\mathrm{eff},i}(p,E) \times \tau_i}{\sum_i A_{\mathrm{eff},i}(p,E) \times \tau_i} \tag{5.4}$$

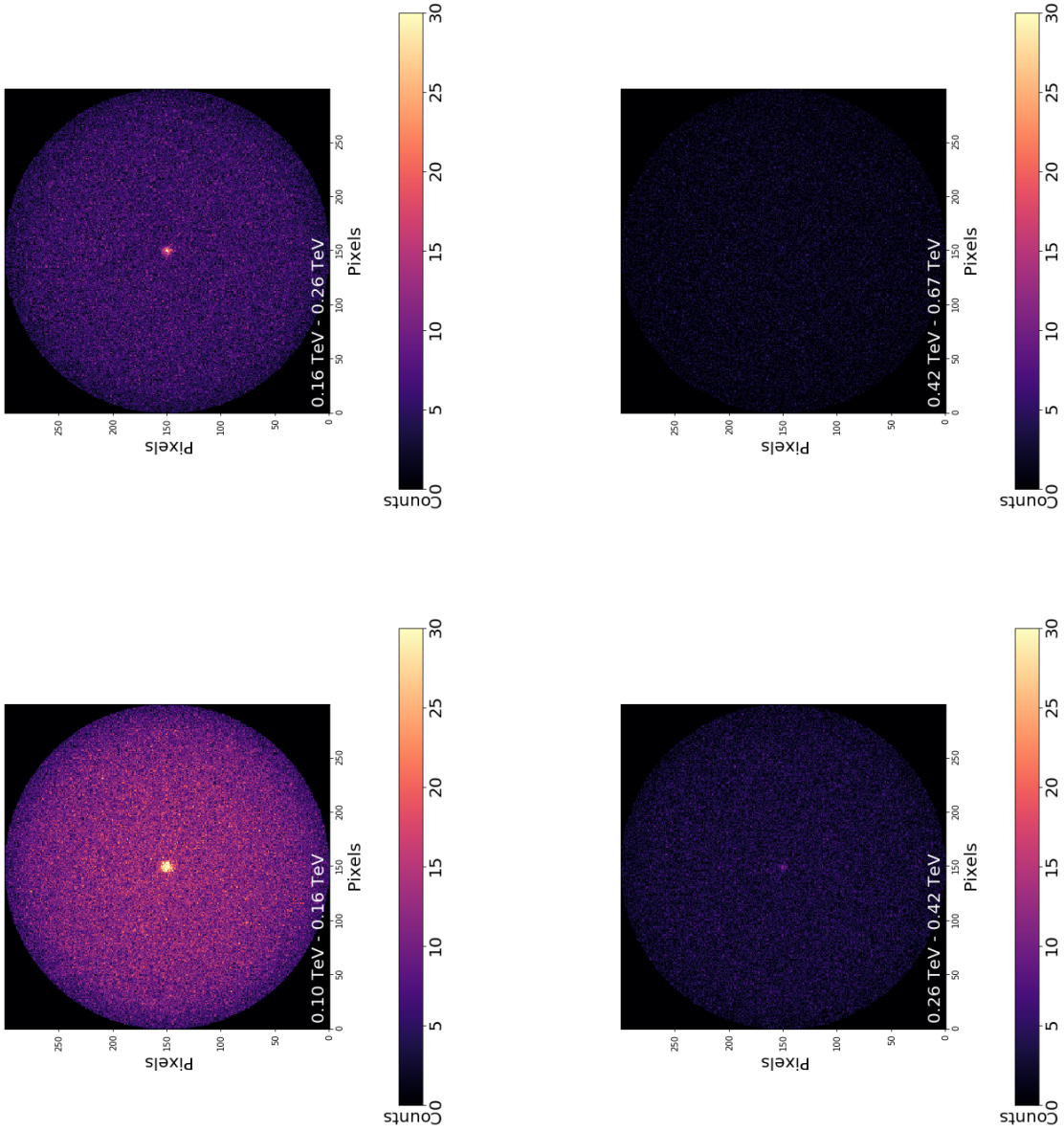

Figure 5.10: Four snapshots of the counts cube showing the distribution of gamma-ray photons in the specified energy intervals over a RoI of radius 3° centred on 3C 279 for the observation period of 20 hours with CTA S. The colour scale shows the number of photons at each pixel in the RoI.

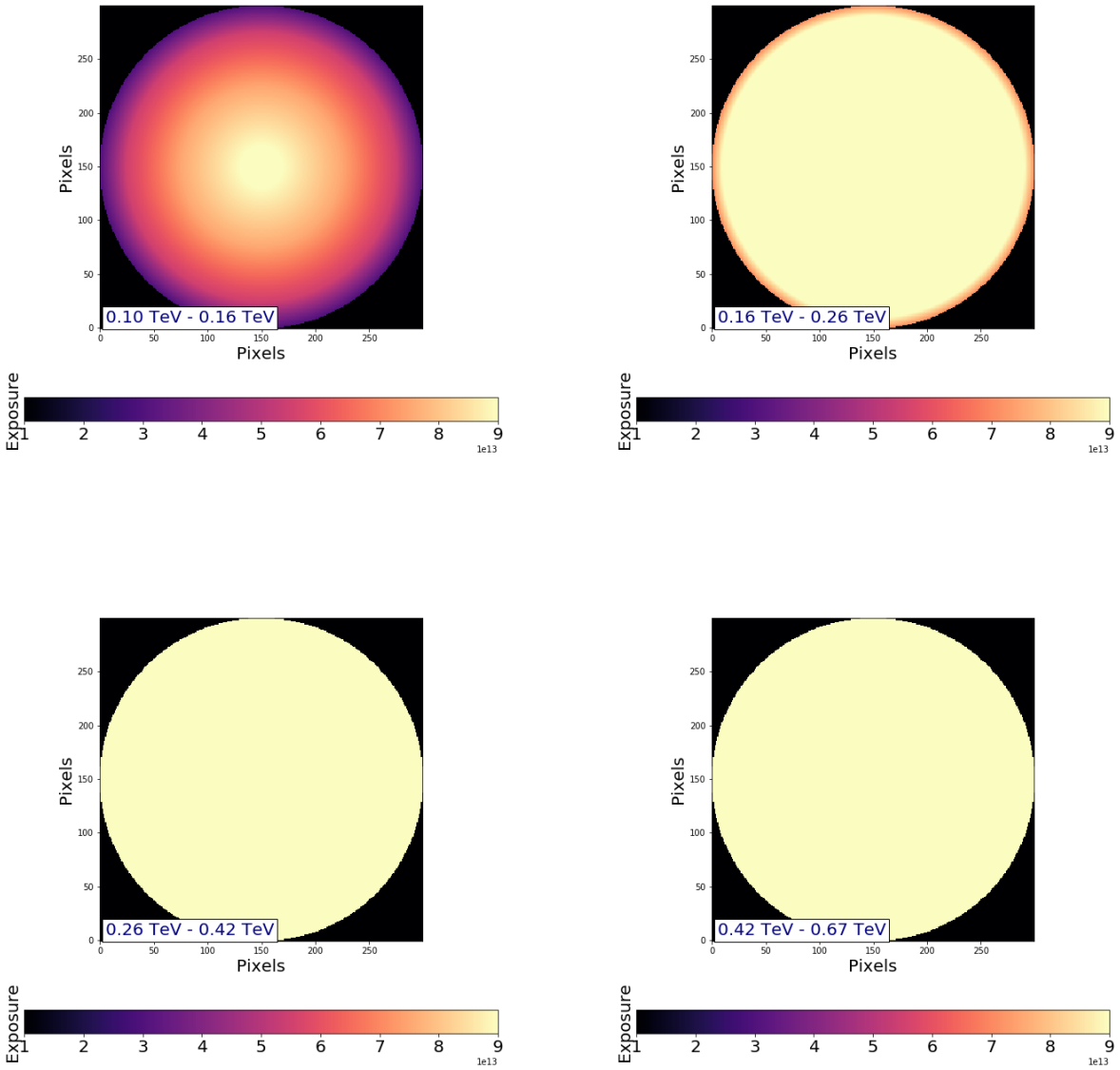

Figure 5.11: Four snapshots of the exposure map in the specified energy intervals over a RoI of radius 3° centred on 3C 279 for the observation period of 20 hours with CTA S. The colour scale shows the total exposure for each pixel in units of cm^2 s.

where δ is the angular separation between the actual and reconstructed photon directions p and p'. The output is a PSF *FITS* file which contains the PSF cube values (in units of sr^{-1}), the energy intervals and a binary table of off-set angles as the three extensions.

The final step involves computing a background cube, a 3-dimensional cube spanning the reconstructed spatial co-ordinates and photon energy computed as:

$$B(p', E') = \frac{\sum_i B_i(p', E') \times \tau_i}{\sum_i \tau_i} \tag{5.5}$$

where $B_i(p', E')$ is an estimate of the background rate for observation i having a reconstructed photon arrival direction p' and energy E' respectively. The number of background counts in each bin is predicted from the input model. This is performed by the *ctbkgcube* tool which creates a *FITS* file containing two extensions, namely the background cube values (in units of $\mathrm{MeV}^{-1}\mathrm{s}^{-1}\mathrm{sr}^{-1}$) and a binary table of the energy boundaries of each bin.

This routine also produces an output file in *XML* format which is the same as the input *XML* file used for the *ctobssim* routine except that the original background model, CTAIrfBackground, is replaced by a different model of type CTACubeBackground. This background model enables the extraction of the background information from the background cube during the likelihood analysis and has a spectral component that is left free during the fitting procedure to avoid uncertainties in the background rate propagating into the flux estimate of the source.

5.3.3 The likelihood analysis

The *ctlike* tool can now be used to perform a maximum likelihood fit to the event data and obtain the significance, flux, spectral index and positional extent of all sources in the model. While this investigation involves the analysis of binned data, the same routine can also be extended to unbinned and On/Off data as well as a combined analysis of CTA simulations and observations made with H.E.S.S. and *Fermi*-LAT.

Along similar lines to the likelihood procedure described for the analysis of *Fermi*-LAT data (see Section 2.3.4), the *ctlike* tool computes the test statistic (TS; Mattox et al. (1996)):

$$\mathrm{TS} = 2\ln L(M_s + M_b) - 2\ln L(M_b) \tag{5.6}$$

where $\ln L(M_s + M_b)$ is the log likelihood value obtained when fitting both the source and background to the data and $\ln L(M_b)$ is the log likelihood value obtained from fitting only the background to the data i.e. with the source removed.

For a sufficiently large number of counts, the TS is asymptotically distributed as χ^2_n where the degrees of freedom, n, correspond to the number of free parameters in the additional source component (Cash (1979)). The presence of an additional source will result in a fluctuation from this distribution. A large TS value (typically TS $\geq$ 25) quantifies the presence of an additional source (i.e. the null hypothesis is incorrect).

All free parameters in the model file are adjusted by the *ctlike* tool and an output *XML* file is produced containing the best fit results along with an estimate of their associated uncertainties. The maximum likelihood fit can be inspected by computing the fit residuals. The *csresmap* routine creates a residual counts map with the events corresponding to the fitted model components having been subtracted. This method is sensitive to both positive and negative fluctuations making it a useful technique for assessing the goodness-of-fit.

Among the different algorithms that may be implemented for inspecting the residuals, it is often useful to extract a map of the percentage residuals obtained from the sky map and model map as:

$$\text{Percentage Residual} = \frac{\text{Sky Map} - \text{Model Map}}{\text{Model Map}}. \tag{5.7}$$

The residual map obtained during an instance of simulation for 3C 279 is shown in Figure 5.12. No significant residuals ($\geq \pm 1\%$) are found, indicating that the model fit was satisfactory.

5.3.4 Further analysis

The *ctlike* tool computes the significance of detection, the number of source and background photons and the best fit spectral parameters, along with their corresponding uncertainties

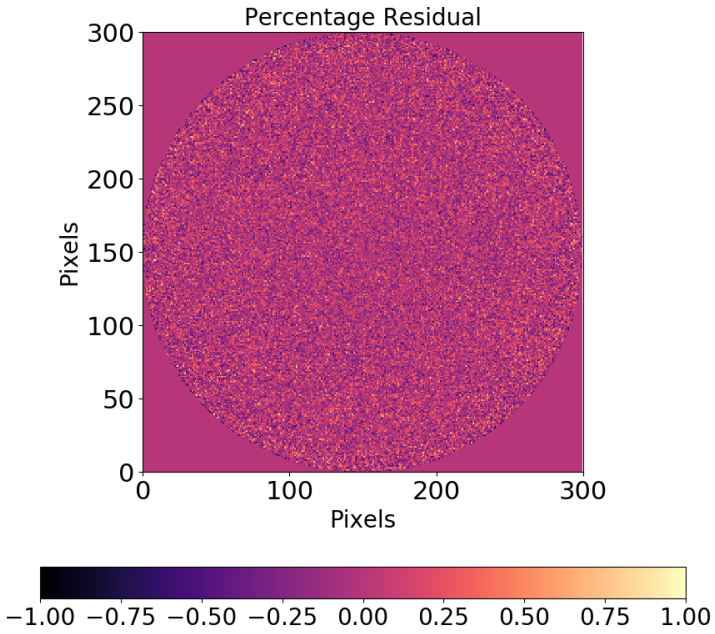

Figure 5.12: The percentage residual map obtained over a RoI of radius 3° centred on 3C 279 for an observation period of 20 hours with CTA S. The colour scale shows the percentage residual (see equation 5.7) at each pixel in the counts map.

and the upper flux limits for the source, to within a confidence interval of 95 %. While these comprise the main results of this investigation, further steps can also be performed using *ctools*.

The SED of a source can be derived using the *csspec* script. The source spectrum is obtained by performing a maximum likelihood fit to compute the source flux along with its corresponding uncertainty for a number of independent spectral bins spanning the entire energy range of the analysis. For sources not detected within a given spectral bin, an upper flux limit can also be computed. The *csspec* tool generates a *FITS* file containing the fitted source spectrum and the TS values of the source in each bin.

Finally, it is also possible to compute a lightcurve in order to examine the temporal variability in the flux and spectrum of a particular source. The *cslightcrv* script performs

a maximum likelihood fit over a series of time intervals and outputs a *FITS* file containing the best fit spectral parameters along with their uncertainties along with the TS values and flux limits for each temporal bin.

5.4 Results

5.4.1 Overview

The number of extragalactic AGN of each classification predicted to be detected for 5 and 20 hour observations with CTA N and CTA S at energy thresholds of 30, 50, 100, 300, 500 and 1000 GeV under the power law extrapolation scheme are shown in Table 5.1. Also stated for each sub-sample are the number of these objects already detected in the VHE regime with current generation IACTs *. It should be noted that the detections with current generation instruments involve a range of energy thresholds, observation times and flux states and while the numbers do not facilitate a direct comparison, they do provide a useful estimate of the increase in detections anticipated with the CTA.

Furthermore, sources having a declination roughly in the interval $-36^\circ \leq \mathrm{DEC} \leq 40^\circ$ are expected to be observable from both arrays, leading to some overlap in the tabulated results. For example, out of the 19 FSRQs expected to be detected with CTA S in 5 hour observations at an energy threshold of 100 GeV, 10 are also expected to be detected with CTA N at the same energy threshold and period of observation.

Figures 5.13 - 5.16 show skymaps of all sources from the sample expected to be detected with CTA N and CTA S for observation times of 5 and 20 hours respectively, together with the significance of each detection. These results assume a power law extrapolation scheme with an energy threshold of 100 GeV and highlight the expected enhancements for extragalactic population studies in the VHE regime through the CTA KSPs and dedicated proposals.

*`http://tevcat.uchicago.edu/`, accessed on 11/01/21.

Table 5.1: The number of extragalactic sources of each class from the 4FGL catalog expected to be detected with CTA N and CTA S at energy thresholds of 30, 50, 100, 300, 500 and 1000 GeV under the power law extrapolation scheme for the observation times of 5 and 20 hours respectively. Also shown for each sub-sample are the number of objects expected to be detected at an energy threshold of 100 GeV for each configuration that have already been detected with current generation IACTs. Other includes Seyfert galaxies, compact steep spectrum quasars, soft spectrum radio quasars and other non-blazar active galaxies.

CTA N														
	5 h							20 h						
Class	TeVCat	30 GeV	50 GeV	100 GeV	300 GeV	500 GeV	1000 GeV	TeVCat	30 GeV	50 GeV	100 GeV	300 GeV	500 GeV	1000 GeV
BL Lac	41	81	81	143	118	95	80	43	125	124	218	167	140	114
FSRQ	6	12	12	13	5	1	0	7	21	21	34	10	4	1
BCU	1	3	3	12	12	10	9	1	7	7	23	18	15	14
RDG	5	11	11	14	14	13	8	5	13	13	21	20	17	18
NLSY	0	0	0	0	0	0	0	0	1	1	1	0	0	0
Other	0	2	2	2	1	1	1	0	2	2	3	2	2	1
CTA S														
	5 h							20 h						
Class	TeVCat	30 GeV	50 GeV	100 GeV	300 GeV	500 GeV	1000 GeV	TeVCat	30 GeV	50 GeV	100 GeV	300 GeV	500 GeV	1000 GeV
BL Lac	33	80	80	154	121	107	81	33	114	114	220	165	142	124
FSRQ	4	11	11	19	5	1	0	5	22	22	34	12	5	2
BCU	2	13	14	18	15	15	15	2	20	20	29	26	23	18
RDG	3	4	4	13	13	12	9	3	6	6	17	18	17	15
NLSY	0	0	0	0	0	0	0	0	0	0	0	0	0	0
Other	0	2	2	2	2	2	2	0	2	2	4	4	4	3

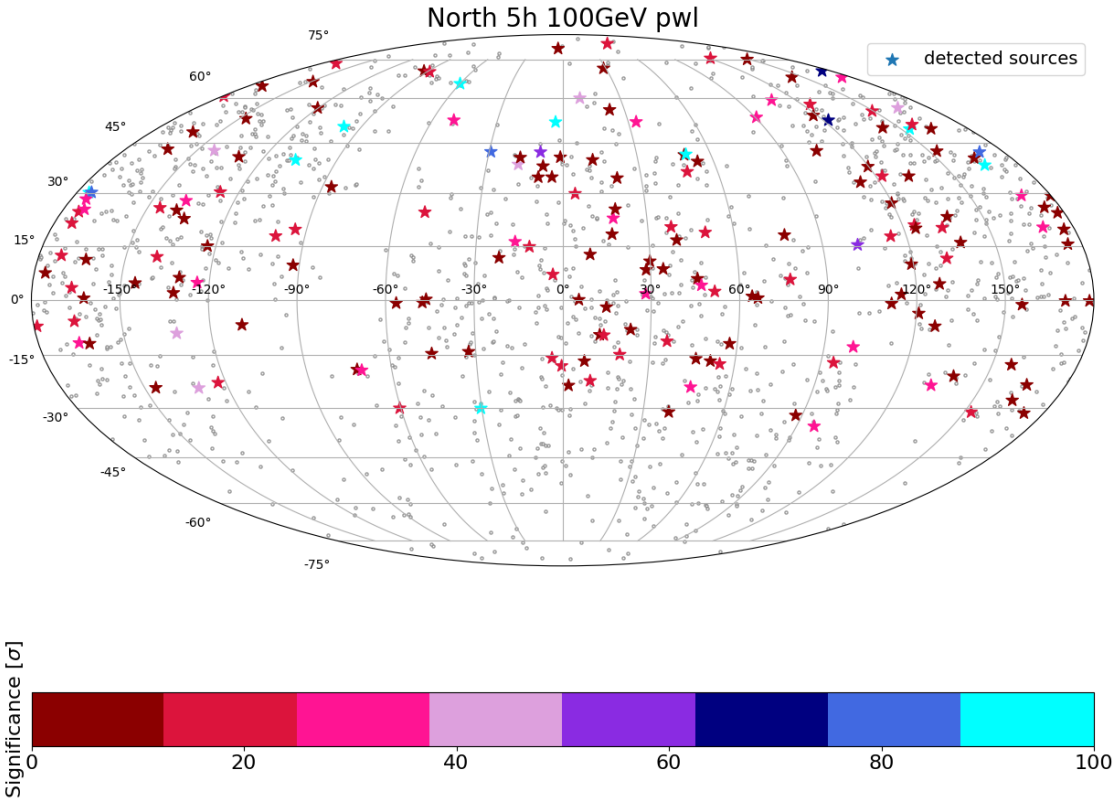

Figure 5.13: A skymap, in celestial co-ordinates, of the extragalactic sources expected to be detectable with CTA N at an energy threshold of 100 GeV under the power law extrapolation scheme for an observation time of 5 hours. The colour scheme corresponds to the significance of detection in σ.

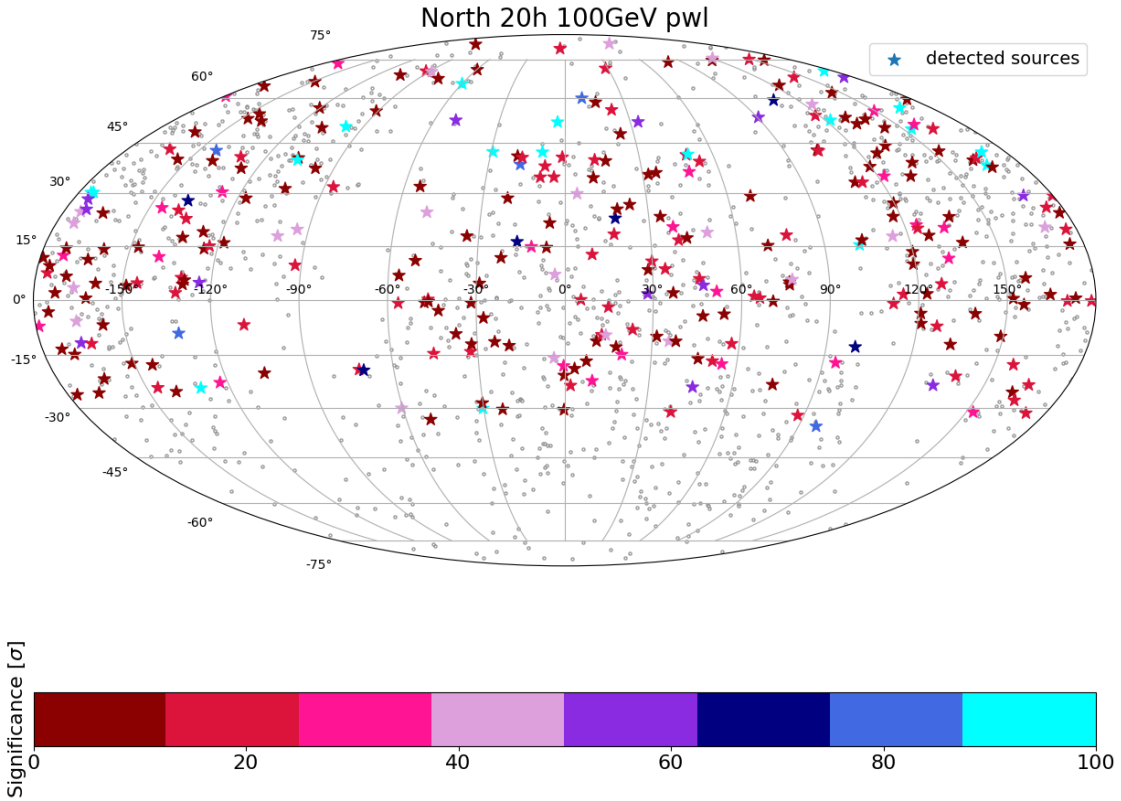

Figure 5.14: A skymap, in celestial co-ordinates, of the extragalactic sources expected to be detectable with CTA N at an energy threshold of 100 GeV under the power law extrapolation scheme for an observation time of 20 hours. The colour scheme corresponds to the significance of detection in σ.

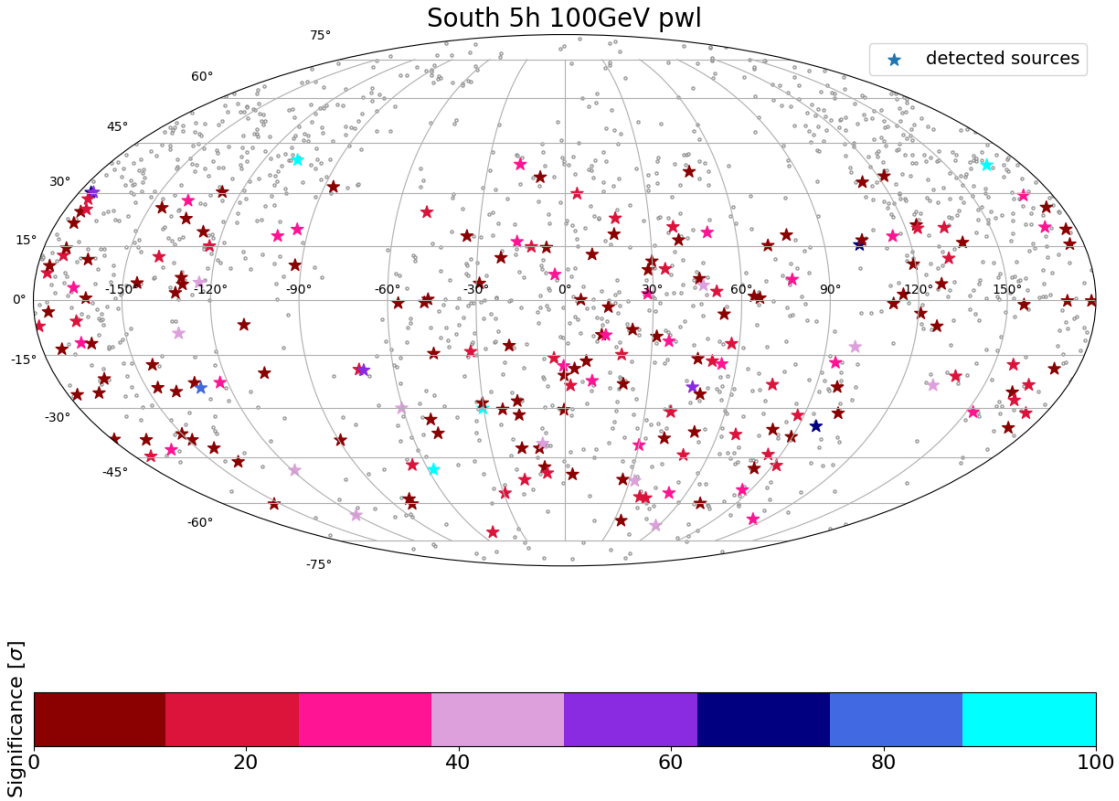

Figure 5.15: A skymap, in celestial co-ordinates, of the extragalactic sources expected to be detectable with CTA S at an energy threshold of 100 GeV under the power law extrapolation scheme for an observation time of 5 hours. The colour scheme corresponds to the significance of detection in σ.

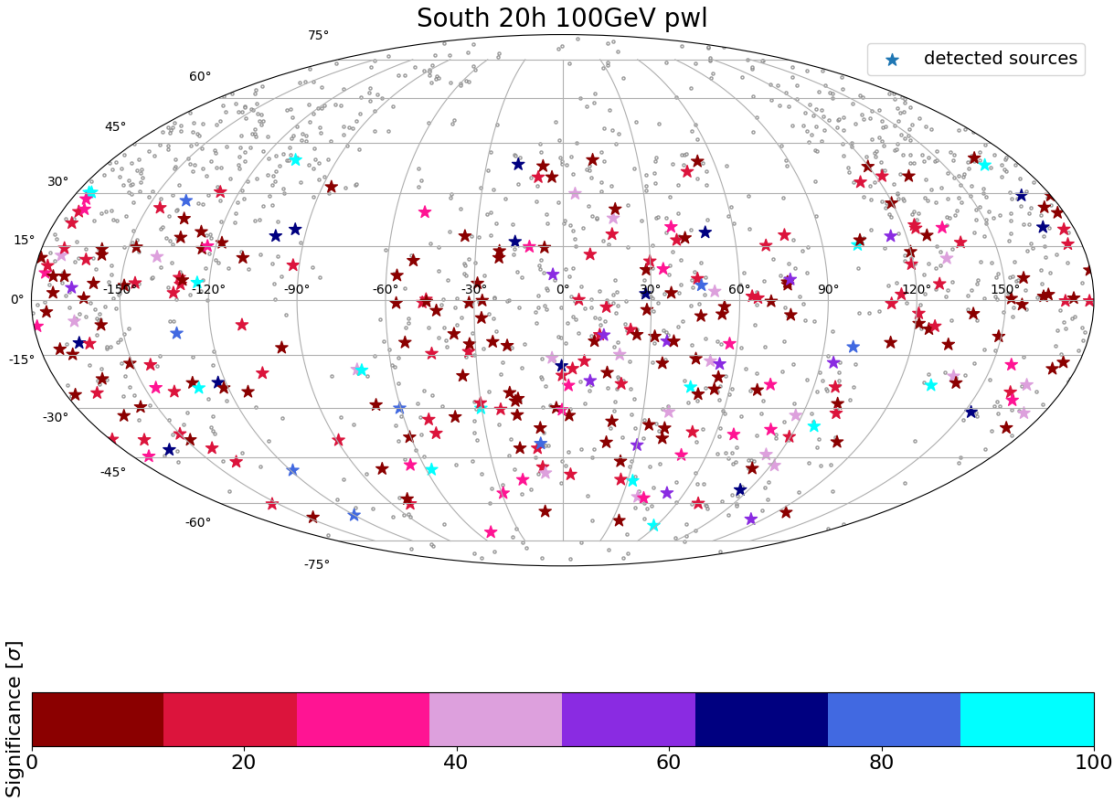

Figure 5.16: A skymap, in celestial co-ordinates, of the extragalactic sources expected to be detectable with CTA S at an energy threshold of 100 GeV under the power law extrapolation scheme for an observation time of 20 hours. The colour scheme corresponds to the significance of detection in σ.

It should be noted that the results presented in this work are based on the expected performance of the full CTA baseline array (see Section 4.4). The initial construction phase of the CTA, referred to as the alpha configuration, will consist of 4 LSTs and 9 MSTs for the Northern array and 14 MSTs and 37 SSTs for the Southern array. The full array, referred to as the omega configuration, will be completed in a later phase of construction subject to the availability of funds.

The impact of the lower sensitivity and sky coverage of the alpha configuration has been investigated in Brown et al. (2021). As expected, the alpha configuration is found to perform worse than the omega configuration, with the most significant difference found for the Southern array, a result of the lack of LSTs in the initial configuration for CTA S.

For example, Brown et al. (2021) expect only 100 sources to be detectable with CTA S at an energy threshold of 100 GeV under the power law extrapolation scheme for an observation time of 20 hours. It should be noted that the results presented in Brown et al. (2021) were obtained using a standard ON-OFF (or aperture photometry) approach and the *GAMMAPY* software package (Deil et al. (2017), Nigro et al. (2019)). For comparison, my analysis predicts 304 sources to be detected at the same energy threshold and for the same period of observation.

5.4.2 Scientific Objectives

The increased number of detections and improved statistics provided with the CTA will help address a wide range of questions in VHE astronomy. A non-exhaustive list of such questions are discussed in this section within the context of my results.

Will we detect the FSRQs investigated in Chapter 3?

Despite being some of the brightest sources detected with the *Fermi*-LAT, only 8 FSRQs have been detected above $E_\gamma \geq 100$ GeV at the time of writing*, namely, PKS 1510-089, 3C 279, 4C 21.35, S3 0218+35, PKS 0736+017, Ton 599, B2 1420+32 and PKS 1441+25. This can be explained by invoking the blazar sequence (for example Fossati et al. (1998),

*`http://tevcat.uchicago.edu/`, accessed on 11/01/21.

Table 5.2: The expected detection significance, best fit spectral index, γ, and photon flux for the sample of FSRQs studied in Chapter 3 above an energy threshold of 100 GeV. The results are obtained under the power law extrapolation scheme for an observation time of 5 hours and represent the mean values from 100 independent instances of simulation. B2 1520+31 and PKS 1502+106 are not expected to be detected at a significance of 5σ and the corresponding best fit spectral index and flux values are listed as NA.

4FGL name	Common name	RA [deg]	DEC [deg]	z	CTA Site	Significance [σ]	γ	Flux [$10^{-10} cm^{-2} s^{-1}$]
J2253.9+1609	3C 454.3	343.50	16.15	0.86	N	31.83 ± 1.18	2.26 ± 0.21	0.39 ± 0.02
J2232.6+1143	CTA 102	338.15	11.73	1.03	N	5.39 ± 0.96	2.47 ± 1.48	0.06 ± 0.01
J1522.1+3144	B2 1520+31	230.55	31.74	1.49	N	1.53 ± 0.89	NA	NA
J1512.8-0906	PKS 1510-089	228.22	-9.11	0.36	S	42.48 ± 1.31	2.35 ± 0.08	0.39 ± 0.01
J1504.4+1029	PKS 1502+106	226.10	10.49	1.84	N	2.24 ± 1.10	NA	NA
J1427.9-4206	PKS 1424-41	216.99	-42.11	1.52	S	9.78 ± 0.98	2.12 ± 0.98	0.09 ± 0.01
J1256.1-0547	3C 279	194.04	-5.79	0.54	S	24.22 ± 1.30	2.32 ± 0.17	0.22 ± 0.01
J1224.9+2122	4C 21.35	186.23	21.38	0.43	N	20.91 ± 1.75	2.25 ± 0.17	0.22 ± 0.01
J0457.0-2324	PKS 0454-234	74.26	-23.41	1.00	S	13.91 ± 1.09	2.09 ± 0.45	0.13 ± 0.01

Ghisellini et al. (2017)). While the IC peaks of BL Lacs predominantly occur at relatively higher energies, FSRQs peak in the sub-GeV range and are mostly detected only during flaring periods.

Furthermore FSRQs, which typically have redshifts above 1 (see Figure 5.2), are harder to detect with current generation IACTs as a consequence of pair production with the EBL photons. The CTA is expected to increase the number of FSRQs detected in the VHE regime with, for example, 34 such sources expected to be detected with CTA S in 20 hour observations at an energy threshold of 100 GeV.

The results obtained from extrapolating the eight year time-averaged flux states of the FSRQ sample investigated in Chapter 3 are presented in Table 5.2. Each source is simulated for the CTA site providing the largest elevation, calculated from the difference in latitudes of the location of the observing array (28.76° N for CTA N and 24.68° S for CTA S) and the declination of the source. The simulations indicate that 7 of the 9 sources investigated in Chapter 3 are expected to be detected at a significance of 5σ. The two exceptions are B2 1520+31 and PKS 1502+106, while CTA 102 is found to be a marginal detection with an expected significance of 5.39 ± 0.96 σ.

What other source classes emit VHE gamma-rays?

While blazars are expected to form the most numerous class of the detections with the

detection of ∼ 250 such sources forecast for 20 hour observations at an energy threshold of 100 GeV, the CTA is also expected to detect sources from non-blazar populations and enable further studies of the emission mechanisms taking place in these objects. The AGN unification model (see Section 1.2.3) suggests that radio galaxies differ from blazars primarily due to an unfavourable alignment of their jets to our line of sight and observations with the CTA will allow scientists to explore this further. 21 radio galaxies are expected to be detected with CTA N in 20 hour observations at an energy threshold of 100 GeV, an increase of a factor of 4 on current IACT detections.

An investigation by Romano et al. (2018) found the Narrow-Line Seyfert 1 galaxy SBS 0846+513 to be observable with CTA N in its average flux state which agrees with my results. The Circinus Galaxy is the only radio-quiet Seyfert galaxy to have been detected with the *Fermi*-LAT at GeV energies (Hayashida et al. (2013)) and my analysis indicates that it will also be detected for the first time in the VHE regime with the CTA. A handful of other non-blazar active galaxies are also expected to be observable with the CTA namely B3 1009+427, PKS 0521-36, PKS B1353-171 and CGCG 050-083.

Will we also detect sources at high redshift and why are these detections useful?

As seen in the redshift distributions of the detected sources presented in Figures 5.17 and 5.18, the CTA is expected to detect sources at redshifts higher than 0.5, with for example, the detection of 18 such sources predicted in 5 hour observations with CTA S at an energy threshold of 100 GeV. For comparison, only 4 such sources namely PKS 1441+25, 3C 279, Ton 599 and B2 0218+357, have been detected with current generation IACTs.

The results highlight that the CTA will not only multiply the number of sources detected, but also expand the horizons to which we can observe the gamma-ray sky. As described in Abdalla et al. (2021), the detection of high redshift blazars will enable scientists to explore a range of topics in astronomy, cosmology and fundamental physics. These include the measurement of the gamma-ray absorption by the EBL, investigations of intergalactic magnetic fields, searches for evidence of axion-like particles and multiple tests for Lorentz invariance violation (LIV).

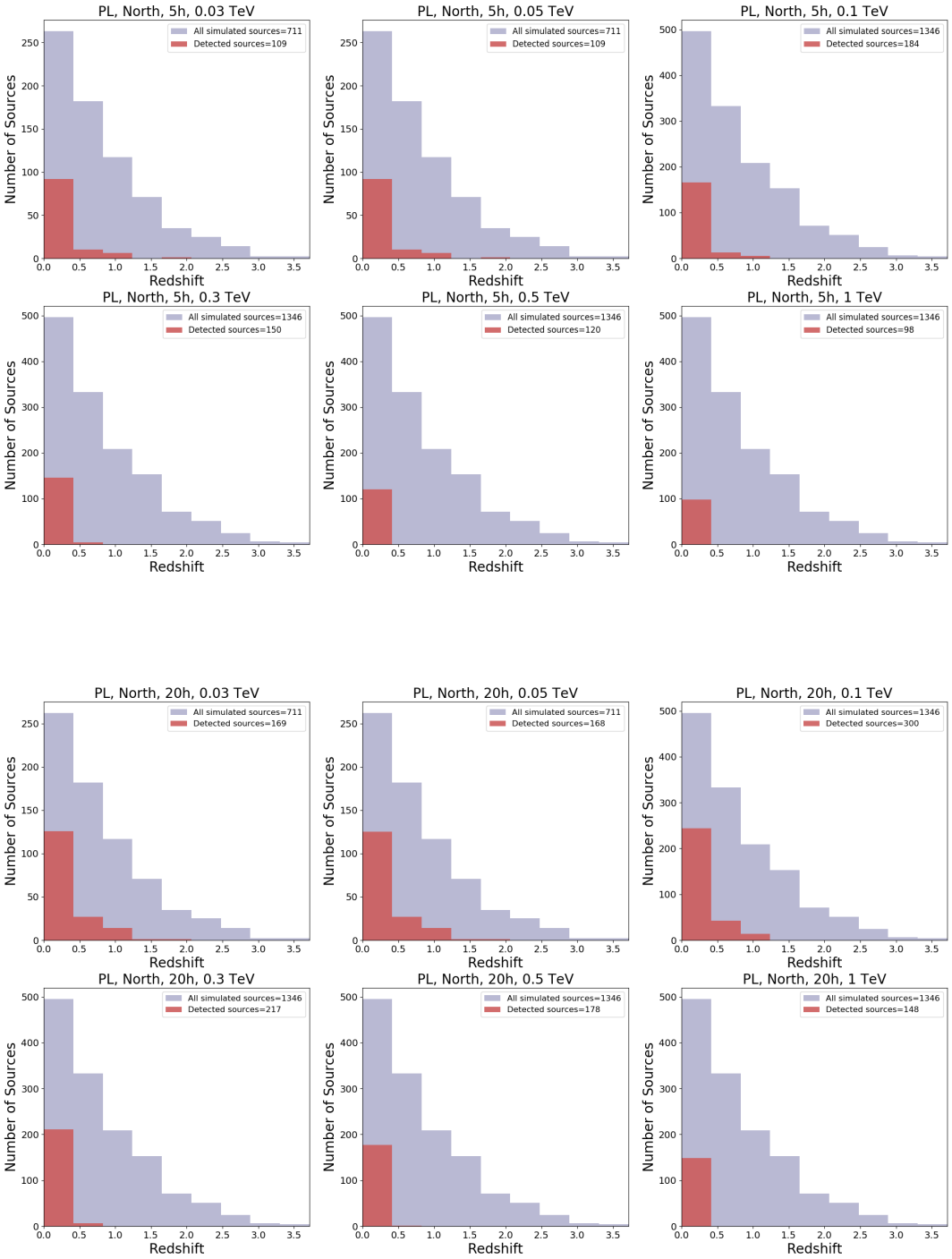

Figure 5.17: The redshift distribution of sources expected to be detectable with CTA N at energy thresholds of 30, 50, 100, 300, 500 and 1000 GeV under the power law extrapolation scheme for the observation times of 5 hours (top) and 20 hours (bottom) respectively. Also shown is the redshift distribution of all simulated sources for each particular configuration.

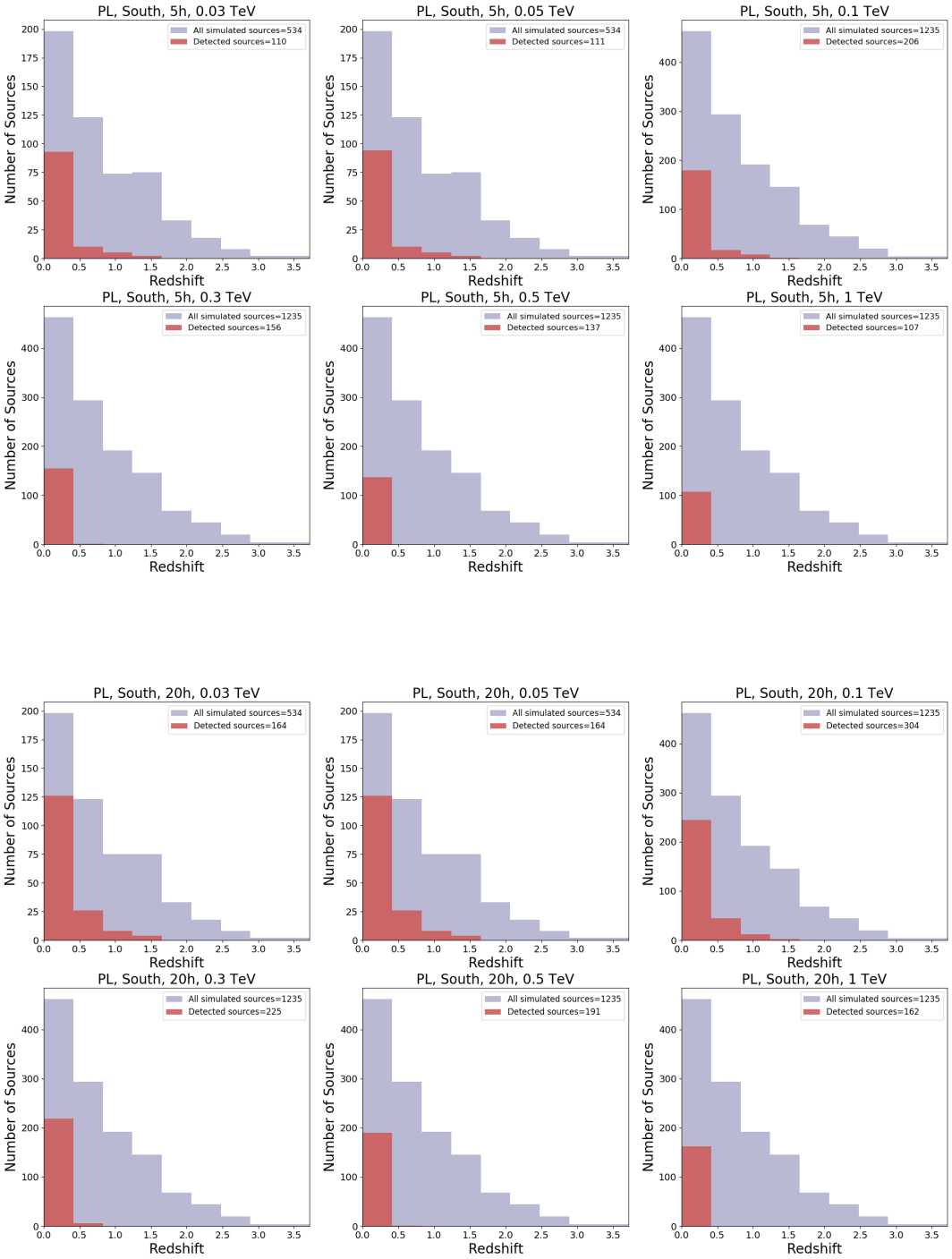

Figure 5.18: The redshift distribution of sources expected to be detectable with CTA S at energy thresholds of 30, 50, 100, 300, 500 and 1000 GeV under the power law extrapolation scheme for the observation times of 5 hours (top) and 20 hours (bottom) respectively. Also shown is the redshift distribution of all simulated sources for each particular configuration.

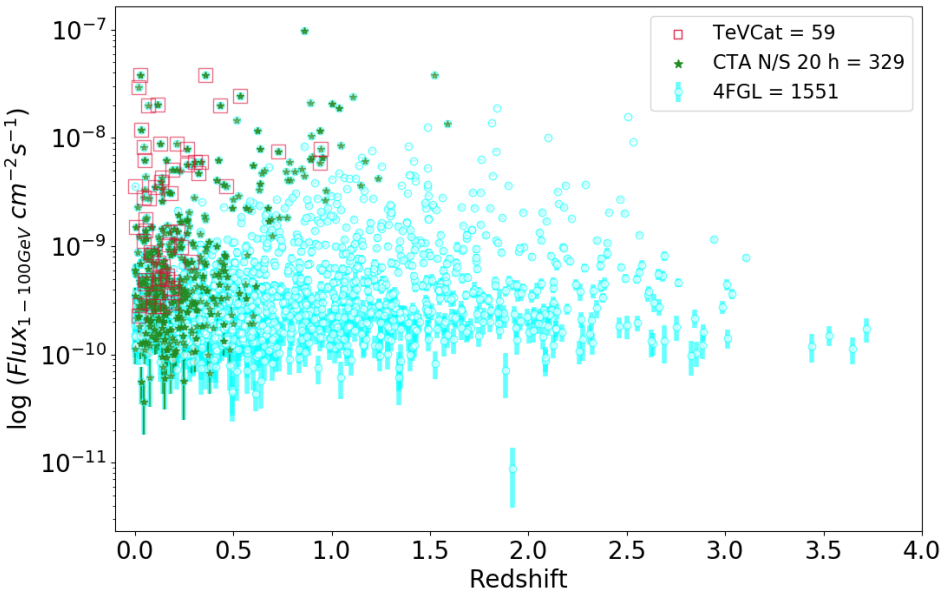

Figure 5.19: The *Fermi*-LAT fluxes in the energy range 1 GeV $\leq E_\gamma \leq$ 100 GeV versus the redshift of all sources in the sample. The red outlined sources are those already detected with current generation IACTs and highlighted in green are the AGN expected to be detectable in 20 hour observations with either CTA N or CTA S above an energy threshold of 100 GeV under the power law extrapolation scheme.

The distribution of GeV fluxes measured with the *Fermi*-LAT against redshift of all sources in the sample is shown in Figure 5.19, highlighting the sources which have been detected with current generation IACTs and those expected to be visible with CTA N or CTA S in 20 hour observations. In addition to bright high redshift sources, the CTA is also expected to detect fainter objects at relatively lower redshifts. The increased number of sources will provide a basis for a first ever reliable estimate of the LF of blazars (see Section 5.5) and help investigate the evolution of the different source populations in the VHE regime.

What are the brightest sources of each AGN class expected to be detected?

The extragalactic survey will also include the long-term monitoring of sources with the aim of generating VHE lightcurves. In order to construct a representative sample of potential targets for the CTA, it is important to include sources from each AGN class and an example of such a list is given in Table 12.1 of Acharya et al. (2013). Table 5.3 presents the results of a similar sample when observed with CTA N and CTA S for an exposure time of 5 hours at

an energy threshold of 100 GeV. It is expected that the list of targets will be reviewed every five years once the CTA is fully operational and potentially reduced to the most interesting objects for further monitoring over the entire lifetime of the CTA.

What is the shortest observing time required for detection and why is this important?

As seen in Table 5.3, Mkn 421 is expected to be the brightest source detectable with the CTA with an expected significance of 757.44 ± 2.01 σ in 5 hours of observation. This result is not surprising given that at a redshift of z = 0.03, Mkn 421 is one of the closest known BL Lac objects and was the first extragalactic source to be detected in the TeV regime (Punch et al. (1992)).

An important consequence of this expected result will be the ability to observe variability in short timescales possibly less than a minute. This is particularly important for Mkn 421 as the source has a history of fast flaring events (for example Gaidos et al. (1996), Fossati et al. (2008), Acciari et al. (2011)). Investigating short timescale variability will aid in understanding the mechanisms involved in the production of gamma-rays as well as in localising the emission region (as studied for FSRQs in Chapter 3).

To put this in context, Abeysekara et al. (2020) investigated the February 2010 flare using VHE observations at $E_\gamma \geq 110$ GeV with VERITAS and multi-wavelength data from partner observatories. The high statistics provided from this extraordinary flare, having a peak flux of 27 Crab Units above 1 TeV, allowed the VERITAS data to be binned in 2 minute and 5 minute intervals. The study concluded that the multi-wavelength observations were difficult to explain using a classical one-zone emission model.

Indeed short timescale variability at high energies, in general, indicates emission mechanisms more complex than single-zone emission as the bulk Lorentz factors required are incompatible with the results obtained from radio observations (Piner and Edwards (2018)). A similar study of the July 2006 flare from PKS 2155-304, another of the brightest sources expected to be observable with the CTA, using H.E.S.S. data (Aharonian et al. (2009)) also suggested the need for two emission zones. The improved statistics provided with the CTA when investigating short timescale variability will enable even further conclusions to be

Table 5.3: The expected detection significance, best fit spectral index, γ, and energy flux for a sample of list of targets for long-term monitoring with CTA N (top) and CTA S (bottom). The results are obtained under the power law extrapolation scheme for an observation time of 5 hours and represent the mean values from 100 independent instances of simulation. The final column states whether the object is present in the TeVCat with P indicating a TeV source and N implying no known association.

CTA N									
4FGL name	Common name	Class	RA [deg]	DEC [deg]	z	Significance [σ]	γ	Flux [$10^{-10} cm^{-2} s^{-1}$]	TevCat
J2202.7+4216	BL Lac	BL Lac	330.69	42.28	0.07	79.92 ± 1.61	2.22 ± 0.03	0.59 ± 0.02	P
J2000.0+6508	1ES 1959+650	BL Lac	300.01	65.15	0.05	249.96 ± 1.81	1.82 ± 0.01	1.66 ± 0.02	P
J1728.3+5013	I Zw 187	BL Lac	262.08	50.23	0.06	93.50 ± 1.69	1.77 ± 0.02	0.42 ±0.01	P
J1653.8+3945	Mkn 501	BL Lac	253.47	39.76	0.03	393.28 ± 1.79	1.74 ± 0.01	3.36 ± 0.03	P
J1104.4+3812	Mkn 421	BL Lac	166.12	38.21	0.03	757.44 ± 2.01	1.77 ± 0.01	9.94 ± 0.05	P
J2253.9+1609	3C 454.3	FSRQ	343.50	16.15	0.86	31.83 ± 1.18	2.26 ± 0.21	0.39 ± 0.02	N
J0319.8+4130	NGC 1275	RDG	49.96	41.51	0.02	121.41 ± 1.43	2.12 ± 0.02	1.17 ± 0.02	P
J0602.0+5315	GB6 J0601+5315	BCU	90.51	53.27	0.05	30.36 ± 1.63	1.94 ± 0.06	0.11 ± 0.01	N
J1543.6+0452	CGCG 050-083	Other	235.91	4.87	0.04	30.17 ± 1.56	1.86 ± 0.06	0.08 ± 0.01	N
CTA S									
4FGL name	Common name	Class	RA [deg]	DEC [deg]	z	Significance [σ]	γ	Flux [$10^{-10} cm^{-2} s^{-1}$]	TevCat
J2158.8-3013	PKS 2155-304	BL Lac	329.71	-30.23	0.12	314.78 ± 1.61	1.85 ± 0.01	2.91 ± 0.03	P
J2009.4-4849	PKS 2005-489	BL Lac	302.36	-48.82	0.07	131.37 ± 1.79	1.83 ± 0.01	0.51 ± 0.01	P
J1917.7-1921	1H 1914-194	BL Lac	289.44	-19.36	0.14	61.36 ± 1.33	1.94 ± 0.03	0.33± 0.01	N
J1517.7-2422	AP Librae	BL Lac	229.43	-24.37	0.05	80.02 ± 1.64	2.12 ± 0.02	0.32 ± 0.01	P
J0303.4-2407	PKS 0301-243	BL Lac	45.86	-24.12	0.27	62.80 ±1.30	1.89 ± 0.04	0.51 ± 0.01	P
J1512.8-0906	PKS 1510-089	FSRQ	228.22	-9.11	0.36	42.48 ± 1.31	2.35 ± 0.08	0.39 ± 0.01	P
J1256.1-0547	3C 279	FSRQ	194.04	-5.79	0.54	24.22 ± 1.30	2.32 ± 0.17	0.22 ± 0.01	P
J0627.0-3529	PKS 0625-35	RDG	96.77	-35.49	0.05	67.66 ± 1.59	1.90 ± 0.03	0.19 ± 0.01	P
J0847.0-2336	PMN J0847-2337	BCU	131.76	-23.61	0.06	50.91 ± 1.43	1.93 ± 0.03	0.14 ± 0.02	N

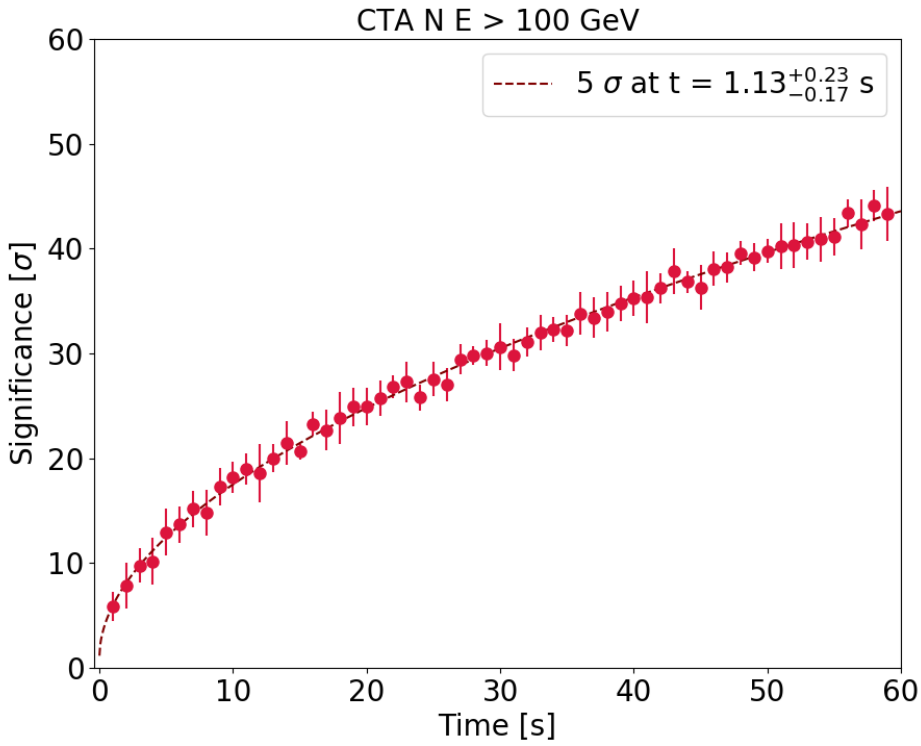

Figure 5.20: The expected significance of Mkn 421 as a function of observation times evenly spaced in the interval 1 - 60 seconds when observed with CTA N at an energy threshold of 100 GeV. The dashed curve indicates the best fit and the predicted time required for a 5σ detection is shown in the legend.

drawn regarding the nature of the emission region.

Figure 5.20 plots the expected significance of Mkn 421 as a function of observation time for sub-minute timescales when observed with CTA N at an energy threshold of 100 GeV. From interpolating the fit, it is shown that a 5σ detection of the source in its average flux state is, in principle, expected for an observation period of $1.13^{+0.23}_{-0.17}$ seconds. It should be noted that this estimate is obtained from simulations and may not be reached in practice, but nevertheless, highlights the anticipated ability to observe variability in unprecedented short timescales with the CTA.

Furthermore, the observation of AGN in short timescales will enable multiple tests for LIV. A possible energy dependence in the speed of light has been predicted within the framework of quantum gravity (for example Ellis et al. (2008)). Due to its improved sensitivity, the

CTA is expected to facilitate precise investigations into the energy dependence in the arrival times of high energy photons and be able to distinguish between any modification effects intrinsic to the source and those induced during propagation (Doro et al. (2013)). Previous studies in the VHE regime, for example using H.E.S.S. observations of PKS 2155-304 (Aharonian et al. (2008a)) while finding no significant evidence of a time-lag, have derived lower limits on any possible energy dependence.

What is the effect of spectral curvature on the number of detections?

As expected, the results of the simulation are strongly linked to the spectral model assumed. Figure 5.21 shows a comparison between the source significances obtained under the power law and log parabola extrapolation schemes for 5 hour observations with CTA N and CTA S. In general, the power law extrapolation scheme yields higher significances with the exceptions being the 231 sources having negative curvature (i.e. an upward-curved-spectrum) in the 4FGL catalog (The *Fermi*-LAT collaboration (2019a)). The redshift distributions of extragalactic sources expected to be detected in 5 hour observations with CTA N and CTA S under the log parabola extrapolation scheme are shown in Figure 5.22.

5.5 Towards a blazar Luminosity Function with the CTA

Having studied the detection prospects of individual AGN with the CTA, I now move on to considering the objects as a source population. The evolutionary properties of blazars in the TeV regime are poorly understood, primarily due to the intrinsic biases involved in observations with current generation IACTs. Investigating these properties for different classes of AGN will help reveal how these sources are distributed in space and also how they evolve over cosmic time.

The CTA extragalactic survey will aim to provide the flux and spectral shapes of all sources in the survey region down to a minimum achievable flux based on the sensitivity of the survey. In conjunction with the redshift range over which the survey is conducted, this will allow the space density of the source populations to be derived for any assumed cosmological model.

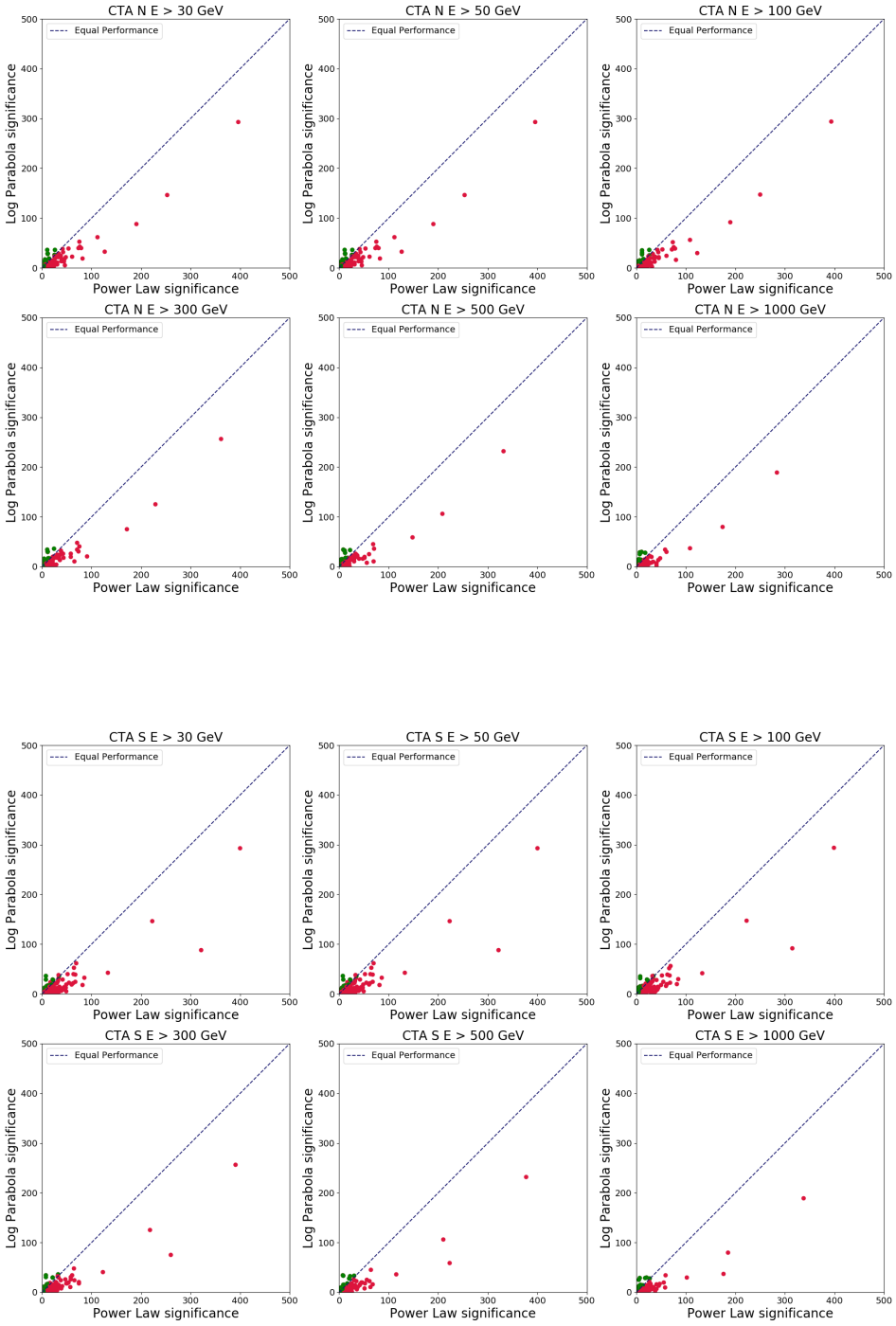

Figure 5.21: A comparison between the significances obtained under the power law and log parabola extrapolation schemes for CTA N (top) and CTA S (bottom) respectively. The dashed line indicates equal performance. The green points represent sources having a negative curvature as reported in the 4FGL catalog (The *Fermi*-LAT collaboration (2019a)).

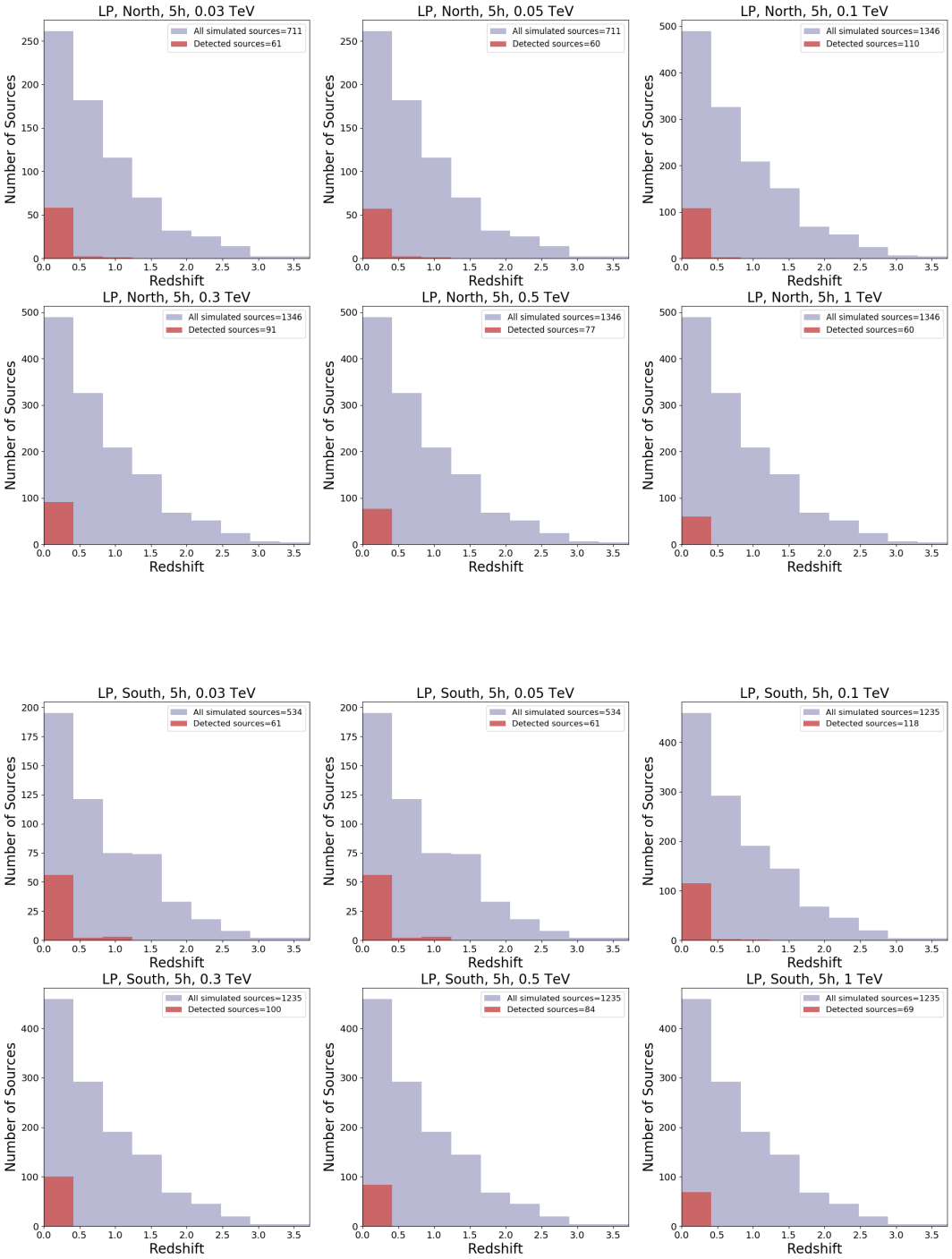

Figure 5.22: The redshift distribution of sources expected to be detected with CTA N (top) and CTA S (bottom) at energy thresholds of 30, 50, 100, 300, 500 and 1000 GeV under the log parabola extrapolation scheme for observation times of 5 hours. Also shown is the redshift distribution of all simulated sources for each particular configuration.

The luminosity function (LF) describes the number of sources per unit comoving volume per unit luminosity and is usually expressed as a function of redshift. An increasing LF with redshift indicates positive evolution, meaning there were more sources in the past. A decreasing LF, on the other hand, implies negative evolution, meaning fewer sources in the past.

An unbiased and reliable measurement of the LF is pivotal to answering a number of key scientific questions. For instance, integrating the LF of blazars followed by the subtraction of the contributions from known sources would allow for the measurement of the contribution of unresolved blazars to the diffuse isotropic gamma-ray background (IGRB; Abdo et al. (2010e)).

As discussed in Chapter 1, gamma-ray emission mechanisms may involve the production of neutrinos. An estimate of the energy density of the IGRB can be extrapolated to PeV energies (1 PeV = 10^6 GeV) and then compared to the energy density of cosmic neutrino emission. Such multi-messenger studies might help ascertain if these two signals have a common origin and quantify the extent of neutrino emission in blazars (Ahlers (2019)).

Furthermore, a comparison of LF models for different source classes at various wavelengths can be used to verify whether or not all sources belong to the same underlying population as hypothesized in AGN unification models (see Section 1.2.3). Unfortunately, the determination of the LF in the VHE regime has proved quite challenging so far. One of the main reasons for this is the inherent bias in the blazar sample. This is brought about due to targeted observations motivated by flare periods at lower energies (for example with the *Fermi*-LAT).

The limits on the sensitivities of current generation IACTs make it unfeasible to conduct a large uniform survey, especially at higher redshifts where the effects of EBL absorption also hinder these investigations. A preliminary study of sample selection methods towards determining the LF in the TeV regime using observations with VERITAS is conducted in Brill (2019). As discussed in Section 4.4, the CTA is designed to achieve an order of magnitude increase in sensitivity which, in conjunction with a wider field of view,

particularly for the SSTs, will allow for such a survey to be conducted.

Despite this, there have been a number of investigations aimed at determining the gamma-ray LF using one of two main semi-independent approaches. The first is a binned non-parametric measurement using the $1/V_{\rm max}$ test (Schmidt (1968)) as used, for example, in a study of a sample of *EGRET* blazars in the energy range 20 MeV - 30 GeV (Chiang and Mukherjee (1998)). This method is based on using the flux limit of the instrument to determine the largest volume, $V_{\rm max}$, containing an object having the same luminosity as a source in the sample while still being able to detect it.

An important disadvantage of this approach is that it is based on the assumption of the distribution of all galaxies in space being uniform (Binggeli et al. (1988)). This is overcome using the second approach which undertakes a maximum likelihood fit of an analytic model describing the LF to a sample of blazars ordered in luminosity (for example Marshall et al. (1983)). Furthermore, this method can be used to compare different analytical forms of the LF, particularly for small samples which cannot be finely binned in redshift and luminosity, and has been adopted in *Fermi*-LAT studies of BL Lacs (Ajello et al. (2014)) and FSRQs (Ajello et al. (2012)) in the energy range 100 MeV - 100 GeV.

In the remainder of this chapter, I use the second approach to fit the results of the simulations presented previously and make an estimate of the LF expected to be observed with the CTA, the first investigation of this nature in this energy regime. A standard cosmology is adopted, with a Hubble constant of H_0 =71 km s^{-1}Mpc^{-1}, Ω_M = 0.27 an Ω_Λ = 0.73 as derived from the results of the Wilkinson Microwave Anisotropy Probe (Komatsu et al. (2009)).

5.5.1 Source Sample

The quality of the estimated LF depends primarily on having sufficient sources representative of a typical AGN population. This can be achieved through an unbiased, uniform and flux-limited survey of the entire sky. As seen in Table 5.1, blazars constitute by far the majority of the sources expected to be detectable with the CTA. The sample used in the calculation of the LF consists of the 220 BL Lac and 34 FSRQ sources forecast to be

detectable (defined as having TS $\geq$ 25) from CTA S at an energy threshold of 100 GeV in 20 hours of observation.

My choice of sample is motivated by the necessity to have sufficient photon statistics in order to allow for the extraction of the evolutionary parameters. CTA S is expected to produce the largest number of detections from a single source population, marginally more than expected with CTA N at the same threshold. While the results are obtained from a 20 hour all-sky survey using the full CTA baseline array, the methods developed can also be applied to more realistic configurations including, for example reduced observing times or the alpha array, as well as to real data obtained with current generation IACTs.

Furthermore, the detection of AGN in the TeV regime also depends on the flux state of the source during observation. This can introduce a further potential bias in the sample since many sources can only be detected when undergoing flaring periods. Since the results are obtained from the extrapolation of the 8 year time-averaged *Fermi*-LAT spectral parameters (see Section 5.2.2), the sample is not expected to suffer from biases associated with flaring periods. Finally, all the sources have a known spectroscopic redshift measurement and the simulations already account for EBL absorption.

The VHE luminosity, L, is calculated from the predicted CTA energy flux, $S(E_1, E_2)$, in the energy range between $E_1 = 100$ GeV and $E_2 = 200$ TeV using the relation (Ghisellini et al. (2009)):

$$L = 4\pi d_L^2 \frac{S(E_1, E_2)}{(1+z)^{2-\Gamma}}, \tag{5.8}$$

where Γ is the spectral index, z is the redshift and d_L is the luminosity distance:

$$d_L = (1+z)\frac{c}{H_0}\int_0^z \frac{dz'}{\sqrt{\Omega_M (1+z')^3 + \Omega_\Lambda}}. \tag{5.9}$$

The above relation is based on the assumption that $E_2 >> E_1$, which is satisfied by my choice of energy interval. The denominator in equation 5.8 represents the K-correction term, accounting for the redshift modification between the observed and emitted energies. Figure 5.23 shows the distribution of the VHE luminosity plotted against redshift for the sample.

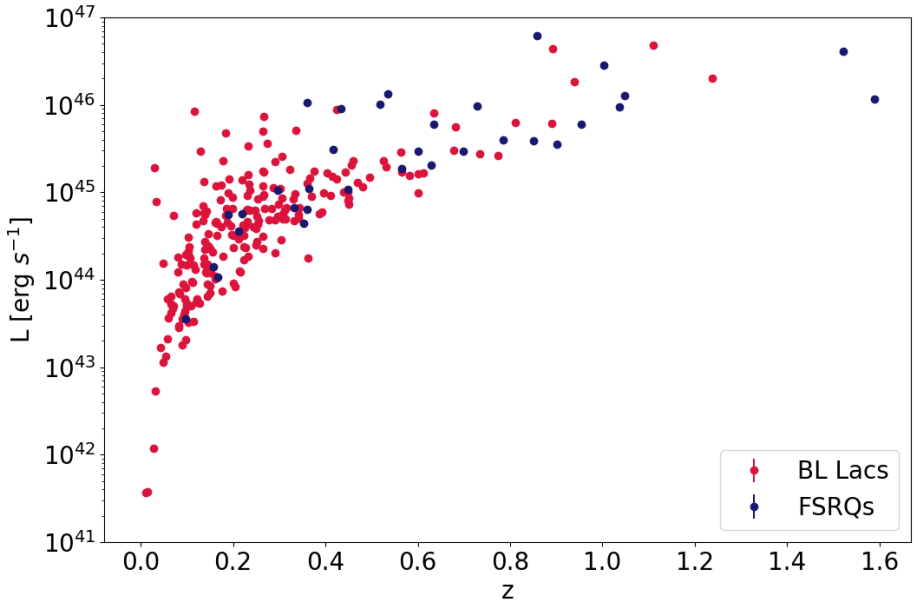

Figure 5.23: The distributions of VHE luminosity against redshift for the sample of BL Lacs and FSRQ sources expected to be detected in 20 hour observations with CTA S above an energy threshold of 100 GeV.

5.5.2 Analysis Method

Similar to the approach adopted in Ajello et al. (2014), the space density of the sample of blazars is obtained as a function of the 100 GeV - 200 TeV CTA rest frame luminosity (L), redshift (z) and spectral index (Γ) from a maximum likelihood fit of the following functional form:

$$\frac{\partial^3 N}{\partial L \partial z \partial \Gamma} = \frac{\partial^3 N}{\partial L \partial V \partial \Gamma} \times \frac{dV}{dz} = \Phi(L, V(z), \Gamma) \times \frac{dV}{dz}. \tag{5.10}$$

Here $\Phi(L, V(z), \Gamma)$ represents the LF and $\frac{dV}{dz}$ the co-moving volume element per unit redshift and unit solid angle (Hogg (1999)):

$$\frac{dV}{dz} = \frac{c d_L^2}{H_0 (1+z)^2 \sqrt{\Omega_M (1+z)^3 + \Omega_\Lambda}} \tag{5.11}$$

As seen in Equation 5.10, the LF will depend on the intrinsic distribution of the photon indices. This distribution is assumed to be independent of redshift as evidenced in a study of *EGRET* detected blazars in Venters and Pavlidou (2007) who also find the spectral index distribution to be compatible with a Gaussian distribution. The same conclusion was obtained by Abdo et al. (2010c) in an investigation of the spectral index distribution of *Fermi*-LAT detected sources based on the first *Fermi*-LAT catalog (1LAC; Abdo et al. (2010b)).

A Gaussian model was also adopted in the derivation of the LF using *Fermi*-LAT observations of BL Lacs (Ajello et al. (2014)) and FSRQs (Ajello et al. (2012)). It should be noted that given the lack of blind AGN surveys in the VHE regime, no chosen spectral index distribution will be absolute at this stage. Nevertheless, for the purpose of this thesis, I also model the spectral index relation with a Gaussian:

$$\Phi(L, V(z), \Gamma) \propto e^{-\frac{(\Gamma-\mu)^2}{2\sigma^2}}, \tag{5.12}$$

where μ and σ are the mean and dispersion of the distribution respectively.

The Ajello et al. (2015) study investigated the *Fermi*-LAT data from a sample of 403 blazars (more specifically 211 BL Lacs, 186 FSRQs and 6 BCUs) in the energy range 100 MeV - 100 GeV and the results were found to better reproduce the overall evolutionary properties than the results presented in Ajello et al. (2014). Three different models for the LF were tested, namely the primarily luminosity evolution (PLE) model, the primarily density evolution (PDE) model, and the luminosity-dependent density evolution (LDDE) model.

In all models, the LF at redshift z=0 is defined as a smoothly-joined double power law multiplied by the photon index distribution:

$$\Phi(L, z=0, \Gamma) = \frac{A}{\ln(10)L}\left(\left(\frac{L}{L_*}\right)^{\gamma_1} + \left(\frac{L}{L_*}\right)^{\gamma_2}\right)^{-1} e^{-\frac{(\Gamma-\mu(L))^2}{2\sigma^2}}, \tag{5.13}$$

where the Gaussian mean, μ, has been allowed to change with luminosity as:

$$\mu(L) = \mu^* + \beta \times [\log(L) - 46]. \tag{5.14}$$

Under the PDE and LDDE models, the space density of the blazar population evolves identically for all source luminosities. An evolutionary factor, $e(z, L)$, describing the changes in the blazar population over cosmic time, is applied to the PDE and LDDE models such that:

$$\Phi(L, z, \Gamma) = \Phi(L, z = 0, \Gamma) \times e(z, L), \tag{5.15}$$

In the PLE model, on the other hand, the form of the LF remains constant but the luminosities change over cosmic time. The evolutionary factor is applied as as:

$$\Phi(L, z, \Gamma) = \Phi(L/e(z, L), z = 0, \Gamma). \tag{5.16}$$

For the PDE and PLE models, the evolutionary factor is defined as:

$$e(z, L) = (1 + z)^k e^{z/\xi}, \tag{5.17}$$

with

$$k = k^* + \tau \times [\log(L) - 46]. \tag{5.18}$$

The final model has 10 free parameters (A, γ_1, γ_2, L_*, k^*, τ, ξ, μ^*, β , and σ) making it hard to constrain, especially with the inherent lack of statistics at high energies.

LFs have also been previously modelled as a power law, perhaps most notably in Schechter (1976), the first analytical determination of the LF. Physically, such a model implies that the probability distribution of the blazar sample is a power law, usually a good first empirical

approximation. For the purpose of this thesis, I model the LF at redshift z as a simple power law with pure luminosity evolution such that:

$$\Phi(L' = L/e(z), \Gamma) = \frac{A}{\ln(10)L'} \left(\frac{L'}{L_0}\right)^{-\alpha} e^{-\frac{(\Gamma-\mu)^2}{2\sigma^2}}. \tag{5.19}$$

where $L_0 = 10^{46}$ erg s^{-1} and the evolutionary factor is defined as:

$$e(z) = (1+z)^k. \tag{5.20}$$

The final model has 5 free parameters (A, α, k, μ and σ). It has been shown (for example Hatziminaoglou et al. (2001), Butler et al. (2019)) that, for a pure power law LF as assumed in this study, the PLE and PDE models are observationally indistinguishable. The LDDE model is not considered at this stage since the additional parameters would make it more difficult to constrain given the lack of statistics.

The observed LF is a result of the convolution of the intrinsic LF with relativistic beaming, where the effect of beaming is to induce the break modelled in equation 5.13. Therefore, modelling the observed LF as a pure power law implies that either there is no significant beaming (this might be the case in the optical band, for example) or that the sensitivity of the instrument or lack of statistics prevents us from resolving the break.

The expected source count distribution for the sample of blazars is expressed as:

$$N(>L) = \int_{\Gamma_{\min}}^{\Gamma_{\max}} \int_{z_{\min}}^{z_{\max}} \int_{L(z,F)}^{L_{\max}} \Phi(L, V(z), \Gamma) \frac{dV}{dz} d\Gamma dz dL \tag{5.21}$$

where $L(z, F)$ is the luminosity of a source having redshift z and a simulated flux F. The best fitting parameters of the LF are obtained by using the Markov chain Monte Carlo (MCMC) technique (Gamerman and Lopes (2006); Hogg and Foreman-Mackey (2018)) to fit the above expression to the results of the simulations. The limits of the integrals correspond to those spanned by the sample investigated.

An important caveat of my approach is that it assumes the sky coverage of the survey, $\Omega(L, z, \Gamma)$, defined here as the probability of detecting in the survey a blazar of luminosity

L and photon index Γ at a redshift z to be uniformly 1. As previously stated, the results presented are therefore a preliminary, optimistic estimate and will benefit from detailed Monte Carlo investigations of the CTA sky coverage similar to that conducted for a sample of *Fermi*-LAT detected blazars in Abdo et al. (2010c). A back-of-the-envelope calculation towards this is presented in Section 5.5.4.

MCMC methods are capable of sampling a probability distribution function (pdf) even in the absence of a full analytical description of the pdf. For the purpose of this computation, the simplest and most commonly used algorithm for MCMC, the Metropolis–Hastings algorithm (Metropolis et al. (1953)) is adopted, using the *emcee* (Foreman-Mackey et al. (2013)) implementation in python*.

The algorithm requires two inputs: the function to be sampled, $f(\theta)$, and a proposal pdf, $q(\theta'|\theta)$, capable of drawing up a new position in the parameter space, θ', from the previous position, θ. The later will include a range of physically acceptable values of the parameters or, if applicable, results obtained from previous experiments.

In principle, the algorithm is simply a biased random walk through the entire parameter space, aimed at finding a set of parameters that best fit the data sample. The steps involved in the algorithm are summarised in Figure 5.24.

5.5.3 Results

The best fit parameters obtained from the MCMC for both BL Lacs and FSRQs are reported in Table 5.4. Figure 5.25 gives an illustrative representation of the one-dimensional distributions of the parameters in the MCMC sample and also includes scatter plots showing the correlations between them. The normalization factor, A, and the slope parameter, α, are both well constrained from the fit. Furthermore, the normalization factor, A, for the BL Lac sample is found to be a factor ~ 2.4 times larger than that of the FSRQ sample.

BL Lacs are found to have a steeper LF than FSRQs and this broadly agrees with the results obtained from *Fermi*-LAT observations, in which the faint-end slope index parameters

*see `https://emcee.readthedocs.io/en/stable/` for full documentation, accessed on 13/03/2021.

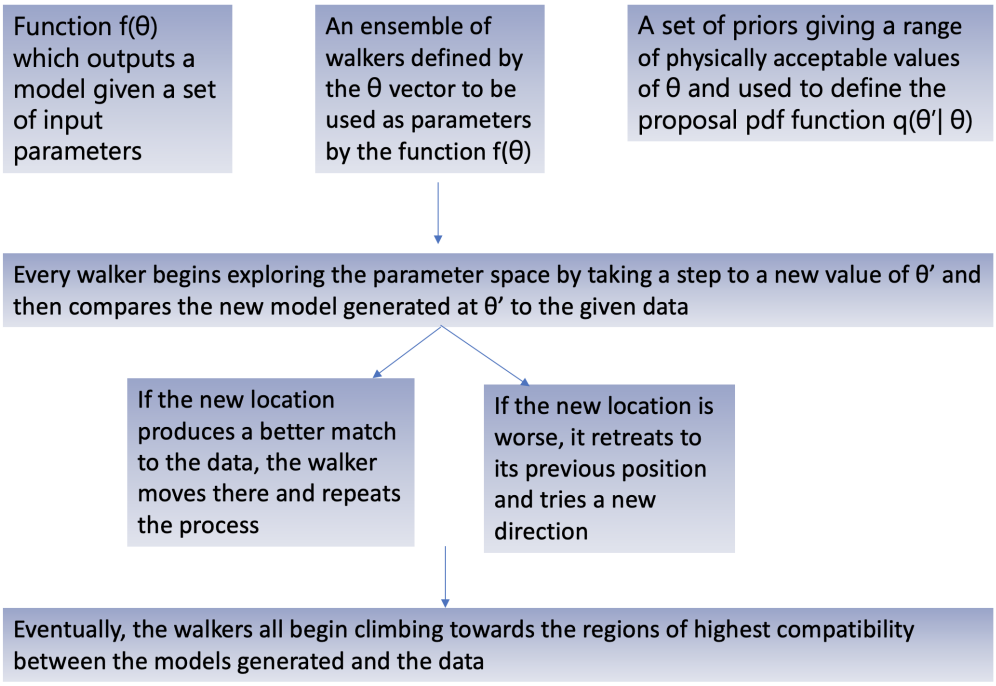

Figure 5.24: A flowchart of the steps involved in a typical MCMC algorithm.

Table 5.4: The parameters, A, α and k, are obtained from the MCMC fit of a simple power law LF (see equation 5.19) to the source count distributions for BL Lacs and FSRQs expected to be detected in 20 hour observations with CTA S at an energy threshold of 100 GeV. The mean and dispersion parameters, μ and σ, are obtained from fitting a Gaussian (see equation 5.12) to the photon index distribution of both samples. The uncertainties represent the 68 % containment regions around the median value.

Class	A [$\mathrm{Mpc^{-3}erg^{-1}s}$]	α	k	μ	σ
BL Lacs	$(0.23 \pm 0.02) \times 10^{-10}$	$2.49^{+0.06}_{-0.06}$	$4.22^{+3.90}_{-3.58}$	1.90 ± 0.02	0.16 ± 0.03
FSRQs	$(0.97 \pm 0.03) \times 10^{-11}$	$0.91^{+0.09}_{-0.07}$	$0.76^{+6.16}_{-6.60}$	2.34 ± 0.01	0.08 ± 0.01

under the PLE models were found to be $\gamma_1 = 1.26^{+0.08}_{-0.20}$ for BL Lacs (Ajello et al. (2014)) and $\gamma_1 = 0.29^{+0.53}_{-0.53}$ for FSRQs (Ajello et al. (2012)) respectively. Such comparisons should be made with extreme caution due to the inherent differences in the samples and energy regimes considered in the investigations; the Ajello et al. (2014) study is based on the first *Fermi*-LAT catalog (1LAC; Abdo et al. (2010b)) and considers the energy range 100 MeV - 100 GeV.

The evolutionary parameter, k, is poorly constrained for both the BL Lac and FSRQ samples. The evolution in both cases is found to be positive ($k > 0$), albeit with large

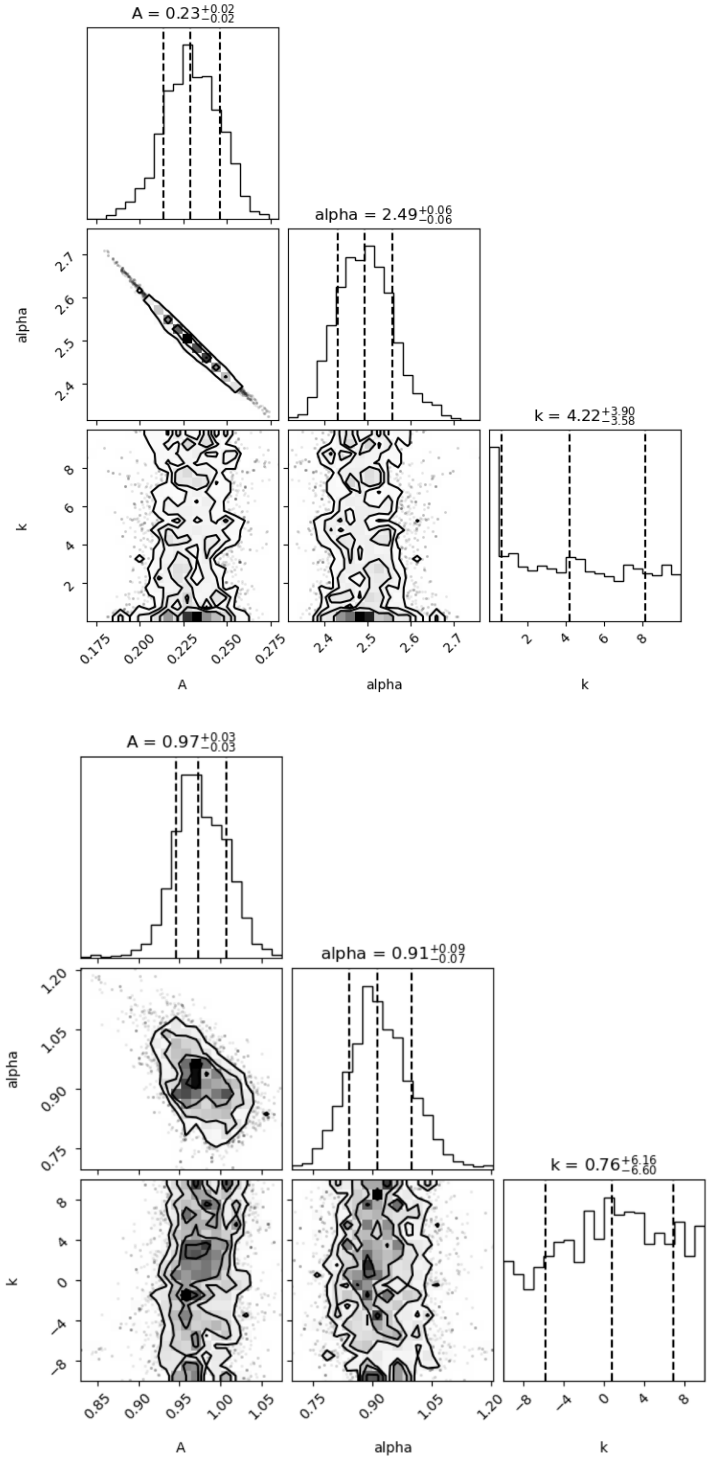

Figure 5.25: A corner plot summarising the results obtained from applying the MCMC algorithm to the BL Lac (top) and FSRQ (bottom) samples. The parameter A is in units of $\mathrm{Mpc}^{-3}\mathrm{erg}^{-1}\mathrm{s}$ and has been scaled by a factor of 10^{10} and 10^{11} for the BL Lac and FSRQ samples respectively.

uncertainties, indicating more sources at higher redshift than at lower redshift. The estimate of k can be improved by increasing the number of steps in the MCMC, currently set at 1000 steps after a 400 step burn-in, or having separate iterations for k after having constrained both A and α.

FSRQs have been found to evolve positively over a range of wavelengths including radio observations (for example Dunlop and Peacock (1990)), X-ray investigations (for example Padovani et al. (2007)) and with the *Fermi*-LAT, for example in Ajello et al. (2012) where the evolutionary factor was found to be $k = 5.70 \pm 1.02$ under the PLE model. The results from previous investigations into the evolutionary properties of BL Lacs are mixed. For example, a study of the radio LF by Marchã and Caccianiga (2013) found evidence for weak positive evolution at a confidence level of 2 - 3 σ.

The *Fermi*-LAT study by Ajello et al. (2014) found the evolutionary factor to be $k = 4.87^{+0.78}_{-5.39}$ under the PLE model and observed a dependence of the speed of evolution on luminosity. High-luminosity sources ($L \geq 10^{47}$ erg s^{-1}) were found to evolve faster than low-luminosity sources ($L \leq 10^{45.5}$ erg s^{-1}) with the latter found to evolve negatively ($k < 0$) indicating more sources at lower redshift than at higher redshift. The negative evolution was established to be predominantly driven by the population of High-synchrotron-peaked (HSP) blazars, a sub-class of BL Lacs having synchrotron-peak frequency $\nu^s_{\rm peak} > 10^{15}$Hz. Negative evolution has also been reported in a separate *Fermi*-LAT investigation by Zeng et al. (2014) where the evolutionary factor was found to be $k = -1.85^{+0.38}_{-0.37}$ under the PLE model.

Figure 5.26 presents a comparison between the observed source count distributions and the count distributions predicted from the best fit LFs (see equation 5.21). In order to examine whether the parameters obtained from the MCMC provide a reasonable description of the results of the simulations, I compute the reduced chi-squared statistic, χ^2_ν. The value of the reduced chi-squared statistic was found to be $\chi^2_\nu = 1.35$ and $\chi^2_\nu = 0.54$ for the BL Lac and FSRQ samples respectively, and are within the 3σ confidence limit of χ^2_ν for the corresponding degrees of freedom (Hughes and Hase (2010)), meaning the null hypothesis cannot be rejected in either case.

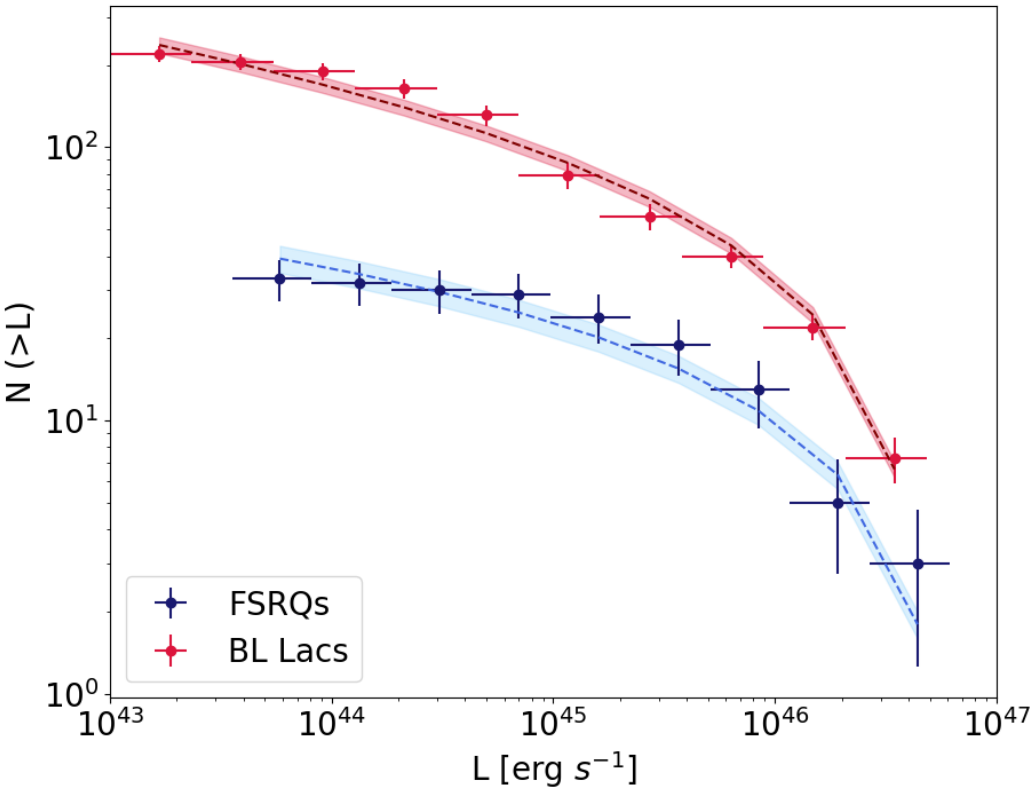

Figure 5.26: The data points correspond to the source count distribution as a function of luminosity for BL Lacs and FSRQs expected to be detectable in 20 hour observations with CTA S above an energy threshold of 100 GeV. The uncertainties correspond to the 1σ Poisson error. The shaded region in both cases represent the predicted distribution from the best fit LFs.

Figure 5.27 shows a comparison between the photon index distributions of both samples and the predicted distributions obtained from the Gaussian model (see equation 5.12). The spectral index distribution of the BL Lac sample, $\mu = 1.90 \pm 0.02$, is found to be, on average, flatter and incompatible with that of FSRQs, $\mu = 2.34 \pm 0.01$. It was not possible to investigate the dependence of μ on luminosity due to lack of statistics.

The local (z=0) LF for BL Lacs and FSRQs obtained from the best fit parameters is shown in Figure 5.28. As expected from their steeper LF and, in general, lower luminosity regime, BL Lac sources are seen to dominate the local LF at low luminosities. The large uncertainties prevent any further conclusions being drawn at this stage. Nevertheless, the

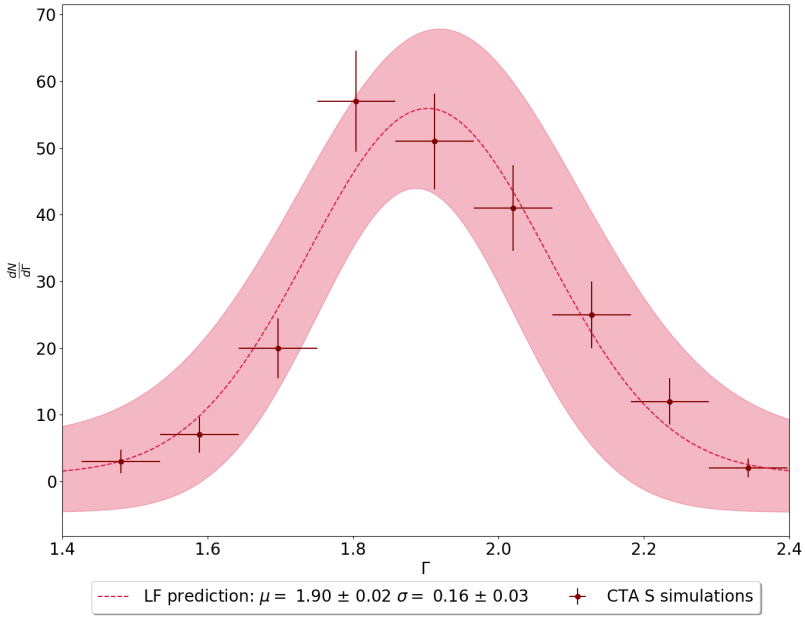

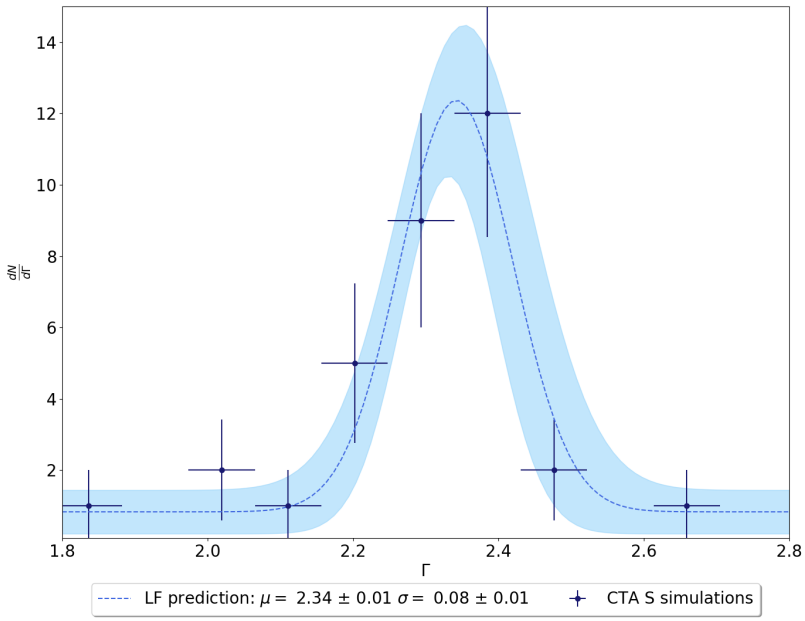

Figure 5.27: The data points correspond to the photon index distributions of the BL Lac (top) and FSRQ (bottom) samples expected to be detectable in 20 hour observations with CTA S above an energy threshold of 100 GeV. The uncertainties correspond to the 1σ Poisson error. The shaded region in both cases represents the predicted distribution from the best fit LFs.

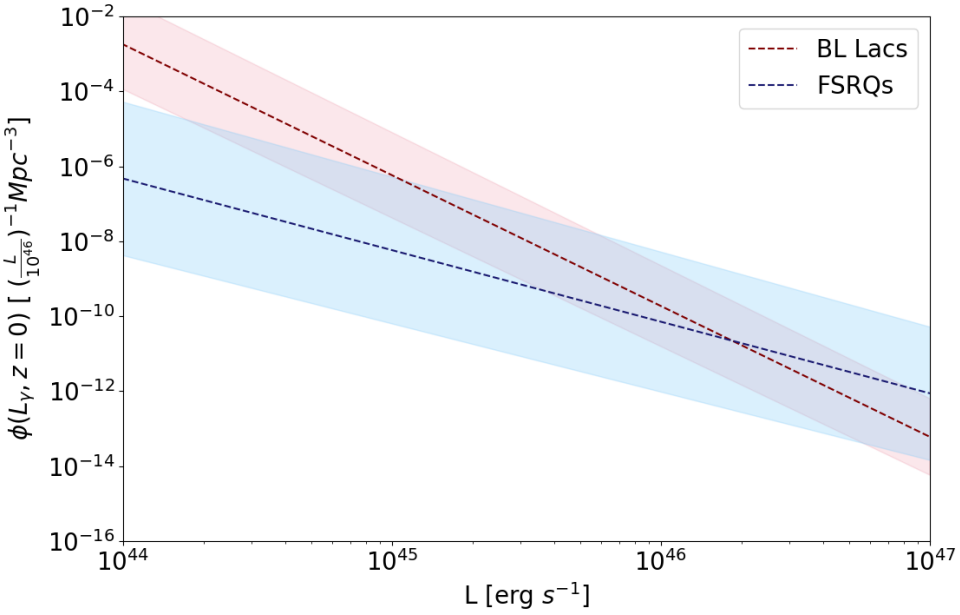

Figure 5.28: The local (z=0) LF derived from the best fit MCMC parameters using a simple power law model for the BL Lacs and FSRQ sample. The shaded regions correspond to the 68 % confidence intervals obtained from the MCMC samples.

results obtained in this preliminary investigation, put together, suggests that the LFs of BL Lacs and FSRQs should be calculated separately in order to then compute their respective contributions to the IGRB, as also indicated in a study of *EGRET* detected blazars by Dermer (2007).

5.5.4 Biases and Systematic Uncertainties

The LF derived in this work is a preliminary result and includes a number of biases and uncertainties which need to be taken into account before a more detailed study can be undertaken. For example, the sample used in the derivation consists of all *Fermi*-LAT detected blazars of known redshift expected to be detectable with CTA S in 20 hours of observation. While the results already represent a significant improvement (a factor of ~ 4) on current IACT detections, the CTA is also expected to detect sources not detected with the *Fermi*-LAT, as well as objects having redshifts yet to be determined, and these cannot be included in the simulations.

It is also essential to investigate the consequences of the Malmquist bias, an effect leading to the preferential detection of intrinsically brighter objects to greater distances. This selection bias affects flux-limited surveys, with AGN sources which are more luminous being detectable to higher redshifts, resulting in a trend of increase in luminosity with redshift as seen for my sample in Figure 5.23.

Not accounting for the Malmquist bias has led to a few mistaken claims in extragalactic astronomy. For example, Hawkins (1962) found evidence for a non-linear redshift-distance relationship and de Vaucouleurs (1972) suggested the increase in the Hubble constant with distance. The conclusions were later found to be a consequence of a distance-dependent selection effect (Sandage and Tammann (1975), Teerikorpi (1975)).

In order to account for the Malmquist bias, a detailed study of the sky coverage of the CTA is required, similar to that conducted for a sample of *Fermi*-LAT detected blazars in Abdo et al. (2010c). As seen in Marshall et al. (1983), the expected source count distribution given in Equation 5.21 will also contain an additional term representing the sky coverage of the survey, $\Omega(L, z, \Gamma)$, quantifying the probability of detecting in the survey a typical blazar having luminosity L and photon index Γ at a redshift z.

As discussed previously, I have so far assumed the sky coverage of the survey to be uniformly 1. I now discuss a simple back-of-the-envelope calculation of how the sky coverage can be approximated using the results of my simulations. For simplicity, I only consider the dependence of the sky coverage on luminosity and redshift. Assuming an uniform survey, the sky coverage, $\Omega(L, z)$, can be expressed as

$$\Omega(L, z) = \Omega_0 p_{\rm det}(L, z) \tag{5.22}$$

where $p_{\rm det}(L, z)$ is the probability of detecting a blazar having luminosity L at a redshift z and Ω_0 is the total solid angle covered by the survey, with $\Omega_0 = 4\pi$ for an all-sky survey. For the special case of an ideal flux limited survey, the sky coverage can be modelled as a

step function:

$$\Omega(L,z) = \Omega_0 \begin{cases} 1 & F(L,z) \geq F_{\rm limit}, \\ 0 & F(L,z) < F_{\rm limit}, \end{cases} \tag{5.23}$$

where $F_{\rm limit}$ is the flux limit of the survey, estimated from the distribution of the VHE flux against the photon indices, shown in Figure 5.29.

Assuming, for simplicity, the minimum flux of the sample represents the flux limit of the survey, the sky coverage of the survey can be obtained and is shown in Figure 5.30. Also shown on the same plot, for comparison, is the distribution of VHE luminosity against redshift for the sample of BL Lacs and FSRQs expected to be detectable in 20 hour observations with CTA S above an energy threshold of 100 GeV. Figure 5.30 implies that sources having luminosity, L $\geq 10^{46}$ erg s^{-1}, could potentially still be detected with the CTA at redshifts z > 1.5.

A detailed measurement of the sky coverage of the CTA will allow for a reliable estimate of the LF. Any potential Malmquist bias in the local (z=0) LF can be accounted for by weighting the contribution of each point to the LF by $V_{\rm max}$, the largest volume containing an object having the same luminosity as a source in the sample while still being able to detect it (Schmidt and Green (1983)):

$$V_{\rm max} = \int_{z_{\rm min}}^{z_{\rm max}} \Omega(L,z) \frac{e(z,L)}{e(z_{\rm min},L)} \frac{dV}{dz} dz \tag{5.24}$$

where $e(z,L)$ is the evolutionary parameter defined in Equation 5.20, $z_{\rm min}$ the redshift to which the LF is de-evolved ($z_{\rm min}$ = 0 in this case), $z_{\rm max}$ the farthest redshift to which the source can be detected in the survey and $\frac{dV}{dz}$ the co-moving volume element per unit redshift and unit solid angle (Hogg (1999)).

My estimate of the flux sensitivity and sky coverage of the CTA can be used to make a first order determination of $z_{\rm max}$ and is shown in Figure 5.31. As expected, the farthest redshift to which a source is visible in the survey increases with increase in the intrinsic luminosity

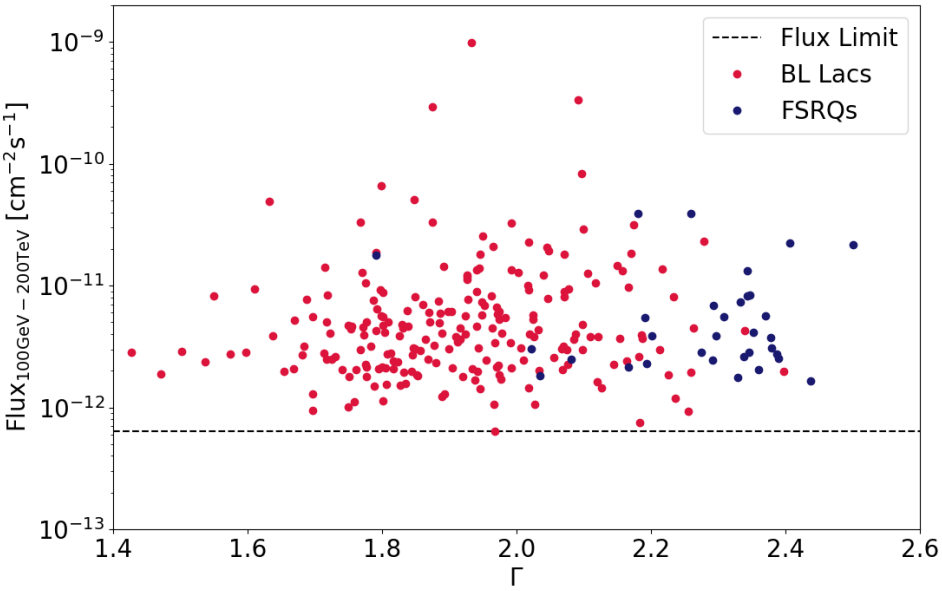

Figure 5.29: The distribution of photon flux in the energy range 100 GeV - 200 TeV as a function of photon index, Γ, for BL Lacs and FSRQs expected to be detectable in 20 hour observations with CTA S above an energy threshold of 100 GeV. The dashed line indicates the minimum flux detected and is assumed to represent the flux limit of the survey.

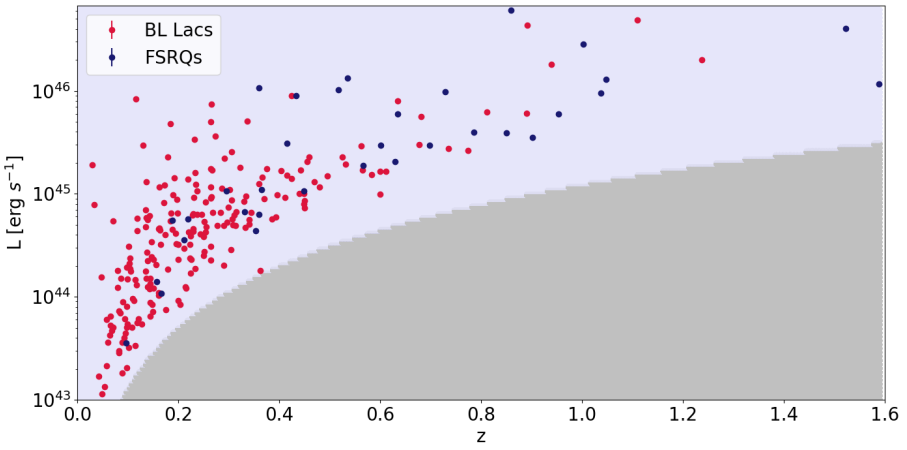

Figure 5.30: An estimate of the sky coverage, $\Omega(L, z, \Gamma)$, with the lavender region corresponding to $\Omega = \Omega_0$ and the grey region corresponding to $\Omega = 0$. Also shown, for comparison, is the VHE luminosity versus redshift distribution for the sample of BL Lacs and FSRQs expected to be detectable in 20 hour observations with CTA S above an energy threshold of 100 GeV.

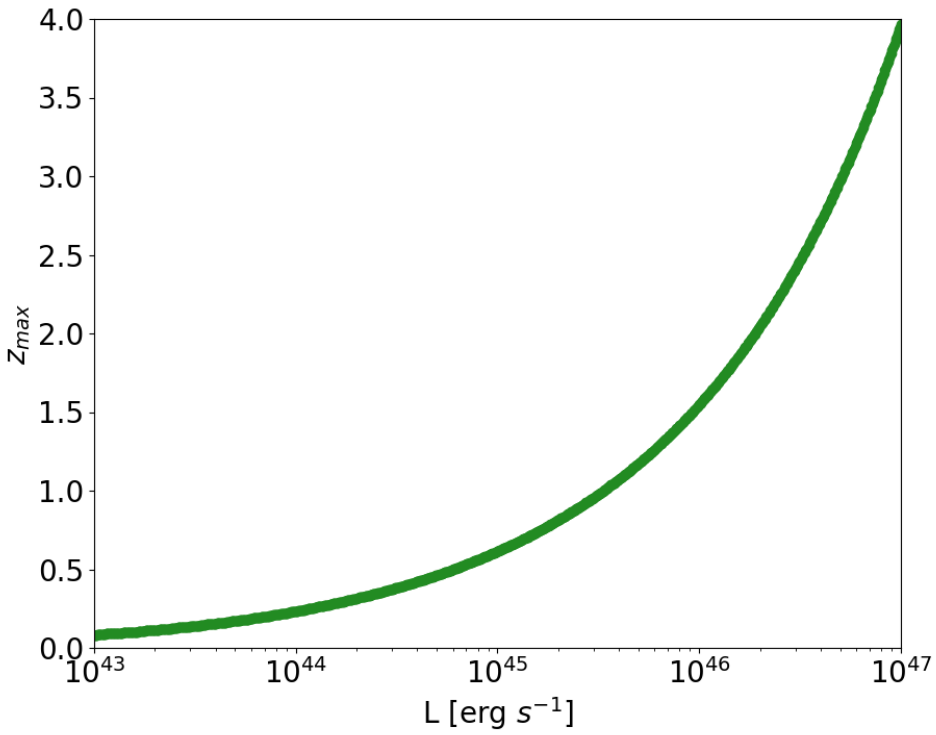

Figure 5.31: The farthest redshift, $z_{\rm max}$, to which a source having luminosity, L, can be detected in the survey as a function of luminosity. This was estimated assuming an ideal flux limited survey in which the minimum flux of the detected sample represents the flux limit of the survey.

of the source. Based on this measurement, the LF shown in Figure 5.28 can be weighted by $V_{\rm max}$. The weighted LF is shown in Figure 5.32 with sources having high-luminosity given less weight since they can be detected to larger distances.

One of the main scientific motivations for a reliable estimate of the LF in the VHE regime is the potential investigation of the blazar sequence. As discussed in Section 1.4, Fossati et al. (1998) found evidence of an anti-correlation between the synchrotron peak frequencies and the bolometric luminosity of a sample of 126 blazars. This trend may be interpreted as evidence of a genetic link between BL Lacs and FSRQs as suggested by Cavaliere and D'Elia (2002) who argue that the two classes differ in their accretion rates. Under this assumption, BL Lacs represent the final, inefficiently accreting and long-term state formed from a short-lived and gas-rich FSRQ.

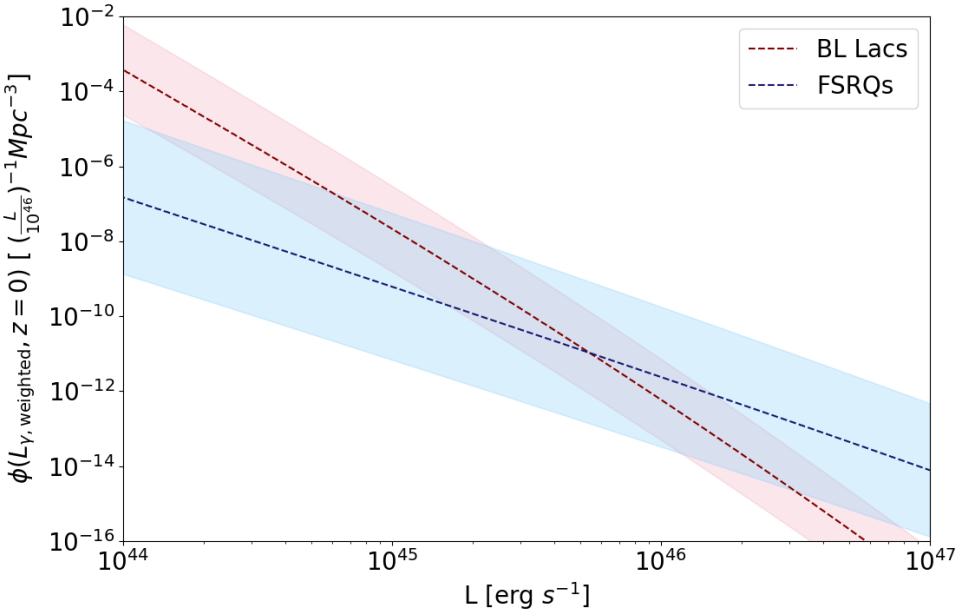

Figure 5.32: The local (z=0) LF derived from the best fit MCMC parameters using a simple power law model for the BL Lacs and FSRQ sample weighted by V_{max}. The shaded regions correspond to the 68 % confidence intervals obtained from the MCMC samples.

This can be investigated using an estimate of the LF. For example, Ajello et al. (2014) find evidence for an increase in the space density of the BL Lac population at roughly the same epoch at which the space density of FSRQs drop off, confirming the theory of a transition from FSRQs to BL Lacs. Unfortunately, the large uncertainties associated with my estimate of the LF prevent such strong conclusions being drawn at this stage.

However, it should be noted that the volume weighted LF in Figure 5.32 shows the LF for the BL Lac population to be, within errors, incompatible with that of FSRQ population at L $\sim 10^{47}$ erg s^{-1}. A more robust calculation of the sky coverage of the CTA, in conjunction with a better estimate of the mass of the SMBH and potential beaming effects would help to further investigate the possibility of a transition.

As discussed in Section 5.2.2, given the lack of a-priori knowledge of the most appropriate functional form for extrapolating the *Fermi*-LAT spectra to the VHE regime, I use a bracketing approach and consider both the power law and log parabolic schemes. Furthermore, the extrapolations will also have an associated uncertainty. This can be quantified as a prob-

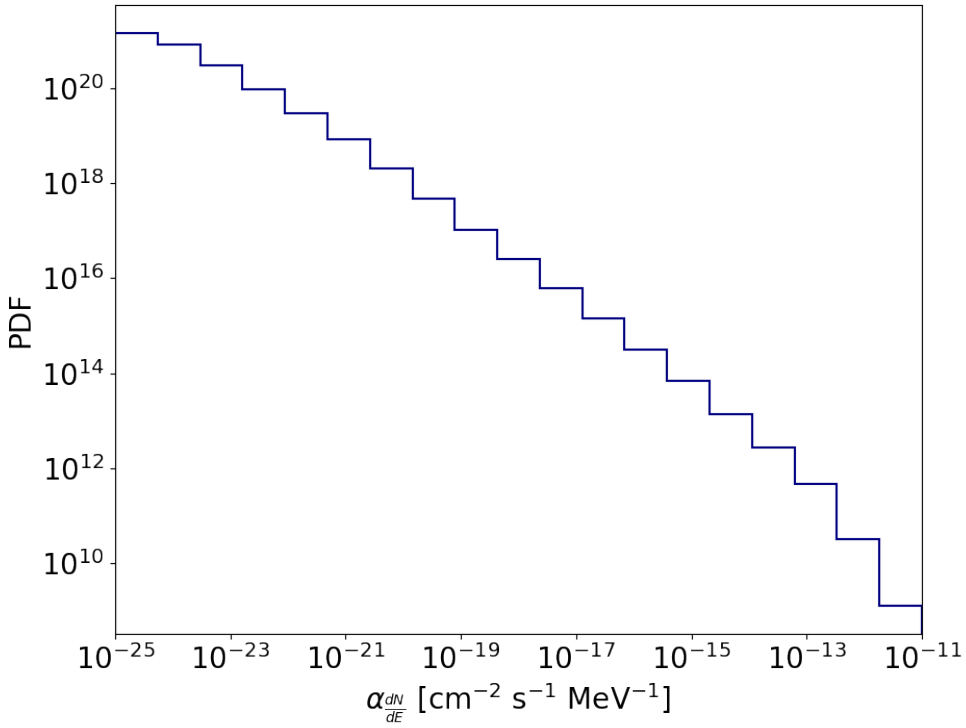

Figure 5.33: A PDF quantifying the uncertainty in the source spectrum, $\alpha_{\frac{dN}{dE}}$, introduced by the choice of extrapolation schemes in this investigation. This determination assumes a range of priors on the level of EBL attenuation corresponding to the limits provided in the Domínguez et al. (2011) model.

ability density function (PDF) and is shown in Figure 5.33. This determination assumes a range of priors on the level of EBL attenuation corresponding to the limits provided in the Domínguez et al. (2011) model.

The results presented do not, as yet, account for the systematic uncertainties arising from discrepancies between the Monte Carlo simulations and the true instrument response of the CTA. A standard approach towards accounting for systematic uncertainties involves the use of bracketing IRFs in which the source parameters are computed while a particular response (for example the effective area) is varied by a certain percentage. A detailed performance evaluation of the CTA instrument response facilitating the use of bracketing IRFs is currently under production.

Finally, it should be noted that the calculation of the LF conducted in this study, in particular

the limits of the integrals in Equation 5.21, correspond specifically to those spanned by the sample investigated. This is particularly important in the case of the redshift distribution of the sample, with the redshift regimes considered being $z \in [0, 1.2]$ and $z \in [0, 1.6]$ for the BL Lac and FSRQ sample respectively.

This is expected to have implications on the results obtained given that many quantities involved, for example the evolutionary factor $e(z, L)$, are functions of redshift. For example, the choice of low redshift regime prevents an investigation into the presence of a potential redshift cut-off in the comoving density. In a study of the radio LF, Dunlop and Peacock (1990) found their FSRQ sample to evolve positively up to a redshift cut-off, followed by a gradual drop-off by a factor of ~ 5 in the interval $z \in [2, 4]$.

The *Fermi*-LAT study by Ajello et al. (2014) found a redshift cut-off in the LF for the BL Lac sample at $z \sim 1.5$, predominantly driven by the populations of LSPs and ISPs. A luminosity dependence in the redshift cut-off, for instance more luminous source peaking at earlier times (for example Ajello et al. (2012)), would suggest an LDDE model for the LF rather than PDE and PLE models, and has also been observed in radio-quiet AGN (for example Ueda et al. (2003)).

5.6 Conclusion

This chapter describes a detailed investigation of the extragalactic source populations expected to be detectable with the CTA when in operation using a sample of 1551 *Fermi*-LAT detected AGN having known spectroscopic redshift measurements. The spectral parameters reported in the 4FGL catalog are extrapolated to the energy range 30 GeV - 200 TeV using both a power law and a log parabolic extrapolation scheme. In both cases, the EBL absorption is taken into account using the opacities stated in the Domínguez et al. (2011) model.

The results are obtained using the *ctools* analysis software package for 5 and 20 hour observations with the both northern and southern arrays. The six energy thresholds considered are 30 GeV, 50 GeV, 100 GeV, 300 GeV, 500 GeV and 1 TeV, and the upper energy limit

of the simulated events in all cases is fixed at 200 TeV. A likelihood analysis is applied to obtain the detection significance, VHE flux limit and the best fit spectral parameters for each source.

The results highlight the impact of the CTA in not only increasing the number of sources detected when compared to current generation IACTs, but also in allowing for a detailed study of many of these sources spanning more than four decades in energy. Over 250 blazars are expected to be detected with the CTA in 20 hours of observation at an energy threshold of 100 GeV. While BL Lacs form the majority of the expected sources, with over 200 detections, the CTA is also expected to detect over 30 FSRQs. For comparison, only 8 FSRQs have been detected in the VHE regime at the time of writing *.

Moreover, the CTA is expected increase the number of observed sources at redshifts higher than 0.5; for example, 18 such sources are predicted to be observable with CTA S in just 5 hours of observation. For comparison, only 4 such sources, namely PKS 1441+25, 3C 279, Ton 599 and B2 0218+357, have been detected with current generation IACTs at the time of writing *. This highlights that the CTA will not only multiply the number of sources detected, but also expand the horizons to which we can observe the gamma-ray sky.

Furthermore, the CTA is expected to detect sources from populations not known to be TeV emitters and enable further studies of the emission mechanisms taking place in these objects. This includes over 20 radio galaxies, the Narrow-Line Seyfert 1 galaxy SBS 0846+513 and the Circinus Galaxy, a radio-quiet Seyfert galaxy detected with the Fermi-LAT at GeV energies but yet to be observed in the VHE regime.

I also present a potential list of promising sources for long-term monitoring. This non-exhaustive sample includes sources from each AGN class. Mkn 421 is expected to be the brightest source observable with the CTA with an expected significance of $757.44 \pm 2.01\ \sigma$ in 5 hours of observation. Further investigation of sub-minute timescales reveals that Mkn 421 is, in principle, expected to be detected at a significance of 5σ in an unprecedented $1.13^{+0.23}_{-0.17}$ seconds.

* `http://tevcat.uchicago.edu/`, accessed on 11/01/21.

It should be noted that the results presented in this chapter are based on the average flux states of each source. Given that blazars are inherently variable sources which often undergo intense flaring episodes, the numbers should be treated as lower limits. This is further illustrated by the fact that the sample used in the derivation consists of all *Fermi*-LAT detected AGN of known redshift and cannot include sources not detected with the *Fermi*-LAT or objects having redshifts yet to be determined.

Nevertheless, the improved statistics already expected with the CTA will help explore a variety of fundamental scientific topics. For example, the high redshift AGN observed will allow for a measurement of the gamma-ray absorption due to the EBL (Abdalla et al. (2021)). Furthermore, the study of AGN in short timescales will not only help draw further conclusions regarding the nature and location of the emission region, but also enable multiple tests for LIV through precise investigations into the energy dependence in the arrival times of high energy photons (Doro et al. (2013)).

The increased number of sources expected to be observable with the CTA will provide a basis for the first ever reliable estimate of the LF in the VHE regime. This is an important step in investigating source populations within the context of the AGN unification theory, as well as answering a number of fundamental scientific questions such as measuring the contribution of unresolved blazars to the diffuse isotropic gamma-ray background.

A preliminary investigation towards this is undertaken in this chapter using a sample of 220 BL Lac and 34 FSRQ sources forecast to be observable with CTA S at an energy threshold of 100 GeV in 20 hours of observation. The best fit parameters to a simple power law model describing the LF are obtained after applying the MCMC technique to the predicted source count distributions for the sample.

BL Lac sources are seen to dominate the LF for $L \leq 10^{45}$ erg s^{-1} and large uncertainties in the LF prevent any strong conclusions being drawn at higher luminosities. Finally, I discuss some of the challenges that still need to be overcome in order to obtain the final LF such as incompleteness in the sample, biases and accounting for systematic uncertainties.

Chapter 6

Summary and Future work

6.1 Summary

The research presented in this thesis has focused on two main themes:

- localising the gamma-ray emission region in the brightest FSRQs detected with the *Fermi*-LAT, and
- investigating the extragalactic source populations that will be detectable with the CTA, using *Fermi*-LAT observations as a pathfinder.

Chapter 1 begins with a brief historical overview of the discovery of AGN. This is followed by a discussion of the current AGN model including the physical mechanisms underlying

the observations, a description of the different classes of AGN within the context of the AGN unification theory, a summary of the different physical interactions involved in the production and attenuation of gamma-rays in AGN, a discussion on the broad-band SED of AGN and description of the blazar sequence. Finally, I mention some of the current areas of active research in AGN and why they continue to be interesting objects for study.

Chapter 2 introduces the field of space based gamma-ray astronomy starting with a review of some historical telescopes like *Cos B* and *CGRO*, as well as still active experiments like *INTEGRAL* and *AGILE*. From there the discussion focuses solely on the *Fermi*-LAT and includes an overview of the design and methodology, algorithms used in event reconstruction and background rejection, the performance and sensitivity and finally a detailed description of the steps involved in a typical *Fermi*-LAT data analysis.

Chapter 3 presents a temporal and spectral analysis of the gamma-ray emission from a sample of the nine brightest FSRQs observed with the *Fermi*-LAT over the first eight years of operation. Despite being some of the brightest objects in the gamma-ray sky, the close orientation of the jets of FSRQs to our line-of-sight makes it difficult to resolve structures within the jet. Uncovering the location and origin of the emission is therefore an indirect process requiring a variety of different methods.

The two brightest flare periods of each source revealed variability in timescales of a few hours, implying extremely compact emission regions of the order of 10^{13} m for each source. While it should be noted that emission regions within the MT can also be reconciled with the short variability timescales observed, if one assumes that the entire width of the jet is responsible for the emission, the timescales indicate BLR origin.

The flare periods were then studied in more detail to search for the presence of a cut-off in the spectrum which can be interpreted as a consequence of photon-photon pair production within the BLR. An AIC test was undertaken to determine which of a power law and a log parabolic model provided a better fit to the data. I found evidence for spectral cut-off in 7 of the 18 flares investigated, supporting a BLR origin for the emission during these events. No conclusive evidence for a cut-off was found for the other 11 flares.

This was followed by an investigation into the energy dependence in cooling timescales by applying LCCFs to search for correlations between the high energy (1 - 300 GeV) and low energy (0.1 - 1 GeV) flux. 4 flares are found to have a LCCF compatible with a peak at 0, indicating no energy dependence and implying a BLR origin for the emission. A further 6 flares show evidence of a time-lag between the high- and low- energy flux components of the emission which can be interpreted as indicating the presence of multiple emission regions. Among these, 4 flares have a positive time-lag suggesting emission regions within the MT and 2 showed evidence for a negative time-lag. The results from the remaining flares were found to be inconclusive, with the lack of photon statistics preventing the calculation of LCCFs.

The final investigation considered the VHE ($E_\gamma \geq 20$ GeV) photon emission from the sample of FSRQs. A likelihood analysis of all photons in the energy range 20 - 300 GeV over the entire eight year observation period revealed significant emission from all sources at a confidence level of $> 5\sigma$. Monte Carlo simulations were then used to compare the most energetic photon observed with the *Fermi*-LAT for each source to the expected photon energy distribution assuming BLR origin of emission. Only three of the sources, namely, 3C 279, 3C 454.3 and 4C 21.35, are found to have VHE photon emission compatible with the expected BLR Lyman alpha photon interaction suggesting that the VHE emission in the other sources is being produced in emission regions within the MT.

The results of the different investigations, put together, lead to the natural conclusion that a more complex emission model than a simple one-zone leptonic model is required. The apparent contradictions regarding the origin of the gamma-ray emission found in the sample can be reconciled by invoking the presence of multiple simultaneously active emission regions both within the BLR and the MT.

Despite the remarkable success of the *Fermi* mission, an important disadvantage of space based gamma-ray detectors is the smaller effective area leading to a reduced sensitivity at the highest energies, typically above a few hundred GeV. This is also the energy regime in which ground-based telescopes become important in conducting a study of the Cherenkov radiation produced by the VHE photons on entering the Earth's atmosphere.

Chapter 4 introduces the field of ground-based gamma-ray astronomy starting with a description of the underlying physical processes involved in the production and propagation of electromagnetic air showers and how they differ from hadronic air showers. This is followed by an explanation of the physical origin of the Frank-Tamm relation and a review of the current generation IACTs, namely MAGIC, H.E.S.S. and VERITAS.

From there I introduce the CTA, the next generation observatory in ground-based gamma-ray astronomy. This includes a discussion of the proposed layout of both the northern and southern array, the affect of the choice of array geometry on the observations and the ideal spacing between telescopes. Finally, I give an overview of the expected performance and sensitivity and finally summarise the key scientific cases to be investigated with the CTA.

Chapter 5 presents a detailed investigation of the extragalactic source populations expected to be detectable with the CTA using a sample of 1551 *Fermi*-LAT detected AGN having a known redshift measurement. The results are obtained using the *ctools* analysis software package for 5 and 20 hour observations with both the northern and southern arrays. The six energy thresholds considered are 30 GeV, 50 GeV, 100 GeV, 300 GeV, 500 GeV and 1 TeV, and the upper energy limit in all cases is fixed at 200 TeV. A likelihood analysis is applied to obtain the detection significance, VHE flux limit and the best fit spectral parameters for each source.

Over 300 sources are expected to be detected with the CTA in 20 hours of observation at an energy threshold of 100 GeV and a list of promising candidates from each AGN class is presented. The results highlight the impact of the CTA in not only increasing the number of sources detected when compared to current generation IACTs, but also in allowing for a detailed study of many of these sources spanning more than four decades in energy. Moreover, the CTA is expected increase the number of observed sources at redshifts higher than 0.5 thereby expanding the horizons to which we can observe the gamma-ray sky and allowing a range of scientific topics to be explored.

The increased number of sources expected to be observable with the CTA will provide a basis for the first ever reliable estimate of the LF in the VHE regime. This is an important

step in investigating source populations within the context of the AGN unification theory, as well as answering a number of fundamental scientific questions such as measuring the contribution of unresolved blazars to the diffuse isotropic gamma-ray background. A preliminary investigation towards this is undertaken in Chapter 5 using a sample of 220 BL Lac and 34 FSRQ sources forecast to be observable with CTA S at an energy threshold of 100 GeV in 20 hours of observation.

The best fit parameters to a simple power law model describing the LF are obtained after applying the MCMC technique to the predicted source count distributions of the sample. BL Lac sources are seen to dominate the LF for $L \leq 10^{45}$ erg s^{-1} and large uncertainties in the LF prevent any strong conclusions being drawn at higher luminosities. A first order correction is then applied to the local LF by weighing the contribution of each point to the LF by the largest volume over which a source having the same luminosity can still be detected.

Unfortunately, the large uncertainties associated with my estimate of the LF prevent strong conclusions on the blazar sequence being drawn at this stage. Furthermore, the redshift distribution of the sample prevents an investigation into the presence of a potential redshift cut-off in the comoving density. In conclusion, the LF derived in this work is a preliminary result and I conclude with a discussion of the challenges that still need to be overcome in order to obtain the final LF such as incompleteness in the sample, inherent biases and accounting for systematic uncertainties.

6.2 Future work

6.2.1 Revisiting the *Fermi*-LAT FSRQ sample

In Chapter 3, I investigated the location of the gamma-ray emission in FSRQs using a sample of the nine brightest FSRQs detected with the *Fermi*-LAT during its first eight years of operation. Each source was required to have had flaring episodes with averaged

daily fluxes $\geq 10^{-6}$ cm^{-2} s^{-1} within uncertainties of 1σ above 100 MeV as reported in the *Fermi*-LAT list of monitored sources[†] as well as a known redshift measurement.

As seen in Figure 5.2, as many as 688 FSRQs with known redshifts have been detected above a significance of 4σ in the 4FGL catalog (The *Fermi*-LAT collaboration (2019a)). My choice of sample was motivated by the necessity to have sufficient photon statistics in order to allow for a detailed study of the gamma-ray emission. The next five brightest FSRQs which satisfy my selection criteria are 3C 273, 4C 01.02, 4C 55.17, PKS 2326-502 and PKS 0402-362 and comprise a potential list of targets for future investigations.

Five further FSRQs, namely, S3 0218+35, PKS 0736+017, Ton 599, B2 1420+32 and PKS 1441+25 have been detected in the VHE regime[*] with current generation IACTs. However, the detections took place during flare periods and the sources, with the exception of Ton 599 are, on average, not among the twenty brightest FSRQs detected with the *Fermi*-LAT, making them unsuitable for my work. Nevertheless, the increased statistics provided during these detections can be used to constrain the emission region in future investigations.

Moreover, it is important to keep observing recent *Fermi*-LAT data from the sources already investigated in Chapter 3 for further flare periods. Figure 6.1 shows the ten year gamma-ray lightcurve obtained for CTA 102 with the shaded region indicating the two year time span just after the period examined in this thesis.

Towards the end of 2016, CTA 102 underwent an extreme flaring event in which the flux increased by a factor of ~ 50, making it among the brightest sources in the gamma-ray sky. However, a Target of Opportunity investigation of this flare with H.E.S.S. did not reveal significant VHE emission above an energy threshold of 100 GeV (Schüssler et al. (2017)). The methods discussed in this work can be applied to this and other recent flares to allow for even stronger conclusions to be made regarding the nature of the emission regions.

[†] `https://fermi.gsfc.nasa.gov/ssc/data/access/lat/msl_lc/`, accessed on 11/03/2021.
[*] `http://tevcat.uchicago.edu/`, accessed on 11/01/21.

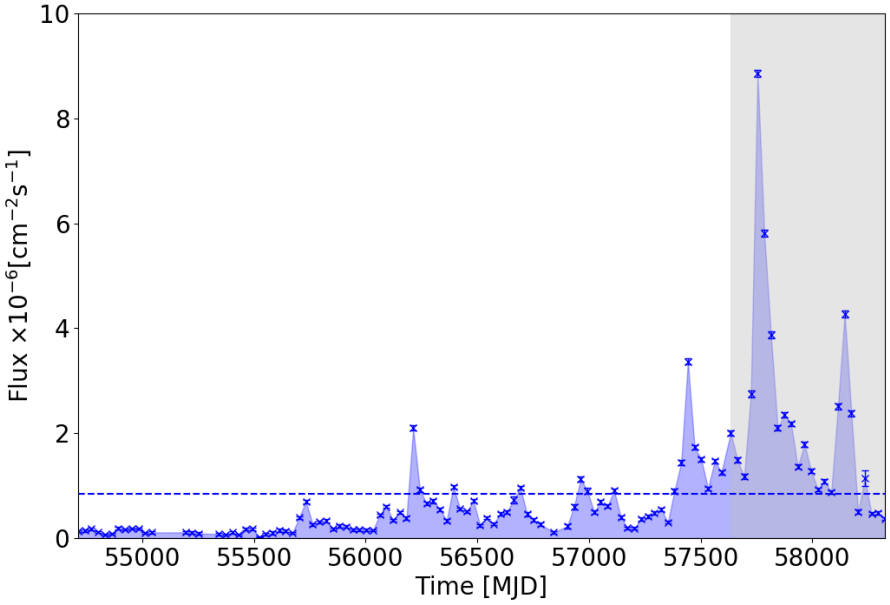

Figure 6.1: The ten year gamma-ray lightcurve for CTA 102 between August 4, 2008 (MJD 54682.66) and August 4, 2018 (MJD 58334.66) binned in monthly periods. The errors are purely statistical and only data points with TS $\geq$ 10 are shown. The horizontal line indicates the average flux of the source during the entire period. The shaded region corresponds to the two year time span just after the period investigated in this thesis.

6.2.2 Localising the VHE emission region in FSRQs with the CTA

Future study of the gamma-ray emission from FSRQs as well as other sources in the VHE regime will be enhanced by the construction of the CTA. As discussed in Chapter 4, the CTA is expected to provide unprecedented insight over a wide energy range of 20 GeV - 300 TeV and improve on the sensitivity of current ground-based telescopes by more than an order of magnitude.

The results of my simulations presented in Section 5.4.2 indicate that 7 of the 9 sources investigated in Chapter 3 should be detectable with the CTA in just 5 hours of observation. The two exceptions are B2 1520+31 and PKS 1502+106, while CTA 102 is found to be a marginal detection with an expected significance of 5.39 $\pm$ 0.96 σ. On the whole, 34 FSRQ sources are expected to be detectable with CTA S in 20 hour observations at an energy threshold of 100 GeV. For comparison, only 8 FSRQs have been detected above

$E_\gamma \geq 100$ GeV at the time of writing*.

The methods described in Chapter 3 can be applied to CTA data to make even stronger conclusions regarding the nature of the emission regions. For example, the increased statistics provided with the CTA will facilitate a detailed measurement of variability timescales in the VHE regime. Furthermore, cross-correlation studies between contemporaneous light-curves obtained with the CTA and the *Fermi*-LAT will help investigate whether the VHE and GeV emission is produced co-spatially.

6.2.3 Next steps in the population study

In Chapter 5, I presented a detailed investigation of the extragalactic source populations expected to be detectable with the CTA using a sample of 1551 *Fermi*-LAT detected AGN having a known redshift measurement. An incremental version of the 4FGL catalog, 4FGL Data Release 2 (4FGL-DR2; Ballet et al. (2020)), was released during the production of the simulations and will be used in future work. Furthermore, the final simulations will be based on the next IRF production which does not assume nominal telescope pointing.

6.2.4 The VHE Luminosity Function

The preliminary investigation of the VHE LF conducted in Section 5.5 can be improved by increasing the number of steps in the MCMC in order to better constrain the evolutionary parameter, k. Furthermore, a detailed study of the sky coverage of the CTA, assumed to be uniformly 1, will allow to investigate the effect of the Malmquist bias. Moreover, a preliminary study of sample selection methods towards determining the LF in the TeV regime using observations with VERITAS is conducted in Brill (2019) and my methods can also be applied to observed source count distributions with current generation IACTS in order to obtain the parameters of the LF.

* `http://tevcat.uchicago.edu/`, accessed on 11/01/21.

Finally, BL Lac objects detected with the *Fermi*-LAT can be classified into the following sub-categories based on the synchrotron-peak frequency, $\nu^s_{\rm peak}$,of the broadband SED (Abdo et al. (2010a)):

- High-synchrotron-peaked blazars (HSPs) if $\nu^s_{\rm peak} > 10^{15}$Hz;
- Intermediate-synchrotron-peaked blazars (ISPs) if 10^{14}Hz $< \nu^s_{\rm peak} < 10^{15}$Hz;
- Low-synchrotron-peaked blazars (LSPs) if $\nu^s_{\rm peak} < 10^{14}$Hz.

Using the catalog of 3HSP sources listed in Chang et al. (2019) [†], the sample of BL Lacs expected to be detected with CTA S at an energy threshold of 100 GeV in 20 hours of observation can be further subdivided into 141 HSPs and 79 ISPs and LSPs having the redshift distributions shown in Figure 6.2. Obtaining an unbiased estimate of the LF for each sub-sample of BL Lacs will help investigate the evolution of each population, especially within the context of the blazar sequence (Padovani (2007)).

6.2.5 Final Remarks

The future of gamma-ray astronomy promises to be exciting with the construction of the CTA. This will be accompanied by extensive multi-wavelength studies including simultaneous optical and radio observations, analysis of *Fermi*-LAT data, Target of Opportunity observations in the X-ray regime and, more recently, advancements in multi-messenger investigations of neutrinos and gravitational waves. While there still remain many open questions, it is hoped that recent advancements in instrumentation will facilitate an enhanced understanding of the underlying physics and provide the opportunity to obtain answers over the coming years.

[†] obtained from `https://www.ssdc.asi.it/3hsp`, accessed on 25/02/2021.

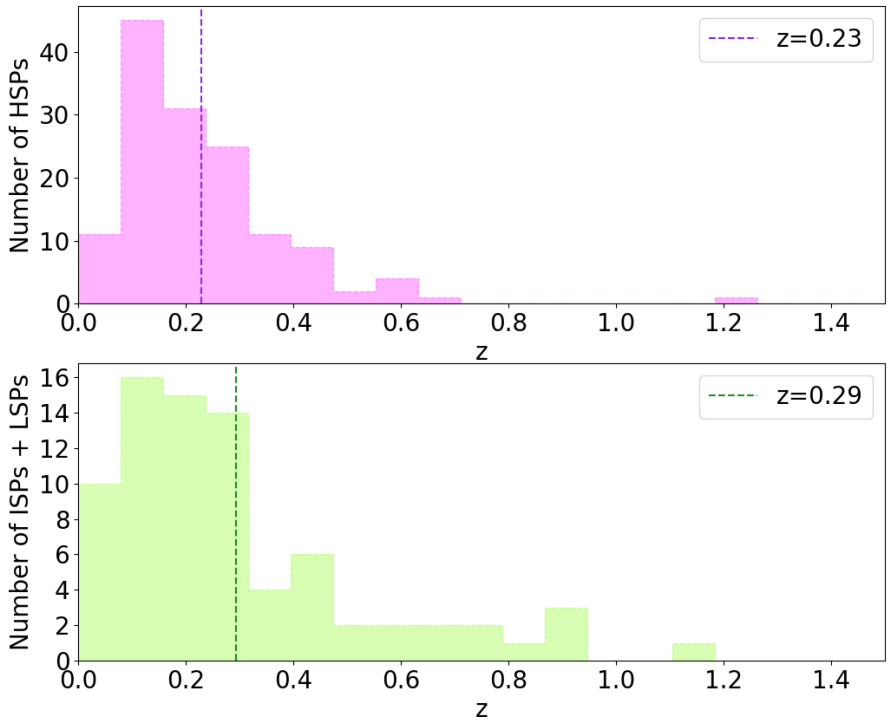

Figure 6.2: The redshift distribution of HSPs (top) and ISPs + LSPs (bottom) expected to be detected with CTA S at an energy threshold of 100 GeV in 20 hours of observation. The vertical lines represent the mean redshift of each sample, shown in legend.

Appendix A

Lightcurves during flares

Figures A.1 plots the $0.1 \leq E_\gamma \leq 300$ GeV lightcurves of each flare from all sources in 3 hour time bins. The error bars are purely statistical. Only data points with TS ≥ 10 are shown. The insets show zoomed in sections of the lightcurves containing the data points used to calculate the intrinsic timescales (shown in legend).

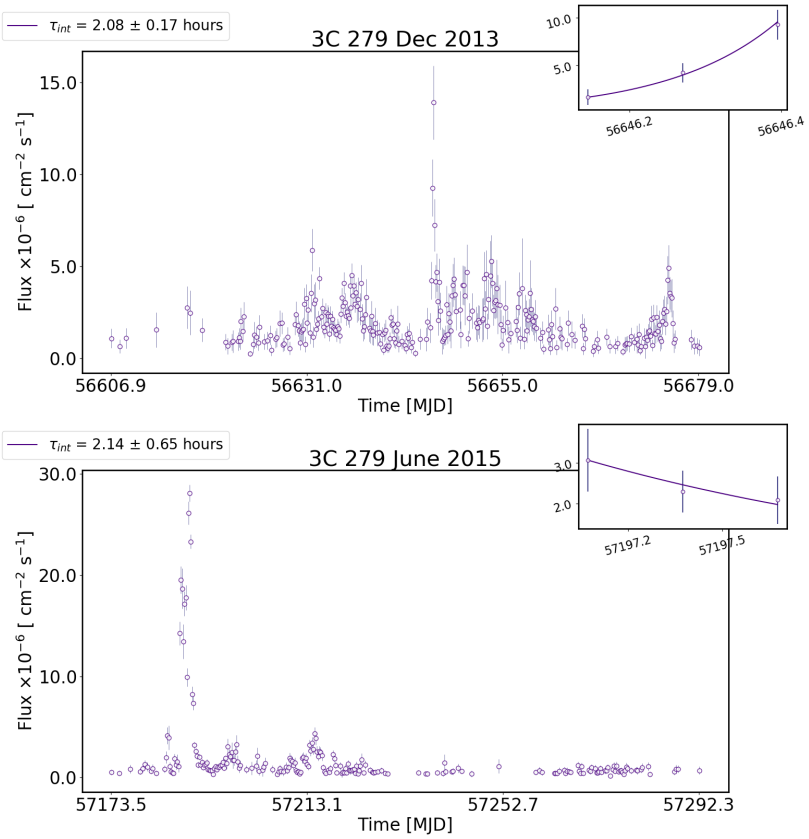

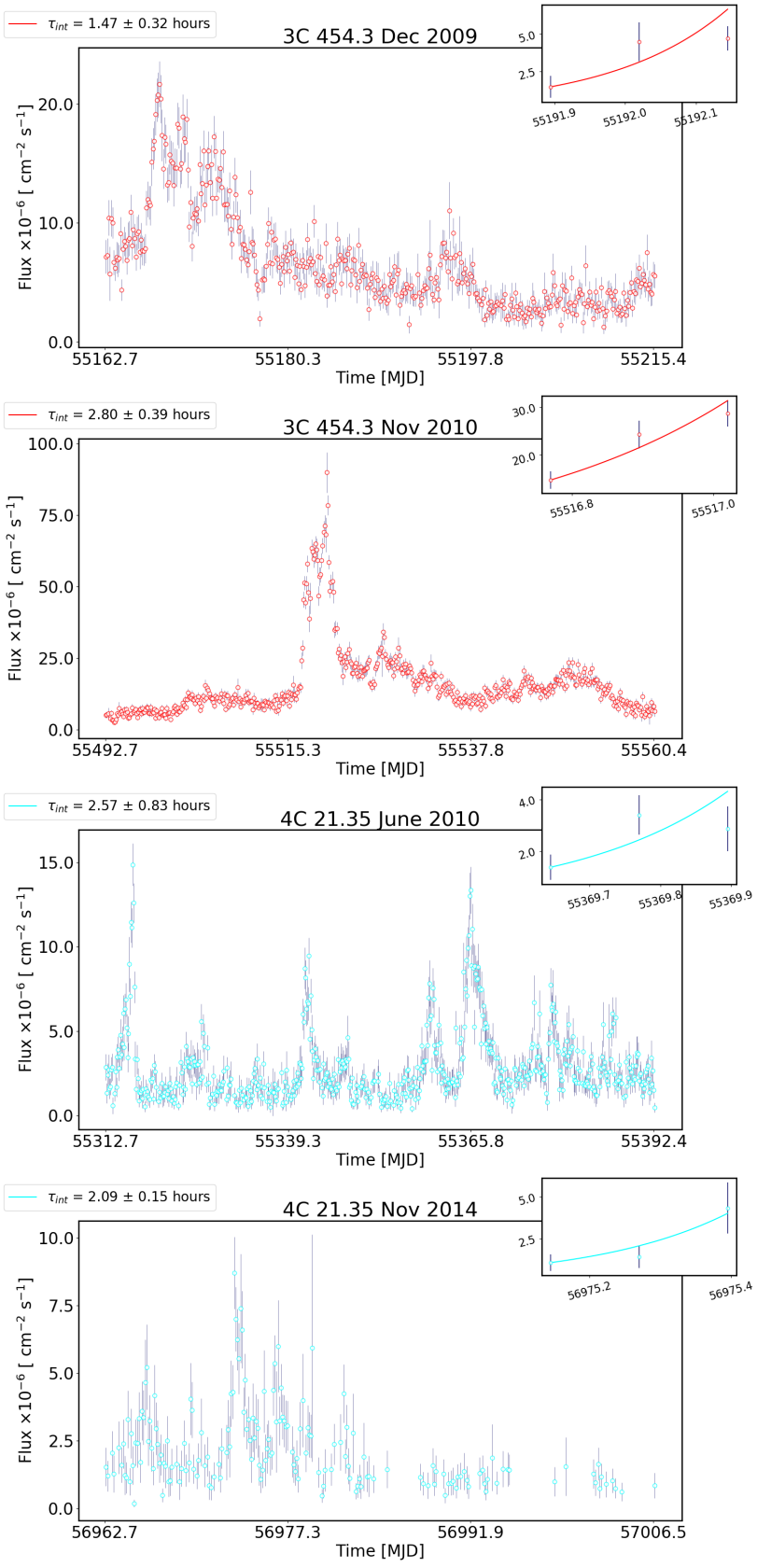
τint = 1.47 ± 0.32 hours
3C 454.3 Dec 2009
Flux ×10⁻⁶ [cm⁻² s⁻¹]
Time [MJD]
τint = 2.80 ± 0.39 hours
3C 454.3 Nov 2010
τint = 2.57 ± 0.83 hours
4C 21.35 June 2010
τint = 2.09 ± 0.15 hours
4C 21.35 Nov 2014

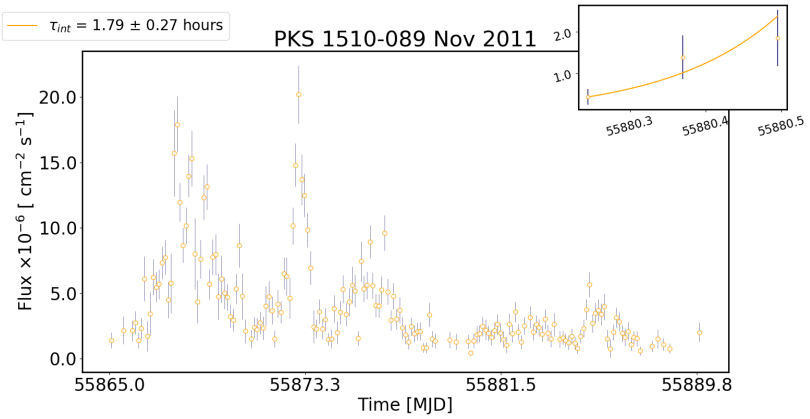
τ_{int} = 1.79 ± 0.27 hours
PKS 1510-089 Nov 2011
Flux ×10^{-6} [cm^{-2} s^{-1}]
Time [MJD]
55865.0
55873.3
55881.5
55889.8
55880.3
55880.4
55880.5

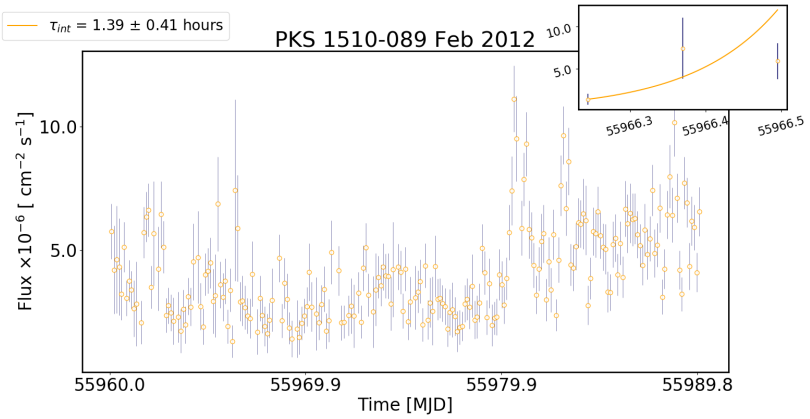
τ_{int} = 1.39 ± 0.41 hours
PKS 1510-089 Feb 2012
Flux ×10^{-6} [cm^{-2} s^{-1}]
Time [MJD]
55960.0
55969.9
55979.9
55989.8
55966.3
55966.4
55966.5

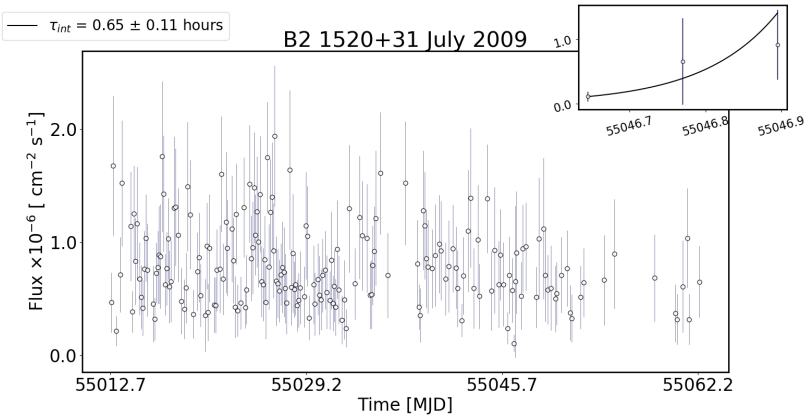
τ_{int} = 0.65 ± 0.11 hours
B2 1520+31 July 2009
Flux ×10^{-6} [cm^{-2} s^{-1}]
Time [MJD]
55012.7
55029.2
55045.7
55062.2
55046.7
55046.8
55046.9

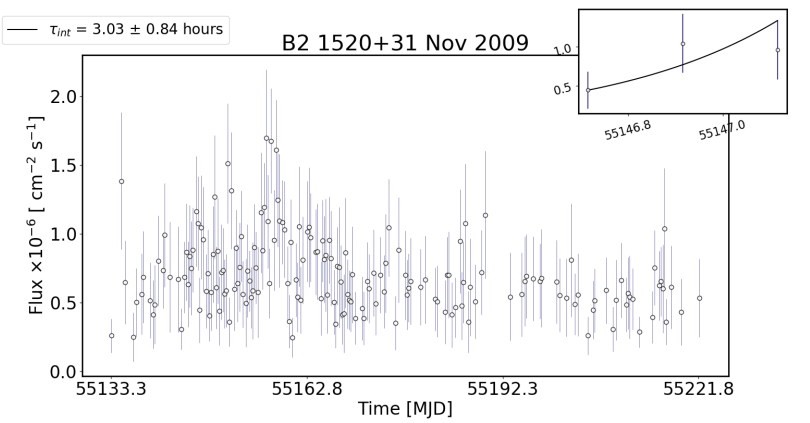
τ_{int} = 3.03 ± 0.84 hours
B2 1520+31 Nov 2009
Flux ×10^{-6} [cm^{-2} s^{-1}]
Time [MJD]
55133.3
55162.8
55192.3
55221.8
55146.8
55147.0

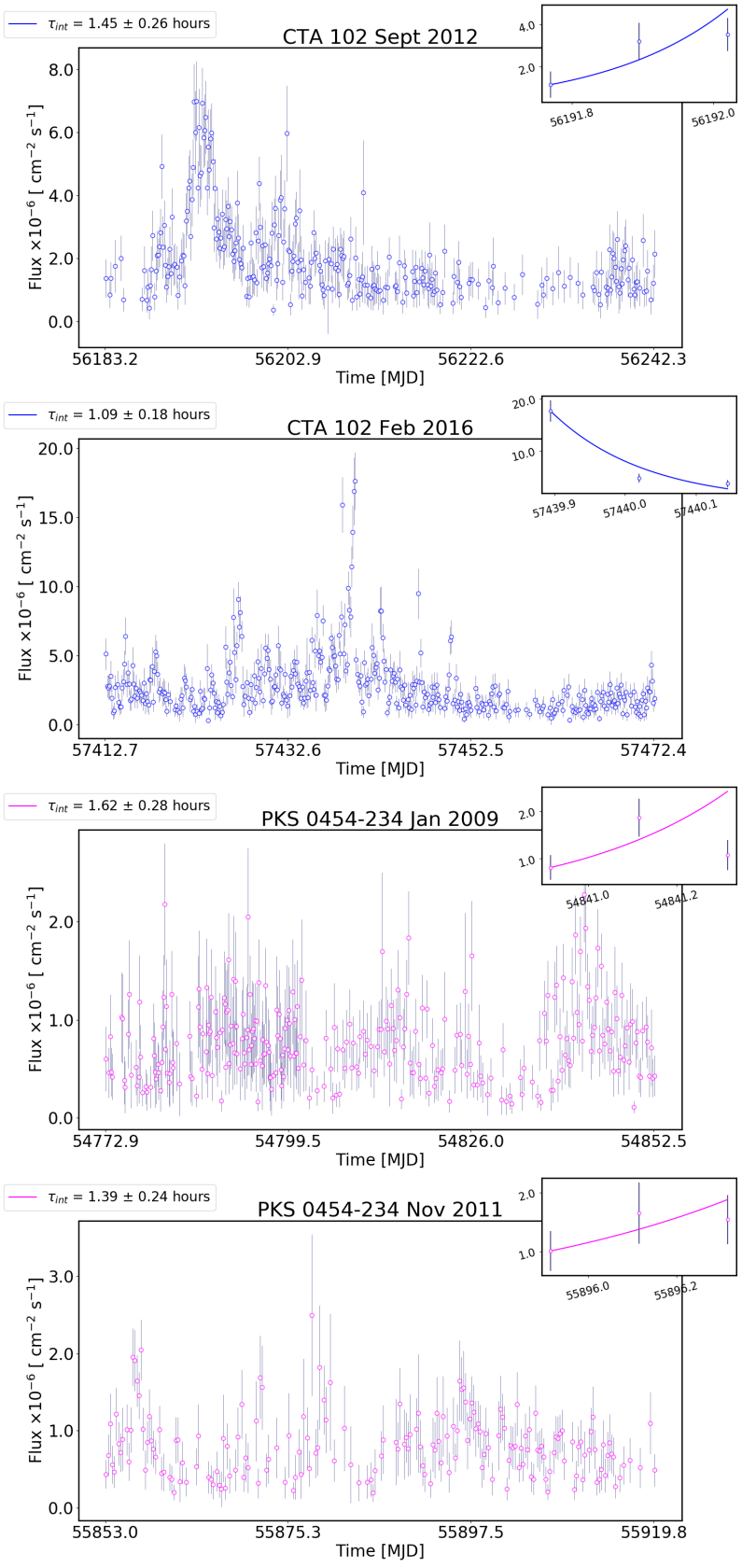
τint = 1.45 ± 0.26 hours
CTA 102 Sept 2012
Flux ×10⁻⁶ [cm⁻² s⁻¹]
Time [MJD]
τint = 1.09 ± 0.18 hours
CTA 102 Feb 2016
τint = 1.62 ± 0.28 hours
PKS 0454-234 Jan 2009
τint = 1.39 ± 0.24 hours
PKS 0454-234 Nov 2011

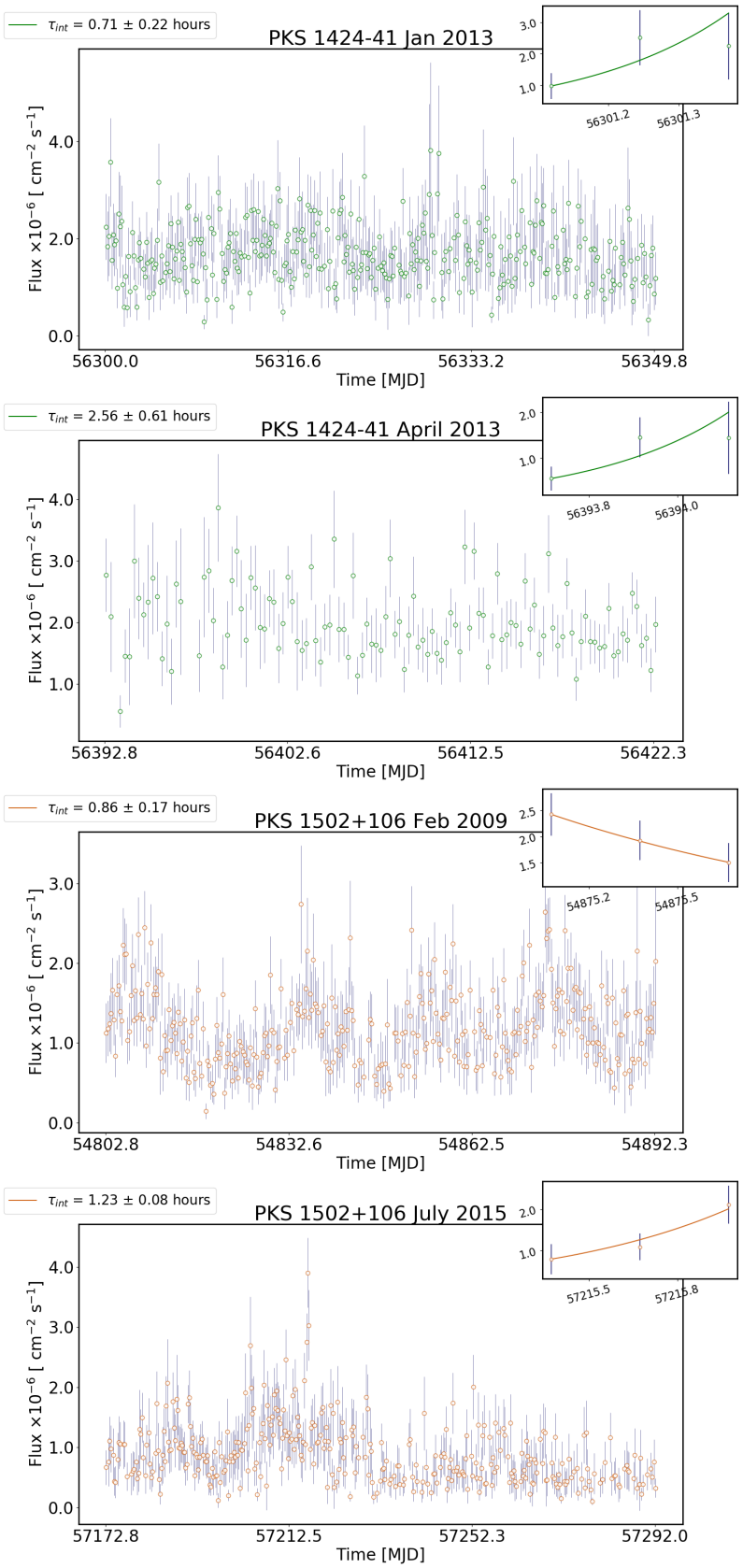

Figure A.1: Evolution of flux in 3 hr bins during each flare period considered.

APPENDIX **B**

Energy dependent Lightcurves during flares

Figures B.1 plots the energy separated lightcurves of each flare from all sources in 6 hour time bins. The low energy flux ($0.1 \leq E_\gamma \leq 1$ GeV) is plotted as blue circles (top panel) and the high energy flux ($1 \leq E_\gamma \leq 300$ GeV) is plotted using red circles (bottom panel). To aid visual comparison, the individual flux values have been divided by the mean flux in the corresponding energy ranges for each flare. The error bars are purely statistical. Only data points with TS ≥ 10 are shown.

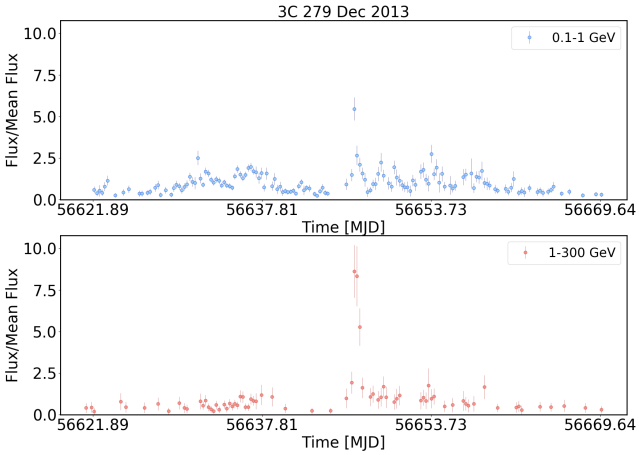
3C 279 Dec 2013
0.1-1 GeV
Flux/Mean Flux
10.0
7.5
5.0
2.5
0.0
56621.89
56637.81
56653.73
56669.64
Time [MJD]
1-300 GeV
Flux/Mean Flux
10.0
7.5
5.0
2.5
0.0
56621.89
56637.81
56653.73
56669.64
Time [MJD]

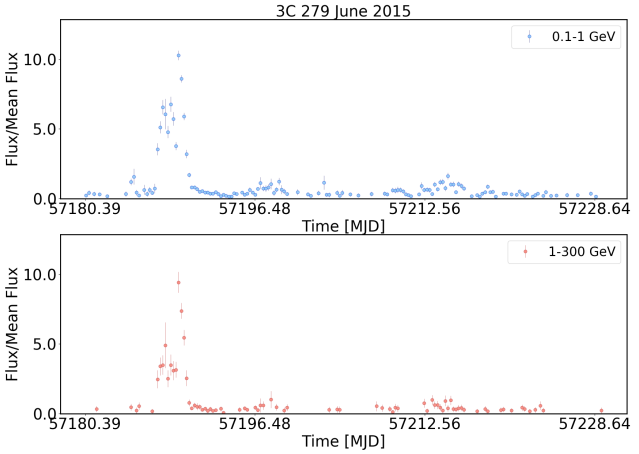
3C 279 June 2015
0.1-1 GeV
Flux/Mean Flux
10.0
5.0
0.0
57180.39
57196.48
57212.56
57228.64
Time [MJD]
1-300 GeV
Flux/Mean Flux
10.0
5.0
0.0
57180.39
57196.48
57212.56
57228.64
Time [MJD]

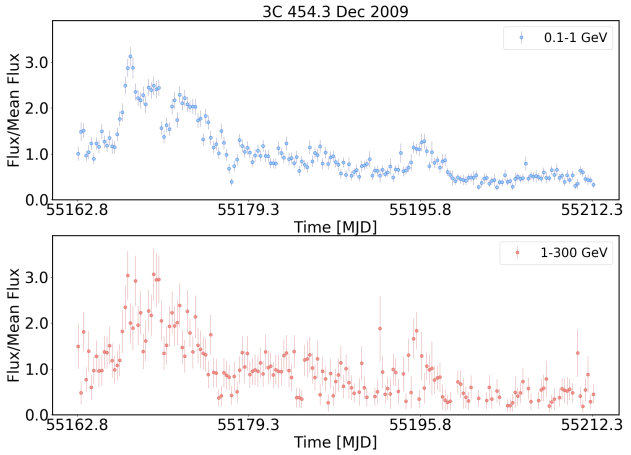
3C 454.3 Dec 2009
0.1-1 GeV
Flux/Mean Flux
3.0
2.0
1.0
0.0
55162.8
55179.3
55195.8
55212.3
Time [MJD]
1-300 GeV
Flux/Mean Flux
3.0
2.0
1.0
0.0
55162.8
55179.3
55195.8
55212.3
Time [MJD]

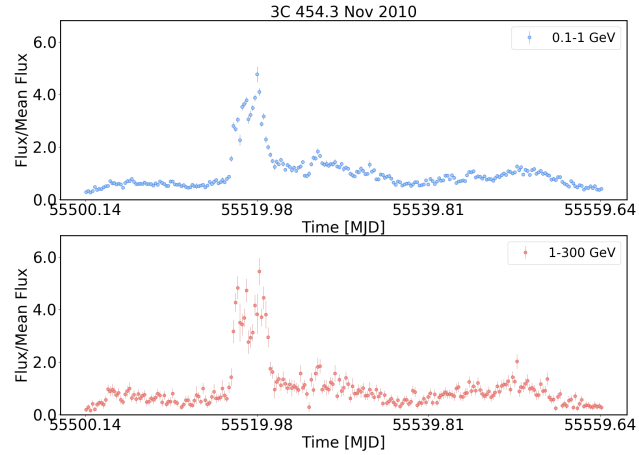
3C 454.3 Nov 2010
0.1-1 GeV
Flux/Mean Flux
6.0
4.0
2.0
0.0
55500.14
55519.98
55539.81
55559.64
Time [MJD]
1-300 GeV
Flux/Mean Flux
6.0
4.0
2.0
0.0
55500.14
55519.98
55539.81
55559.64
Time [MJD]

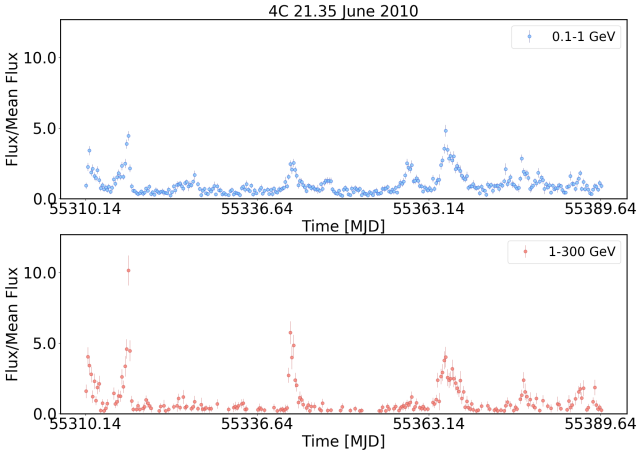
4C 21.35 June 2010
0.1-1 GeV
Flux/Mean Flux
10.0
5.0
0.0
55310.14
55336.64
55363.14
55389.64
Time [MJD]
1-300 GeV
Flux/Mean Flux
10.0
5.0
0.0
55310.14
55336.64
55363.14
55389.64
Time [MJD]

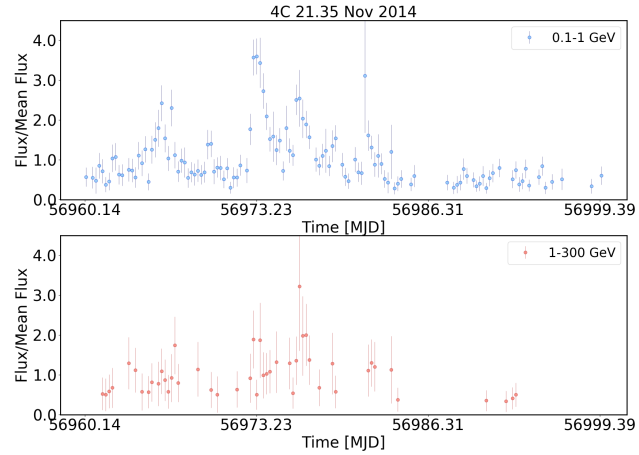
4C 21.35 Nov 2014
0.1-1 GeV
Flux/Mean Flux
4.0
3.0
2.0
1.0
0.0
56960.14
56973.23
56986.31
56999.39
Time [MJD]
1-300 GeV
Flux/Mean Flux
4.0
3.0
2.0
1.0
0.0
56960.14
56973.23
56986.31
56999.39
Time [MJD]

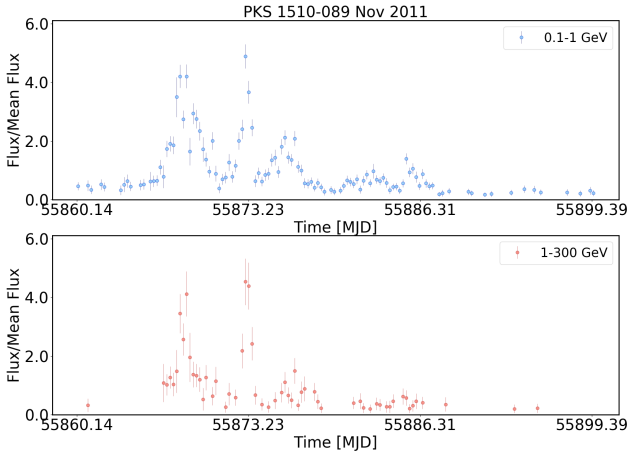
PKS 1510-089 Nov 2011
0.1-1 GeV
Flux/Mean Flux
6.0
4.0
2.0
0.0
55860.14
55873.23
55886.31
55899.39
Time [MJD]
1-300 GeV
Flux/Mean Flux
6.0
4.0
2.0
0.0
55860.14
55873.23
55886.31
55899.39
Time [MJD]

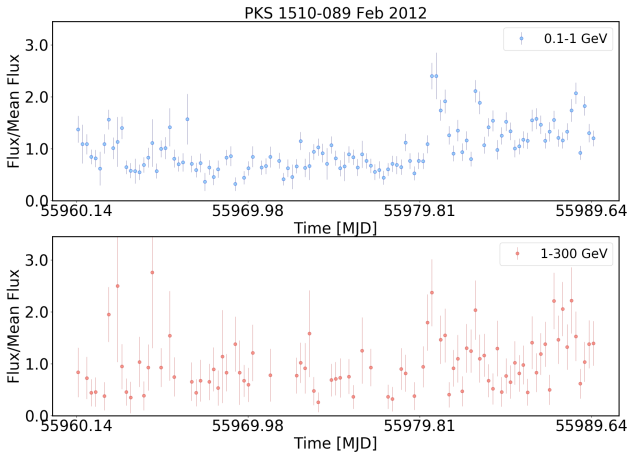
PKS 1510-089 Feb 2012
0.1-1 GeV
Flux/Mean Flux
3.0
2.0
1.0
0.0
55960.14
55969.98
55979.81
55989.64
Time [MJD]
1-300 GeV
Flux/Mean Flux
3.0
2.0
1.0
0.0
55960.14
55969.98
55979.81
55989.64
Time [MJD]

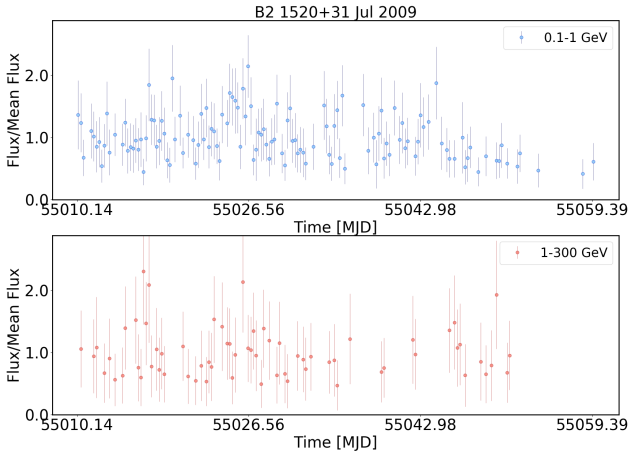
B2 1520+31 Jul 2009
0.1-1 GeV
Flux/Mean Flux
2.0
1.0
0.0
55010.14
55026.56
55042.98
55059.39
Time [MJD]
1-300 GeV
Flux/Mean Flux
2.0
1.0
0.0
55010.14
55026.56
55042.98
55059.39
Time [MJD]

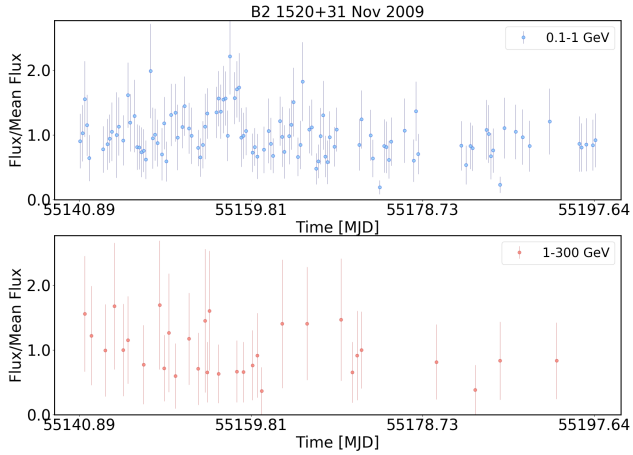
B2 1520+31 Nov 2009
0.1-1 GeV
Flux/Mean Flux
0.0
1.0
2.0
55140.89
55159.81
55178.73
55197.64
Time [MJD]
1-300 GeV
Flux/Mean Flux
0.0
1.0
2.0
55140.89
55159.81
55178.73
55197.64
Time [MJD]

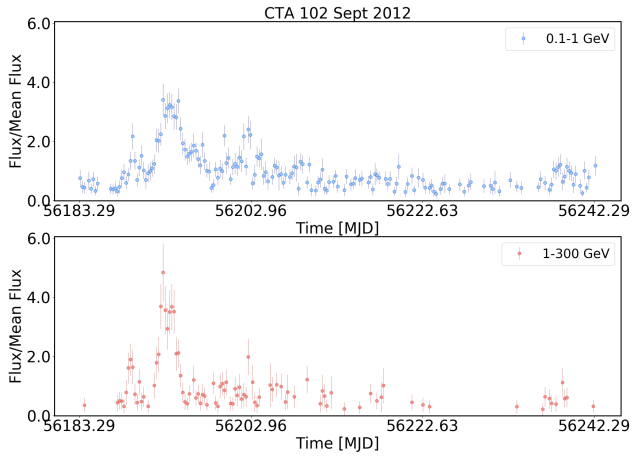
CTA 102 Sept 2012
0.1-1 GeV
Flux/Mean Flux
0.0
2.0
4.0
6.0
56183.29
56202.96
56222.63
56242.29
Time [MJD]
1-300 GeV
Flux/Mean Flux
0.0
2.0
4.0
6.0
56183.29
56202.96
56222.63
56242.29
Time [MJD]

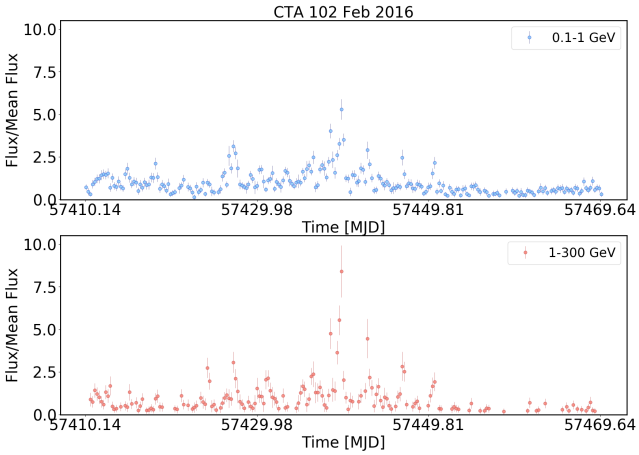
CTA 102 Feb 2016
0.1-1 GeV
Flux/Mean Flux
0.0
2.5
5.0
7.5
10.0
57410.14
57429.98
57449.81
57469.64
Time [MJD]
1-300 GeV
Flux/Mean Flux
0.0
2.5
5.0
7.5
10.0
57410.14
57429.98
57449.81
57469.64
Time [MJD]

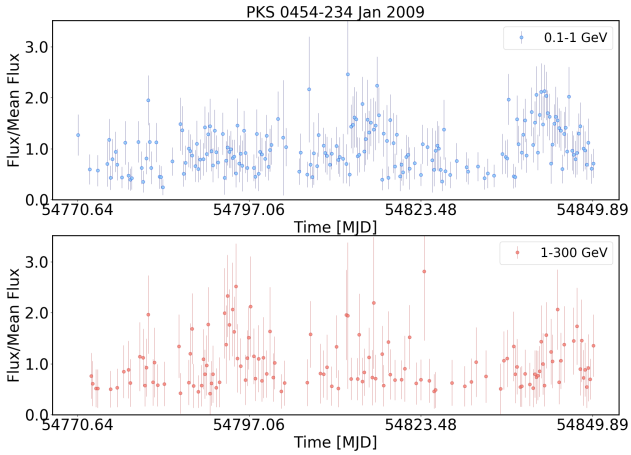
PKS 0454-234 Jan 2009
0.1-1 GeV
Flux/Mean Flux
0.0
1.0
2.0
3.0
54770.64
54797.06
54823.48
54849.89
Time [MJD]
1-300 GeV
Flux/Mean Flux
0.0
1.0
2.0
3.0
54770.64
54797.06
54823.48
54849.89
Time [MJD]

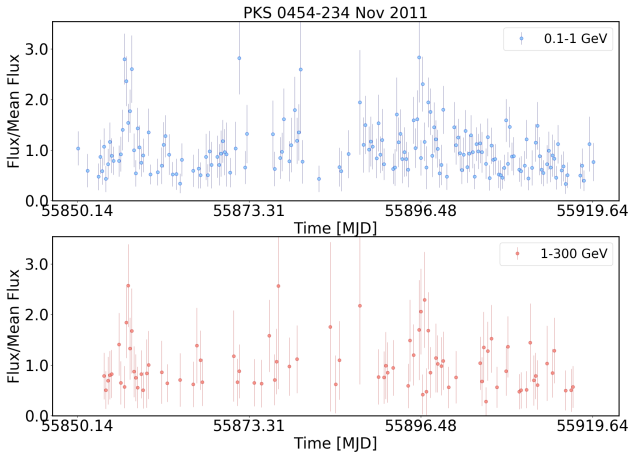
PKS 0454-234 Nov 2011
0.1-1 GeV
Flux/Mean Flux
0.0
1.0
2.0
3.0
55850.14
55873.31
55896.48
55919.64
Time [MJD]
1-300 GeV
Flux/Mean Flux
0.0
1.0
2.0
3.0
55850.14
55873.31
55896.48
55919.64
Time [MJD]

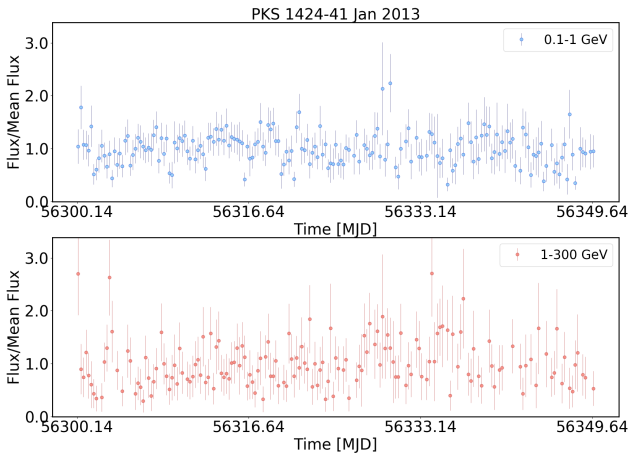
PKS 1424-41 Jan 2013
0.1-1 GeV
Flux/Mean Flux
0.0
1.0
2.0
3.0
56300.14
56316.64
56333.14
56349.64
Time [MJD]
1-300 GeV
Flux/Mean Flux
0.0
1.0
2.0
3.0
56300.14
56316.64
56333.14
56349.64
Time [MJD]

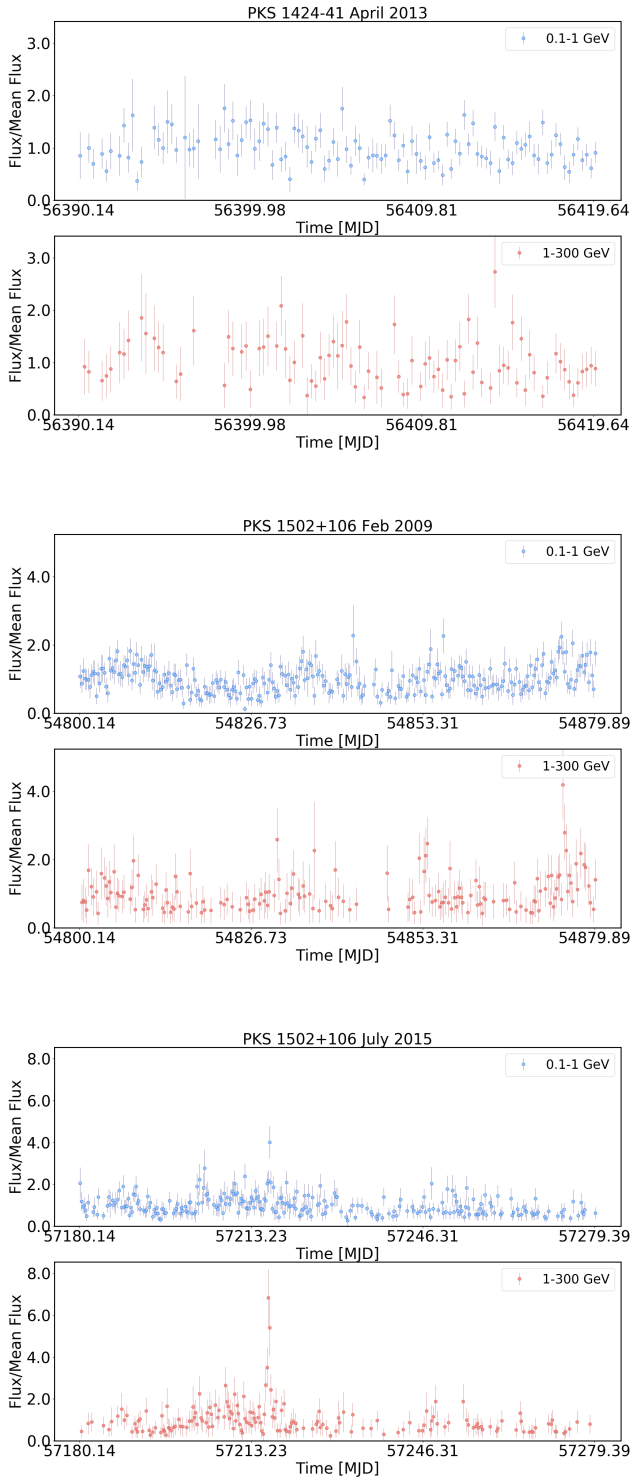

Figure B.1: Evolution of high- and low-energy flux in 6 hr bins during each flare periods considered.

Appendix C

The Hillas parameters

Typically, an electromagnetic air shower in the field of view of the telescope results in a camera image in the form of an ellipse which is then parameterised to extract essential information about the air shower and also distinguish gamma-ray showers from the cosmic ray background. Parameterisation is done using the approach proposed by Hillas (1985) which defines the image as a function of second moments obtained from fitting the image with an ellipse.

The first order moments are defined as the co-ordinates of the center of the ellipse:

$$\langle x \rangle = \frac{\sum_i I_i x_i}{\sum_i I_i}, \langle y \rangle = \frac{\sum_i I_i y_i}{\sum_i I_i}, \tag{C.1}$$

where I_i is the post calibration pixel intensity of each pixel i having co-ordinates x_i and y_i. The second moments are then given by:

$$\langle x^2 \rangle = \frac{\sum_i I_i x_i^2}{\sum_i I_i}, \langle y^2 \rangle = \frac{\sum_i I_i y_i^2}{\sum_i I_i}, \langle xy \rangle = \frac{\sum_i I_i x_i y_i}{\sum_i I_i}, \tag{C.2}$$

and used to calculate the variance and co-variance of each parameter:

$$\sigma_x^2 = \langle x^2 \rangle - \langle x \rangle^2, \sigma_y^2 = \langle y^2 \rangle - \langle y \rangle^2, \sigma_{xy} = \langle xy \rangle - \langle x \rangle \langle y \rangle. \tag{C.3}$$

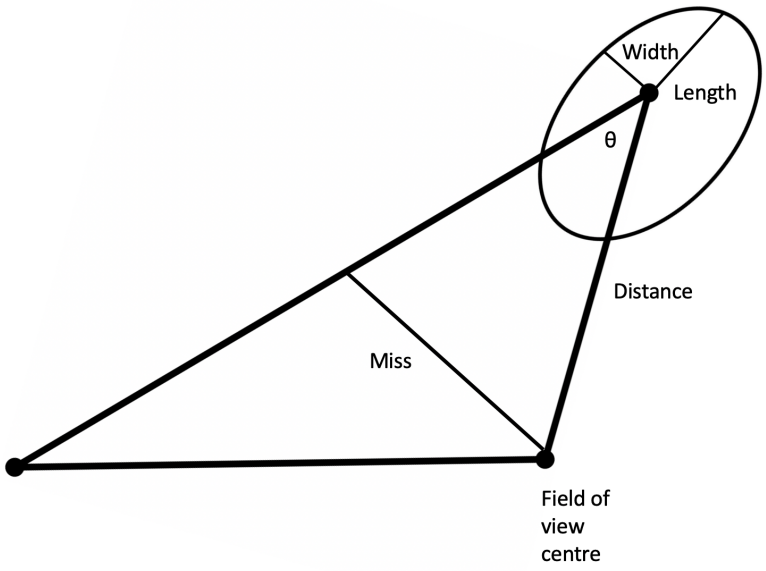

Figure C.1: Illustration of the Hillas parameters of a shower image modelled as an ellipse.

Furthermore, after defining the following:

$$d = \sigma_x^2 - \sigma_y^2, z = \sqrt{d^2 + 4\sigma_{xy}^2}, u = 1 + \frac{d}{z}, v = 2 - u, \tag{C.4}$$

one can derive the Hillas parameters illustrated in Figure C.1 and namely:

- Width, W, and length, L, of the ellipse showing the lateral and vertical development of the air shower respectively:

$$W = \sqrt{\frac{\sigma_x^2 + \sigma_y^2 + z}{2}}, L = \sqrt{\frac{\sigma_x^2 + \sigma_y^2 - z}{2}}. \tag{C.5}$$

- Distance between the centre of gravity of the image and the centre of the field of view, D, which is used to determine the distance between the core impact point of the air shower and the telescope:

$$D = \sqrt{\langle x \rangle^2 + \langle y \rangle^2}. \tag{C.6}$$

- Size of the image, S, which can be correlated to the energy of the primary air shower:

$$S = \sum_i I_i. \tag{C.7}$$

- Miss, M, defined as the perpendicular distance between the major axis of the image and the centre of the field of view and used to calculate the orientation of the shower:

$$M = \sqrt{\frac{1}{3}(u\langle x\rangle^2 + v\langle y\rangle^2) - \frac{2\sigma_{xy}\langle x\rangle\langle y\rangle}{z}}. \tag{C.8}$$

- Angle, θ, between the major axis of the image and the distance parameter, D, specifying the direction of the shower:

$$\alpha = \arcsin\left(\frac{M}{D}\right). \tag{C.9}$$

Bibliography

M. G. Aartsen, M. Ackermann, J. Adams, J. A. Aguilar, M. Ahlers, M. Ahrens, D. Altmann, T. Anderson, C. Arguelles, T. C. Arlen, J. Auffenberg, X. Bai, S. W. Barwick, V. Baum, J. J. Beatty, J. Becker Tjus, K. H. Becker, S. BenZvi, P. Berghaus, D. Berley, E. Bernardini, A. Bernhard, D. Z. Besson, G. Binder, D. Bindig, M. Bissok, E. Blaufuss, J. Blumenthal, D. J. Boersma, C. Bohm, D. Bose, S. Böser, O. Botner, L. Brayeur, H. P. Bretz, A. M. Brown, J. Casey, M. Casier, D. Chirkin, A. Christov, B. Christy, K. Clark, L. Classen, F. Clevermann, S. Coenders, D. F. Cowen, A. H. Cruz Silva, M. Danninger, J. Daughhetee, J. C. Davis, M. Day, J. P. A. M. de André, C. De Clercq, S. De Ridder, P. Desiati, K. D. de Vries, M. de With, T. DeYoung, J. C. Díaz-Vélez, M. Dunkman, R. Eagan, B. Eberhardt, B. Eichmann, J. Eisch, S. Euler, P. A. Evenson, O. Fadiran, A. R. Fazely, A. Fedynitch, J. Feintzeig, J. Felde, T. Feusels, K. Filimonov, C. Finley, T. Fischer-Wasels, S. Flis, A. Franckowiak, K. Frantzen, T. Fuchs, T. K. Gaisser, J. Gallagher, L. Gerhardt, D. Gier, L. Gladstone, T. Glüsenkamp, A. Goldschmidt, G. Golup, J. G. Gonzalez, J. A. Goodman, D. Góra, D. T. Grandmont, D. Grant, P. Gretskov, J. C. Groh, A. Groß, C. Ha, C. Haack, A. Haj Ismail, P. Hallen, A. Hallgren, F. Halzen, K. Hanson, D. Hebecker, D. Heereman, D. Heinen, K. Helbing, R. Hellauer, D. Hellwig, S. Hickford, G. C. Hill, K. D. Hoffman, R. Hoffmann, A. Homeier, K. Hoshina, F. Huang, W. Huelsnitz, P. O. Hulth, K. Hultqvist, S. Hussain, A. Ishihara, E. Jacobi, J. Jacobsen, K. Jagielski, G. S. Japaridze, K. Jero, O. Jlelati, M. Jurkovic, B. Kaminsky, A. Kappes, T. Karg, A. Karle, M. Kauer, J. L. Kelley, A. Kheirandish, J. Kiryluk, J. Kläs, S. R. Klein,

J. H. Köhne, G. Kohnen, H. Kolanoski, A. Koob, L. Köpke, C. Kopper, S. Kopper, D. J. Koskinen, M. Kowalski, A. Kriesten, K. Krings, G. Kroll, J. Kunnen, N. Kurahashi, T. Kuwabara, M. Labare, D. T. Larsen, M. J. Larson, M. Lesiak-Bzdak, M. Leuermann, J. Leute, J. Lünemann, O. Macías, J. Madsen, G. Maggi, R. Maruyama, K. Mase, H. S. Matis, F. McNally, K. Meagher, A. Meli, T. Meures, S. Miarecki, E. Middell, E. Middlemas, N. Milke, J. Miller, L. Mohrmann, T. Montaruli, R. Morse, R. Nahnhauer, U. Naumann, H. Niederhausen, S. C. Nowicki, D. R. Nygren, A. Obertacke, S. Odrowski, A. Olivas, A. Omairat, A. O'Murchadha, T. Palczewski, L. Paul, Ö. Penek, J. A. Pepper, C. Pérez de los Heros, C. Pfendner, D. Pieloth, E. Pinat, J. Posselt, P. B. Price, G. T. Przybylski, J. Pütz, M. Quinnan, L. Rädel, M. Rameez, K. Rawlins, P. Redl, I. Rees, R. Reimann, E. Resconi, W. Rhode, M. Richman, B. Riedel, S. Robertson, J. P. Rodrigues, M. Rongen, C. Rott, T. Ruhe, B. Ruzybayev, D. Ryckbosch, S. M. Saba, H. G. Sand er, M. Santander, S. Sarkar, K. Schatto, F. Scheriau, T. Schmidt, M. Schmitz, S. Schoenen, S. Schöneberg, A. Schönwald, A. Schukraft, L. Schulte, O. Schulz, D. Seckel, Y. Sestayo, S. Seunarine, R. Shanidze, C. Sheremata, M. W. E. Smith, D. Soldin, G. M. Spiczak, C. Spiering, M. Stamatikos, T. Stanev, N. A. Stanisha, A. Stasik, T. Stezelberger, R. G. Stokstad, A. Stößl, E. A. Strahler, R. Ström, N. L. Strotjohann, G. W. Sullivan, H. Taavola, I. Taboada, A. Tamburro, A. Tepe, S. Ter-Antonyan, A. Terliuk, G. Tešić, S. Tilav, P. A. Toale, M. N. Tobin, D. Tosi, M. Tselengidou, E. Unger, M. Usner, S. Vallecorsa, N. van Eijndhoven, J. Vandenbroucke, J. van Santen, M. Vehring, M. Voge, M. Vraeghe, C. Walck, M. Wallraff, C. Weaver, M. Wellons, C. Wendt, S. Westerhoff, B. J. Whelan, N. Whitehorn, C. Wichary, K. Wiebe, C. H. Wiebusch, D. R. Williams, H. Wissing, M. Wolf, T. R. Wood, K. Woschnagg, D. L. Xu, X. W. Xu, J. P. Yanez, G. Yodh, S. Yoshida, P. Zarzhitsky, J. Ziemann, S. Zierke, M. Zoll, and IceCube Collaboration. Observation of High-Energy Astrophysical Neutrinos in Three Years of IceCube Data. , 113(10):101101, Sept. 2014. doi: 10.1103/PhysRevLett.113.101101.

M. G. Aartsen, M. Ackermann, J. Adams, J. A. Aguilar, M. Ahlers, M. Ahrens, D. Altmann, K. Andeen, T. Anderson, I. Ansseau, G. Anton, M. Archinger, C. Argüelles, R. Auer, J. Auffenberg, S. Axani, J. Baccus, X. Bai, S. Barnet, S. W. Barwick, V. Baum,

R. Bay, K. Beattie, J. J. Beatty, J. Becker Tjus, K. H. Becker, T. Bendfelt, S. BenZvi, D. Berley, E. Bernardini, A. Bernhard, D. Z. Besson, G. Binder, D. Bindig, M. Bissok, E. Blaufuss, S. Blot, D. Boersma, C. Bohm, M. Börner, F. Bos, D. Bose, S. Böser, O. Botner, A. Bouchta, J. Braun, L. Brayeur, H. P. Bretz, S. Bron, A. Burgman, C. Burreson, T. Carver, M. Casier, E. Cheung, D. Chirkin, A. Christov, K. Clark, L. Classen, S. Coenders, G. H. Collin, J. M. Conrad, D. F. Cowen, R. Cross, C. Day, M. Day, J. P. A. M. de André, C. De Clercq, E. del Pino Rosendo, H. Dembinski, S. De Ridder, F. Descamps, P. Desiati, K. D. de Vries, G. de Wasseige, M. de With, T. DeYoung, J. C. Díaz-Vélez, V. di Lorenzo, H. Dujmovic, J. P. Dumm, M. Dunkman, B. Eberhardt, W. R. Edwards, T. Ehrhardt, B. Eichmann, P. Eller, S. Euler, P. A. Evenson, S. Fahey, A. R. Fazely, J. Feintzeig, J. Felde, K. Filimonov, C. Finley, S. Flis, C. C. Fösig, A. Franckowiak, M. Frère, E. Friedman, T. Fuchs, T. K. Gaisser, J. Gallagher, L. Gerhardt, K. Ghorbani, W. Giang, L. Gladstone, T. Glauch, D. Glowacki, T. Glüsenkamp, A. Goldschmidt, J. G. Gonzalez, D. Grant, Z. Griffith, L. Gustafsson, C. Haack, A. Hallgren, F. Halzen, E. Hansen, T. Hansmann, K. Hanson, J. Haugen, D. Hebecker, D. Heereman, K. Helbing, R. Hellauer, R. Heller, S. Hickford, J. Hignight, G. C. Hill, K. D. Hoffman, R. Hoffmann, K. Hoshina, F. Huang, M. Huber, P. O. Hulth, K. Hultqvist, S. In, M. Inaba, A. Ishihara, E. Jacobi, J. Jacobsen, G. S. Japaridze, M. Jeong, K. Jero, A. Jones, B. J. P. Jones, J. Joseph, W. Kang, A. Kappes, T. Karg, A. Karle, U. Katz, M. Kauer, A. Keivani, J. L. Kelley, J. Kemp, A. Kheirandish, J. Kim, M. Kim, T. Kintscher, J. Kiryluk, N. Kitamura, T. Kittler, S. R. Klein, S. Kleinfelder, M. Kleist, G. Kohnen, R. Koirala, H. Kolanoski, R. Konietz, L. Köpke, C. Kopper, S. Kopper, D. J. Koskinen, M. Kowalski, M. Krasberg, K. Krings, M. Kroll, G. Krückl, C. Krüger, J. Kunnen, S. Kunwar, N. Kurahashi, T. Kuwabara, M. Labare, K. Laihem, H. Landsman, J. L. Lanfranchi, M. J. Larson, F. Lauber, A. Laundrie, D. Lennarz, H. Leich, M. Lesiak-Bzdak, M. Leuermann, L. Lu, J. Ludwig, J. Lünemann, C. Mackenzie, J. Madsen, G. Maggi, K. B. M. Mahn, S. Mancina, M. Mandelartz, R. Maruyama, K. Mase, H. Matis, R. Maunu, F. McNally, C. P. McParland, P. Meade, K. Meagher, M. Medici, M. Meier, A. Meli, T. Menne, G. Merino, T. Meures, S. Miarecki, R. H.

Minor, T. Montaruli, M. Moulai, T. Murray, R. Nahnhauer, U. Naumann, G. Neer, M. Newcomb, H. Niederhausen, S. C. Nowicki, D. R. Nygren, A. Obertacke Pollmann, A. Olivas, A. O'Murchadha, T. Palczewski, H. Pandya, D. V. Pankova, S. Patton, P. Peiffer, Ö. Penek, J. A. Pepper, C. Pérez de los Heros, C. Pettersen, D. Pieloth, E. Pinat, P. B. Price, G. T. Przybylski, M. Quinnan, C. Raab, L. Rädel, M. Rameez, K. Rawlins, R. Reimann, B. Relethford, M. Relich, E. Resconi, W. Rhode, M. Richman, B. Riedel, S. Robertson, M. Rongen, C. Roucelle, C. Rott, T. Ruhe, D. Ryckbosch, D. Rysewyk, L. Sabbatini, S. E. Sanchez Herrera, A. Sandrock, J. Sandroos, P. Sandstrom, S. Sarkar, K. Satalecka, P. Schlunder, T. Schmidt, S. Schoenen, S. Schöneberg, A. Schukraft, L. Schumacher, D. Seckel, S. Seunarine, M. Solarz, D. Soldin, M. Song, G. M. Spiczak, C. Spiering, T. Stanev, A. Stasik, J. Stettner, A. Steuer, T. Stezelberger, R. G. Stokstad, A. Stößl, R. Ström, N. L. Strotjohann, K. H. Sulanke, G. W. Sullivan, M. Sutherland, H. Taavola, I. Taboada, J. Tatar, F. Tenholt, S. Ter-Antonyan, A. Terliuk, G. Tešić, L. Thollander, S. Tilav, P. A. Toale, M. N. Tobin, S. Toscano, D. Tosi, M. Tselengidou, A. Turcati, E. Unger, M. Usner, J. Vandenbroucke, N. van Eijndhoven, S. Vanheule, M. van Rossem, J. van Santen, M. Vehring, M. Voge, E. Vogel, M. Vraeghe, D. Wahl, C. Walck, A. Wallace, M. Wallraff, N. Wandkowsky, C. Weaver, M. J. Weiss, C. Wendt, S. Westerhoff, D. Wharton, B. J. Whelan, S. Wickmann, K. Wiebe, C. H. Wiebusch, L. Wille, D. R. Williams, L. Wills, P. Wisniewski, M. Wolf, T. R. Wood, E. Woolsey, K. Woschnagg, D. L. Xu, X. W. Xu, Y. Xu, J. P. Yanez, G. Yodh, S. Yoshida, and M. Zoll. The IceCube Neutrino Observatory: instrumentation and online systems. *Journal of Instrumentation*, 12(3):P03012, Mar. 2017. doi: 10.1088/1748-0221/12/03/P03012.

B. P. Abbott, R. Abbott, T. D. Abbott, M. R. Abernathy, F. Acernese, K. Ackley, C. Adams, T. Adams, P. Addesso, R. X. Adhikari, V. B. Adya, C. Affeldt, M. Agathos, K. Agatsuma, N. Aggarwal, O. D. Aguiar, L. Aiello, A. Ain, P. Ajith, B. Allen, A. Allocca, P. A. Altin, S. B. Anderson, W. G. Anderson, K. Arai, M. A. Arain, M. C. Araya, C. C. Arceneaux, J. S. Areeda, N. Arnaud, K. G. Arun, S. Ascenzi, G. Ashton, M. Ast, S. M. Aston, P. Astone, P. Aufmuth, C. Aulbert, S. Babak, P. Bacon, M. K. M. Bader, P. T. Baker, F. Baldaccini, G. Ballardin, S. W. Ballmer, J. C. Barayoga, S. E. Barclay, B. C. Barish,

D. Barker, F. Barone, B. Barr, L. Barsotti, M. Barsuglia, D. Barta, J. Bartlett, M. A. Barton, I. Bartos, R. Bassiri, A. Basti, J. C. Batch, C. Baune, V. Bavigadda, M. Bazzan, B. Behnke, M. Bejger, C. Belczynski, A. S. Bell, C. J. Bell, B. K. Berger, J. Bergman, G. Bergmann, C. P. L. Berry, D. Bersanetti, A. Bertolini, J. Betzwieser, S. Bhagwat, R. Bhandare, I. A. Bilenko, G. Billingsley, J. Birch, R. Birney, O. Birnholtz, S. Biscans, A. Bisht, M. Bitossi, C. Biwer, M. A. Bizouard, J. K. Blackburn, C. D. Blair, D. G. Blair, R. M. Blair, S. Bloemen, O. Bock, T. P. Bodiya, M. Boer, G. Bogaert, C. Bogan, A. Bohe, P. Bojtos, C. Bond, F. Bondu, R. Bonnand, B. A. Boom, R. Bork, V. Boschi, S. Bose, Y. Bouffanais, A. Bozzi, C. Bradaschia, P. R. Brady, V. B. Braginsky, M. Branchesi, J. E. Brau, T. Briant, A. Brillet, M. Brinkmann, V. Brisson, P. Brockill, A. F. Brooks, D. A. Brown, D. D. Brown, N. M. Brown, C. C. Buchanan, A. Buikema, T. Bulik, H. J. Bulten, A. Buonanno, D. Buskulic, C. Buy, R. L. Byer, M. Cabero, L. Cadonati, G. Cagnoli, C. Cahillane, J. C. Bustillo, T. Callister, E. Calloni, J. B. Camp, K. C. Cannon, J. Cao, C. D. Capano, E. Capocasa, F. Carbognani, S. Caride, J. Casanueva Diaz, C. Casentini, S. Caudill, M. Cavaglià, F. Cavalier, R. Cavalieri, G. Cella, C. B. Cepeda, L. C. Baiardi, G. Cerretani, E. Cesarini, R. Chakraborty, T. Chalermsongsak, S. J. Chamberlin, M. Chan, S. Chao, P. Charlton, E. Chassande-Mottin, H. Y. Chen, Y. Chen, C. Cheng, A. Chincarini, A. Chiummo, H. S. Cho, M. Cho, J. H. Chow, N. Christensen, Q. Chu, S. Chua, S. Chung, G. Ciani, F. Clara, J. A. Clark, F. Cleva, E. Coccia, P. F. Cohadon, A. Colla, C. G. Collette, L. Cominsky, M. Constancio, A. Conte, L. Conti, D. Cook, T. R. Corbitt, N. Cornish, A. Corsi, S. Cortese, C. A. Costa, M. W. Coughlin, S. B. Coughlin, J. P. Coulon, S. T. Countryman, P. Couvares, E. E. Cowan, D. M. Coward, M. J. Cowart, D. C. Coyne, R. Coyne, K. Craig, J. D. E. Creighton, T. D. Creighton, J. Cripe, S. G. Crowder, A. M. Cruise, A. Cumming, L. Cunningham, E. Cuoco, T. Dal Canton, S. L. Danilishin, S. D'Antonio, K. Danzmann, N. S. Darman, C. F. Da Silva Costa, V. Dattilo, I. Dave, H. P. Daveloza, M. Davier, G. S. Davies, E. J. Daw, R. Day, S. De, D. DeBra, G. Debreczeni, J. Degallaix, M. De Laurentis, S. Deléglise, W. Del Pozzo, T. Denker, T. Dent, H. Dereli, V. Dergachev, R. T. DeRosa, R. De Rosa, R. DeSalvo, S. Dhurandhar, M. C. Díaz, L. Di Fiore, M. Di Giovanni, A. Di

Lieto, S. Di Pace, I. Di Palma, A. Di Virgilio, G. Dojcinoski, V. Dolique, F. Donovan, K. L. Dooley, S. Doravari, R. Douglas, T. P. Downes, M. Drago, R. W. P. Drever, J. C. Driggers, Z. Du, M. Ducrot, S. E. Dwyer, T. B. Edo, M. C. Edwards, A. Effler, H. B. Eggenstein, P. Ehrens, J. Eichholz, S. S. Eikenberry, W. Engels, R. C. Essick, T. Etzel, M. Evans, T. M. Evans, R. Everett, M. Factourovich, V. Fafone, H. Fair, S. Fairhurst, X. Fan, Q. Fang, S. Farinon, B. Farr, W. M. Farr, M. Favata, M. Fays, H. Fehrmann, M. M. Fejer, D. Feldbaum, I. Ferrante, E. C. Ferreira, F. Ferrini, F. Fidecaro, L. S. Finn, I. Fiori, D. Fiorucci, R. P. Fisher, R. Flaminio, M. Fletcher, H. Fong, J. D. Fournier, S. Franco, S. Frasca, F. Frasconi, M. Frede, Z. Frei, A. Freise, R. Frey, V. Frey, T. T. Fricke, P. Fritschel, V. V. Frolov, P. Fulda, M. Fyffe, H. A. G. Gabbard, J. R. Gair, L. Gammaitoni, S. G. Gaonkar, F. Garufi, A. Gatto, G. Gaur, N. Gehrels, G. Gemme, B. Gendre, E. Genin, A. Gennai, J. George, L. Gergely, V. Germain, A. Ghosh, A. Ghosh, S. Ghosh, J. A. Giaime, K. D. Giardina, A. Giazotto, K. Gill, A. Glaefke, J. R. Gleason, E. Goetz, R. Goetz, L. Gondan, G. González, J. M. G. Castro, A. Gopakumar, N. A. Gordon, M. L. Gorodetsky, S. E. Gossan, M. Gosselin, R. Gouaty, C. Graef, P. B. Graff, M. Granata, A. Grant, S. Gras, C. Gray, G. Greco, A. C. Green, R. J. S. Greenhalgh, P. Groot, H. Grote, S. Grunewald, G. M. Guidi, X. Guo, A. Gupta, M. K. Gupta, K. E. Gushwa, E. K. Gustafson, R. Gustafson, J. J. Hacker, B. R. Hall, E. D. Hall, G. Hammond, M. Haney, M. M. Hanke, J. Hanks, C. Hanna, M. D. Hannam, J. Hanson, T. Hardwick, J. Harms, G. M. Harry, I. W. Harry, M. J. Hart, M. T. Hartman, C. J. Haster, K. Haughian, J. Healy, J. Heefner, A. Heidmann, M. C. Heintze, G. Heinzel, H. Heitmann, P. Hello, G. Hemming, M. Hendry, I. S. Heng, J. Hennig, A. W. Heptonstall, M. Heurs, S. Hild, D. Hoak, K. A. Hodge, D. Hofman, S. E. Hollitt, K. Holt, D. E. Holz, P. Hopkins, D. J. Hosken, J. Hough, E. A. Houston, E. J. Howell, Y. M. Hu, S. Huang, E. A. Huerta, D. Huet, B. Hughey, S. Husa, S. H. Huttner, T. Huynh-Dinh, A. Idrisy, N. Indik, D. R. Ingram, R. Inta, H. N. Isa, J. M. Isac, M. Isi, G. Islas, T. Isogai, B. R. Iyer, K. Izumi, M. B. Jacobson, T. Jacqmin, H. Jang, K. Jani, P. Jaranowski, S. Jawahar, F. Jiménez-Forteza, W. W. Johnson, N. K. Johnson-McDaniel, D. I. Jones, R. Jones, R. J. G. Jonker, L. Ju, K. Haris, C. V. Kalaghatgi, V. Kalogera,

S. Kandhasamy, G. Kang, J. B. Kanner, S. Karki, M. Kasprzack, E. Katsavounidis, W. Katzman, S. Kaufer, T. Kaur, K. Kawabe, F. Kawazoe, F. Kéfélian, M. S. Kehl, D. Keitel, D. B. Kelley, W. Kells, R. Kennedy, D. G. Keppel, J. S. Key, A. Khalaidovski, F. Y. Khalili, I. Khan, S. Khan, Z. Khan, E. A. Khazanov, N. Kijbunchoo, C. Kim, J. Kim, K. Kim, N.-G. Kim, N. Kim, Y. M. Kim, E. J. King, P. J. King, D. L. Kinzel, J. S. Kissel, L. Kleybolte, S. Klimenko, S. M. Koehlenbeck, K. Kokeyama, S. Koley, V. Kondrashov, A. Kontos, S. Koranda, M. Korobko, W. Z. Korth, I. Kowalska, D. B. Kozak, V. Kringel, B. Krishnan, A. Królak, C. Krueger, G. Kuehn, P. Kumar, R. Kumar, L. Kuo, A. Kutynia, P. Kwee, B. D. Lackey, M. Landry, J. Lange, B. Lantz, P. D. Lasky, A. Lazzarini, C. Lazzaro, P. Leaci, S. Leavey, E. O. Lebigot, C. H. Lee, H. K. Lee, H. M. Lee, K. Lee, A. Lenon, M. Leonardi, J. R. Leong, N. Leroy, N. Letendre, Y. Levin, B. M. Levine, T. G. F. Li, A. Libson, T. B. Littenberg, N. A. Lockerbie, J. Logue, A. L. Lombardi, L. T. London, J. E. Lord, M. Lorenzini, V. Loriette, M. Lormand, G. Losurdo, J. D. Lough, C. O. Lousto, G. Lovelace, H. Lück, A. P. Lundgren, J. Luo, R. Lynch, Y. Ma, T. MacDonald, B. Machenschalk, M. MacInnis, D. M. Macleod, F. Magaña-Sandoval, R. M. Magee, M. Mageswaran, E. Majorana, I. Maksimovic, V. Malvezzi, N. Man, I. Mandel, V. Mandic, V. Mangano, G. L. Mansell, M. Manske, M. Mantovani, F. Marchesoni, F. Marion, S. Márka, Z. Márka, A. S. Markosyan, E. Maros, F. Martelli, L. Martellini, I. W. Martin, R. M. Martin, D. V. Martynov, J. N. Marx, K. Mason, A. Masserot, T. J. Massinger, M. Masso-Reid, F. Matichard, L. Matone, N. Mavalvala, N. Mazumder, G. Mazzolo, R. McCarthy, D. E. McClelland, S. McCormick, S. C. McGuire, G. McIntyre, J. McIver, D. J. McManus, S. T. McWilliams, D. Meacher, G. D. Meadors, J. Meidam, A. Melatos, G. Mendell, D. Mendoza-Gandara, R. A. Mercer, E. Merilh, M. Merzougui, S. Meshkov, C. Messenger, C. Messick, P. M. Meyers, F. Mezzani, H. Miao, C. Michel, H. Middleton, E. E. Mikhailov, L. Milano, J. Miller, M. Millhouse, Y. Minenkov, J. Ming, S. Mirshekari, C. Mishra, S. Mitra, V. P. Mitrofanov, G. Mitselmakher, R. Mittleman, A. Moggi, M. Mohan, S. R. P. Mohapatra, M. Montani, B. C. Moore, C. J. Moore, D. Moraru, G. Moreno, S. R. Morriss, K. Mossavi, B. Mours, C. M. Mow-Lowry, C. L. Mueller, G. Mueller, A. W.

Muir, A. Mukherjee, D. Mukherjee, S. Mukherjee, N. Mukund, A. Mullavey, J. Munch, D. J. Murphy, P. G. Murray, A. Mytidis, I. Nardecchia, L. Naticchioni, R. K. Nayak, V. Necula, K. Nedkova, G. Nelemans, M. Neri, A. Neunzert, G. Newton, T. T. Nguyen, A. B. Nielsen, S. Nissanke, A. Nitz, F. Nocera, D. Nolting, M. E. N. Normandin, L. K. Nuttall, J. Oberling, E. Ochsner, J. O'Dell, E. Oelker, G. H. Ogin, J. J. Oh, S. H. Oh, F. Ohme, M. Oliver, P. Oppermann, R. J. Oram, B. O'Reilly, R. O'Shaughnessy, C. D. Ott, D. J. Ottaway, R. S. Ottens, H. Overmier, B. J. Owen, A. Pai, S. A. Pai, J. R. Palamos, O. Palashov, C. Palomba, A. Pal-Singh, H. Pan, Y. Pan, C. Pankow, F. Pannarale, B. C. Pant, F. Paoletti, A. Paoli, M. A. Papa, H. R. Paris, W. Parker, D. Pascucci, A. Pasqualetti, R. Passaquieti, D. Passuello, B. Patricelli, Z. Patrick, B. L. Pearlstone, M. Pedraza, R. Pedurand, L. Pekowsky, A. Pele, S. Penn, A. Perreca, H. P. Pfeiffer, M. Phelps, O. Piccinni, M. Pichot, M. Pickenpack, F. Piergiovanni, V. Pierro, G. Pillant, L. Pinard, I. M. Pinto, M. Pitkin, J. H. Poeld, R. Poggiani, P. Popolizio, A. Post, J. Powell, J. Prasad, V. Predoi, S. S. Premachandra, T. Prestegard, L. R. Price, M. Prijatelj, M. Principe, S. Privitera, R. Prix, G. A. Prodi, L. Prokhorov, O. Puncken, M. Punturo, P. Puppo, M. Pürrer, H. Qi, J. Qin, V. Quetschke, E. A. Quintero, R. Quitzow-James, F. J. Raab, D. S. Rabeling, H. Radkins, P. Raffai, S. Raja, M. Rakhmanov, C. R. Ramet, P. Rapagnani, V. Raymond, M. Razzano, V. Re, J. Read, C. M. Reed, T. Regimbau, L. Rei, S. Reid, D. H. Reitze, H. Rew, S. D. Reyes, F. Ricci, K. Riles, N. A. Robertson, R. Robie, F. Robinet, A. Rocchi, L. Rolland, J. G. Rollins, V. J. Roma, J. D. Romano, R. Romano, G. Romanov, J. H. Romie, D. Rosińska, S. Rowan, A. Rüdiger, P. Ruggi, K. Ryan, S. Sachdev, T. Sadecki, L. Sadeghian, L. Salconi, M. Saleem, F. Salemi, A. Samajdar, L. Sammut, L. M. Sampson, E. J. Sanchez, V. Sandberg, B. Sandeen, G. H. Sanders, J. R. Sanders, B. Sassolas, B. S. Sathyaprakash, P. R. Saulson, O. Sauter, R. L. Savage, A. Sawadsky, P. Schale, R. Schilling, J. Schmidt, P. Schmidt, R. Schnabel, R. M. S. Schofield, A. Schönbeck, E. Schreiber, D. Schuette, B. F. Schutz, J. Scott, S. M. Scott, D. Sellers, A. S. Sengupta, D. Sentenac, V. Sequino, A. Sergeev, G. Serna, Y. Setyawati, A. Sevigny, D. A. Shaddock, T. Shaffer, S. Shah, M. S. Shahriar, M. Shaltev, Z. Shao, B. Shapiro, P. Shawhan, A. Sheperd, D. H. Shoemaker, D. M.

Shoemaker, K. Siellez, X. Siemens, D. Sigg, A. D. Silva, D. Simakov, A. Singer, L. P. Singer, A. Singh, R. Singh, A. Singhal, A. M. Sintes, B. J. J. Slagmolen, J. R. Smith, M. R. Smith, N. D. Smith, R. J. E. Smith, E. J. Son, B. Sorazu, F. Sorrentino, T. Souradeep, A. K. Srivastava, A. Staley, M. Steinke, J. Steinlechner, S. Steinlechner, D. Steinmeyer, B. C. Stephens, S. P. Stevenson, R. Stone, K. A. Strain, N. Straniero, G. Stratta, N. A. Strauss, S. Strigin, R. Sturani, A. L. Stuver, T. Z. Summerscales, L. Sun, P. J. Sutton, B. L. Swinkels, M. J. Szczepańczyk, M. Tacca, D. Talukder, D. B. Tanner, M. Tápai, S. P. Tarabrin, A. Taracchini, R. Taylor, T. Theeg, M. P. Thirugnanasambandam, E. G. Thomas, M. Thomas, P. Thomas, K. A. Thorne, K. S. Thorne, E. Thrane, S. Tiwari, V. Tiwari, K. V. Tokmakov, C. Tomlinson, M. Tonelli, C. V. Torres, C. I. Torrie, D. Töyrä, F. Travasso, G. Traylor, D. Trifirò, M. C. Tringali, L. Trozzo, M. Tse, M. Turconi, D. Tuyenbayev, D. Ugolini, C. S. Unnikrishnan, A. L. Urban, S. A. Usman, H. Vahlbruch, G. Vajente, G. Valdes, M. Vallisneri, N. van Bakel, M. van Beuzekom, J. F. J. van den Brand, C. Van Den Broeck, D. C. Vander-Hyde, L. van der Schaaf, J. V. van Heijningen, A. A. van Veggel, M. Vardaro, S. Vass, M. Vasúth, R. Vaulin, A. Vecchio, G. Vedovato, J. Veitch, P. J. Veitch, K. Venkateswara, D. Verkindt, F. Vetrano, A. Viceré, S. Vinciguerra, D. J. Vine, J. Y. Vinet, S. Vitale, T. Vo, H. Vocca, C. Vorvick, D. Voss, W. D. Vousden, S. P. Vyatchanin, A. R. Wade, L. E. Wade, M. Wade, S. J. Waldman, M. Walker, L. Wallace, S. Walsh, G. Wang, H. Wang, M. Wang, X. Wang, Y. Wang, H. Ward, R. L. Ward, J. Warner, M. Was, B. Weaver, L. W. Wei, M. Weinert, A. J. Weinstein, R. Weiss, T. Welborn, L. Wen, P. Weßels, T. Westphal, K. Wette, J. T. Whelan, S. E. Whitcomb, D. J. White, B. F. Whiting, K. Wiesner, C. Wilkinson, P. A. Willems, L. Williams, R. D. Williams, A. R. Williamson, J. L. Willis, B. Willke, M. H. Wimmer, L. Winkelmann, W. Winkler, C. C. Wipf, A. G. Wiseman, H. Wittel, G. Woan, J. Worden, J. L. Wright, G. Wu, J. Yablon, I. Yakushin, W. Yam, H. Yamamoto, C. C. Yancey, M. J. Yap, H. Yu, M. Yvert, A. ZadroŻny, L. Zangrando, M. Zanolin, J. P. Zendri, M. Zevin, F. Zhang, L. Zhang, M. Zhang, Y. Zhang, C. Zhao, M. Zhou, Z. Zhou, X. J. Zhu, M. E. Zucker, S. E. Zuraw, J. Zweizig, LIGO Scientific Collaboration, and Virgo Collaboration. Observation of Gravitational Waves from a Binary Black Hole

Merger. , 116(6):061102, Feb. 2016a. doi: 10.1103/PhysRevLett.116.061102.

B. P. Abbott, R. Abbott, T. D. Abbott, M. R. Abernathy, F. Acernese, K. Ackley, C. Adams, T. Adams, P. Addesso, R. X. Adhikari, V. B. Adya, C. Affeldt, M. Agathos, K. Agatsuma, N. Aggarwal, O. D. Aguiar, L. Aiello, A. Ain, P. Ajith, B. Allen, A. Allocca, P. A. Altin, S. B. Anderson, W. G. Anderson, K. Arai, M. C. Araya, C. C. Arceneaux, J. S. Areeda, N. Arnaud, K. G. Arun, S. Ascenzi, G. Ashton, M. Ast, S. M. Aston, P. Astone, P. Aufmuth, C. Aulbert, S. Babak, P. Bacon, M. K. M. Bader, P. T. Baker, F. Baldaccini, G. Ballardin, S. W. Ballmer, J. C. Barayoga, S. E. Barclay, B. C. Barish, D. Barker, F. Barone, B. Barr, L. Barsotti, M. Barsuglia, D. Barta, J. Bartlett, I. Bartos, R. Bassiri, A. Basti, J. C. Batch, C. Baune, V. Bavigadda, M. Bazzan, M. Bejger, A. S. Bell, B. K. Berger, G. Bergmann, C. P. L. Berry, D. Bersanetti, A. Bertolini, J. Betzwieser, S. Bhagwat, R. Bhandare, I. A. Bilenko, G. Billingsley, J. Birch, R. Birney, O. Birnholtz, S. Biscans, A. Bisht, M. Bitossi, C. Biwer, M. A. Bizouard, J. K. Blackburn, C. D. Blair, D. G. Blair, R. M. Blair, S. Bloemen, O. Bock, M. Boer, G. Bogaert, C. Bogan, A. Bohe, C. Bond, F. Bondu, R. Bonnand, B. A. Boom, R. Bork, V. Boschi, S. Bose, Y. Bouffanais, A. Bozzi, C. Bradaschia, P. R. Brady, V. B. Braginsky, M. Branchesi, J. E. Brau, T. Briant, A. Brillet, M. Brinkmann, V. Brisson, P. Brockill, J. E. Broida, A. F. Brooks, D. A. Brown, D. D. Brown, N. M. Brown, S. Brunett, C. C. Buchanan, A. Buikema, T. Bulik, H. J. Bulten, A. Buonanno, D. Buskulic, C. Buy, R. L. Byer, M. Cabero, L. Cadonati, G. Cagnoli, C. Cahillane, J. Calderón Bustillo, T. Callister, E. Calloni, J. B. Camp, K. C. Cannon, J. Cao, C. D. Capano, E. Capocasa, F. Carbognani, S. Caride, J. Casanueva Diaz, C. Casentini, S. Caudill, M. Cavaglià, F. Cavalier, R. Cavalieri, G. Cella, C. B. Cepeda, L. Cerboni Baiardi, G. Cerretani, E. Cesarini, S. J. Chamberlin, M. Chan, S. Chao, P. Charlton, E. Chassande-Mottin, B. D. Cheeseboro, H. Y. Chen, Y. Chen, C. Cheng, A. Chincarini, A. Chiummo, H. S. Cho, M. Cho, J. H. Chow, N. Christensen, Q. Chu, S. Chua, S. Chung, G. Ciani, F. Clara, J. A. Clark, F. Cleva, E. Coccia, P. F. Cohadon, A. Colla, C. G. Collette, L. Cominsky, M. Constancio, A. Conte, L. Conti, D. Cook, T. R. Corbitt, N. Cornish, A. Corsi, S. Cortese, C. A. Costa, M. W. Coughlin, S. B. Coughlin, J. P. Coulon, S. T. Countryman, P. Couvares, E. E. Cowan, D. M. Coward, M. J.

Cowart, D. C. Coyne, R. Coyne, K. Craig, J. D. E. Creighton, J. Cripe, S. G. Crowder, A. Cumming, L. Cunningham, E. Cuoco, T. Dal Canton, S. L. Danilishin, S. D'Antonio, K. Danzmann, N. S. Darman, A. Dasgupta, C. F. Da Silva Costa, V. Dattilo, I. Dave, M. Davier, G. S. Davies, E. J. Daw, R. Day, S. De, D. DeBra, G. Debreczeni, J. Degallaix, M. De Laurentis, S. Deléglise, W. Del Pozzo, T. Denker, T. Dent, V. Dergachev, R. De Rosa, R. T. DeRosa, R. DeSalvo, R. C. Devine, S. Dhurandhar, M. C. Díaz, L. Di Fiore, M. Di Giovanni, T. Di Girolamo, A. Di Lieto, S. Di Pace, I. Di Palma, A. Di Virgilio, V. Dolique, F. Donovan, K. L. Dooley, S. Doravari, R. Douglas, T. P. Downes, M. Drago, R. W. P. Drever, J. C. Driggers, M. Ducrot, S. E. Dwyer, T. B. Edo, M. C. Edwards, A. Effler, H. B. Eggenstein, P. Ehrens, J. Eichholz, S. S. Eikenberry, W. Engels, R. C. Essick, T. Etzel, M. Evans, T. M. Evans, R. Everett, M. Factourovich, V. Fafone, H. Fair, S. Fairhurst, X. Fan, Q. Fang, S. Farinon, B. Farr, W. M. Farr, M. Favata, M. Fays, H. Fehrmann, M. M. Fejer, E. Fenyvesi, I. Ferrante, E. C. Ferreira, F. Ferrini, F. Fidecaro, I. Fiori, D. Fiorucci, R. P. Fisher, R. Flaminio, M. Fletcher, H. Fong, J. D. Fournier, S. Frasca, F. Frasconi, Z. Frei, A. Freise, R. Frey, V. Frey, P. Fritschel, V. V. Frolov, P. Fulda, M. Fyffe, H. A. G. Gabbard, S. Gaebel, J. R. Gair, L. Gammaitoni, S. G. Gaonkar, F. Garufi, G. Gaur, N. Gehrels, G. Gemme, P. Geng, E. Genin, A. Gennai, J. George, L. Gergely, V. Germain, A. Ghosh, A. Ghosh, S. Ghosh, J. A. Giaime, K. D. Giardina, A. Giazotto, K. Gill, A. Glaefke, E. Goetz, R. Goetz, L. Gondan, G. González, J. M. Gonzalez Castro, A. Gopakumar, N. A. Gordon, M. L. Gorodetsky, S. E. Gossan, M. Gosselin, R. Gouaty, A. Grado, C. Graef, P. B. Graff, M. Granata, A. Grant, S. Gras, C. Gray, G. Greco, A. C. Green, P. Groot, H. Grote, S. Grunewald, G. M. Guidi, X. Guo, A. Gupta, M. K. Gupta, K. E. Gushwa, E. K. Gustafson, R. Gustafson, J. J. Hacker, B. R. Hall, E. D. Hall, H. Hamilton, G. Hammond, M. Haney, M. M. Hanke, J. Hanks, C. Hanna, M. D. Hannam, J. Hanson, T. Hardwick, J. Harms, G. M. Harry, I. W. Harry, M. J. Hart, M. T. Hartman, C. J. Haster, K. Haughian, J. Healy, A. Heidmann, M. C. Heintze, H. Heitmann, P. Hello, G. Hemming, M. Hendry, I. S. Heng, J. Hennig, J. Henry, A. W. Heptonstall, M. Heurs, S. Hild, D. Hoak, D. Hofman, K. Holt, D. E. Holz, P. Hopkins, J. Hough, E. A. Houston, E. J. Howell, Y. M. Hu, S. Huang, E. A.

Huerta, D. Huet, B. Hughey, S. Husa, S. H. Huttner, T. Huynh-Dinh, N. Indik, D. R. Ingram, R. Inta, H. N. Isa, J. M. Isac, M. Isi, T. Isogai, B. R. Iyer, K. Izumi, T. Jacqmin, H. Jang, K. Jani, P. Jaranowski, S. Jawahar, L. Jian, F. Jiménez-Forteza, W. W. Johnson, N. K. Johnson-McDaniel, D. I. Jones, R. Jones, R. J. G. Jonker, L. Ju, H. K, C. V. Kalaghatgi, V. Kalogera, S. Kandhasamy, G. Kang, J. B. Kanner, S. J. Kapadia, S. Karki, K. S. Karvinen, M. Kasprzack, E. Katsavounidis, W. Katzman, S. Kaufer, T. Kaur, K. Kawabe, F. Kéfélian, M. S. Kehl, D. Keitel, D. B. Kelley, W. Kells, R. Kennedy, J. S. Key, F. Y. Khalili, I. Khan, S. Khan, Z. Khan, E. A. Khazanov, N. Kijbunchoo, C.-W. Kim, C. Kim, J. Kim, K. Kim, N. Kim, W. Kim, Y. M. Kim, S. J. Kimbrell, E. J. King, P. J. King, J. S. Kissel, B. Klein, L. Kleybolte, S. Klimenko, S. M. Koehlenbeck, S. Koley, V. Kondrashov, A. Kontos, M. Korobko, W. Z. Korth, I. Kowalska, D. B. Kozak, V. Kringel, B. Krishnan, A. Królak, C. Krueger, G. Kuehn, P. Kumar, R. Kumar, L. Kuo, A. Kutynia, B. D. Lackey, M. Landry, J. Lange, B. Lantz, P. D. Lasky, M. Laxen, A. Lazzarini, C. Lazzaro, P. Leaci, S. Leavey, E. O. Lebigot, C. H. Lee, H. K. Lee, H. M. Lee, K. Lee, A. Lenon, M. Leonardi, J. R. Leong, N. Leroy, N. Letendre, Y. Levin, J. B. Lewis, T. G. F. Li, A. Libson, T. B. Littenberg, N. A. Lockerbie, A. L. Lombardi, L. T. London, J. E. Lord, M. Lorenzini, V. Loriette, M. Lormand, G. Losurdo, J. D. Lough, C. Lousto, H. Lück, A. P. Lundgren, R. Lynch, Y. Ma, B. Machenschalk, M. MacInnis, D. M. Macleod, F. Magaña-Sandoval, L. Magaña Zertuche, R. M. Magee, E. Majorana, I. Maksimovic, V. Malvezzi, N. Man, I. Mandel, V. Mandic, V. Mangano, G. L. Mansell, M. Manske, M. Mantovani, F. Marchesoni, F. Marion, S. Márka, Z. Márka, A. S. Markosyan, E. Maros, F. Martelli, L. Martellini, I. W. Martin, D. V. Martynov, J. N. Marx, K. Mason, A. Masserot, T. J. Massinger, M. Masso-Reid, S. Mastrogiovanni, F. Matichard, L. Matone, N. Mavalvala, N. Mazumder, R. McCarthy, D. E. McClelland, S. McCormick, S. C. McGuire, G. McIntyre, J. McIver, D. J. McManus, T. McRae, S. T. McWilliams, D. Meacher, G. D. Meadors, J. Meidam, A. Melatos, G. Mendell, R. A. Mercer, E. L. Merilh, M. Merzougui, S. Meshkov, C. Messenger, C. Messick, R. Metzdorff, P. M. Meyers, F. Mezzani, H. Miao, C. Michel, H. Middleton, E. E. Mikhailov, L. Milano, A. L. Miller, A. Miller, B. B. Miller, J. Miller, M. Millhouse, Y. Minenkov,

J. Ming, S. Mirshekari, C. Mishra, S. Mitra, V. P. Mitrofanov, G. Mitselmakher, R. Mittleman, A. Moggi, M. Mohan, S. R. P. Mohapatra, M. Montani, B. C. Moore, C. J. Moore, D. Moraru, G. Moreno, S. R. Morriss, K. Mossavi, B. Mours, C. M. Mow-Lowry, G. Mueller, A. W. Muir, A. Mukherjee, D. Mukherjee, S. Mukherjee, N. Mukund, A. Mullavey, J. Munch, D. J. Murphy, P. G. Murray, A. Mytidis, I. Nardecchia, L. Naticchioni, R. K. Nayak, K. Nedkova, G. Nelemans, T. J. N. Nelson, M. Neri, A. Neunzert, G. Newton, T. T. Nguyen, A. B. Nielsen, S. Nissanke, A. Nitz, F. Nocera, D. Nolting, M. E. N. Normandin, L. K. Nuttall, J. Oberling, E. Ochsner, J. O'Dell, E. Oelker, G. H. Ogin, J. J. Oh, S. H. Oh, F. Ohme, M. Oliver, P. Oppermann, R. J. Oram, B. O'Reilly, R. O'Shaughnessy, D. J. Ottaway, H. Overmier, B. J. Owen, A. Pai, S. A. Pai, J. R. Palamos, O. Palashov, C. Palomba, A. Pal-Singh, H. Pan, Y. Pan, C. Pankow, F. Pannarale, B. C. Pant, F. Paoletti, A. Paoli, M. A. Papa, H. R. Paris, W. Parker, D. Pascucci, A. Pasqualetti, R. Passaquieti, D. Passuello, B. Patricelli, Z. Patrick, B. L. Pearlstone, M. Pedraza, R. Pedurand, L. Pekowsky, A. Pele, S. Penn, A. Perreca, L. M. Perri, H. P. Pfeiffer, M. Phelps, O. J. Piccinni, M. Pichot, F. Piergiovanni, V. Pierro, G. Pillant, L. Pinard, I. M. Pinto, M. Pitkin, M. Poe, R. Poggiani, P. Popolizio, E. Porter, A. Post, J. Powell, J. Prasad, V. Predoi, T. Prestegard, L. R. Price, M. Prijatelj, M. Principe, S. Privitera, R. Prix, G. A. Prodi, L. Prokhorov, O. Puncken, M. Punturo, P. Puppo, M. Pürrer, H. Qi, J. Qin, S. Qiu, V. Quetschke, E. A. Quintero, R. Quitzow-James, F. J. Raab, D. S. Rabeling, H. Radkins, P. Raffai, S. Raja, C. Rajan, M. Rakhmanov, P. Rapagnani, V. Raymond, M. Razzano, V. Re, J. Read, C. M. Reed, T. Regimbau, L. Rei, S. Reid, D. H. Reitze, H. Rew, S. D. Reyes, F. Ricci, K. Riles, M. Rizzo, N. A. Robertson, R. Robie, F. Robinet, A. Rocchi, L. Rolland, J. G. Rollins, V. J. Roma, J. D. Romano, R. Romano, G. Romanov, J. H. Romie, D. Rosińska, S. Rowan, A. Rüdiger, P. Ruggi, K. Ryan, S. Sachdev, T. Sadecki, L. Sadeghian, M. Sakellariadou, L. Salconi, M. Saleem, F. Salemi, A. Samajdar, L. Sammut, E. J. Sanchez, V. Sandberg, B. Sandeen, J. R. Sanders, B. Sassolas, B. S. Sathyaprakash, P. R. Saulson, O. E. S. Sauter, R. L. Savage, A. Sawadsky, P. Schale, R. Schilling, J. Schmidt, P. Schmidt, R. Schnabel, R. M. S. Schofield, A. Schönbeck, E. Schreiber, D. Schuette, B. F. Schutz, J. Scott, S. M. Scott,

D. Sellers, A. S. Sengupta, D. Sentenac, V. Sequino, A. Sergeev, Y. Setyawati, D. A. Shaddock, T. Shaffer, M. S. Shahriar, M. Shaltev, B. Shapiro, P. Shawhan, A. Sheperd, D. H. Shoemaker, D. M. Shoemaker, K. Siellez, X. Siemens, M. Sieniawska, D. Sigg, A. D. Silva, A. Singer, L. P. Singer, A. Singh, R. Singh, A. Singhal, A. M. Sintes, B. J. J. Slagmolen, J. R. Smith, N. D. Smith, R. J. E. Smith, E. J. Son, B. Sorazu, F. Sorrentino, T. Souradeep, A. K. Srivastava, A. Staley, M. Steinke, J. Steinlechner, S. Steinlechner, D. Steinmeyer, B. C. Stephens, S. Stevenson, R. Stone, K. A. Strain, N. Straniero, G. Stratta, N. A. Strauss, S. Strigin, R. Sturani, A. L. Stuver, T. Z. Summerscales, L. Sun, S. Sunil, P. J. Sutton, B. L. Swinkels, M. J. Szczepańczyk, M. Tacca, D. Talukder, D. B. Tanner, M. Tápai, S. P. Tarabrin, A. Taracchini, R. Taylor, T. Theeg, M. P. Thirugnanasambandam, E. G. Thomas, M. Thomas, P. Thomas, K. A. Thorne, E. Thrane, S. Tiwari, V. Tiwari, K. V. Tokmakov, K. Toland, C. Tomlinson, M. Tonelli, Z. Tornasi, C. V. Torres, C. I. Torrie, D. Töyrä, F. Travasso, G. Traylor, D. Trifirò, M. C. Tringali, L. Trozzo, M. Tse, M. Turconi, D. Tuyenbayev, D. Ugolini, C. S. Unnikrishnan, A. L. Urban, S. A. Usman, H. Vahlbruch, G. Vajente, G. Valdes, M. Vallisneri, N. van Bakel, M. van Beuzekom, J. F. J. van den Brand, C. Van Den Broeck, D. C. Vander-Hyde, L. van der Schaaf, J. V. van Heijningen, A. A. van Veggel, M. Vardaro, S. Vass, M. Vasúth, R. Vaulin, A. Vecchio, G. Vedovato, J. Veitch, P. J. Veitch, K. Venkateswara, D. Verkindt, F. Vetrano, A. Viceré, S. Vinciguerra, D. J. Vine, J. Y. Vinet, S. Vitale, T. Vo, H. Vocca, C. Vorvick, D. V. Voss, W. D. Vousden, S. P. Vyatchanin, A. R. Wade, L. E. Wade, M. Wade, M. Walker, L. Wallace, S. Walsh, G. Wang, H. Wang, M. Wang, X. Wang, Y. Wang, R. L. Ward, J. Warner, M. Was, B. Weaver, L. W. Wei, M. Weinert, A. J. Weinstein, R. Weiss, L. Wen, P. Weßels, T. Westphal, K. Wette, J. T. Whelan, S. E. Whitcomb, B. F. Whiting, R. D. Williams, A. R. Williamson, J. L. Willis, B. Willke, M. H. Wimmer, W. Winkler, C. C. Wipf, H. Wittel, G. Woan, J. Woehler, J. Worden, J. L. Wright, D. S. Wu, G. Wu, J. Yablon, W. Yam, H. Yamamoto, C. C. Yancey, H. Yu, M. Yvert, A. ZadroŻny, L. Zangrando, M. Zanolin, J. P. Zendri, M. Zevin, L. Zhang, M. Zhang, Y. Zhang, C. Zhao, M. Zhou, Z. Zhou, X. J. Zhu, M. E. Zucker, S. E. Zuraw, J. Zweizig, LIGO Scientific Collaboration, and Virgo Collaboration. Binary Black Hole

Mergers in the First Advanced LIGO Observing Run. *Physical Review X*, 6(4):041015, Oct. 2016b. doi: 10.1103/PhysRevX.6.041015.

H. Abdalla, H. Abe, F. Acero, A. Acharyya, R. Adam, I. Agudo, A. Aguirre-Santaella, R. Alfaro, J. Alfaro, C. Alispach, R. Aloisio, R. Alves Batista, L. Amati, E. Amato, G. Ambrosi, E. O. Angüner, A. Araudo, T. Armstrong, F. Arqueros, L. Arrabito, K. Asano, Y. Ascasíbar, M. Ashley, M. Backes, C. Balazs, M. Balbo, B. Balmaverde, A. Baquero Larriva, V. Barbosa Martins, M. Barkov, L. Baroncelli, U. Barres de Almeida, J. A. Barrio, P. I. Batista, J. Becerra González, Y. Becherini, G. Beck, J. Becker Tjus, R. Belmont, W. Benbow, E. Bernardini, A. Berti, M. Berton, B. Bertucci, V. Beshley, B. Bi, B. Biasuzzi, A. Biland, E. Bissaldi, J. Biteau, O. Blanch, F. Bocchino, C. Boisson, J. Bolmont, G. Bonanno, L. Bonneau Arbeletche, G. Bonnoli, P. Bordas, E. Bottacini, M. Böttcher, V. Bozhilov, J. Bregeon, A. Brill, A. M. Brown, P. Bruno, A. Bruno, A. Bulgarelli, M. Burton, M. Buscemi, A. Caccianiga, R. Cameron, M. Capasso, M. Caprai, A. Caproni, R. Capuzzo-Dolcetta, P. Caraveo, R. Carosi, A. Carosi, S. Casanova, E. Cascone, D. Cauz, K. Cerny, M. Cerruti, P. Chadwick, S. Chaty, A. Chen, M. Chernyakova, G. Chiaro, A. Chiavassa, L. Chytka, V. Conforti, F. Conte, J. L. Contreras, J. Coronado-Blazquez, J. Cortina, A. Costa, H. Costantini, S. Covino, P. Cristofari, O. Cuevas, F. D'Ammando, M. K. Daniel, J. Davies, F. Dazzi, A. De Angelis, M. de Bony de Lavergne, V. De Caprio, R. de Cássia dos Anjos, E. M. de Gouveia Dal Pino, B. De Lotto, D. De Martino, M. de Naurois, E. de Oña Wilhelmi, F. De Palma, V. de Souza, C. Delgado, R. Della Ceca, D. della Volpe, D. Depaoli, T. Di Girolamo, F. Di Pierro, C. Díaz, C. Díaz-Bahamondes, S. Diebold, A. Djannati-Ataï, A. Dmytriiev, A. Domínguez, A. Donini, D. Dorner, M. Doro, J. Dournaux, V. V. Dwarkadas, J. Ebr, C. Eckner, S. Einecke, T. R. N. Ekoume, D. Elsässer, G. Emery, C. Evoli, M. Fairbairn, D. Falceta-Goncalves, S. Fegan, Q. Feng, G. Ferrand, E. Fiandrini, A. Fiasson, V. Fioretti, L. Foffano, M. V. Fonseca, L. Font, G. Fontaine, F. J. Franco, L. Freixas Coromina, S. Fukami, Y. Fukazawa, Y. Fukui, D. Gaggero, G. Galanti, V. Gammaldi, E. Garcia, M. Garczarczyk, D. Gascon, M. Gaug, A. Gent, A. Ghalumyan, G. Ghirlanda, F. Gianotti, M. Giarrusso, G. Giavitto, N. Giglietto, F. Giordano, J. Glicenstein, P. Goldoni,

J. M. González, K. Gourgouliatos, T. Grabarczyk, P. Grandi, J. Granot, D. Grasso, J. Green, J. Grube, O. Gueta, S. Gunji, A. Halim, M. Harvey, T. Hassan Collado, K. Hayashi, M. Heller, S. Hernández Cadena, O. Hervet, J. Hinton, N. Hiroshima, B. Hnatyk, R. Hnatyk, D. Hoffmann, W. Hofmann, J. Holder, D. Horan, J. Hörandel, P. Horvath, T. Hovatta, M. Hrabovsky, D. Hrupec, G. Hughes, M. Hütten, M. Iarlori, T. Inada, S. Inoue, A. Insolia, M. Ionica, M. Iori, M. Jacquemont, M. Jamrozy, P. Janecek, I. Jiménez Martínez, W. Jin, I. Jung-Richardt, J. Jurysek, P. Kaaret, V. Karas, S. Karkar, N. Kawanaka, D. Kerszberg, B. Khélifi, R. Kissmann, J. Knödlseder, Y. Kobayashi, K. Kohri, N. Komin, A. Kong, K. Kosack, H. Kubo, N. La Palombara, G. Lamanna, R. G. Lang, J. Lapington, P. Laporte, J. Lefaucheur, M. Lemoine-Goumard, J. Lenain, F. Leone, G. Leto, F. Leuschner, E. Lindfors, S. Lloyd, T. Lohse, S. Lombardi, F. Longo, A. Lopez, M. López, R. López-Coto, S. Loporchio, F. Lucarelli, P. L. Luque-Escamilla, E. Lyard, C. Maggio, A. Majczyna, M. Makariev, M. Mallamaci, D. Mandat, G. Maneva, M. Manganaro, G. Manicò, A. Marcowith, M. Marculewicz, S. Markoff, P. Marquez, J. Martí, O. Martinez, M. Martínez, G. Martínez, H. Martínez-Huerta, G. Maurin, D. Mazin, J. D. Mbarubucyeye, D. Medina Miranda, M. Meyer, S. Micanovic, T. Miener, M. Minev, J. M. Miranda, A. Mitchell, T. Mizuno, B. Mode, R. Moderski, L. Mohrmann, E. Molina, T. Montaruli, A. Moralejo, J. Morales Merino, D. Morcuende-Parrilla, A. Morselli, R. Mukherjee, C. Mundell, T. Murach, H. Muraishi, A. Nagai, T. Nakamori, R. Nemmen, J. Niemiec, D. Nieto, M. Nievas, M. Nikolajuk, K. Nishijima, K. Noda, D. Nosek, S. Nozaki, P. O'Brien, Y. Ohira, M. Ohishi, T. Oka, R. A. Ong, M. Orienti, R. Orito, M. Orlandini, E. Orlando, J. P. Osborne, M. Ostrowski, I. Oya, A. Pagliaro, M. Palatka, D. Paneque, F. R. Pantaleo, J. M. Paredes, N. Parmiggiani, B. Patricelli, L. Pavletić, A. Pe'er, M. Pech, M. Pecimotika, M. Peresano, M. Persic, O. Petruk, K. Pfrang, P. Piatteli, E. Pietropaolo, R. Pillera, B. Pilszyk, D. Pimentel, F. Pintore, S. Pita, M. Pohl, V. Poireau, M. Polo, R. R. Prado, J. Prast, G. Principe, N. Produit, H. Prokoph, M. Prouza, H. Przybilski, E. Pueschel, G. Pühlhofer, M. L. Pumo, M. Punch, F. Queiroz, A. Quirrenbach, R. Rando, S. Razzaque, E. Rebert, S. Recchia, P. Reichherzer, O. Reimer, A. Reimer, Y. Renier, T. Reposeur, W. Rhode, D. Ribeiro, M. Ribó,

T. Richtler, J. Rico, F. Rieger, V. Rizi, J. Rodriguez, G. Rodriguez Fernandez, J. C. Rodriguez Ramirez, J. J. Rodríguez Vázquez, P. Romano, G. Romeo, M. Roncadelli, J. Rosado, A. Rosales de Leon, G. Rowell, B. Rudak, W. Rujopakarn, F. Russo, I. Sadeh, L. Saha, T. Saito, F. Salesa Greus, D. Sanchez, M. Sánchez-Conde, P. Sangiorgi, H. Sano, M. Santander, E. M. Santos, A. Sanuy, S. Sarkar, F. G. Saturni, U. Sawangwit, A. Scherer, B. Schleicher, P. Schovanek, F. Schussler, U. Schwanke, E. Sciacca, S. Scuderi, M. Seglar Arroyo, O. Sergijenko, M. Servillat, K. Seweryn, A. Shalchi, P. Sharma, R. C. Shellard, H. Siejkowski, A. Sinha, V. Sliusar, A. Slowikowska, A. Sokolenko, H. Sol, A. Specovius, S. Spencer, D. Spiga, A. Stamerra, S. Stanič, R. Starling, T. Stolarczyk, U. Straumann, J. Strišković, Y. Suda, P. Świerk, G. Tagliaferri, H. Takahashi, M. Takahashi, F. Tavecchio, L. Taylor, L. A. Tejedor, P. Temnikov, R. Terrier, T. Terzic, V. Testa, W. Tian, L. Tibaldo, D. Tonev, D. F. Torres, E. Torresi, L. Tosti, N. Tothill, G. Tovmassian, P. Travnicek, S. Truzzi, F. Tuossenel, G. Umana, M. Vacula, V. Vagelli, M. Valentino, B. Vallage, P. Vallania, C. van Eldik, G. S. Varner, V. Vassiliev, M. Vázquez Acosta, M. Vecchi, J. Veh, S. Vercellone, S. Vergani, V. Verguilov, G. P. Vettolani, A. Viana, C. F. Vigorito, V. Vitale, S. Vorobiov, I. Vovk, T. Vuillaume, S. J. Wagner, R. Walter, J. Watson, M. White, R. White, R. Wiemann, A. Wierzcholska, M. Will, D. A. Williams, R. Wischnewski, A. Wolter, R. Yamazaki, S. Yanagita, L. Yang, T. Yoshikoshi, M. Zacharias, G. Zaharijas, D. Zaric, M. Zavrtanik, D. Zavrtanik, A. A. Zdziarski, A. Zech, H. Zechlin, V. I. Zhdanov, and M. Živec. Sensitivity of the Cherenkov Telescope Array for probing cosmology and fundamental physics with gamma-ray propagation. , 2021(2):048, Feb. 2021. doi: 10.1088/1475-7516/2021/02/048.

A. A. Abdo, M. Ackermann, I. Agudo, M. Ajello, H. D. Aller, M. F. Aller, E. Angelakis, A. A. Arkharov, M. Axelsson, U. Bach, L. Baldini, J. Ballet, G. Barbiellini, D. Bastieri, B. M. Baughman, K. Bechtol, R. Bellazzini, E. Benitez, A. Berdyugin, B. Berenji, R. D. Blandford, E. D. Bloom, M. Boettcher, E. Bonamente, A. W. Borgland, J. Bregeon, A. Brez, M. Brigida, P. Bruel, T. H. Burnett, D. Burrows, S. Buson, G. A. Caliandro, L. Calzoletti, R. A. Cameron, M. Capalbi, P. A. Caraveo, D. Carosati, J. M. Casandjian, E. Cavazzuti, C. Cecchi, Ö. Çelik, E. Charles, S. Chaty, A. Chekhtman, W. P. Chen,

J. Chiang, G. Chincarini, S. Ciprini, R. Claus, J. Cohen-Tanugi, S. Colafrancesco, L. R. Cominsky, J. Conrad, L. Costamante, S. Cutini, F. D'ammando, R. Deitrick, V. D'Elia, C. D. Dermer, A. de Angelis, F. de Palma, S. W. Digel, I. Donnarumma, E. d. C. e. Silva, P. S. Drell, R. Dubois, D. Dultzin, D. Dumora, A. Falcone, C. Farnier, C. Favuzzi, S. J. Fegan, W. B. Focke, E. Forné, P. Fortin, M. Frailis, L. Fuhrmann, Y. Fukazawa, S. Funk, P. Fusco, J. L. Gómez, F. Gargano, D. Gasparrini, N. Gehrels, S. Germani, B. Giebels, N. Giglietto, P. Giommi, F. Giordano, A. Giuliani, T. Glanzman, G. Godfrey, I. A. Grenier, C. Gronwall, J. E. Grove, L. Guillemot, S. Guiriec, M. A. Gurwell, D. Hadasch, Y. Hanabata, A. K. Harding, M. Hayashida, E. Hays, S. E. Healey, J. Heidt, D. Hiriart, D. Horan, E. A. Hoversten, R. E. Hughes, R. Itoh, M. S. Jackson, G. Jóhannesson, A. S. Johnson, W. N. Johnson, S. G. Jorstad, M. Kadler, T. Kamae, H. Katagiri, J. Kataoka, N. Kawai, J. Kennea, M. Kerr, G. Kimeridze, J. Knödlseder, M. L. Kocian, E. N. Kopatskaya, E. Koptelova, T. S. Konstantinova, Y. Y. Kovalev, Y. A. Kovalev, O. M. Kurtanidze, M. Kuss, J. Lande, V. M. Larionov, L. Latronico, P. Leto, E. Lindfors, F. Longo, F. Loparco, B. Lott, M. N. Lovellette, P. Lubrano, G. M. Madejski, A. Makeev, P. Marchegiani, A. P. Marscher, F. Marshall, W. Max-Moerbeck, M. N. Mazziotta, W. McConville, J. E. McEnery, C. Meurer, P. F. Michelson, W. Mitthumsiri, T. Mizuno, A. A. Moiseev, C. Monte, M. E. Monzani, A. Morselli, I. V. Moskalenko, S. Murgia, I. Nestoras, K. Nilsson, N. A. Nizhelsky, P. L. Nolan, J. P. Norris, E. Nuss, T. Ohsugi, R. Ojha, N. Omodei, E. Orlando, J. F. Ormes, J. Osborne, M. Ozaki, L. Pacciani, P. Padovani, C. Pagani, K. Page, D. Paneque, J. H. Panetta, D. Parent, M. Pasanen, V. Pavlidou, V. Pelassa, M. Pepe, M. Perri, M. Pesce-Rollins, S. Piranomonte, F. Piron, C. Pittori, T. A. Porter, S. Puccetti, F. Rahoui, S. Rainò, C. Raiteri, R. Rando, M. Razzano, A. Reimer, O. Reimer, T. Reposeur, J. L. Richards, S. Ritz, L. S. Rochester, A. Y. Rodriguez, R. W. Romani, J. A. Ros, M. Roth, P. Roustazadeh, F. Ryde, H. F. W. Sadrozinski, A. Sadun, D. Sanchez, A. Sander, P. M. Saz Parkinson, J. D. Scargle, A. Sellerholm, C. Sgrò, M. S. Shaw, L. A. Sigua, E. J. Siskind, D. A. Smith, P. D. Smith, G. Spandre, P. Spinelli, J. L. Starck, M. Stevenson, G. Stratta, M. S. Strickman, D. J. Suson, H. Tajima, H. Takahashi, T. Takahashi, L. O.

Takalo, T. Tanaka, J. B. Thayer, J. G. Thayer, D. J. Thompson, L. Tibaldo, D. F. Torres, G. Tosti, A. Tramacere, Y. Uchiyama, T. L. Usher, V. Vasileiou, F. Verrecchia, N. Vilchez, M. Villata, V. Vitale, A. P. Waite, P. Wang, B. L. Winer, K. S. Wood, T. Ylinen, J. A. Zensus, G. V. Zhekanis, and M. Ziegler. The Spectral Energy Distribution of Fermi Bright Blazars. , 716(1):30–70, June 2010a. doi: 10.1088/0004-637X/716/1/30.

A. A. Abdo, M. Ackermann, M. Ajello, A. Allafort, E. Antolini, W. B. Atwood, M. Axelsson, L. Baldini, J. Ballet, G. Barbiellini, D. Bastieri, B. M. Baughman, K. Bechtol, R. Bellazzini, B. Berenji, R. D. Blandford, E. D. Bloom, J. R. Bogart, E. Bonamente, A. W. Borgland, A. Bouvier, J. Bregeon, A. Brez, M. Brigida, P. Bruel, R. Buehler, T. H. Burnett, S. Buson, G. A. Caliandro, R. A. Cameron, A. Cannon, P. A. Caraveo, S. Carrigan, J. M. Casandjian, E. Cavazzuti, C. Cecchi, Ö. Çelik, A. Celotti, E. Charles, A. Chekhtman, A. W. Chen, C. C. Cheung, J. Chiang, S. Ciprini, R. Claus, J. Cohen-Tanugi, J. Conrad, L. Costamante, G. Cotter, S. Cutini, V. D'Elia, C. D. Dermer, A. de Angelis, F. de Palma, A. De Rosa, S. W. Digel, E. d. C. e. Silva, P. S. Drell, R. Dubois, D. Dumora, L. Escande, C. Farnier, C. Favuzzi, S. J. Fegan, E. C. Ferrara, W. B. Focke, P. Fortin, M. Frailis, Y. Fukazawa, S. Funk, P. Fusco, F. Gargano, D. Gasparrini, N. Gehrels, S. Germani, B. Giebels, N. Giglietto, P. Giommi, F. Giordano, M. Giroletti, T. Glanzman, G. Godfrey, P. Grandi, I. A. Grenier, M. H. Grondin, J. E. Grove, S. Guiriec, D. Hadasch, A. K. Harding, M. Hayashida, E. Hays, S. E. Healey, A. B. Hill, D. Horan, R. E. Hughes, G. Iafrate, R. Itoh, G. Jóhannesson, A. S. Johnson, R. P. Johnson, T. J. Johnson, W. N. Johnson, T. Kamae, H. Katagiri, J. Kataoka, N. Kawai, M. Kerr, J. Knödlseder, M. Kuss, J. Lande, L. Latronico, C. Lavalley, M. Lemoine-Goumard, M. Llena Garde, F. Longo, F. Loparco, B. Lott, M. N. Lovellette, P. Lubrano, G. M. Madejski, A. Makeev, G. Malaguti, E. Massaro, M. N. Mazziotta, W. McConville, J. E. McEnery, S. McGlynn, P. F. Michelson, W. Mitthumsiri, T. Mizuno, A. A. Moiseev, C. Monte, M. E. Monzani, A. Morselli, I. V. Moskalenko, S. Murgia, P. L. Nolan, J. P. Norris, E. Nuss, M. Ohno, T. Ohsugi, N. Omodei, E. Orlando, J. F. Ormes, M. Ozaki, D. Paneque, J. H. Panetta, D. Parent, V. Pelassa, M. Pepe, M. Pesce-Rollins, S. Piranomonte, F. Piron, T. A. Porter, S. Rainò, R. Rando, M. Razzano, A. Reimer,

O. Reimer, T. Reposeur, J. Ripken, S. Ritz, A. Y. Rodriguez, R. W. Romani, M. Roth, F. Ryde, H. F. W. Sadrozinski, D. Sanchez, A. Sander, P. M. Saz Parkinson, J. D. Scargle, C. Sgrò, M. S. Shaw, E. J. Siskind, P. D. Smith, G. Spandre, P. Spinelli, J. L. Starck, Ł. Stawarz, M. S. Strickman, D. J. Suson, H. Tajima, H. Takahashi, T. Takahashi, T. Tanaka, G. B. Taylor, J. B. Thayer, J. G. Thayer, D. J. Thompson, L. Tibaldo, D. F. Torres, G. Tosti, A. Tramacere, P. Ubertini, Y. Uchiyama, T. L. Usher, V. Vasileiou, N. Vilchez, M. Villata, V. Vitale, A. P. Waite, E. Wallace, P. Wang, B. L. Winer, K. S. Wood, Z. Yang, T. Ylinen, and M. Ziegler. The First Catalog of Active Galactic Nuclei Detected by the Fermi Large Area Telescope. , 715(1):429–457, May 2010b. doi: 10.1088/0004-637X/715/1/429.

A. A. Abdo, M. Ackermann, M. Ajello, E. Antolini, L. Baldini, J. Ballet, G. Barbiellini, D. Bastieri, B. M. Baughman, K. Bechtol, R. Bellazzini, B. Berenji, R. D. Blandford, E. D. Bloom, E. Bonamente, A. W. Borgland, A. Bouvier, J. Bregeon, A. Brez, M. Brigida, P. Bruel, T. H. Burnett, S. Buson, G. A. Caliandro, R. A. Cameron, P. A. Caraveo, S. Carrigan, J. M. Casandjian, E. Cavazzuti, C. Cecchi, Ö. Çelik, E. Charles, A. Chekhtman, C. C. Cheung, J. Chiang, S. Ciprini, R. Claus, J. Cohen-Tanugi, J. Conrad, L. Costamante, S. Cutini, C. D. Dermer, A. de Angelis, F. de Palma, E. d. C. e. Silva, P. S. Drell, R. Dubois, D. Dumora, C. Farnier, C. Favuzzi, S. J. Fegan, W. B. Focke, Y. Fukazawa, S. Funk, P. Fusco, F. Gargano, D. Gasparrini, N. Gehrels, S. Germani, N. Giglietto, P. Giommi, F. Giordano, T. Glanzman, G. Godfrey, I. A. Grenier, J. E. Grove, S. Guiriec, D. Hadasch, M. Hayashida, E. Hays, S. E. Healey, D. Horan, R. E. Hughes, R. Itoh, G. Jóhannesson, A. S. Johnson, T. J. Johnson, W. N. Johnson, T. Kamae, H. Katagiri, J. Kataoka, N. Kawai, J. Knödlseder, M. Kuss, J. Lande, L. Latronico, S. H. Lee, M. Lemoine-Goumard, M. Llena Garde, F. Longo, F. Loparco, B. Lott, M. N. Lovellette, P. Lubrano, G. M. Madejski, A. Makeev, M. N. Mazziotta, W. McConville, J. E. McEnery, C. Meurer, P. F. Michelson, W. Mitthumsiri, T. Mizuno, C. Monte, M. E. Monzani, A. Morselli, I. V. Moskalenko, S. Murgia, P. L. Nolan, J. P. Norris, E. Nuss, T. Ohsugi, N. Omodei, E. Orlando, J. F. Ormes, M. Ozaki, D. Paneque, J. H. Panetta, D. Parent, V. Pelassa, M. Pepe, M. Pesce-Rollins, F. Piron, T. A. Porter, S. Rainò,

R. Rando, M. Razzano, A. Reimer, O. Reimer, S. Ritz, L. S. Rochester, A. Y. Rodriguez, R. W. Romani, M. Roth, H. F. W. Sadrozinski, A. Sander, P. M. Saz Parkinson, J. D. Scargle, C. Sgrò, M. S. Shaw, P. D. Smith, G. Spandre, P. Spinelli, J. L. Starck, M. S. Strickman, A. W. Strong, D. J. Suson, H. Tajima, H. Takahashi, T. Takahashi, T. Tanaka, J. B. Thayer, J. G. Thayer, D. J. Thompson, L. Tibaldo, D. F. Torres, G. Tosti, A. Tramacere, Y. Uchiyama, T. L. Usher, V. Vasileiou, N. Vilchez, V. Vitale, A. P. Waite, P. Wang, B. L. Winer, K. S. Wood, Z. Yang, T. Ylinen, M. Ziegler, and Fermi LAT Collaboration. The Fermi-LAT High-Latitude Survey: Source Count Distributions and the Origin of the Extragalactic Diffuse Background. , 720(1):435–453, Sept. 2010c. doi: 10.1088/0004-637X/720/1/435.

A. A. Abdo, M. Ackermann, M. Ajello, W. B. Atwood, M. Axelsson, L. Baldini, J. Ballet, G. Barbiellini, D. Bastieri, B. M. Baughman, K. Bechtol, R. Bellazzini, B. Berenji, E. D. Bloom, G. Bogaert, E. Bonamente, A. W. Borgland , J. Bregeon, A. Brez, M. Brigida, P. Bruel, T. H. Burnett, G. A. Caliandro, R. A. Cameron, P. A. Caraveo, J. M. Casandjian, E. Cavazzuti, C. Cecchi, Ö. Çelik, A. Chekhtman, C. C. Cheung, J. Chiang, S. Ciprini, R. Claus, J. Cohen-Tanugi, J. Conrad, S. Cutini, C. D. Dermer, A. de Angelis, F. de Palma, S. W. Digel, E. d. C. e. Silva, P. S. Drell, R. Dubois, D. Dumora, C. Farnier, C. Favuzzi, S. J. Fegan, E. C. Ferrara, W. B. Focke, M. Frailis, L. Fuhrmann, Y. Fukazawa, S. Funk, P. Fusco, F. Gargano, D. Gasparrini, N. Gehrels, S. Germani, B. Giebels, N. Giglietto, F. Giordano, M. Giroletti, T. Glanzman, G. Godfrey, I. A. Grenier, M. H. Grondin, J. E. Grove, L. Guillemot, S. Guiriec, Y. Hanabata, A. K. Harding, M. Hayashida, E. Hays, R. E. Hughes, G. Jóhannesson, A. S. Johnson, R. P. Johnson, W. N. Johnson, M. Kadler, T. Kamae, H. Katagiri, J. Kataoka, M. Kerr, J. Knödlseder, M. L. Kocian, F. Kuehn, M. Kuss, J. Lande, L. Latronico, M. Lemoine-Goumard, F. Longo, F. Loparco, B. Lott, M. N. Lovellette, P. Lubrano, G. M. Madejski, A. Makeev, M. Marelli, E. Massaro, W. Max-Moerbeck, M. N. Mazziotta, W. McConville, J. E. McEnery, C. Meurer, P. F. Michelson, W. Mitthumsiri, T. Mizuno, A. A. Moiseev, C. Monte, M. E. Monzani, A. Morselli, I. V. Moskalenko, S. Murgia, P. L. Nolan, J. P. Norris, E. Nuss, T. Ohsugi, N. Omodei, E. Orlando, J. F. Ormes, M. Ozaki, D. Paneque, J. H. Panetta, D. Parent,

V. Pavlidou, T. J. Pearson, V. Pelassa, M. Pepe, M. Pesce-Rollins, F. Piron, T. A. Porter, S. Rainò, R. Rando, M. Razzano, S. Razzaque, A. Readhead, A. Reimer, O. Reimer, T. Reposeur, J. L. Richards, S. Ritz, L. S. Rochester, A. Y. Rodriguez, R. W. Romani, M. Roth, F. Ryde, H. F. W. Sadrozinski, D. Sanchez, A. Sander, P. M. Saz Parkinson, J. D. Scargle, C. Sgrò, M. S. Shaw, E. J. Siskind, D. A. Smith, P. D. Smith, G. Spandre, P. Spinelli, M. Stevenson, M. S. Strickman, D. J. Suson, H. Tajima, H. Takahashi, T. Tanaka, J. B. Thayer, J. G. Thayer, D. J. Thompson, L. Tibaldo, O. Tibolla, D. F. Torres, G. Tosti, A. Tramacere, P. Ubertini, Y. Uchiyama, T. L. Usher, V. Vasileiou, N. Vilchez, V. Vitale, A. P. Waite, P. Wang, B. L. Winer, K. S. Wood, H. Yasuda, T. Ylinen, J. A. Zensus, M. Ziegler, Fermi LAT Collaboration, E. Angelakis, T. Hovatta, E. Hoversten, Y. Ikejiri, K. S. Kawabata, Y. Y. Kovalev, Y. A. Kovalev, T. P. Krichbaum, M. L. Lister, A. Lähteenmäki, N. Marchili, P. Ogle, C. Pagani, A. B. Pushkarev, K. Sakimoto, M. Sasada, M. Tornikoski, M. Uemura, M. Yamanaka, T. Yamashita, Fermi LAT Collaboration, and Multifrequency Campaign Collaboration. PKS 1502+106: A New and Distant Gamma-ray Blazar in Outburst Discovered by the Fermi Large Area Telescope. , 710(1):810–827, Feb. 2010d. doi: 10.1088/0004-637X/710/1/810.

A. A. Abdo, M. Ackermann, M. Ajello, W. B. Atwood, L. Baldini, J. Ballet, G. Barbiellini, D. Bastieri, B. M. Baughman, K. Bechtol, R. Bellazzini, B. Berenji, R. D. Blandford, E. D. Bloom, E. Bonamente, A. W. Borgland, J. Bregeon, A. Brez, M. Brigida, P. Bruel, T. H. Burnett, S. Buson, G. A. Caliandro, R. A. Cameron, P. A. Caraveo, J. M. Casandjian, E. Cavazzuti, C. Cecchi, Ö. Çelik, E. Charles, A. Chekhtman, C. C. Cheung, J. Chiang, S. Ciprini, R. Claus, J. Cohen-Tanugi, L. R. Cominsky, J. Conrad, S. Cutini, C. D. Dermer, A. de Angelis, F. de Palma, S. W. Digel, G. di Bernardo, E. do Couto e Silva, P. S. Drell, A. Drlica-Wagner, R. Dubois, D. Dumora, C. Farnier, C. Favuzzi, S. J. Fegan, W. B. Focke, P. Fortin, M. Frailis, Y. Fukazawa, S. Funk, P. Fusco, D. Gaggero, F. Gargano, D. Gasparrini, N. Gehrels, S. Germani, B. Giebels, N. Giglietto, P. Giommi, F. Giordano, T. Glanzman, G. Godfrey, I. A. Grenier, M. H. Grondin, J. E. Grove, L. Guillemot, S. Guiriec, M. Gustafsson, Y. Hanabata, A. K. Harding, M. Hayashida, R. E. Hughes, R. Itoh, M. S. Jackson, G. Jóhannesson, A. S. Johnson, R. P. Johnson, T. J. Johnson, W. N.

Johnson, T. Kamae, H. Katagiri, J. Kataoka, N. Kawai, M. Kerr, J. Knödlseder, M. L. Kocian, F. Kuehn, M. Kuss, J. Lande, L. Latronico, M. Lemoine-Goumard, F. Longo, F. Loparco, B. Lott, M. N. Lovellette, P. Lubrano, G. M. Madejski, A. Makeev, M. N. Mazziotta, W. McConville, J. E. McEnery, C. Meurer, P. F. Michelson, W. Mitthumsiri, T. Mizuno, A. A. Moiseev, C. Monte, M. E. Monzani, A. Morselli, I. V. Moskalenko, S. Murgia, P. L. Nolan, J. P. Norris, E. Nuss, T. Ohsugi, N. Omodei, E. Orlando, J. F. Ormes, D. Paneque, J. H. Panetta, D. Parent, V. Pelassa, M. Pepe, M. Pesce-Rollins, F. Piron, T. A. Porter, S. Rainò, R. Rando, M. Razzano, A. Reimer, O. Reimer, T. Reposeur, S. Ritz, L. S. Rochester, A. Y. Rodriguez, M. Roth, F. Ryde, H. F. W. Sadrozinski, D. Sanchez, A. Sander, P. M. S. Parkinson, J. D. Scargle, A. Sellerholm, C. Sgrò, M. S. Shaw, E. J. Siskind, D. A. Smith, P. D. Smith, G. Spandre, P. Spinelli, J. L. Starck, M. S. Strickman, A. W. Strong, D. J. Suson, H. Tajima, H. Takahashi, T. Takahashi, T. Tanaka, J. B. Thayer, J. G. Thayer, D. J. Thompson, L. Tibaldo, D. F. Torres, G. Tosti, A. Tramacere, Y. Uchiyama, T. L. Usher, V. Vasileiou, N. Vilchez, V. Vitale, A. P. Waite, P. Wang, B. L. Winer, K. S. Wood, T. Ylinen, M. Ziegler, and Fermi LAT Collaboration. Spectrum of the Isotropic Diffuse Gamma-Ray Emission Derived from First-Year Fermi Large Area Telescope Data. , 104(10):101101, Mar. 2010e. doi: 10.1103/PhysRevLett.104.101101.

A. A. Abdo, M. Ackermann, M. Ajello, A. Allafort, L. Baldini, J. Ballet, G. Barbiellini, D. Bastieri, R. Bellazzini, B. Berenji, R. D. Bland ford, E. D. Bloom, E. Bonamente, A. W. Borgland , A. Bouvier, J. Bregeon, M. Brigida, P. Bruel, R. Buehler, S. Buson, G. A. Caliandro, R. A. Cameron, P. A. Caraveo, J. M. Casandjian, E. Cavazzuti, C. Cecchi, E. Charles, A. Chekhtman, C. C. Cheung, J. Chiang, S. Ciprini, R. Claus, J. Conrad, S. Cutini, F. D'Ammando, A. de Angelis, F. de Palma, C. D. Dermer, S. W. Digel, E. d. C. e. Silva, P. S. Drell, R. Dubois, D. Dumora, L. Escande, C. Favuzzi, S. J. Fegan, E. C. Ferrara, P. Fortin, Y. Fukazawa, P. Fusco, F. Gargano, D. Gasparrini, N. Gehrels, S. Germani, N. Giglietto, P. Giommi, F. Giordano, M. Giroletti, T. Glanzman, G. Godfrey, I. A. Grenier, J. E. Grove, S. Guiriec, D. Hadasch, M. Hayashida, E. Hays, D. Horan, R. Itoh, G. Jóhannesson, A. S. Johnson, T. Kamae, H. Katagiri, J. Kataoka, J. Knödlseder,

M. Kuss, J. Lande, S. Larsson, L. Latronico, S. H. Lee, F. Longo, F. Loparco, B. Lott, M. N. Lovellette, P. Lubrano, G. M. Madejski, A. Makeev, M. N. Mazziotta, W. McConville, J. E. McEnery, P. F. Michelson, W. Mitthumsiri, T. Mizuno, A. A. Moiseev, C. Monte, M. E. Monzani, A. Morselli, I. V. Moskalenko, S. Murgia, M. Naumann-Godo, S. Nishino, P. L. Nolan, J. P. Norris, E. Nuss, T. Ohsugi, A. Okumura, E. Orlando, J. F. Ormes, D. Paneque, V. Pelassa, M. Pesce-Rollins, M. Pierbattista, F. Piron, T. A. Porter, S. Rainò, R. Rando, S. Razzaque, A. Reimer, O. Reimer, S. Ritz, M. Roth, H. F. W. Sadrozinski, D. Sanchez, J. D. Scargle, T. L. Schalk, C. Sgrò, E. J. Siskind, P. D. Smith, G. Spandre, P. Spinelli, M. S. Strickman, H. Takahashi, T. Takahashi, T. Tanaka, Y. Tanaka, J. G. Thayer, J. B. Thayer, D. J. Thompson, L. Tibaldo, D. F. Torres, G. Tosti, A. Tramacere, E. Troja, J. Vand enbroucke, V. Vasileiou, G. Vianello, N. Vilchez, V. Vitale, A. P. Waite, P. Wang, B. L. Winer, K. S. Wood, Z. Yang, and M. Ziegler. Fermi Gamma-ray Space Telescope Observations of the Gamma-ray Outburst from 3C454.3 in November 2010. , 733(2):L26, June 2011. doi: 10.1088/2041-8205/733/2/L26.

A. U. Abeysekara, A. Archer, W. Benbow, R. Bird, A. Brill, R. Brose, J. H. Buckley, J. L. Christiansen, A. J. Chromey, M. K. Daniel, A. Falcone, Q. Feng, J. P. Finley, L. Fortson, A. Furniss, G. H. Gillanders, O. Gueta, D. Hanna, O. Hervet, J. Holder, G. Hughes, T. B. Humensky, C. A. Johnson, P. Kaaret, P. Kar, N. Kelley-Hoskins, M. Kertzman, D. Kieda, M. Krause, F. Krennrich, M. J. Lang, P. Moriarty, R. Mukherjee, S. O'Brien, R. A. Ong, A. N. Otte, N. Park, A. Petrashyk, M. Pohl, E. Pueschel, J. Quinn, K. Ragan, P. T. Reynolds, G. T. Richards, E. Roache, C. Rulten, I. Sadeh, M. Santander, S. S. Scott, G. H. Sembroski, K. Shahinyan, J. Tyler, S. P. Wakely, A. Weinstein, R. M. Wells, P. Wilcox, A. Wilhelm, D. A. Williams, T. J. Williamson, B. Zitzer, VERITAS Collaboration, and A. Kaur. VERITAS Observations of the BL Lac Object TXS 0506+056. , 861(2):L20, July 2018. doi: 10.3847/2041-8213/aad053.

A. U. Abeysekara, W. Benbow, R. Bird, A. Brill, R. Brose, M. Buchovecky, J. H. Buckley, J. L. Christiansen, A. J. Chromey, M. K. Daniel, J. Dumm, A. Falcone, Q. Feng, J. P. Finley, L. Fortson, A. Furniss, N. Galante, A. Gent, G. H. Gillanders, C. Giuri, O. Gueta, T. Hassan, O. Hervet, J. Holder, G. Hughes, T. B. Humensky, C. A. Johnson, P. Kaaret,

P. Kar, N. Kelley-Hoskins, M. Kertzman, D. Kieda, M. Krause, F. Krennrich, S. Kumar, M. J. Lang, P. Moriarty, R. Mukherjee, T. Nelson, D. Nieto, M. Nievas-Rosillo, S. O'Brien, R. A. Ong, A. N. Otte, N. Park, A. Petrashyk, A. Pichel, M. Pohl, R. R. Prado, E. Pueschel, J. Quinn, K. Ragan, P. T. Reynolds, G. T. Richards, E. Roache, A. C. Rovero, C. Rulten, I. Sadeh, M. Santander, G. H. Sembroski, K. Shahinyan, B. Stevenson, I. Sushch, J. Tyler, V. V. Vassiliev, S. P. Wakely, A. Weinstein, R. M. Wells, P. Wilcox, A. Wilhelm, D. A. Williams, B. Zitzer, V. A. Acciari, S. Ansoldi, L. A. Antonelli, A. Arbet Engels, D. Baack, A. Babić, B. Banerjee, U. Barres de Almeida, J. A. Barrio, J. Becerra González, W. Bednarek, L. Bellizzi, E. Bernardini, A. Berti, J. Besenrieder, W. Bhattacharyya, C. Bigongiari, A. Biland, O. Blanch, G. Bonnoli, G. Busetto, R. Carosi, G. Ceribella, Y. Chai, S. Cikota, S. M. Colak, U. Colin, E. Colombo, J. L. Contreras, J. Cortina, S. Covino, V. D'Elia, P. Da Vela, F. Dazzi, A. De Angelis, B. De Lotto, M. Delfino, J. Delgado, F. Di Pierro, E. Do Souto Espiñera, D. Dominis Prester, D. Dorner, M. Doro, S. Einecke, D. Elsaesser, V. Fallah Ramazani, A. Fattorini, A. Fernández-Barral, G. Ferrara, D. Fidalgo, L. Foffano, M. V. Fonseca, L. Font, C. Fruck, D. Galindo, S. Gallozzi, R. J. García López, M. Garczarczyk, S. Gasparyan, M. Gaug, N. Godinović, D. Green, D. Guberman, D. Hadasch, A. Hahn, J. Herrera, J. Hoang, D. Hrupec, S. Inoue, K. Ishio, Y. Iwamura, H. Kubo, J. Kushida, A. Lamastra, D. Lelas, F. Leone, E. Lindfors, S. Lombardi, F. Longo, M. López, R. López-Coto, A. López-Oramas, B. Machado de Oliveira Fraga, C. Maggio, P. Majumdar, M. Makariev, M. Mallamaci, G. Maneva, M. Manganaro, K. Mannheim, L. Maraschi, M. Mariotti, M. Martínez, S. Masuda, D. Mazin, D. Miceli, M. Minev, J. M. Miranda, R. Mirzoyan, E. Molina, A. Moralejo, D. Morcuende, V. Moreno, E. Moretti, P. Munar-Adrover, V. Neustroev, A. Niedzwiecki, M. Nievas Rosillo, C. Nigro, K. Nilsson, D. Ninci, K. Nishijima, K. Noda, L. Nogués, M. Nöthe, S. Paiano, J. Palacio, M. Palatiello, D. Paneque, R. Paoletti, J. M. Paredes, P. Peñil, M. Peresano, M. Persic, P. G. Prada Moroni, E. Prandini, I. Puljak, W. Rhode, M. Ribó, J. Rico, C. Righi, A. Rugliancich, L. Saha, N. Sahakyan, T. Saito, K. Satalecka, T. Schweizer, J. Sitarek, I. Šnidarić, D. Sobczynska, A. Somero, A. Stamerra, D. Strom, M. Strzys, S. Sun,

T. Surić, F. Tavecchio, P. Temnikov, T. Terzić, M. Teshima, N. Torres-Albà, S. Tsujimoto, J. van Scherpenberg, G. Vanzo, M. Vazquez Acosta, I. Vovk, M. Will, D. Zarić, H. D. Aller, M. F. Aller, M. T. Carini, D. Horan, B. Jordan, S. G. Jorstad, O. M. Kurtanidze, S. O. Kurtanidze, A. Lähteenmäki, V. M. Larionov, E. G. Larionova, G. Madejski, A. P. Marscher, W. Max-Moerbeck, J. W. Moody, D. A. Morozova, M. G. Nikolashvili, C. M. Raiteri, A. C. S. Readhead, J. L. Richards, A. C. Sadun, T. Sakamoto, L. A. Sigua, P. S. Smith, H. Talvikki, J. Tammi, M. Tornikoski, I. S. Troitsky, and M. Villata. The Great Markarian 421 Flare of 2010 February: Multiwavelength Variability and Correlation Studies. , 890(2):97, Feb. 2020. doi: 10.3847/1538-4357/ab6612.

A. Abramowski, F. Acero, F. Aharonian, A. G. Akhperjanian, G. Anton, S. Balenderan, A. Balzer, A. Barnacka, Y. Becherini, and et al. H.E.S.S. discovery of VHE γ-rays from the quasar PKS 1510-089. , 554:A107, June 2013. doi: 10.1051/0004-6361/201321135.

A. Abramowski, F. Aharonian, F. Ait Benkhali, A. G. Akhperjanian, E. O. Angüner, M. Backes, S. Balenderan, A. Balzer, A. Barnacka, Y. Becherini, J. Becker Tjus, D. Berge, S. Bernhard, K. Bernlöhr, E. Birsin, J. Biteau, M. Böttcher, C. Boisson, J. Bolmont, P. Bordas, J. Bregeon, F. Brun, P. Brun, M. Bryan, T. Bulik, S. Carrigan, S. Casanova, P. M. Chadwick, N. Chakraborty, R. Chalme-Calvet, R. C. G. Chaves, M. Chrétien, S. Colafrancesco, G. Cologna, J. Conrad, C. Couturier, Y. Cui, I. D. Davids, B. Degrange, C. Deil, P. deWilt, A. Djannati-Ataï, W. Domainko, A. Donath, L. O. Drury, G. Dubus, K. Dutson, J. Dyks, M. Dyrda, T. Edwards, K. Egberts, P. Eger, P. Espigat, C. Farnier, S. Fegan, F. Feinstein, M. V. Fernandes, D. Fernand ez, A. Fiasson, G. Fontaine, A. Förster, M. Füßling, S. Gabici, M. Gajdus, Y. A. Gallant, T. Garrigoux, G. Giavitto, B. Giebels, J. F. Glicenstein, D. Gottschall, M. H. Grondin, M. Grudzińska, D. Hadasch, S. Häffner, J. Hahn, J. Harris, G. Heinzelmann, G. Henri, G. Hermann, O. Hervet, A. Hillert, J. A. Hinton, W. Hofmann, P. Hofverberg, M. Holler, D. Horns, A. Ivascenko, A. Jacholkowska, C. Jahn, M. Jamrozy, M. Janiak, F. Jankowsky, I. Jung-Richardt, M. A. Kastendieck, K. Katarzyński, U. Katz, S. Kaufmann, B. Khélifi, M. Kieffer, S. Klepser, D. Klochkov, W. Kluźniak, D. Kolitzus, N. Komin, K. Kosack, S. Krakau, F. Krayzel, P. P. Krüger, H. Laffon, G. Lamanna, J. Lefaucheur, V. Le-

franc, A. Lemière, M. Lemoine-Goumard, J. P. Lenain, T. Lohse, A. Lopatin, C. C. Lu, V. Marandon, A. Marcowith, R. Marx, G. Maurin, N. Maxted, M. Mayer, T. J. L. McComb, J. Méhault, P. J. Meintjes, U. Menzler, M. Meyer, A. M. W. Mitchell, R. Moderski, M. Mohamed, K. Morâ, E. Moulin, T. Murach, M. de Naurois, J. Niemiec, S. J. Nolan, L. Oakes, H. Odaka, S. Ohm, B. Opitz, M. Ostrowski, I. Oya, M. Panter, R. D. Parsons, M. Paz Arribas, N. W. Pekeur, G. Pelletier, P. O. Petrucci, B. Peyaud, S. Pita, H. Poon, G. Pühlhofer, M. Punch, A. Quirrenbach, S. Raab, I. Reichardt, A. Reimer, O. Reimer, M. Renaud, R. de los Reyes, F. Rieger, C. Romoli, S. Rosier-Lees, G. Rowell, B. Rudak, C. B. Rulten, V. Sahakian, D. Salek, D. A. Sanchez, A. Santangelo, R. Schlickeiser, F. Schüssler, A. Schulz, U. Schwanke, S. Schwarzburg, S. Schwemmer, H. Sol, F. Spanier, G. Spengler, F. Spies, Ł. Stawarz, R. Steenkamp, C. Stegmann, F. Stinzing, K. Stycz, I. Sushch, J. P. Tavernet, T. Tavernier, A. M. Taylor, R. Terrier, M. Tluczykont, C. Trichard, K. Valerius, C. van Eldik, B. van Soelen, G. Vasileiadis, J. Veh, C. Venter, A. Viana, P. Vincent, J. Vink, H. J. Völk, F. Volpe, M. Vorster, T. Vuillaume, S. J. Wagner, P. Wagner, R. M. Wagner, M. Ward, M. Weidinger, Q. Weitzel, R. White, A. Wierzcholska, P. Willmann, A. Wörnlein, D. Wouters, R. Yang, V. Zabalza, D. Zaborov, M. Zacharias, A. A. Zdziarski, A. Zech, H. S. Zechlin, Y. Fukui, and H. E. S. S. Collaboration. Diffuse Galactic gamma-ray emission with H.E.S.S. , 90(12): 122007, Dec. 2014. doi: 10.1103/PhysRevD.90.122007.

V. A. Acciari, E. Aliu, M. Beilicke, W. Benbow, M. Böttcher, S. M. Bradbury, J. H. Buckley, V. Bugaev, Y. Butt, O. Celik, A. Cesarini, L. Ciupik, Y. C. K. Chow, P. Cogan, P. Colin, W. Cui, M. K. Daniel, T. Ergin, A. D. Falcone, S. J. Fegan, J. P. Finley, G. Finnegan, P. Fortin, L. F. Fortson, A. Furniss, D. Gall, G. H. Gilland ers, J. Grube, R. Guenette, G. Gyuk, D. Hanna, E. Hays, J. Holder, D. Horan, C. M. Hui, T. B. Humensky, A. Imran, P. Kaaret, N. Karlsson, M. Kertzman, D. B. Kieda, A. Konopelko, H. Krawczynski, F. Krennrich, M. J. Lang, S. LeBohec, K. Lee, G. Maier, A. McCann, M. McCutcheon, P. Moriarty, R. Mukherjee, T. Nagai, J. Niemiec, R. A. Ong, D. Pandel, J. S. Perkins, D. Petry, M. Pohl, J. Quinn, K. Ragan, L. C. Reyes, P. T. Reynolds, E. Roache, H. J. Rose, M. Schroedter, G. H. Sembroski, A. W. Smith, D. Steele, S. P. Swordy, J. A. Toner,

V. V. Vassiliev, R. Wagner, S. P. Wakely, J. E. Ward, T. C. Weekes, A. Weinstein, R. J. White, D. A. Williams, S. A. Wissel, M. Wood, and B. Zitzer. VERITAS Discovery of >200 GeV Gamma-Ray Emission from the Intermediate-Frequency-Peaked BL Lacertae Object W Comae. , 684(2):L73, Sept. 2008. doi: 10.1086/592244.

V. A. Acciari, E. Aliu, T. Arlen, M. Bautista, M. Beilicke, W. Benbow, S. M. Bradbury, J. H. Buckley, V. Bugaev, Y. Butt, K. Byrum, A. Cannon, O. Celik, A. Cesarini, Y. C. Chow, L. Ciupik, P. Cogan, W. Cui, R. Dickherber, S. J. Fegan, J. P. Finley, P. Fortin, L. Fortson, A. Furniss, D. Gall, G. H. Gillanders, J. Grube, R. Guenette, G. Gyuk, D. Hanna, J. Holder, D. Horan, C. M. Hui, T. B. Humensky, A. Imran, P. Kaaret, N. Karlsson, D. Kieda, J. Kildea, A. Konopelko, H. Krawczynski, F. Krennrich, M. J. Lang, S. LeBohec, G. Maier, A. McCann, M. McCutcheon, J. Millis, P. Moriarty, R. A. Ong, A. N. Otte, D. Pandel, J. S. Perkins, D. Petry, M. Pohl, J. Quinn, K. Ragan, L. C. Reyes, P. T. Reynolds, E. Roache, E. Roache, H. J. Rose, M. Schroedter, G. H. Sembroski, A. W. Smith, S. P. Swordy, M. Theiling, J. A. Toner, A. Varlotta, S. Vincent, S. P. Wakely, J. E. Ward, T. C. Weekes, A. Weinstein, D. A. Williams, S. Wissel, M. Wood, R. C. Walker, F. Davies, P. E. Hardee, W. Junor, C. Ly, F. Aharonian, A. G. Akhperjanian, G. Anton, U. Barres de Almeida, A. R. Bazer-Bachi, Y. Becherini, B. Behera, K. Bernlöhr, A. Bochow, C. Boisson, J. Bolmont, V. Borrel, J. Brucker, F. Brun, P. Brun, R. Bühler, T. Bulik, I. Büsching, T. Boutelier, P. M. Chadwick, A. Charbonnier, R. C. G. Chaves, A. Cheesebrough, L. M. Chounet, A. C. Clapson, G. Coignet, M. Dalton, M. K. Daniel, I. D. Davids, B. Degrange, C. Deil, H. J. Dickinson, A. Djannati-Ataï, W. Domainko, L. O. C. Drury, F. Dubois, G. Dubus, J. Dyks, M. Dyrda, K. Egberts, D. Emmanoulopoulos, P. Espigat, C. Farnier, F. Feinstein, A. Fiasson, A. Förster, G. Fontaine, M. Füßling, S. Gabici, Y. A. Gallant, L. Gérard, D. Gerbig, B. Giebels, J. F. Glicenstein, B. Glück, P. Goret, D. Göhring, D. Hauser, M. Hauser, S. Heinz, G. Heinzelmann, G. Henri, G. Hermann, J. A. Hinton, A. Hoffmann, W. Hofmann, M. Holleran, S. Hoppe, D. Horns, A. Jacholkowska, O. C. de Jager, C. Jahn, I. Jung, K. Katarzyński, U. Katz, S. Kaufmann, E. Kendziorra, M. Kerschhaggl, D. Khangulyan, B. Khélifi, D. Keogh, W. Kluźniak, T. Kneiske, N. Komin, K. Kosack, G. Lamanna, J. P. Lenain,

T. Lohse, V. Marandon, J. M. Martin, O. Martineau-Huynh, A. Marcowith, D. Maurin, T. J. L. McComb, M. C. Medina, R. Moderski, E. Moulin, M. Naumann-Godo, M. de Naurois, D. Nedbal, D. Nekrassov, B. Nicholas, J. Niemiec, S. J. Nolan, S. Ohm, J. F. Olive, E. Oña de Wilhelmi, K. J. Orford, M. Ostrowski, M. Panter, M. Paz Arribas, G. Pedaletti, G. Pelletier, P. O. Petrucci, S. Pita, G. Pühlhofer, M. Punch, A. Quirrenbach, B. C. Raubenheimer, M. Raue, S. M. Rayner, M. Renaud, F. Rieger, J. Ripken, L. Rob, S. Rosier-Lees, G. Rowell, B. Rudak, C. B. Rulten, J. Ruppel, V. Sahakian, A. Santangelo, R. Schlickeiser, F. M. Schöck, R. Schröder, U. Schwanke, S. Schwarzburg, S. Schwemmer, A. Shalchi, M. Sikora, J. L. Skilton, H. Sol, D. Spangler, Ł. Stawarz, R. Steenkamp, C. Stegmann, F. Stinzing, G. Superina, A. Szostek, P. H. Tam, J. P. Tavernet, R. Terrier, O. Tibolla, M. Tluczykont, C. van Eldik, G. Vasileiadis, C. Venter, L. Venter, J. P. Vialle, P. Vincent, M. Vivier, H. J. Völk, F. Volpe, S. J. Wagner, M. Ward, A. A. Zdziarski, A. Zech, H. Anderhub, L. A. Antonelli, P. Antoranz, M. Backes, C. Baixeras, S. Balestra, J. A. Barrio, D. Bastieri, J. Becerra González, J. K. Becker, W. Bednarek, K. Berger, E. Bernardini, A. Biland, R. K. Bock, G. Bonnoli, P. Bordas, D. B. Tridon, V. Bosch-Ramon, D. Bose, I. Braun, T. Bretz, I. Britvitch, M. Camara, E. Carmona, S. Commichau, J. L. Contreras, J. Cortina, M. T. Costado, S. Covino, V. Curtef, F. Dazzi, A. De Angelis, E. de Cea del Pozo, C. Delgado Mendez, R. De los Reyes, B. De Lotto, M. De Maria, F. De Sabata, A. Dominguez, D. Dorner, M. Doro, D. Elsaesser, M. Errando, D. Ferenc, E. Fernández, R. Firpo, M. V. Fonseca, L. Font, N. Galante, R. J. García López, M. Garczarczyk, M. Gaug, F. Goebel, D. Hadasch, M. Hayashida, A. Herrero, D. Hildebrand, D. Höhne-Mönch, J. Hose, C. C. Hsu, T. Jogler, D. Kranich, A. La Barbera, A. Laille, E. Leonardo, E. Lindfors, S. Lombardi, F. Longo, M. López, E. Lorenz, P. Majumdar, G. Maneva, N. Mankuzhiyil, K. Mannheim, L. Maraschi, M. Mariotti, M. Martínez, D. Mazin, M. Meucci, J. M. Miranda, R. Mirzoyan, H. Miyamoto, J. Moldón, M. Moles, A. Moralejo, D. Nieto, K. Nilsson, J. Ninkovic, I. Oya, R. Paoletti, J. M. Paredes, M. Pasanen, D. Pascoli, F. Pauss, R. G. Pegna, M. A. Perez-Torres, M. Persic, L. Peruzzo, F. Prada, E. Prandini, N. Puchades, I. Reichardt, W. Rhode, M. Ribó, J. Rico, M. Rissi, A. Robert, S. Rügamer, A. Sag-

gion, T. Y. Saito, M. Salvati, M. Sanchez-Conde, K. Satalecka, V. Scalzotto, V. Scapin, T. Schweizer, M. Shayduk, S. N. Shore, N. Sidro, A. Sierpowska-Bartosik, A. Sillanpää, J. Sitarek, D. Sobczynska, F. Spanier, A. Stamerra, L. S. Stark, L. Takalo, F. Tavecchio, P. Temnikov, D. Tescaro, M. Teshima, D. F. Torres, N. Turini, H. Vankov, R. M. Wagner, V. Zabalza, F. Zandanel, R. Zanin, J. Zapatero, VERITAS Collaboration, VLBA 43 GHz M87 Monitoring Team, H. E. S. S. Collaboration, and MAGIC Collaboration. Radio Imaging of the Very-High-Energy γ-Ray Emission Region in the Central Engine of a Radio Galaxy. *Science*, 325(5939):444, July 2009a. doi: 10.1126/science.1175406.

V. A. Acciari, E. Aliu, T. Arlen, M. Beilicke, W. Benbow, S. M. Bradbury, J. H. Buckley, V. Bugaev, Y. Butt, K. L. Byrum, O. Celik, A. Cesarini, L. Ciupik, Y. C. K. Chow, P. Cogan, P. Colin, W. Cui, M. K. Daniel, T. Ergin, A. D. Falcone, S. J. Fegan, J. P. Finley, P. Fortin, L. F. Fortson, A. Furniss, G. H. Gillanders, J. Grube, R. Guenette, G. Gyuk, D. Hanna, E. Hays, J. Holder, D. Horan, C. M. Hui, T. B. Humensky, A. Imran, P. Kaaret, N. Karlsson, M. Kertzman, D. B. Kieda, J. Kildea, A. Konopelko, H. Krawczynski, F. Krennrich, M. J. Lang, S. LeBohec, G. Maier, A. McCann, M. McCutcheon, P. Moriarty, R. Mukherjee, T. Nagai, J. Niemiec, R. A. Ong, D. Pandel, J. S. Perkins, M. Pohl, J. Quinn, K. Ragan, L. C. Reyes, P. T. Reynolds, H. J. Rose, M. Schroedter, G. H. Sembroski, A. W. Smith, D. Steele, S. P. Swordy, J. A. Toner, L. Valcarcel, V. V. Vassiliev, R. Wagner, S. P. Wakely, J. E. Ward, T. C. Weekes, A. Weinstein, R. J. White, D. A. Williams, S. A. Wissel, M. Wood, and B. Zitzer. VERITAS Observations of the BL Lac Object 1ES 1218+304. , 695(2):1370–1375, Apr. 2009b. doi: 10.1088/0004-637X/695/2/1370.

V. A. Acciari, E. Aliu, T. Arlen, T. Aune, M. Beilicke, W. Benbow, D. Boltuch, S. M. Bradbury, J. H. Buckley, V. Bugaev, K. Byrum, A. Cannon, A. Cesarini, L. Ciupik, W. Cui, R. Dickherber, C. Duke, A. Falcone, J. P. Finley, G. Finnegan, L. Fortson, A. Furniss, N. Galante, D. Gall, G. H. Gillanders, S. Godambe, J. Grube, R. Guenette, G. Gyuk, D. Hanna, J. Holder, C. M. Hui, T. B. Humensky, A. Imran, P. Kaaret, N. Karlsson, M. Kertzman, D. Kieda, A. Konopelko, H. Krawczynski, F. Krennrich, M. J. Lang, G. Maier, S. McArthur, M. McCutcheon, P. Moriarty, R. A. Ong, A. N.

Otte, M. Ouellette, D. Pandel, J. S. Perkins, A. Pichel, M. Pohl, J. Quinn, K. Ragan, L. C. Reyes, P. T. Reynolds, E. Roache, H. J. Rose, A. C. Rovero, M. Schroedter, G. H. Sembroski, G. D. Senturk, D. Steele, S. P. Swordy, M. Theiling, S. Thibadeau, A. Varlotta, V. V. Vassiliev, S. Vincent, R. G. Wagner, S. P. Wakely, J. E. Ward, T. C. Weekes, A. Weinstein, T. Weisgarber, D. A. Williams, S. Wissel, M. Wood, B. Zitzer, I. Garson, A., K. Lee, A. C. Sadun, M. Carini, D. Barnaby, K. Cook, J. Maune, A. Pease, S. Smith, R. Walters, A. Berdyugin, E. Lindfors, K. Nilsson, M. Pasanen, J. Sainio, A. Sillanpaa, L. O. Takalo, C. Villforth, T. Montaruli, M. Baker, A. Lahteenmaki, M. Tornikoski, T. Hovatta, E. Nieppola, H. D. Aller, and M. F. Aller. TeV and Multi-wavelength Observations of Mrk 421 in 2006-2008. , 738(1):25, Sept. 2011. doi: 10.1088/0004-637X/738/1/25.

B. S. Acharya, M. Actis, T. Aghajani, G. Agnetta, J. Aguilar, F. Aharonian, M. Ajello, A. Akhperjanian, M. Alcubierre, J. Aleksić, R. Alfaro, E. Aliu, A. J. Allafort, D. Allan, I. Allekotte, E. Amato, J. Anderson, E. O. Angüner, L. A. Antonelli, P. Antoranz, A. Aravantinos, T. Arlen, T. Armstrong, H. Arnaldi, L. Arrabito, K. Asano, T. Ashton, H. G. Asorey, Y. Awane, H. Baba, A. Babic, N. Baby, J. Bähr, A. Bais, C. Baixeras, S. Bajtlik, M. Balbo, D. Balis, C. Balkowski, A. Bamba, R. Bandiera, A. Barber, C. Barbier, M. Barceló, A. Barnacka, J. Barnstedt, U. Barres de Almeida, J. A. Barrio, A. Basili, S. Basso, D. Bastieri, C. Bauer, A. Baushev, J. Becerra, Y. Becherini, K. C. Bechtol, J. Becker Tjus, V. Beckmann, W. Bednarek, B. Behera, M. Belluso, W. Benbow, J. Berdugo, K. Berger, F. Bernard, T. Bernardino, K. Bernlöhr, N. Bhat, S. Bhattacharyya, C. Bigongiari, A. Biland, S. Billotta, T. Bird, E. Birsin, E. Bissaldi, J. Biteau, M. Bitossi, S. Blake, O. Blanch Bigas, P. Blasi, A. Bobkov, V. Boccone, M. Boettcher, L. Bogacz, J. Bogart, M. Bogdan, C. Boisson, J. Boix Gargallo, J. Bolmont, G. Bonanno, A. Bonardi, T. Bonev, P. Bonifacio, G. Bonnoli, P. Bordas, A. Borgland, J. Borkowski, R. Bose, O. Botner, A. Bottani, L. Bouchet, M. Bourgeat, C. Boutonnet, A. Bouvier, S. Brau-Nogué, I. Braun, T. Bretz, M. Briggs, T. Bringmann, P. Brook, P. Brun, L. Brunetti, T. Buanes, J. Buckley, R. Buehler, V. Bugaev, A. Bulgarelli, T. Bulik, G. Busetto, S. Buson, K. Byrum, M. Cailles, R. Cameron, J. Camprecios,

R. Canestrari, S. Cantu, M. Capalbi, P. Caraveo, E. Carmona, A. Carosi, J. Carr, P. H. Carton, S. Casanova, M. Casiraghi, O. Catalano, S. Cavazzani, S. Cazaux, M. Cerruti, E. Chabanne, P. Chadwick, C. Champion, A. Chen, J. Chiang, L. Chiappetti, M. Chikawa, V. R. Chitnis, F. Chollet, J. Chudoba, M. Cieślar, A. Cillis, J. Cohen-Tanugi, S. Colafrancesco, P. Colin, J. Colome, S. Colonges, M. Compin, P. Conconi, V. Conforti, V. Connaughton, J. Conrad, J. L. Contreras, P. Coppi, P. Corona, D. Corti, J. Cortina, L. Cossio, H. Costantini, G. Cotter, B. Courty, S. Couturier, S. Covino, G. Crimi, S. J. Criswell, J. Croston, G. Cusumano, M. Dafonseca, O. Dale, M. Daniel, J. Darling, I. Davids, F. Dazzi, A. De Angelis, V. De Caprio, F. De Frondat, E. M. de Gouveia Dal Pino, I. de la Calle, G. A. De La Vega, R. de los Reyes Lopez, B. De Lotto, A. De Luca, J. R. T. de Mello Neto, M. de Naurois, Y. de Oliveira, E. de Oña Wilhelmi, V. de Souza, G. Decerprit, G. Decock, C. Deil, E. Delagnes, G. Deleglise, C. Delgado, D. Della Volpe, P. Demange, G. Depaola, A. Dettlaff, A. Di Paola, F. Di Pierro, C. Díaz, J. Dick, R. Dickherber, H. Dickinson, V. Diez-Blanco, S. Digel, D. Dimitrov, G. Disset, A. Djannati-Ataï, M. Doert, M. Dohmke, W. Domainko, D. Dominis Prester, A. Donat, D. Dorner, M. Doro, J. L. Dournaux, G. Drake, D. Dravins, L. Drury, F. Dubois, R. Dubois, G. Dubus, C. Dufour, D. Dumas, J. Dumm, D. Durand, J. Dyks, M. Dyrda, J. Ebr, E. Edy, K. Egberts, P. Eger, S. Einecke, C. Eleftheriadis, S. Elles, D. Emmanoulopoulos, D. Engelhaupt, R. Enomoto, J. P. Ernenwein, M. Errando, A. Etchegoyen, P. Evans, A. Falcone, D. Fantinel, K. Farakos, C. Farnier, G. Fasola, B. Favill, E. Fede, S. Federici, S. Fegan, F. Feinstein, D. Ferenc, P. Ferrando, M. Fesquet, A. Fiasson, E. Fillin-Martino, D. Fink, C. Finley, J. P. Finley, M. Fiorini, R. Firpo Curcoll, H. Flores, D. Florin, W. Focke, C. Föhr, E. Fokitis, L. Font, G. Fontaine, M. Fornasa, A. Förster, L. Fortson, N. Fouque, A. Franckowiak, C. Fransson, G. Fraser, R. Frei, I. F. M. Albuquerque, L. Fresnillo, C. Fruck, Y. Fujita, Y. Fukazawa, Y. Fukui, S. Funk, W. Gäbele, S. Gabici, R. Gabriele, A. Gadola, N. Galante, D. Gall, Y. Gallant, J. Gámez-García, B. García, R. Garcia López, D. Gardiol, D. Garrido, L. Garrido, D. Gascon, M. Gaug, J. Gaweda, L. Gebremedhin, N. Geffroy, L. Gerard, A. Ghedina, M. Ghigo, E. Giannakaki, F. Gianotti, S. Giarrusso, G. Giavitto, B. Giebels, V. Gika, P. Giommi, N. Girard,

E. Giro, A. Giuliani, T. Glanzman, J. F. Glicenstein, N. Godinovic, V. Golev, M. Gomez Berisso, J. Gómez-Ortega, M. M. Gonzalez, A. González, F. González, A. González Muñoz, K. S. Gothe, M. Gougerot, R. Graciani, P. Grandi, F. Grañena, J. Granot, G. Grasseau, R. Gredig, A. Green, T. Greenshaw, T. Grégoire, O. Grimm, J. Grube, M. Grudzinska, V. Gruev, S. Grünewald, J. Grygorczuk, V. Guarino, S. Gunji, G. Gyuk, D. Hadasch, R. Hagiwara, J. Hahn, N. Hakansson, A. Hallgren, N. Hamer Heras, S. Hara, M. J. Hardcastle, J. Harris, T. Hassan, K. Hatanaka, T. Haubold, A. Haupt, T. Hayakawa, M. Hayashida, R. Heller, F. Henault, G. Henri, G. Hermann, R. Hermel, A. Herrero, N. Hidaka, J. Hinton, D. Hoffmann, W. Hofmann, P. Hofverberg, J. Holder, D. Horns, D. Horville, J. Houles, M. Hrabovsky, D. Hrupec, H. Huan, B. Huber, J. M. Huet, G. Hughes, T. B. Humensky, J. Huovelin, A. Ibarra, J. M. Illa, D. Impiombato, S. Incorvaia, S. Inoue, Y. Inoue, K. Ioka, E. Ismailova, C. Jablonski, A. Jacholkowska, M. Jamrozy, M. Janiak, P. Jean, C. Jeanney, J. J. Jimenez, T. Jogler, T. Johnson, L. Journet, C. Juffroy, I. Jung, P. Kaaret, S. Kabuki, M. Kagaya, J. Kakuwa, C. Kalkuhl, R. Kankanyan, A. Karastergiou, K. Kärcher, M. Karczewski, S. Karkar, J. Kasperek, D. Kastana, H. Katagiri, J. Kataoka, K. Katarzyński, U. Katz, N. Kawanaka, B. Kellner-Leidel, H. Kelly, E. Kendziorra, B. Khélifi, D. B. Kieda, T. Kifune, T. Kihm, T. Kishimoto, K. Kitamoto, W. Kluźniak, C. Knapic, J. Knapp, J. Knödlseder, F. Köck, J. Kocot, K. Kodani, J. H. Köhne, K. Kohri, K. Kokkotas, D. Kolitzus, N. Komin, I. Kominis, Y. Konno, H. Köppel, P. Korohoda, K. Kosack, G. Koss, R. Kossakowski, P. Kostka, R. Koul, G. Kowal, S. Koyama, J. Kozioł, T. Krähenbühl, J. Krause, H. Krawzcynski, F. Krennrich, A. Krepps, A. Kretzschmann, R. Krobot, P. Krueger, H. Kubo, V. A. Kudryavtsev, J. Kushida, A. Kuznetsov, A. La Barbera, N. La Palombara, V. La Parola, G. La Rosa, K. Lacombe, G. Lamanna, J. Lande, D. Languignon, J. Lapington, P. Laporte, C. Lavalley, T. Le Flour, A. Le Padellec, S. H. Lee, W. H. Lee, M. A. Leigui de Oliveira, D. Lelas, J. P. Lenain, D. J. Leopold, T. Lerch, L. Lessio, B. Lieunard, E. Lindfors, A. Liolios, A. Lipniacka, H. Lockart, T. Lohse, S. Lombardi, A. Lopatin, M. Lopez, R. López-Coto, A. López-Oramas, A. Lorca, E. Lorenz, P. Lubinski, F. Lucarelli, H. Lüdecke, J. Ludwin, P. L. Luque-Escamilla, W. Lustermann, O. Luz, E. Lyard, M. C.

Maccarone, T. J. Maccarone, G. M. Madejski, A. Madhavan, M. Mahabir, G. Maier, P. Majumdar, G. Malaguti, S. Maltezos, A. Manalaysay, A. Mancilla, D. Mand at, G. Maneva, A. Mangano, P. Manigot, K. Mannheim, I. Manthos, N. Maragos, A. Marcowith, M. Mariotti, M. Marisaldi, S. Markoff, A. Marszałek, C. Martens, J. Martí, J. M. Martin, P. Martin, G. Martínez, F. Martínez, M. Martínez, A. Masserot, A. Mastichiadis, A. Mathieu, H. Matsumoto, F. Mattana, S. Mattiazzo, G. Maurin, S. Maxfield, J. Maya, D. Mazin, L. Mc Comb, N. McCubbin, I. McHardy, R. McKay, C. Medina, C. Melioli, D. Melkumyan, S. Mereghetti, P. Mertsch, M. Meucci, J. Michałowski, P. Micolon, A. Mihailidis, T. Mineo, M. Minuti, N. Mirabal, F. Mirabel, J. M. Miranda, R. Mirzoyan, T. Mizuno, B. Moal, R. Moderski, I. Mognet, E. Molinari, M. Molinaro, T. Montaruli, I. Monteiro, P. Moore, A. Moralejo Olaizola, M. Mordalska, C. Morello, K. Mori, F. Mottez, Y. Moudden, E. Moulin, I. Mrusek, R. Mukherjee, P. Munar-Adrover, H. Muraishi, K. Murase, A. Murphy, S. Nagataki, T. Naito, D. Nakajima, T. Nakamori, K. Nakayama, C. Naumann, D. Naumann, M. Naumann-Godo, P. Nayman, D. Nedbal, D. Neise, L. Nellen, V. Neustroev, N. Neyroud, L. Nicastro, J. Nicolau-Kukliński, A. Niedźwiecki, J. Niemiec, D. Nieto, A. Nikolaidis, K. Nishijima, S. Nolan, R. Northrop, D. Nosek, N. Nowak, A. Nozato, P. O'Brien, Y. Ohira, M. Ohishi, S. Ohm, H. Ohoka, T. Okuda, A. Okumura, J. F. Olive, R. A. Ong, R. Orito, M. Orr, J. Osborne, M. Ostrowski, L. A. Otero, N. Otte, E. Ovcharov, I. Oya, A. Ozieblo, L. Padilla, S. Paiano, D. Paillot, A. Paizis, S. Palanque, M. Palatka, J. Pallota, K. Panagiotidis, J. L. Panazol, D. Paneque, M. Panter, R. Paoletti, A. Papayannis, G. Papyan, J. M. Paredes, G. Pareschi, G. Parks, J. M. Parraud, D. Parsons, M. Paz Arribas, M. Pech, G. Pedaletti, V. Pelassa, D. Pelat, M. d. C. Perez, M. Persic, P. O. Petrucci, B. Peyaud, A. Pichel, S. Pita, F. Pizzolato, Ł. Platos, R. Platzer, L. Pogosyan, M. Pohl, G. Pojmanski, J. D. Ponz, W. Potter, J. Poutanen, E. Prandini, J. Prast, R. Preece, F. Profeti, H. Prokoph, M. Prouza, M. Proyetti, I. Puerto-Gimenez, G. Pühlhofer, I. Puljak, M. Punch, R. Pyzioł, E. J. Quel, J. Quinn, A. Quirrenbach, E. Racero, P. J. Rajda, P. Ramon, R. Rando, R. C. Rannot, M. Rataj, M. Raue, P. Reardon, O. Reimann, A. Reimer, O. Reimer, K. Reitberger, M. Renaud, S. Renner, B. Reville, W. Rhode, M. Ribó, M. Ribordy, M. G. Richer,

J. Rico, J. Ridky, F. Rieger, P. Ringegni, J. Ripken, P. R. Ristori, A. Riviére, S. Rivoire, L. Rob, U. Roeser, R. Rohlfs, G. Rojas, P. Romano, W. Romaszkan, G. E. Romero, S. Rosen, S. Rosier Lees, D. Ross, G. Rouaix, J. Rousselle, S. Rousselle, A. C. Rovero, F. Roy, S. Royer, B. Rudak, C. Rulten, M. Rupiński, F. Russo, F. Ryde, B. Sacco, E. O. Saemann, A. Saggion, V. Sahakian, K. Saito, T. Saito, Y. Saito, N. Sakaki, R. Sakonaka, A. Salini, F. Sanchez, M. Sanchez-Conde, A. Sandoval, H. Sand aker, E. Sant'Ambrogio, A. Santangelo, E. M. Santos, A. Sanuy, L. Sapozhnikov, S. Sarkar, N. Sartore, H. Sasaki, K. Satalecka, M. Sawada, V. Scalzotto, V. Scapin, M. Scarcioffolo, J. Schafer, T. Schanz, S. Schlenstedt, R. Schlickeiser, T. Schmidt, J. Schmoll, P. Schovanek, M. Schroedter, C. Schultz, J. Schultze, A. Schulz, K. Schure, T. Schwab, U. Schwanke, J. Schwarz, S. Schwarzburg, T. Schweizer, S. Schwemmer, A. Segreto, J. H. Seiradakis, G. H. Sembroski, K. Seweryn, M. Sharma, M. Shayduk, R. C. Shellard, J. Shi, T. Shibata, A. Shibuya, E. Shum, L. Sidoli, M. Sidz, J. Sieiro, M. Sikora, J. Silk, A. Sillanpää, B. B. Singh, J. Sitarek, C. Skole, R. Smareglia, A. Smith, D. Smith, J. Smith, N. Smith, D. Sobczyńska, H. Sol, G. Sottile, M. Sowiński, F. Spanier, D. Spiga, S. Spyrou, V. Stamatescu, A. Stamerra, R. Starling, Ł. Stawarz, R. Steenkamp, C. Stegmann, S. Steiner, N. Stergioulas, R. Sternberger, M. Sterzel, F. Stinzing, M. Stodulski, U. Straumann, E. Strazzeri, L. Stringhetti, A. Suarez, M. Suchenek, R. Sugawara, K. H. Sulanke, S. Sun, A. D. Supanitsky, T. Suric, P. Sutcliffe, J. Sykes, M. Szanecki, T. Szepieniec, A. Szostek, G. Tagliaferri, H. Tajima, H. Takahashi, K. Takahashi, L. Takalo, H. Takami, G. Talbot, J. Tammi, M. Tanaka, S. Tanaka, J. Tasan, M. Tavani, J. P. Tavernet, L. A. Tejedor, I. Telezhinsky, P. Temnikov, C. Tenzer, Y. Terada, R. Terrier, M. Teshima, V. Testa, D. Tezier, D. Thuermann, L. Tibaldo, O. Tibolla, A. Tiengo, M. Tluczykont, C. J. Todero Peixoto, F. Tokanai, M. Tokarz, K. Toma, K. Torii, M. Tornikoski, D. F. Torres, M. Torres, G. Tosti, T. Totani, F. Toussenel, G. Tovmassian, P. Travnicek, M. Trifoglio, I. Troyano, K. Tsinganos, H. Ueno, K. Umehara, S. S. Upadhya, T. Usher, M. Uslenghi, J. F. Valdes-Galicia, P. Vallania, G. Vallejo, W. van Driel, C. van Eldik, J. Vandenbrouke, J. Vand erwalt, H. Vankov, G. Vasileiadis, V. Vassiliev, D. Veberic, I. Vegas, S. Vercellone, S. Vergani, C. Veyssiére, J. P. Vialle, A. Viana, M. Videla,

P. Vincent, S. Vincent, J. Vink, N. Vlahakis, L. Vlahos, P. Vogler, A. Vollhardt, H. P. von Gunten, S. Vorobiov, C. Vuerli, V. Waegebaert, R. Wagner, R. G. Wagner, S. Wagner, S. P. Wakely, R. Walter, T. Walther, K. Warda, R. Warwick, P. Wawer, R. Wawrzaszek, N. Webb, P. Wegner, A. Weinstein, Q. Weitzel, R. Welsing, M. Werner, H. Wetteskind, R. White, A. Wierzcholska, S. Wiesand, M. Wilkinson, D. A. Williams, R. Willingale, K. Winiarski, R. Wischnewski, Ł. Wiśniewski, M. Wood, A. Wörnlein, Q. Xiong, K. K. Yadav, H. Yamamoto, T. Yamamoto, R. Yamazaki, S. Yanagita, J. M. Yebras, D. Yelos, A. Yoshida, T. Yoshida, T. Yoshikoshi, V. Zabalza, M. Zacharias, A. Zajczyk, R. Zanin, A. Zdziarski, A. Zech, A. Zhao, X. Zhou, K. Ziętara, J. Ziolkowski, P. Ziółkowski, V. Zitelli, C. Zurbach, P. Żychowski, and CTA Consortium. Introducing the CTA concept. *Astroparticle Physics*, 43:3–18, Mar 2013. doi: 10.1016/j.astropartphys.2013.01.007.

A. Acharyya, I. Agudo, E. O. Angüner, R. Alfaro, J. Alfaro, C. Alispach, R. Aloisio, R. Alves Batista, J. P. Amans, L. Amati, and et al. Monte Carlo studies for the optimisation of the Cherenkov Telescope Array layout. *Astroparticle Physics*, 111:35–53, Sept. 2019. doi: 10.1016/j.astropartphys.2019.04.001.

A. Acharyya, P. M. Chadwick, and A. M. Brown. Locating the gamma-ray emission region in the brightest Fermi-LAT Flat Spectrum Radio Quasars. , Nov. 2020. doi: 10.1093/mnras/staa3483.

A. Acharyya, R. Adam, C. Adams, I. Agudo, A. Aguirre-Santaella, R. Alfaro, J. Alfaro, C. Alispach, R. Aloisio, R. Alves Batista, L. Amati, G. Ambrosi, E. O. Angüner, L. A. Antonelli, C. Aramo, A. Araudo, T. Armstrong, F. Arqueros, K. Asano, Y. Ascasíbar, M. Ashley, C. Balazs, O. Ballester, A. Baquero Larriva, V. Barbosa Martins, M. Barkov, U. Barres de Almeida, J. A. Barrio, D. Bastieri, J. Becerra, G. Beck, J. Becker Tjus, W. Benbow, M. Benito, D. Berge, E. Bernardini, K. Bernlöhr, A. Berti, B. Bertucci, V. Beshley, B. Biasuzzi, A. Biland, E. Bissaldi, J. Biteau, O. Blanch, J. Blazek, F. Bocchino, C. Boisson, L. Bonneau Arbeletche, P. Bordas, Z. Bosnjak, E. Bottacini, V. Bozhilov, J. Bregeon, A. Brill, T. Bringmann, A. M. Brown, P. Brun, F. Brun, P. Bruno, A. Bulgarelli, M. Burton, A. Burtovoi, M. Buscemi, R. Cameron,

M. Capasso, A. Caproni, R. Capuzzo-Dolcetta, P. Caraveo, R. Carosi, A. Carosi, S. Casanova, E. Cascone, F. Cassol, F. Catalani, D. Cauz, M. Cerruti, P. Chadwick, S. Chaty, A. Chen, M. Chernyakova, G. Chiaro, A. Chiavassa, M. Chikawa, J. Chudoba, M. Çolak, V. Conforti, R. Coniglione, F. Conte, J. L. Contreras, J. Coronado-Blazquez, A. Costa, H. Costantini, G. Cotter, P. Cristofari, A. D'Aimath, F. D'Ammando, L. A. Damone, M. K. Daniel, F. Dazzi, A. De Angelis, V. De Caprio, R. de Cássia dos Anjos, E. M. de Gouveia Dal Pino, B. De Lotto, D. De Martino, E. de Oña Wilhelmi, F. De Palma, V. de Souza, C. Delgado, A. G. Delgado Giler, D. della Volpe, D. Depaoli, T. Di Girolamo, F. Di Pierro, L. Di Venere, S. Diebold, A. Dmytriiev, A. Domínguez, A. Donini, M. Doro, J. Ebr, C. Eckner, T. D. P. Edwards, T. R. N. Ekoume, D. Elsässer, C. Evoli, D. Falceta-Goncalves, E. Fedorova, S. Fegan, Q. Feng, G. Ferrand, G. Ferrara, E. Fiandrini, A. Fiasson, M. Filipovic, V. Fioretti, M. Fiori, L. Foffano, G. Fontaine, O. Fornieri, F. J. Franco, S. Fukami, Y. Fukui, D. Gaggero, G. Galaz, V. Gammaldi, E. Garcia, M. Garczarczyk, D. Gascon, A. Gent, A. Ghalumyan, F. Gianotti, M. Giarrusso, G. Giavitto, N. Giglietto, F. Giordano, A. Giuliani, J. Glicenstein, R. Gnatyk, P. Goldoni, M. M. González, K. Gourgouliatos, J. Granot, D. Grasso, J. Green, A. Grillo, O. Gueta, S. Gunji, A. Halim, T. Hassan, M. Heller, S. Hernández Cadena, N. Hiroshima, B. Hnatyk, W. Hofmann, J. Holder, D. Horan, J. Hörandel, P. Horvath, T. Hovatta, M. Hrabovsky, D. Hrupec, G. Hughes, T. B. Humensky, M. Hütten, M. Iarlori, T. Inada, S. Inoue, F. Iocco, M. Iori, M. Jamrozy, P. Janecek, W. Jin, L. Jouvin, J. Jurysek, E. Karukes, K. Katarzyński, D. Kazanas, D. Kerszberg, M. C. Kherlakian, R. Kissmann, J. Knödlseder, Y. Kobayashi, K. Kohri, N. Komin, H. Kubo, J. Kushida, G. Lamanna, J. Lapington, P. Laporte, M. A. Leigui de Oliveira, J. Lenain, F. Leone, G. Leto, E. Lindfors, T. Lohse, S. Lombardi, F. Longo, A. Lopez, M. López, R. López-Coto, S. Loporchio, P. L. Luque-Escamilla, E. Mach, C. Maggio, G. Maier, M. Mallamaci, R. Malta Nunes de Almeida, D. Mandat, M. Manganaro, S. Mangano, G. Manicò, M. Marculewicz, M. Mariotti, S. Markoff, P. Marquez, J. Martí, O. Martinez, M. Martínez, G. Martínez, H. Martínez-Huerta, G. Maurin, D. Mazin, J. D. Mbarubucyeye, D. Medina Miranda, M. Meyer, M. Miceli, T. Miener, M. Minev, J. M. Miranda, R. Mirzoyan, T. Mizuno, B. Mode,

R. Moderski, L. Mohrmann, E. Molina, T. Montaruli, A. Moralejo, D. Morcuende-Parrilla, A. Morselli, R. Mukherjee, C. Mundell, A. Nagai, T. Nakamori, R. Nemmen, J. Niemiec, D. Nieto, M. Nikołajuk, D. Ninci, K. Noda, D. Nosek, S. Nozaki, Y. Ohira, M. Ohishi, Y. Ohtani, T. Oka, A. Okumura, R. A. Ong, M. Orienti, R. Orito, M. Orlandini, S. Orlando, E. Orlando, M. Ostrowski, I. Oya, I. Pagano, A. Pagliaro, M. Palatiello, F. R. Pantaleo, J. M. Paredes, G. Pareschi, N. Parmiggiani, B. Patricelli, L. Pavletić, A. Pe'er, M. Pecimotika, J. Pérez-Romero, M. Persic, O. Petruk, K. Pfrang, G. Piano, P. Piatteli, E. Pietropaolo, R. Pillera, B. Pilszyk, F. Pintore, M. Pohl, V. Poireau, R. R. Prado, E. Prandini, J. Prast, G. Principe, H. Prokoph, M. Prouza, H. Przybilski, G. Pühlhofer, M. L. Pumo, F. Queiroz, A. Quirrenbach, S. Rainò, R. Rando, S. Razzaque, S. Recchia, O. Reimer, A. Reisenegger, Y. Renier, W. Rhode, D. Ribeiro, M. Ribó, T. Richtler, J. Rico, F. Rieger, L. Rinchiuso, V. Rizi, J. Rodriguez, G. Rodriguez Fernandez, J. C. Rodriguez Ramirez, G. Rojas, P. Romano, G. Romeo, J. Rosado, G. Rowell, B. Rudak, F. Russo, I. Sadeh, E. Sæther Hatlen, S. Safi-Harb, F. Salesa Greus, G. Salina, D. Sanchez, M. Sánchez-Conde, P. Sangiorgi, H. Sano, M. Santander, E. M. Santos, R. Santos-Lima, A. Sanuy, S. Sarkar, F. G. Saturni, U. Sawangwit, F. Schussler, U. Schwanke, E. Sciacca, S. Scuderi, M. Seglar-Arroyo, O. Sergijenko, M. Servillat, K. Seweryn, A. Shalchi, P. Sharma, R. C. Shellard, H. Siejkowski, J. Silk, C. Siqueira, V. Sliusar, A. Słowikowska, A. Sokolenko, H. Sol, S. Spencer, A. Stamerra, S. Stanič, R. Starling, T. Stolarczyk, U. Straumann, J. Strišković, Y. Suda, T. Suomijarvi, P. Świerk, F. Tavecchio, L. Taylor, L. A. Tejedor, M. Teshima, V. Testa, L. Tibaldo, C. J. Todero Peixoto, F. Tokanai, D. Tonev, G. Tosti, L. Tosti, N. Tothill, S. Truzzi, P. Travnicek, V. Vagelli, B. Vallage, P. Vallania, C. van Eldik, J. Vandenbroucke, G. S. Varner, V. Vassiliev, M. Vázquez Acosta, M. Vecchi, S. Ventura, S. Vercellone, S. Vergani, G. Verna, A. Viana, C. F. Vigorito, J. Vink, V. Vitale, S. Vorobiov, I. Vovk, T. Vuillaume, S. J. Wagner, R. Walter, J. Watson, C. Weniger, R. White, M. White, R. Wiemann, A. Wierzcholska, M. Will, D. A. Williams, R. Wischnewski, S. Yanagita, L. Yang, T. Yoshikoshi, M. Zacharias, G. Zaharijas, A. A. Zakaria, L. Zampieri, R. Zanin, D. Zaric, M. Zavrtanik, D. Zavrtanik, A. A. Zdziarski, A. Zech, H. Zechlin, V. I. Zhdanov, and M. Živec. Sensit-

ivity of the Cherenkov Telescope Array to a dark matter signal from the Galactic centre. , 2021(1):057, Jan. 2021. doi: 10.1088/1475-7516/2021/01/057.

M. Ackermann, M. Ajello, A. Albert, A. Allafort, W. B. Atwood, M. Axelsson, L. Baldini, J. Ballet, G. Barbiellini, D. Bastieri, K. Bechtol, R. Bellazzini, E. Bissaldi, R. D. Blandford, E. D. Bloom, J. R. Bogart, E. Bonamente, A. W. Borgland, E. Bottacini, A. Bouvier, T. J. Brandt, J. Bregeon, M. Brigida, P. Bruel, R. Buehler, T. H. Burnett, S. Buson, G. A. Caliandro, R. A. Cameron, P. A. Caraveo, J. M. Casandjian, E. Cavazzuti, C. Cecchi, Ö. Çelik, E. Charles, R. C. G. Chaves, A. Chekhtman, C. C. Cheung, J. Chiang, S. Ciprini, R. Claus, J. Cohen-Tanugi, J. Conrad, R. Corbet, S. Cutini, F. D'Ammando, D. S. Davis, A. de Angelis, M. DeKlotz, F. de Palma, C. D. Dermer, S. W. Digel, E. d. C. e. Silva, P. S. Drell, A. Drlica-Wagner, R. Dubois, C. Favuzzi, S. J. Fegan, E. C. Ferrara, W. B. Focke, P. Fortin, Y. Fukazawa, S. Funk, P. Fusco, F. Gargano, D. Gasparrini, N. Gehrels, B. Giebels, N. Giglietto, F. Giordano, M. Giroletti, T. Glanzman, G. Godfrey, I. A. Grenier, J. E. Grove, S. Guiriec, D. Hadasch, M. Hayashida, E. Hays, D. Horan, X. Hou, R. E. Hughes, M. S. Jackson, T. Jogler, G. Jóhannesson, R. P. Johnson, T. J. Johnson, W. N. Johnson, T. Kamae, H. Katagiri, J. Kataoka, M. Kerr, J. Knödlseder, M. Kuss, J. Lande, S. Larsson, L. Latronico, C. Lavalley, M. Lemoine-Goumard, F. Longo, F. Loparco, B. Lott, M. N. Lovellette, P. Lubrano, M. N. Mazziotta, W. McConville, J. E. McEnery, J. Mehault, P. F. Michelson, W. Mitthumsiri, T. Mizuno, A. A. Moiseev, C. Monte, M. E. Monzani, A. Morselli, I. V. Moskalenko, S. Murgia, M. Naumann-Godo, R. Nemmen, S. Nishino, J. P. Norris, E. Nuss, M. Ohno, T. Ohsugi, A. Okumura, N. Omodei, M. Orienti, E. Orlando, J. F. Ormes, D. Paneque, J. H. Panetta, J. S. Perkins, M. Pesce-Rollins, M. Pierbattista, F. Piron, G. Pivato, T. A. Porter, J. L. Racusin, S. Rainò, R. Rando, M. Razzano, S. Razzaque, A. Reimer, O. Reimer, T. Reposeur, L. C. Reyes, S. Ritz, L. S. Rochester, C. Romoli, M. Roth, H. F. W. Sadrozinski, D. A. Sanchez, P. M. Saz Parkinson, C. Sbarra, J. D. Scargle, C. Sgrò, J. Siegal-Gaskins, E. J. Siskind, G. Spandre, P. Spinelli, T. E. Stephens, D. J. Suson, H. Tajima, H. Takahashi, T. Tanaka, J. G. Thayer, J. B. Thayer, D. J. Thompson, L. Tibaldo, M. Tinivella, G. Tosti, E. Troja, T. L. Usher, J. Vandenbroucke, B. Van Klaveren, V. Vasileiou, G. Vianello, V. Vitale, A. P. Waite,

E. Wallace, B. L. Winer, D. L. Wood, K. S. Wood, M. Wood, Z. Yang, and S. Zimmer. The Fermi Large Area Telescope on Orbit: Event Classification, Instrument Response Functions, and Calibration. , 203(1):4, Nov. 2012. doi: 10.1088/0067-0049/203/1/4.

M. Ackermann, M. Ajello, W. B. Atwood, L. Baldini, J. Ballet, G. Barbiellini, D. Bastieri, J. Becerra Gonzalez, R. Bellazzini, E. Bissaldi, R. D. Bland ford, E. D. Bloom, R. Bonino, E. Bottacini, T. J. Brandt, J. Bregeon, R. J. Britto, P. Bruel, R. Buehler, S. Buson, G. A. Caliandro, R. A. Cameron, M. Caragiulo, P. A. Caraveo, B. Carpenter, J. M. Casandjian, E. Cavazzuti, C. Cecchi, E. Charles, A. Chekhtman, C. C. Cheung, J. Chiang, G. Chiaro, S. Ciprini, R. Claus, J. Cohen-Tanugi, L. R. Cominsky, J. Conrad, S. Cutini, R. D'Abrusco, F. D'Ammando, A. de Angelis, R. Desiante, S. W. Digel, L. Di Venere, P. S. Drell, C. Favuzzi, S. J. Fegan, E. C. Ferrara, J. Finke, W. B. Focke, A. Franckowiak, L. Fuhrmann, Y. Fukazawa, A. K. Furniss, P. Fusco, F. Gargano, D. Gasparrini, N. Giglietto, P. Giommi, F. Giordano, M. Giroletti, T. Glanzman, G. Godfrey, I. A. Grenier, J. E. Grove, S. Guiriec, J. W. Hewitt, A. B. Hill, D. Horan, R. Itoh, G. Jóhannesson, A. S. Johnson, W. N. Johnson, J. Kataoka, T. Kawano, F. Krauss, M. Kuss, G. La Mura, S. Larsson, L. Latronico, C. Leto, J. Li, L. Li, F. Longo, F. Loparco, B. Lott, M. N. Lovellette, P. Lubrano, G. M. Madejski, M. Mayer, M. N. Mazziotta, J. E. McEnery, P. F. Michelson, T. Mizuno, A. A. Moiseev, M. E. Monzani, A. Morselli, I. V. Moskalenko, S. Murgia, E. Nuss, M. Ohno, T. Ohsugi, R. Ojha, N. Omodei, M. Orienti, E. Orland o, A. Paggi, D. Paneque, J. S. Perkins, M. Pesce-Rollins, F. Piron, G. Pivato, T. A. Porter, S. Rainò, R. Rando, M. Razzano, S. Razzaque, A. Reimer, O. Reimer, R. W. Romani, D. Salvetti, M. Schaal, F. K. Schinzel, A. Schulz, C. Sgrò, E. J. Siskind, K. V. Sokolovsky, F. Spada, G. Spandre, P. Spinelli, L. Stawarz, D. J. Suson, H. Takahashi, T. Takahashi, Y. Tanaka, J. G. Thayer, J. B. Thayer, L. Tibaldo, D. F. Torres, E. Torresi, G. Tosti, E. Troja, Y. Uchiyama, G. Vianello, B. L. Winer, K. S. Wood, and S. Zimmer. The Third Catalog of Active Galactic Nuclei Detected by the Fermi Large Area Telescope. , 810 (1):14, Sept. 2015. doi: 10.1088/0004-637X/810/1/14.

M. Ackermann, R. Anantua, K. Asano, L. Baldini, G. Barbiellini, D. Bastieri, J. Becerra Gonzalez, R. Bellazzini, E. Bissaldi, R. D. Blandford, E. D. Bloom, R. Bonino,

E. Bottacini, P. Bruel, R. Buehler, G. A. Caliandro, R. A. Cameron, M. Caragiulo, P. A. Caraveo, E. Cavazzuti, C. Cecchi, C. C. Cheung, J. Chiang, G. Chiaro, S. Ciprini, J. Cohen-Tanugi, F. Costanza, S. Cutini, F. D'Ammando, F. de Palma, R. Desiante, S. W. Digel, N. Di Lalla, M. Di Mauro, L. Di Venere, P. S. Drell, C. Favuzzi, S. J. Fegan, E. C. Ferrara, Y. Fukazawa, S. Funk, P. Fusco, F. Gargano, D. Gasparrini, N. Giglietto, F. Giordano, M. Giroletti, I. A. Grenier, L. Guillemot, S. Guiriec, M. Hayashida, E. Hays, D. Horan, G. Jóhannesson, S. Kensei, D. Kocevski, M. Kuss, G. La Mura, S. Larsson, L. Latronico, J. Li, F. Longo, F. Loparco, B. Lott, M. N. Lovellette, P. Lubrano, G. M. Madejski, J. D. Magill, S. Maldera, A. Manfreda, M. Mayer, M. N. Mazziotta, P. F. Michelson, N. Mirabal, T. Mizuno, M. E. Monzani, A. Morselli, I. V. Moskalenko, K. Nalewajko, M. Negro, E. Nuss, T. Ohsugi, E. Orlando, D. Paneque, J. S. Perkins, M. Pesce-Rollins, F. Piron, G. Pivato, T. A. Porter, G. Principe, R. Rando, M. Razzano, S. Razzaque, A. Reimer, J. D. Scargle, C. Sgrò, M. Sikora, D. Simone, E. J. Siskind, F. Spada, P. Spinelli, L. Stawarz, J. B. Thayer, D. J. Thompson, D. F. Torres, E. Troja, Y. Uchiyama, Y. Yuan, and S. Zimmer. Minute-timescale >100 MeV γ-Ray Variability during the Giant Outburst of Quasar 3C 279 Observed by Fermi-LAT in 2015 June. , 824(2):L20, June 2016. doi: 10.3847/2041-8205/824/2/L20.

I. Agudo, S. G. Jorstad, A. P. Marscher, V. M. Larionov, J. L. Gómez, A. Lähteenmäki, M. Gurwell, P. S. Smith, H. Wiesemeyer, C. Thum, J. Heidt, D. A. Blinov, F. D. D'Arcangelo, V. A. Hagen-Thorn, D. A. Morozova, E. Nieppola, M. Roca-Sogorb, G. D. Schmidt, B. Taylor, M. Tornikoski, and I. S. Troitsky. Location of γ-ray Flare Emission in the Jet of the BL Lacertae Object OJ287 More than 14 pc from the Central Engine. , 726(1):L13, Jan 2011. doi: 10.1088/2041-8205/726/1/L13.

F. Aharonian, A. G. Akhperjanian, U. Barres de Almeida, A. R. Bazer-Bachi, Y. Becherini, B. Behera, M. Beilicke, W. Benbow, K. Bernlöhr, C. Boisson, A. Bochow, V. Borrel, I. Braun, E. Brion, J. Brucker, P. Brun, R. Bühler, T. Bulik, I. Büsching, T. Boutelier, S. Carrigan, P. M. Chadwick, A. Charbonnier, R. C. G. Chaves, L. M. Chounet, A. C. Clapson, G. Coignet, L. Costamante, M. Dalton, B. Degrange, C. Deil, H. J. Dickinson, A. Djannati-Ataï, W. Domainko, L. O. C. Drury, F. Dubois, G. Dubus, J. Dyks,

K. Egberts, D. Emmanoulopoulos, P. Espigat, C. Farnier, F. Feinstein, A. Fiasson, A. Förster, G. Fontaine, M. Füßling, S. Gabici, Y. A. Gallant, L. Gérard, B. Giebels, J. F. Glicenstein, B. Glück, P. Goret, C. Hadjichristidis, D. Hauser, M. Hauser, S. Heinz, G. Heinzelmann, G. Henri, G. Hermann, J. A. Hinton, A. Hoffmann, W. Hofmann, M. Holleran, S. Hoppe, D. Horns, A. Jacholkowska, O. C. de Jager, I. Jung, K. Katarzyński, S. Kaufmann, E. Kendziorra, M. Kerschhaggl, D. Khangulyan, B. Khélifi, D. Keogh, N. Komin, K. Kosack, G. Lamanna, J. P. Lenain, T. Lohse, V. Marandon, J. M. Martin, O. Martineau-Huynh, A. Marcowith, D. Maurin, T. J. L. McComb, C. Medina, R. Moderski, E. Moulin, M. Naumann-Godo, M. de Naurois, D. Nedbal, D. Nekrassov, J. Niemiec, S. J. Nolan, S. Ohm, J. F. Olive, E. de Oña Wilhelmi, K. J. Orford, J. L. Osborne, M. Ostrowski, M. Panter, G. Pedaletti, G. Pelletier, P. O. Petrucci, S. Pita, G. Pühlhofer, M. Punch, A. Quirrenbach, B. C. Raubenheimer, M. Raue, S. M. Rayner, M. Renaud, F. Rieger, J. Ripken, L. Rob, S. Rosier-Lees, G. Rowell, B. Rudak, J. Ruppel, V. Sahakian, A. Santangelo, R. Schlickeiser, F. M. Schöck, R. Schröder, U. Schwanke, S. Schwarzburg, S. Schwemmer, A. Shalchi, J. L. Skilton, H. Sol, D. Spangler, Ł. Stawarz, R. Steenkamp, C. Stegmann, G. Superina, P. H. Tam, J. P. Tavernet, R. Terrier, O. Tibolla, C. van Eldik, G. Vasileiadis, C. Venter, J. P. Vialle, P. Vincent, M. Vivier, H. J. Völk, F. Volpe, S. J. Wagner, M. Ward, A. A. Zdziarski, A. Zech, and H. E. S. S. Collaboration. Limits on an Energy Dependence of the Speed of Light from a Flare of the Active Galaxy PKS 2155-304. , 101(17):170402, Oct. 2008a. doi: 10.1103/PhysRevLett.101.170402.

F. Aharonian, A. G. Akhperjanian, U. Barres de Almeida, A. R. Bazer-Bachi, B. Behera, M. Beilicke, W. Benbow, K. Bernlöhr, C. Boisson, O. Bolz, V. Borrel, I. Braun, E. Brion, A. M. Brown, R. Bühler, T. Bulik, I. Büsching, T. Boutelier, S. Carrigan, P. M. Chadwick, L. M. Chounet, A. C. Clapson, G. Coignet, R. Cornils, L. Costamante, M. Dalton, B. Degrange, H. J. Dickinson, A. Djannati-Ataï, W. Domainko, L. O. Drury, F. Dubois, G. Dubus, J. Dyks, K. Egberts, D. Emmanoulopoulos, P. Espigat, C. Farnier, F. Feinstein, A. Fiasson, A. Förster, G. Fontaine, S. Funk, M. Füßling, Y. A. Gallant, B. Giebels, J. F. Glicenstein, B. Glück, P. Goret, C. Hadjichristidis, D. Hauser, M. Hauser, G. Heinzel-

mann, G. Henri, G. Hermann, J. A. Hinton, A. Hoffmann, W. Hofmann, M. Holleran, S. Hoppe, D. Horns, A. Jacholkowska, O. C. de Jager, I. Jung, K. Katarzyński, E. Kendziorra, M. Kerschhaggl, B. Khélifi, D. Keogh, N. Komin, K. Kosack, G. Lamanna, I. J. Latham, A. Lemière, M. Lemoine-Goumard, J. P. Lenain, T. Lohse, J. M. Martin, O. Martineau-Huynh, A. Marcowith, C. Masterson, D. Maurin, G. Maurin, T. J. L. McComb, R. Moderski, E. Moulin, M. de Naurois, D. Nedbal, S. J. Nolan, S. Ohm, J. P. Olive, E. de Oña Wilhelmi, K. J. Orford, J. L. Osborne, M. Ostrowski, M. Panter, G. Pedaletti, G. Pelletier, P. O. Petrucci, S. Pita, G. Pühlhofer, M. Punch, S. Ranchon, B. C. Raubenheimer, M. Raue, S. M. Rayner, M. Renaud, J. Ripken, L. Rob, L. Rolland, S. Rosier-Lees, G. Rowell, B. Rudak, J. Ruppel, V. Sahakian, A. Santangelo, R. Schlickeiser, F. Schöck, R. Schröder, U. Schwanke, S. Schwarzburg, S. Schwemmer, A. Shalchi, H. Sol, D. Spangler, Ł. Stawarz, R. Steenkamp, C. Stegmann, G. Superina, P. H. Tam, J. P. Tavernet, R. Terrier, C. van Eldik, G. Vasileiadis, C. Venter, J. P. Vialle, P. Vincent, M. Vivier, H. J. Völk, F. Volpe, S. J. Wagner, M. Ward, A. A. Zdziarski, and A. Zech. HESS very-high-energy gamma-ray sources without identified counterparts. , 477(1):353–363, Jan. 2008b. doi: 10.1051/0004-6361:20078516.

F. Aharonian, A. G. Akhperjanian, G. Anton, U. Barres de Almeida, A. R. Bazer-Bachi, Y. Becherini, B. Behera, K. Bernlöhr, C. Boisson, A. Bochow, V. Borrel, E. Brion, J. Brucker, P. Brun, R. Bühler, T. Bulik, I. Büsching, T. Boutelier, P. M. Chadwick, A. Charbonnier, R. C. G. Chaves, A. Cheesebrough, L. M. Chounet, A. C. Clapson, G. Coignet, M. Dalton, M. K. Daniel, I. D. Davids, B. Degrange, C. Deil, H. J. Dickinson, A. Djannati-Ataï, W. Domainko, L. O'C. Drury, F. Dubois, G. Dubus, J. Dyks, M. Dyrda, K. Egberts, D. Emmanoulopoulos, P. Espigat, C. Farnier, F. Feinstein, A. Fiasson, A. Förster, G. Fontaine, M. Füßling, S. Gabici, Y. A. Gallant, L. Gérard, B. Giebels, J. F. Glicenstein, B. Glück, P. Goret, D. Göhring, D. Hauser, M. Hauser, S. Heinz, G. Heinzelmann, G. Henri, G. Hermann, J. A. Hinton, A. Hoffmann, W. Hofmann, M. Holleran, S. Hoppe, D. Horns, A. Jacholkowska, O. C. de Jager, C. Jahn, I. Jung, K. Katarzyński, U. Katz, S. Kaufmann, E. Kendziorra, M. Kerschhaggl, D. Khangulyan, B. Khélifi, D. Keogh, W. Kluźniak, N. Komin, K. Kosack, G. Lamanna, J. P. Lenain,

T. Lohse, V. Marandon, J. M. Martin, O. Martineau-Huynh, A. Marcowith, D. Maurin, T. J. L. McComb, M. C. Medina, R. Moderski, E. Moulin, M. Naumann-Godo, M. de Naurois, D. Nedbal, D. Nekrassov, J. Niemiec, S. J. Nolan, S. Ohm, J. F. Olive, E. de Oña Wilhelmi, K. J. Orford, M. Ostrowski, M. Panter, M. P. Arribas, G. Pedaletti, G. Pelletier, P. O. Petrucci, S. Pita, G. Pühlhofer, M. Punch, A. Quirrenbach, B. C. Raubenheimer, M. Raue, S. M. Rayner, M. Renaud, F. Rieger, J. Ripken, L. Rob, S. Rosier-Lees, G. Rowell, B. Rudak, C. B. Rulten, J. Ruppel, V. Sahakian, A. Santangelo, R. Schlickeiser, F. M. Schöck, R. Schröder, U. Schwanke, S. Schwarzburg, S. Schwemmer, A. Shalchi, M. Sikora, J. L. Skilton, H. Sol, D. Spangler, Ł. Stawarz, R. Steenkamp, C. Stegmann, G. Superina, A. Szostek, P. H. Tam, J. P. Tavernet, R. Terrier, O. Tibolla, C. van Eldik, G. Vasileiadis, C. Venter, L. Venter, J. P. Vialle, P. Vincent, M. Vivier, H. J. Völk, F. Volpe, S. J. Wagner, M. Ward, A. A. Zdziarski, A. Zech, H. E. S. S. Collaboration, A. A. Abdo, M. Ackermann, M. Ajello, W. B. Atwood, M. Axelsson, L. Baldini, J. Ballet, G. Barbiellini, M. G. Baring, D. Bastieri, M. Battelino, B. M. Baughman, K. Bechtol, R. Bellazzini, B. Berenji, E. D. Bloom, E. Bonamente, A. W. Borgland, J. Bregeon, A. Brez, M. Brigida, P. Bruel, G. A. Caliandro, R. A. Cameron, P. A. Caraveo, J. M. Casandjian, E. Cavazzuti, C. Cecchi, E. Charles, A. Chekhtman, A. W. Chen, C. C. Cheung, J. Chiang, S. Ciprini, R. Claus, J. Cohen-Tanugi, S. Colafrancesco, J. Conrad, L. Costamante, S. Cutini, C. D. Dermer, A. de Angelis, F. de Palma, S. W. Digel, E. do Couto e Silva, P. S. Drell, R. Dubois, G. Dubus, D. Dumora, C. Farnier, C. Favuzzi, S. J. Fegan, E. C. Ferrara, P. Fleury, W. B. Focke, M. Frailis, Y. Fukazawa, S. Funk, P. Fusco, F. Gargano, D. Gasparrini, N. Gehrels, S. Germani, B. Giebels, N. Giglietto, F. Giordano, M. H. Grondin, J. E. Grove, L. Guillemot, S. Guiriec, Y. Hanabata, A. K. Harding, M. Hayashida, E. Hays, D. Horan, G. Jóhannesson, A. S. Johnson, R. P. Johnson, W. N. Johnson, M. Kadler, T. Kamae, H. Katagiri, J. Kataoka, M. Kerr, J. Knödlseder, F. Kuehn, M. Kuss, J. Lande, L. Latronico, S. H. Lee, M. Lemoine-Goumard, F. Longo, F. Loparco, B. Lott, M. N. Lovellette, G. M. Madejski, A. Makeev, M. N. Mazziotta, J. E. McEnery, C. Meurer, P. F. Michelson, W. Mitthumsiri, T. Mizuno, A. A. Moiseev, C. Monte, M. E. Monzani, A. Morselli, I. V. Moskalenko, S. Murgia,

P. L. Nolan, E. Nuss, T. Ohsugi, N. Omodei, E. Orlando, J. F. Ormes, D. Paneque, J. H. Panetta, D. Parent, V. Pelassa, M. Pepe, M. Pesce-Rollins, F. Piron, T. A. Porter, S. Rainò, M. Razzano, A. Reimer, O. Reimer, T. Reposeur, S. Ritz, A. Y. Rodriguez, F. Ryde, H. F. W. Sadrozinski, D. Sanchez, A. Sander, J. D. Scargle, T. L. Schalk, A. Sellerholm, C. Sgrò, M. Shaw, D. A. Smith, G. Spandre, P. Spinelli, J. L. Starck, M. S. Strickman, H. Tajima, H. Takahashi, T. Takahashi, T. Tanaka, J. G. Thayer, D. J. Thompson, L. Tibaldo, D. F. Torres, G. Tosti, A. Tramacere, Y. Uchiyama, T. L. Usher, N. Vilchez, M. Villata, V. Vitale, A. P. Waite, K. S. Wood, T. Ylinen, M. Ziegler, and Fermi LAT Collaboration. Simultaneous Observations of PKS 2155-304 with HESS, Fermi, RXTE, and Atom: Spectral Energy Distributions and Variability in a Low State. , 696(2):L150–L155, May 2009. doi: 10.1088/0004-637X/696/2/L150.

M. Ahlers. Neutrino Sources from a Multi-Messenger Perspective. In *European Physical Journal Web of Conferences*, volume 209 of *European Physical Journal Web of Conferences*, page 01013, Sept. 2019. doi: 10.1051/epjconf/201920901013.

M. Ajello, M. S. Shaw, R. W. Romani, C. D. Dermer, L. Costamante, O. G. King, W. Max-Moerbeck, A. Readhead, A. Reimer, J. L. Richards, and M. Stevenson. The Luminosity Function of Fermi-detected Flat-spectrum Radio Quasars. , 751(2):108, June 2012. doi: 10.1088/0004-637X/751/2/108.

M. Ajello, R. W. Romani, D. Gasparrini, M. S. Shaw, J. Bolmer, G. Cotter, J. Finke, J. Greiner, S. E. Healey, O. King, W. Max-Moerbeck, P. F. Michelson, W. J. Potter, A. Rau, A. C. S. Readhead, J. L. Richards, and P. Schady. The Cosmic Evolution of Fermi BL Lacertae Objects. , 780(1):73, Jan. 2014. doi: 10.1088/0004-637X/780/1/73.

M. Ajello, D. Gasparrini, M. Sánchez-Conde, G. Zaharijas, M. Gustafsson, J. Cohen-Tanugi, C. D. Dermer, Y. Inoue, D. Hartmann, M. Ackermann, K. Bechtol, A. Franckowiak, A. Reimer, R. W. Romani, and A. W. Strong. The Origin of the Extragalactic Gamma-Ray Background and Implications for Dark Matter Annihilation. , 800(2):L27, Feb. 2015. doi: 10.1088/2041-8205/800/2/L27.

H. Akaike. A New Look at the Statistical Model Identification. *IEEE Transactions on Automatic Control*, 19:716–723, Jan. 1974.

J. Aleksić, L. A. Antonelli, P. Antoranz, M. Backes, J. A. Barrio, D. Bastieri, J. Becerra González, W. Bednarek, A. Berdyugin, K. Berger, E. Bernardini, A. Biland, O. Blanch, R. K. Bock, A. Boller, G. Bonnoli, D. Borla Tridon, I. Braun, T. Bretz, A. Cañellas, E. Carmona, A. Carosi, P. Colin, E. Colombo, J. L. Contreras, J. Cortina, L. Cossio, S. Covino, F. Dazzi, A. De Angelis, E. De Cea del Pozo, B. De Lotto, C. Delgado Mendez, A. Diago Ortega, M. Doert, A. Domínguez, D. Dominis Prester, D. Dorner, M. Doro, D. Elsaesser, D. Ferenc, M. V. Fonseca, L. Font, C. Fruck, R. J. García López, M. Garczarczyk, D. Garrido, G. Giavitto, N. Godinović, D. Hadasch, D. Häfner, A. Herrero, D. Hildebrand , D. Höhne-Mönch, J. Hose, D. Hrupec, B. Huber, T. Jogler, S. Klepser, T. Krähenbühl, J. Krause, A. La Barbera, D. Lelas, E. Leonardo, E. Lindfors, S. Lombardi, M. López, E. Lorenz, M. Makariev, G. Maneva, N. Mankuzhiyil, K. Mannheim, L. Maraschi, M. Mariotti, M. Martínez, D. Mazin, M. Meucci, J. M. Miranda, R. Mirzoyan, H. Miyamoto, J. Moldón, A. Moralejo, D. Nieto, K. Nilsson, R. Orito, I. Oya, D. Paneque, R. Paoletti, S. Pardo, J. M. Paredes, S. Partini, M. Pasanen, F. Pauss, M. A. Perez-Torres, M. Persic, L. Peruzzo, M. Pilia, J. Pochon, F. Prada, P. G. Prada Moroni, E. Prandini, I. Puljak, I. Reichardt, R. Reinthal, W. Rhode, M. Ribó, J. Rico, S. Rügamer, A. Saggion, K. Saito, T. Y. Saito, M. Salvati, K. Satalecka, V. Scalzotto, V. Scapin, C. Schultz, T. Schweizer, M. Shayduk, S. N. Shore, A. Sillanpää, J. Sitarek, D. Sobczynska, F. Spanier, S. Spiro, A. Stamerra, B. Steinke, J. Storz, N. Strah, T. Surić, L. Takalo, F. Tavecchio, P. Temnikov, T. Terzić, D. Tescaro, M. Teshima, M. Thom, O. Tibolla, D. F. Torres, A. Treves, H. Vankov, P. Vogler, R. M. Wagner, Q. Weitzel, V. Zabalza, F. Zandanel, R. Zanin, MAGIC Collaboration, Y. T. Tanaka, D. L. Wood, and S. Buson. MAGIC Discovery of Very High Energy Emission from the FSRQ PKS 1222+21. , 730(1):L8, Mar. 2011. doi: 10.1088/2041-8205/730/1/L8.

J. Aleksić, S. Ansoldi, L. A. Antonelli, P. Antoranz, A. Babic, P. Bangale, J. A. Barrio, J. B. González, W. Bednarek, E. Bernardini, B. Biasuzzi, A. Biland, O. Blanch, S. Bonnefoy, G. Bonnoli, F. Borracci, T. Bretz, E. Carmona, A. Carosi, P. Colin, E. Colombo, J. L.

Contreras, J. Cortina, S. Covino, P. Da Vela, F. Dazzi, A. De Angelis, G. De Caneva, B. De Lotto, E. d. O. Wilhelmi, C. D. Mendez, D. D. Prester, D. Dorner, M. Doro, S. Einecke, D. Eisenacher, D. Elsaesser, M. V. Fonseca, L. Font, K. Frantzen, C. Fruck, D. Galindo, R. J. G. López, M. Garczarczyk, D. G. Terrats, M. Gaug, N. Godinović, A. G. Muñoz, S. R. Gozzini, D. Hadasch, Y. Hanabata, M. Hayashida, J. Herrera, D. Hildebrand , J. Hose, D. Hrupec, W. Idec, V. Kadenius, H. Kellermann, K. Kodani, Y. Konno, J. Krause, H. Kubo, J. Kushida, A. La Barbera, D. Lelas, N. Lewandowska, E. Lindfors, S. Lombardi, F. Longo, M. López, R. López-Coto, A. López-Oramas, E. Lorenz, I. Lozano, M. Makariev, K. Mallot, G. Maneva, N. Mankuzhiyil, K. Mannheim, L. Maraschi, B. Marcote, M. Mariotti, M. Martínez, D. Mazin, U. Menzel, J. M. Mirand a, R. Mirzoyan, A. Moralejo, P. Munar-Adrover, D. Nakajima, A. Niedzwiecki, K. Nilsson, K. Nishijima, K. Noda, R. Orito, A. Overkemping, S. Paiano, M. Palatiello, D. Paneque, R. Paoletti, J. M. Paredes, X. Paredes-Fortuny, M. Persic, J. Poutanen, P. G. P. Moroni, E. Prandini, I. Puljak, R. Reinthal, W. Rhode, M. Ribó, J. Rico, J. R. Garcia, S. Rügamer, T. Saito, K. Saito, K. Satalecka, V. Scalzotto, V. Scapin, C. Schultz, T. Schweizer, S. N. Shore, A. Sillanpää, J. Sitarek, I. Snidaric, D. Sobczynska, F. Spanier, V. Stamatescu, A. Stamerra, T. Steinbring, J. Storz, M. Strzys, L. Takalo, H. Takami, F. Tavecchio, P. Temnikov, T. Terzić, D. Tescaro, M. Teshima, J. Thaele, O. Tibolla, D. F. Torres, T. Toyama, A. Treves, M. Uellenbeck, P. Vogler, R. Zanin, M. Kadler, R. Schulz, E. Ros, U. Bach, F. Krauß, and J. Wilms. Black hole lightning due to particle acceleration at subhorizon scales. *Science*, 346(6213):1080–1084, Nov. 2014. doi: 10.1126/science.1256183.

R. Antonucci. Unified models for active galactic nuclei and quasars. , 31:473–521, Jan. 1993. doi: 10.1146/annurev.aa.31.090193.002353.

R. G. Arendt, N. Odegard, J. L. Weiland, T. J. Sodroski, M. G. Hauser, E. Dwek, T. Kelsall, S. H. Moseley, R. F. Silverberg, D. Leisawitz, K. Mitchell, W. T. Reach, and E. L. Wright. The COBE Diffuse Infrared Background Experiment Search for the Cosmic Infrared Background. III. Separation of Galactic Emission from the Infrared Sky Brightness. , 508(1):74–105, Nov. 1998. doi: 10.1086/306381.

T. Armstrong, A. M. Brown, and P. M. Chadwick. Fermi-LAT high-z active galactic nuclei and the extragalactic background light. , 470(4):4089–4098, Oct. 2017. doi: 10.1093/mnras/stx1309.

K. Asada and M. Nakamura. The Structure of the M87 Jet: A Transition from Parabolic to Conical Streamlines. , 745(2):L28, Feb. 2012. doi: 10.1088/2041-8205/745/2/L28.

W. Atwood, A. Albert, L. Baldini, M. Tinivella, J. Bregeon, M. Pesce-Rollins, C. Sgrò, P. Bruel, E. Charles, A. Drlica-Wagner, A. Franckowiak, T. Jogler, L. Rochester, T. Usher, M. Wood, J. Cohen-Tanugi, and S. Zimmer. Pass 8: Toward the Full Realization of the Fermi-LAT Scientific Potential. *arXiv e-prints*, art. arXiv:1303.3514, Mar. 2013.

W. B. Atwood, A. A. Abdo, M. Ackermann, W. Althouse, B. Anderson, M. Axelsson, L. Baldini, J. Ballet, D. L. Band, G. Barbiellini, J. Bartelt, D. Bastieri, B. M. Baughman, K. Bechtol, D. Bédérède, F. Bellardi, R. Bellazzini, B. Berenji, G. F. Bignami, D. Bisello, E. Bissaldi, R. D. Blandford, E. D. Bloom, J. R. Bogart, E. Bonamente, J. Bonnell, A. W. Borgland , A. Bouvier, J. Bregeon, A. Brez, M. Brigida, P. Bruel, T. H. Burnett, G. Busetto, G. A. Caliandro, R. A. Cameron, P. A. Caraveo, S. Carius, P. Carlson, J. M. Casandjian, E. Cavazzuti, M. Ceccanti, C. Cecchi, E. Charles, A. Chekhtman, C. C. Cheung, J. Chiang, R. Chipaux, A. N. Cillis, S. Ciprini, R. Claus, J. Cohen-Tanugi, S. Condamoor, J. Conrad, R. Corbet, L. Corucci, L. Costamante, S. Cutini, D. S. Davis, D. Decotigny, M. DeKlotz, C. D. Dermer, A. de Angelis, S. W. Digel, E. do Couto e Silva, P. S. Drell, R. Dubois, D. Dumora, Y. Edmonds, D. Fabiani, C. Farnier, C. Favuzzi, D. L. Flath, P. Fleury, W. B. Focke, S. Funk, P. Fusco, F. Gargano, D. Gasparrini, N. Gehrels, F. X. Gentit, S. Germani, B. Giebels, N. Giglietto, P. Giommi, F. Giordano, T. Glanzman, G. Godfrey, I. A. Grenier, M. H. Grondin, J. E. Grove, L. Guillemot, S. Guiriec, G. Haller, A. K. Harding, P. A. Hart, E. Hays, S. E. Healey, M. Hirayama, L. Hjalmarsdotter, R. Horn, R. E. Hughes, G. Jóhannesson, G. Johansson, A. S. Johnson, R. P. Johnson, T. J. Johnson, W. N. Johnson, T. Kamae, H. Katagiri, J. Kataoka, A. Kavelaars, N. Kawai, H. Kelly, M. Kerr, W. Klamra, J. Knödlseder, M. L. Kocian, N. Komin, F. Kuehn, M. Kuss, D. Landriu, L. Latronico, B. Lee, S. H.

Lee, M. Lemoine-Goumard, A. M. Lionetto, F. Longo, F. Loparco, B. Lott, M. N. Lovellette, P. Lubrano, G. M. Madejski, A. Makeev, B. Marangelli, M. M. Massai, M. N. Mazziotta, J. E. McEnery, N. Menon, C. Meurer, P. F. Michelson, M. Minuti, N. Mirizzi, W. Mitthumsiri, T. Mizuno, A. A. Moiseev, C. Monte, M. E. Monzani, E. Moretti, A. Morselli, I. V. Moskalenko, S. Murgia, T. Nakamori, S. Nishino, P. L. Nolan, J. P. Norris, E. Nuss, M. Ohno, T. Ohsugi, N. Omodei, E. Orlando, J. F. Ormes, A. Paccagnella, D. Paneque, J. H. Panetta, D. Parent, M. Pearce, M. Pepe, A. Perazzo, M. Pesce-Rollins, P. Picozza, L. Pieri, M. Pinchera, F. Piron, T. A. Porter, L. Poupard, S. Rainò, R. Rando, E. Rapposelli, M. Razzano, A. Reimer, O. Reimer, T. Reposeur, L. C. Reyes, S. Ritz, L. S. Rochester, A. Y. Rodriguez, R. W. Romani, M. Roth, J. J. Russell, F. Ryde, S. Sabatini, H. F. W. Sadrozinski, D. Sanchez, A. Sand er, L. Sapozhnikov, P. M. S. Parkinson, J. D. Scargle, T. L. Schalk, G. Scolieri, C. Sgrò, G. H. Share, M. Shaw, T. Shimokawabe, C. Shrader, A. Sierpowska-Bartosik, E. J. Siskind, D. A. Smith, P. D. Smith, G. Spandre, P. Spinelli, J. L. Starck, T. E. Stephens, M. S. Strickman, A. W. Strong, D. J. Suson, H. Tajima, H. Takahashi, T. Takahashi, T. Tanaka, A. Tenze, S. Tether, J. B. Thayer, J. G. Thayer, D. J. Thompson, L. Tibaldo, O. Tibolla, D. F. Torres, G. Tosti, A. Tramacere, M. Turri, T. L. Usher, N. Vilchez, V. Vitale, P. Wang, K. Watters, B. L. Winer, K. S. Wood, T. Ylinen, and M. Ziegler. The Large Area Telescope on the Fermi Gamma-Ray Space Telescope Mission. , 697(2):1071–1102, June 2009. doi: 10.1088/0004-637X/697/2/1071.

J. Ballet, T. H. Burnett, S. W. Digel, and B. Lott. Fermi Large Area Telescope Fourth Source Catalog Data Release 2. *arXiv e-prints*, art. arXiv:2005.11208, May 2020.

A. Barnacka, R. Moderski, B. Behera, P. Brun, and S. Wagner. PKS 1510-089: a rare example of a flat spectrum radio quasar with a very high-energy emission. , 567:A113, July 2014. doi: 10.1051/0004-6361/201322205.

M. C. Begelman, A. C. Fabian, and M. J. Rees. Implications of very rapid TeV variability in blazars. , 384(1):L19–L23, Feb. 2008. doi: 10.1111/j.1745-3933.2007.00413.x.

G. Bélanger, A. Goldwurm, M. Renaud, R. Terrier, F. Melia, N. Lund, J. Paul, G. Skinner,

and F. Yusef-Zadeh. A Persistent High-Energy Flux from the Heart of the Milky Way: INTEGRAL's View of the Galactic Center. , 636(1):275–289, Jan. 2006. doi: 10.1086/497629.

W. Benbow. Highlights from the VERITAS AGN Observation Program. In *36th International Cosmic Ray Conference (ICRC2019)*, volume 36 of *International Cosmic Ray Conference*, page 632, July 2019.

A. S. Bennett. The revised 3C catalogue of radio sources. , 68:163, Jan. 1962.

K. Bernlöhr, A. Barnacka, Y. Becherini, O. Blanch Bigas, E. Carmona, P. Colin, G. Decerprit, F. Di Pierro, F. Dubois, C. Farnier, S. Funk, G. Hermann, J. A. Hinton, T. B. Humensky, B. Khélifi, T. Kihm, N. Komin, J. P. Lenain, G. Maier, D. Mazin, M. C. Medina, A. Moralejo, S. J. Nolan, S. Ohm, E. de Oña Wilhelmi, R. D. Parsons, M. Paz Arribas, G. Pedaletti, S. Pita, H. Prokoph, C. B. Rulten, U. Schwanke, M. Shayduk, V. Stamatescu, P. Vallania, S. Vorobiov, R. Wischnewski, T. Yoshikoshi, A. Zech, and CTA Consortium. Monte Carlo design studies for the Cherenkov Telescope Array. *Astroparticle Physics*, 43:171–188, Mar. 2013. doi: 10.1016/j.astropartphys.2012.10.002.

B. Binggeli, A. Sandage, and G. A. Tammann. The luminosity function of galaxies. , 26: 509–560, Jan. 1988. doi: 10.1146/annurev.aa.26.090188.002453.

R. D. Blandford and A. Levinson. Pair Cascades in Extragalactic Jets. I. Gamma Rays. , 441:79, Mar. 1995. doi: 10.1086/175338.

R. D. Blandford and C. F. McKee. Reverberation mapping of the emission line regions of Seyfert galaxies and quasars. , 255:419–439, Apr. 1982. doi: 10.1086/159843.

R. D. Blandford and M. J. Rees. A "twin-exhaust" model for double radio sources. , 169: 395–415, Dec. 1974. doi: 10.1093/mnras/169.3.395.

R. D. Blandford and R. L. Znajek. Electromagnetic extraction of energy from Kerr black holes. , 179:433–456, May 1977. doi: 10.1093/mnras/179.3.433.

M. Böttcher. Modeling the emission processes in blazars. , 309(1-4):95–104, June 2007. doi: 10.1007/s10509-007-9404-0.

M. Böttcher and J. Chiang. X-Ray Spectral Variability Signatures of Flares in BL Lacertae Objects. , 581(1):127–142, Dec. 2002. doi: 10.1086/344155.

M. Böttcher and P. Els. Gamma-Gamma Absorption in the Broad Line Region Radiation Fields of Gamma-Ray Blazars. , 821(2):102, Apr. 2016. doi: 10.3847/0004-637X/821/2/102.

M. Böttcher, A. Reimer, and A. P. Marscher. Implications of the very High Energy Gamma-Ray Detection of the Quasar 3C279. , 703(1):1168–1175, Sept. 2009. doi: 10.1088/0004-637X/703/1/1168.

M. Böttcher, A. Reimer, K. Sweeney, and A. Prakash. Leptonic and Hadronic Modeling of Fermi-detected Blazars. , 768(1):54, May 2013. doi: 10.1088/0004-637X/768/1/54.

H. Bozdogan. Model selection and akaike's information criterion (aic): The general theory and its analytical extensions. *Psychometrika*, 52(3):345–370, Sep 1987. ISSN 1860-0980. doi: 10.1007/BF02294361. URL https://doi.org/10.1007/BF02294361.

M. S. Briggs, W. S. Paciesas, G. N. Pendleton, C. A. Meegan, G. J. Fishman, J. M. Horack, M. N. Brock, C. Kouveliotou, D. H. Hartmann, and J. Hakkila. BATSE Observations of the Large-Scale Isotropy of Gamma-Ray Bursts. , 459:40, Mar. 1996. doi: 10.1086/176867.

A. Brill. Towards a Luminosity Function of TeV Gamma-ray Blazars. In *36th International Cosmic Ray Conference (ICRC2019)*, volume 36 of *International Cosmic Ray Conference*, page 638, July 2019.

R. J. G. Britto, S. Razzaque, and B. Lott. Spectral Studies of Flaring FSRQs at GeV Energies Using Pass 8 Fermi-LAT Data. *arXiv e-prints*, art. arXiv:1502.07624, Feb. 2015.

O. Bromberg and A. Levinson. Recollimation and Radiative Focusing of Relativistic Jets: Applications to Blazars and M87. , 699(2):1274–1280, Jul 2009. doi: 10.1088/0004-637X/699/2/1274.

A. M. Brown. Locating the γ-ray emission region of the flat spectrum radio quasar PKS 1510-089. , 431(1):824–835, May 2013. doi: 10.1093/mnras/stt218.

A. M. Brown and J. Adams. High-energy γ-ray properties of the Fanaroff-Riley type I radio galaxy NGC 1275. , 413(4):2785–2790, June 2011. doi: 10.1111/j.1365-2966.2011.18351.x.

A. M. Brown, J. Adams, and P. M. Chadwick. γ-ray observations of extraterrestrial neutrino track events. , 451(1):323–331, July 2015. doi: 10.1093/mnras/stv899.

A. M. Brown, A. Acharyya, A. Dominguez, T. Hassan, J. P. Lenain, S. Pita, and CTA Consortium. Active Galactic Nuclei population studies with the Cherenkov Telescope Array. International Cosmic Ray Conference, 2021. URL `https://pos.sissa.it/395/887/pdf`. [Online; accessed 30-July-2021].

G. R. Burbidge. On Synchrotron Radiation from Messier 87. , 124:416, Sept. 1956. doi: 10.1086/146237.

G. R. Burbidge and E. M. Burbidge. Red-shifts of Quasi-stellar Objects and Related Extragalactic Systems. , 222(5195):735–741, May 1969. doi: 10.1038/222735a0.

K. Burnham and D. Anderson. Kullback–leibler information as a basis for strong inference in ecology. *Wildlife Research*, 28, 04 2001. doi: 10.1071/WR99107.

A. Butler, M. Huynh, A. Kapińska, I. Delvecchio, V. Smolčić, L. Chiappetti, E. Koulouridis, and M. Pierre. The XXL Survey. XXXVI. Evolution and black hole feedback of high-excitation and low-excitation radio galaxies in XXL-S. , 625:A111, May 2019. doi: 10.1051/0004-6361/201834581.

W. Cash. Parameter estimation in astronomy through application of the likelihood ratio. , 228:939–947, Mar. 1979. doi: 10.1086/156922.

A. Cavaliere and V. D'Elia. The Blazar Main Sequence. , 571(1):226–233, May 2002. doi: 10.1086/339778.

Y. L. Chang, B. Arsioli, P. Giommi, P. Padovani, and C. H. Brandt. The 3HSP catalogue of extreme and high-synchrotron peaked blazars. , 632:A77, Dec. 2019. doi: 10.1051/0004-6361/201834526.

M. Chauvin, J. P. Roques, D. J. Clark, and E. Jourdain. Polarimetry in the Hard X-Ray Domain with INTEGRAL SPI. , 769(2):137, June 2013. doi: 10.1088/0004-637X/769/2/137.

Cherenkov Telescope Array Consortium, B. S. Acharya, I. Agudo, I. Al Samarai, R. Alfaro, J. Alfaro, C. Alispach, R. Alves Batista, J. P. Amans, E. Amato, G. Ambrosi, E. Antolini, L. A. Antonelli, C. Aramo, M. Araya, T. Armstrong, F. Arqueros, L. Arrabito, K. Asano, M. Ashley, M. Backes, C. Balazs, M. Balbo, O. Ballester, J. Ballet, A. Bamba, M. Barkov, U. Barres de Almeida, J. A. Barrio, D. Bastieri, Y. Becherini, A. Belfiore, W. Benbow, D. Berge, E. Bernardini, M. G. Bernardini, M. Bernardos, K. Bernlöhr, B. Bertucci, B. Biasuzzi, C. Bigongiari, A. Biland, E. Bissaldi, J. Biteau, O. Blanch, J. Blazek, C. Boisson, J. Bolmont, G. Bonanno, A. Bonardi, C. Bonavolontà, G. Bonnoli, Z. Bosnjak, M. Böttcher, C. Braiding, J. Bregeon, A. Brill, A. M. Brown, P. Brun, G. Brunetti, T. Buanes, J. Buckley, V. Bugaev, R. Bühler, A. Bulgarelli, T. Bulik, M. Burton, A. Burtovoi, G. Busetto, R. Canestrari, M. Capalbi, F. Capitanio, A. Caproni, P. Caraveo, V. Cárdenas, C. Carlile, R. Carosi, E. Carquín, J. Carr, S. Casanova, E. Cascone, F. Catalani, O. Catalano, D. Cauz, M. Cerruti, P. Chadwick, S. Chaty, R. C. G. Chaves, A. Chen, X. Chen, M. Chernyakova, M. Chikawa, A. Christov, J. Chudoba, M. Cieślar, V. Coco, S. Colafrancesco, P. Colin, V. Conforti, V. Connaughton, J. Conrad, J. L. Contreras, J. Cortina, A. Costa, H. Costantini, G. Cotter, S. Covino, R. Crocker, J. Cuadra, O. Cuevas, P. Cumani, A. D'Aì, F. D'Ammando, P. D'Avanzo, D. D'Urso, M. Daniel, I. Davids, B. Dawson, F. Dazzi, A. De Angelis, R. de Cássia dos Anjos, G. De Cesare, A. De Franco, E. M. de Gouveia Dal Pino, I. de la Calle, R. de los Reyes Lopez, B. De Lotto, A. De Luca, M. De Lucia, M. de Naurois, E. de Oña

Wilhelmi, F. De Palma, F. De Persio, V. de Souza, C. Deil, M. Del Santo, C. Delgado, D. della Volpe, T. Di Girolamo, F. Di Pierro, L. Di Venere, C. Díaz, C. Dib, S. Diebold, A. Djannati-Ataï, A. Domínguez, D. Dominis Prester, D. Dorner, M. Doro, H. Drass, D. Dravins, G. Dubus, V. V. Dwarkadas, J. Ebr, C. Eckner, K. Egberts, S. Einecke, T. R. N. Ekoume, D. Elsässer, J. P. Ernenwein, C. Espinoza, C. Evoli, M. Fairbairn, D. Falceta-Goncalves, A. Falcone, C. Farnier, G. Fasola, E. Fedorova, S. Fegan, M. Fernandez-Alonso, A. Fernández-Barral, G. Ferrand, M. Fesquet, M. Filipovic, V. Fioretti, G. Fontaine, M. Fornasa, L. Fortson, L. Freixas Coromina, C. Fruck, Y. Fujita, Y. Fukazawa, S. Funk, M. Füßling, S. Gabici, A. Gadola, Y. Gallant, B. Garcia, R. Garcia López, M. Garczarczyk, J. Gaskins, T. Gasparetto, M. Gaug, L. Gerard, G. Giavitto, N. Giglietto, P. Giommi, F. Giordano, E. Giro, M. Giroletti, A. Giuliani, J. F. Glicenstein, R. Gnatyk, N. Godinovic, P. Goldoni, G. Gómez-Vargas, M. M. González, J. M. González, D. Götz, J. Graham, P. Grandi, J. Granot, A. J. Green, T. Greenshaw, S. Griffiths, S. Gunji, D. Hadasch, S. Hara, M. J. Hardcastle, T. Hassan, K. Hayashi, M. Hayashida, M. Heller, J. C. Helo, G. Hermann, J. Hinton, B. Hnatyk, W. Hofmann, J. Holder, D. Horan, J. Hörandel, D. Horns, P. Horvath, T. Hovatta, M. Hrabovsky, D. Hrupec, T. B. Humensky, M. Hütten, M. Iarlori, T. Inada, Y. Inome, S. Inoue, T. Inoue, Y. Inoue, F. Iocco, K. Ioka, M. Iori, K. Ishio, Y. Iwamura, M. Jamrozy, P. Janecek, D. Jankowsky, P. Jean, I. Jung-Richardt, J. Jurysek, P. Kaaret, S. Karkar, H. Katagiri, U. Katz, N. Kawanaka, D. Kazanas, B. Khélifi, D. B. Kieda, S. Kimeswenger, S. Kimura, S. Kisaka, J. Knapp, J. Knödlseder, B. Koch, K. Kohri, N. Komin, K. Kosack, M. Kraus, M. Krause, F. Krauß, H. Kubo, G. Kukec Mezek, H. Kuroda, J. Kushida, N. La Palombara, G. Lamanna, R. G. Lang, J. Lapington, O. Le Blanc, S. Leach, J. P. Lees, J. Lefaucheur, M. A. Leigui de Oliveira, J. P. Lenain, R. Lico, M. Limon, E. Lindfors, T. Lohse, S. Lombardi, F. Longo, M. López, R. López-Coto, C. C. Lu, F. Lucarelli, P. L. Luque-Escamilla, E. Lyard, M. C. Maccarone, G. Maier, P. Majumdar, G. Malaguti, D. Mandat, G. Maneva, M. Manganaro, S. Mangano, A. Marcowith, J. Marín, S. Markoff, J. Martí, P. Martin, M. Martínez, G. Martínez, N. Masetti, S. Masuda, G. Maurin, N. Maxted, D. Mazin, C. Medina, A. Melandri, S. Mereghetti, M. Meyer, I. A. Minaya, N. Mirabal,

R. Mirzoyan, A. Mitchell, T. Mizuno, R. Moderski, M. Mohammed, L. Mohrmann, T. Montaruli, A. Moralejo, D. Morcuende-Parrilla, K. Mori, G. Morlino, P. Morris, A. Morselli, E. Moulin, R. Mukherjee, C. Mundell, T. Murach, H. Muraishi, K. Murase, A. Nagai, S. Nagataki, T. Nagayoshi, T. Naito, T. Nakamori, Y. Nakamura, J. Niemiec, D. Nieto, M. Nikołajuk, K. Nishijima, K. Noda, D. Nosek, B. Novosyadlyj, S. Nozaki, P. O'Brien, L. Oakes, Y. Ohira, M. Ohishi, S. Ohm, N. Okazaki, A. Okumura, R. A. Ong, M. Orienti, R. Orito, J. P. Osborne, M. Ostrowski, N. Otte, I. Oya, M. Padovani, A. Paizis, M. Palatiello, M. Palatka, R. Paoletti, J. M. Paredes, G. Pareschi, R. D. Parsons, A. Pe'er, M. Pech, G. Pedaletti, M. Perri, M. Persic, A. Petrashyk, P. Petrucci, O. Petruk, B. Peyaud, M. Pfeifer, G. Piano, A. Pisarski, S. Pita, M. Pohl, M. Polo, D. Pozo, E. Prandini, J. Prast, G. Principe, D. Prokhorov, H. Prokoph, M. Prouza, G. Pühlhofer, M. Punch, S. Pürckhauer, F. Queiroz, A. Quirrenbach, S. Rainò, S. Razzaque, O. Reimer, A. Reimer, A. Reisenegger, M. Renaud, A. H. Rezaeian, W. Rhode, D. Ribeiro, M. Ribó, T. Richtler, J. Rico, F. Rieger, M. Riquelme, S. Rivoire, V. Rizi, J. Rodriguez, G. Rodriguez Fernandez, J. J. Rodríguez Vázquez, G. Rojas, P. Romano, G. Romeo, J. Rosado, A. C. Rovero, G. Rowell, B. Rudak, A. Rugliancich, C. Rulten, I. Sadeh, S. Safi-Harb, T. Saito, N. Sakaki, S. Sakurai, G. Salina, M. Sánchez-Conde, H. Sandaker, A. Sandoval, P. Sangiorgi, M. Sanguillon, H. Sano, M. Santander, S. Sarkar, K. Satalecka, F. G. Saturni, E. J. Schioppa, S. Schlenstedt, M. Schneider, H. Schoorlemmer, P. Schovanek, A. Schulz, F. Schussler, U. Schwanke, E. Sciacca, S. Scuderi, I. Seitenzahl, D. Semikoz, O. Sergijenko, M. Servillat, A. Shalchi, R. C. Shellard, L. Sidoli, H. Siejkowski, A. Sillanpää, G. Sironi, J. Sitarek, V. Sliusar, A. Slowikowska, H. Sol, A. Stamerra, S. Stanič, R. Starling, Ł. Stawarz, S. Stefanik, M. Stephan, T. Stolarczyk, G. Stratta, U. Straumann, T. Suomijarvi, A. D. Supanitsky, G. Tagliaferri, H. Tajima, M. Tavani, F. Tavecchio, J. P. Tavernet, K. Tayabaly, L. A. Tejedor, P. Temnikov, Y. Terada, R. Terrier, T. Terzic, M. Teshima, V. Testa, S. Thoudam, W. Tian, L. Tibaldo, M. Tluczykont, C. J. Todero Peixoto, F. Tokanai, J. Tomastik, D. Tonev, M. Tornikoski, D. F. Torres, E. Torresi, G. Tosti, N. Tothill, G. Tovmassian, P. Travnicek, C. Trichard, M. Trifoglio, I. Troyano Pujadas, S. Tsujimoto, G. Umana, V. Vagelli, F. Vagnetti, M. Valentino, P. Vallania,

L. Valore, C. van Eldik, J. Vandenbroucke, G. S. Varner, G. Vasileiadis, V. Vassiliev, M. Vázquez Acosta, M. Vecchi, A. Vega, S. Vercellone, P. Veres, S. Vergani, V. Verzi, G. P. Vettolani, A. Viana, C. Vigorito, J. Villanueva, H. Voelk, A. Vollhardt, S. Vorobiov, M. Vrastil, T. Vuillaume, S. J. Wagner, R. Wagner, R. Walter, J. E. Ward, D. Warren, J. J. Watson, F. Werner, M. White, R. White, A. Wierzcholska, P. Wilcox, M. Will, D. A. Williams, R. Wischnewski, M. Wood, T. Yamamoto, R. Yamazaki, S. Yanagita, L. Yang, T. Yoshida, S. Yoshiike, T. Yoshikoshi, M. Zacharias, G. Zaharijas, L. Zampieri, F. Zandanel, R. Zanin, M. Zavrtanik, D. Zavrtanik, A. A. Zdziarski, A. Zech, H. Zechlin, V. I. Zhdanov, A. Ziegler, and J. Zorn. *Science with the Cherenkov Telescope Array*. 2019. doi: 10.1142/10986.

J. Chiang and R. Mukherjee. The Luminosity Function of the EGRET Gamma-Ray Blazars. , 496(2):752–760, Mar. 1998. doi: 10.1086/305403.

D. P. Cohen, R. W. Romani, A. V. Filippenko, S. B. Cenko, B. Lott, W. Zheng, and W. Li. Temporal Correlations between Optical and Gamma-Ray Activity in Blazars. , 797(2): 137, Dec. 2014. doi: 10.1088/0004-637X/797/2/137.

M. H. Cohen, W. Cannon, G. H. Purcell, D. B. Shaffer, J. J. Broderick, K. I. Kellermann, and D. L. Jauncey. The Small-Scale Structure of Radio Galaxies and Quasi-Stellar Sources at 3.8 Centimeters. , 170:207, Dec. 1971. doi: 10.1086/151204.

P. Colin and S. LeBohec. Optimization of large homogeneous air Cherenkov arrays and application to the design of a 1-100 TeV γ-ray observatory. *Astroparticle Physics*, 32 (5):221–230, Dec. 2009. doi: 10.1016/j.astropartphys.2009.09.002.

R. T. Coogan, A. M. Brown, and P. M. Chadwick. Localizing the γ-ray emission region during the 2014 June outburst of 3C 454.3. , 458(1):354–365, May 2016. doi: 10.1093/mnras/stw199.

R. J. Cooke and M. Fumagalli. Measurement of the primordial helium abundance from the intergalactic medium. *Nature Astronomy*, 2:957–961, Oct. 2018. doi: 10.1038/s41550-018-0584-z.

J. Cortina. MAGIC detects very high energy gamma-ray emission from the FSRQ PKS 1510-089. *The Astronomer's Telegram*, 3965:1, Mar. 2012.

L. Costamante, F. Aharonian, R. Buehler, D. Khangulyan, A. Reimer, and O. Reimer. The new surprising behaviour of the two "prototype" blazars PKS 2155-304 and 3C 279. *arXiv e-prints*, art. arXiv:0907.3966, July 2009.

L. Costamante, S. Cutini, G. Tosti, E. Antolini, and A. Tramacere. On the origin of gamma-rays in Fermi blazars: beyondthe broad-line region. , 477(4):4749–4767, July 2018. doi: 10.1093/mnras/sty887.

H. D. Curtis. Descriptions of 762 Nebulae and Clusters Photographed with the Crossley Reflector. *Publications of Lick Observatory*, 13:9–42, Jan. 1918.

M. K. Daniel. Recent results from VERITAS. In *Journal of Physics Conference Series*, volume 1342 of *Journal of Physics Conference Series*, page 012011, Jan. 2020. doi: 10.1088/1742-6596/1342/1/012011.

J. M. Davies and E. S. Cotton. Design of the quartermaster solar furnace. *Solar Energy*, 1 (2-3):16–22, Apr. 1957. doi: 10.1016/0038-092X(57)90116-0.

G. de Vaucouleurs. The Velocity-Distance Relation and the Hubble Constant for Nearby Groups of Galaxies. In D. S. Evans, D. Wills, and B. J. Wills, editors, *External Galaxies and Quasi-Stellar Objects*, volume 44, page 353, Jan. 1972.

C. Deil, R. Zanin, J. Lefaucheur, C. Boisson, B. Khelifi, R. Terrier, M. Wood, L. Mohrmann, N. Chakraborty, J. Watson, R. Lopez-Coto, S. Klepser, M. Cerruti, J. P. Lenain, F. Acero, A. Djannati-Ataï, S. Pita, Z. Bosnjak, C. Trichard, T. Vuillaume, A. Donath, C. Consortium, J. King, L. Jouvin, E. Owen, B. Sipocz, D. Lennarz, A. Voruganti, M. Spir-Jacob, J. E. Ruiz, and M. P. Arribas. Gammapy - A prototype for the CTA science tools. In *35th International Cosmic Ray Conference (ICRC2017)*, volume 301 of *International Cosmic Ray Conference*, page 766, Jan. 2017.

I. Delvecchio, C. Gruppioni, F. Pozzi, S. Berta, G. Zamorani, A. Cimatti, D. Lutz, D. Scott, C. Vignali, G. Cresci, A. Feltre, A. Cooray, M. Vaccari, J. Fritz, E. Le Floc'h, B. Magnelli,

P. Popesso, S. Oliver, J. Bock, M. Carollo, T. Contini, O. Le Févre, S. Lilly, V. Mainieri, A. Renzini, and M. Scodeggio. Tracing the cosmic growth of supermassive black holes to z ~ 3 with Herschel. , 439(3):2736–2754, Apr. 2014. doi: 10.1093/mnras/stu130.

W. A. Dent. Quasi-stellar Sources: Variation in the Radio Emission of 3C 273. In *Quasars and high-energy astronomy*, page 39, Jan. 1969.

C. D. Dermer. Statistics of Cosmological Black Hole Jet Sources: Blazar Predictions for the Gamma-Ray Large Area Space Telescope. , 659(2):958–975, Apr. 2007. doi: 10.1086/512533.

C. D. Dermer, J. D. Finke, H. Krug, and M. Böttcher. Gamma-Ray Studies of Blazars: Synchro-Compton Analysis of Flat Spectrum Radio Quasars. , 692(1):32–46, Feb. 2009. doi: 10.1088/0004-637X/692/1/32.

C. D. Dermer, D. Yan, L. Zhang, J. D. Finke, and B. Lott. Near-equipartition Jets with Log-parabola Electron Energy Distribution and the Blazar Spectral-index Diagrams. , 809(2):174, Aug. 2015. doi: 10.1088/0004-637X/809/2/174.

A. Domínguez, J. R. Primack, D. J. Rosario, F. Prada, R. C. Gilmore, S. M. Faber, D. C. Koo, R. S. Somerville, M. A. Pérez-Torres, P. Pérez-González, J. S. Huang, M. Davis, P. Guhathakurta, P. Barmby, C. J. Conselice, M. Lozano, J. A. Newman, and M. C. Cooper. Extragalactic background light inferred from AEGIS galaxy-SED-type fractions. , 410(4):2556–2578, Feb 2011. doi: 10.1111/j.1365-2966.2010.17631.x.

A. C. Donea and R. J. Protheroe. Gamma Ray and Infrared Emission from the M87 Jet and Torus. *Progress of Theoretical Physics Supplement*, 151:186–191, Jan. 2003. doi: 10.1143/PTPS.151.186.

M. Doro, J. Conrad, D. Emmanoulopoulos, M. A. Sànchez-Conde, J. A. Barrio, E. Birsin, J. Bolmont, P. Brun, S. Colafrancesco, S. H. Connell, J. L. Contreras, M. K. Daniel, M. Fornasa, M. Gaug, J. F. Glicenstein, A. González-Muñoz, T. Hassan, D. Horns, A. Jacholkowska, C. Jahn, R. Mazini, N. Mirabal, A. Moralejo, E. Moulin, D. Nieto, J. Ripken, H. Sandaker, U. Schwanke, G. Spengler, A. Stamerra, A. Viana, H. S.

Zechlin, S. Zimmer, and CTA Consortium. Dark matter and fundamental physics with the Cherenkov Telescope Array. *Astroparticle Physics*, 43:189–214, Mar. 2013. doi: 10.1016/j.astropartphys.2012.08.002.

A. Dotson, M. Georganopoulos, D. Kazanas, and E. S. Perlman. A Method for Localizing Energy Dissipation in Blazars Using Fermi Variability. , 758(1):L15, Oct. 2012. doi: 10.1088/2041-8205/758/1/L15.

S. P. Driver, S. K. Andrews, L. J. Davies, A. S. G. Robotham, A. H. Wright, R. A. Windhorst, S. Cohen, K. Emig, R. A. Jansen, and L. Dunne. Measurements of Extragalactic Background Light from the Far UV to the Far IR from Deep Ground- and Space-based Galaxy Counts. , 827(2):108, Aug. 2016. doi: 10.3847/0004-637X/827/2/108.

J. S. Dunlop and J. A. Peacock. The redshift cut-off in the luminosity function of radio galaxies and quasars. , 247:19, Nov. 1990.

J. A. Earl. Cloud-Chamber Observations of Primary Cosmic-Ray Electrons. , 6(3):125–128, Feb. 1961. doi: 10.1103/PhysRevLett.6.125.

R. A. Edelson and J. H. Krolik. The Discrete Correlation Function: A New Method for Analyzing Unevenly Sampled Variability Data. , 333:646, Oct 1988. doi: 10.1086/166773.

D. O. Edge, J. R. Shakeshaft, W. B. McAdam, J. E. Baldwin, and S. Archer. A survey of radio sources at a frequency of 159 Mc/s. , 68:37–60, Jan. 1959.

J. Ellis, N. E. Mavromatos, and D. V. Nanopoulos. Derivation of a vacuum refractive index in a stringy space time foam model. *Physics Letters B*, 665(5):412–417, July 2008. doi: 10.1016/j.physletb.2008.06.029.

D. Emmanoulopoulos, I. M. McHardy, and I. E. Papadakis. Generating artificial light curves: revisited and updated. , 433(2):907–927, Aug. 2013. doi: 10.1093/mnras/stt764.

M. Errando, R. Bock, D. Kranich, E. Lorenz, P. Majumdar, M. Mariotti, D. Mazin, E. Prandini, F. Tavecchio, M. Teshima, and et al. Discovery of very high energy

gamma-rays from the flat spectrum radio quasar 3C 279 with the MAGIC telescope. In F. A. Aharonian, W. Hofmann, and F. Rieger, editors, *American Institute of Physics Conference Series*, volume 1085 of *American Institute of Physics Conference Series*, pages 423–426, Dec. 2008. doi: 10.1063/1.3076698.

B. L. Fanaroff and J. M. Riley. The morphology of extragalactic radio sources of high and low luminosity. , 167:31P–36P, May 1974. doi: 10.1093/mnras/167.1.31P.

E. A. Fath. The spectra of some spiral nebulae and globular star clusters. *Lick Observatory Bulletin*, 149:71–77, Jan. 1909. doi: 10.5479/ADS/bib/1909LicOB.5.71F.

D. J. Fegan. TOPICAL REVIEW: ?/hadron separation at TeV energies. *Journal of Physics G Nuclear Physics*, 23(9):1013–1060, Sept. 1997. doi: 10.1088/0954-3899/23/9/004.

C. E. Fichtel, D. L. Bertsch, R. C. Hartman, S. D. Hunter, G. Kanbach, D. A. Kniffen, P. W. Kwok, Y. C. Lin, J. R. Mattox, H. A. Mayer-Hasselwander, P. F. Michelson, C. von Montigny, P. L. Nolan, K. Pinkau, H. Rothermel, E. J. Schneid, M. Sommer, P. Sreekumar, and D. J. Thompson. Overview of the first results from EGRET. , 97: 13–16, Jan. 1993.

D. F. Findley, B. C. Monsell, W. R. Bell, M. C. Otto, and B.-C. Chen. New capabilities and methods of the x-12-arima seasonal-adjustment program. *Journal of Business & Economic Statistics*, 16(2):127–152, 1998. doi: 10.1080/07350015.1998.10524743. URL https://doi.org/10.1080/07350015.1998.10524743.

J. D. Finke. Erratum: "External Compton Scattering in Blazar Jets and the Location of the Gamma-Ray Emitting Region" (<A href="http://doi.org/10.3847/0004-637x/830/2/94">2016, ApJ, 830, 94</A>). , 860(2):178, June 2018. doi: 10.3847/1538-4357/aac9c6.

J. D. Finke, S. Razzaque, and C. D. Dermer. Modeling the extragalactic background light from stars and dust. *The Astrophysical Journal*, 712(1):238–249, Feb 2010. ISSN 1538-4357. doi: 10.1088/0004-637x/712/1/238. URL http://dx.doi.org/10.1088/0004-637X/712/1/238.

D. Foreman-Mackey, D. W. Hogg, D. Lang, and J. Goodman. emcee: The MCMC Hammer. , 125(925):306, Mar. 2013. doi: 10.1086/670067.

L. Foschini, G. Ghisellini, F. Tavecchio, G. Bonnoli, and A. Stamerra. Search for the shortest variability at gamma rays in flat-spectrum radio quasars. , 530:A77, June 2011a. doi: 10.1051/0004-6361/201117064.

L. Foschini, G. Ghisellini, F. Tavecchio, G. Bonnoli, and A. Stamerra. Short time scale variability at gamma rays in FSRQs and implications on the current models. *arXiv e-prints*, art. arXiv:1110.4471, Oct. 2011b.

G. Fossati, L. Maraschi, A. Celotti, A. Comastri, and G. Ghisellini. A unifying view of the spectral energy distributions of blazars. , 299(2):433–448, Sept. 1998. doi: 10.1046/j.1365-8711.1998.01828.x.

G. Fossati, J. H. Buckley, I. H. Bond, S. M. Bradbury, D. A. Carter-Lewis, Y. C. K. Chow, W. Cui, A. D. Falcone, J. P. Finley, J. A. Gaidos, J. Grube, J. Holder, D. Horan, D. Horns, M. M. Jordan, D. B. Kieda, J. Kildea, H. Krawczynski, F. Krennrich, M. J. Lang, S. LeBohec, K. Lee, P. Moriarty, R. A. Ong, D. Petry, J. Quinn, G. H. Sembroski, S. P. Wakely, and T. C. Weekes. Multiwavelength Observations of Markarian 421 in 2001 March: An Unprecedented View on the X-Ray/TeV Correlated Variability. , 677 (2):906–925, Apr. 2008. doi: 10.1086/527311.

A. Franceschini, G. Rodighiero, and M. Vaccari. Extragalactic optical-infrared background radiation, its time evolution and the cosmic photon-photon opacity. , 487(3):837–852, Sept. 2008. doi: 10.1051/0004-6361:200809691.

S. Funk, J. A. Hinton, and CTA Consortium. Comparison of Fermi-LAT and CTA in the region between 10-100 GeV. *Astroparticle Physics*, 43:348–355, Mar. 2013. doi: 10.1016/j.astropartphys.2012.05.018.

Gaia Collaboration. VizieR Online Data Catalog: Gaia DR2 (Gaia Collaboration, 2018). *VizieR Online Data Catalog*, art. I/345, Apr. 2018.

J. A. Gaidos, C. W. Akerlof, S. Biller, P. J. Boyle, A. C. Breslin, J. H. Buckley, D. A. Carter-Lewis, M. Catanese, M. F. Cawley, D. J. Fegan, J. P. Finley, J. B. Gordo, A. M. Hillas, F. Krennrich, R. C. Lamb, R. W. Lessard, J. E. McEnery, C. Masterson, G. Mohanty, P. Moriarty, J. Quinn, A. J. Rodgers, H. J. Rose, F. Samuelson, M. S. Schubnell, G. H. Sembroski, R. Srinivasan, T. C. Weekes, C. L. Wilson, and J. Zweerink. Extremely rapid bursts of TeV photons from the active galaxy Markarian 421. , 383(6598):319–320, Sept. 1996. doi: 10.1038/383319a0.

G. Galanti, F. Tavecchio, M. Roncadelli, and C. Evoli. Blazar VHE spectral alterations induced by photon-ALP oscillations. , 487(1):123–132, July 2019. doi: 10.1093/mnras/stz1144.

D. Gamerman and H. Lopes. *Markov Chain Monte Carlo: Stochastic Simulation for Bayesian Inference, Second Edition*. Chapman & Hall/CRC Texts in Statistical Science. CRC Press, 2006. ISBN 9781482296426. URL `https://books.google.co.in/books?id=X01ZDwAAQBAJ`.

M. Georganopoulos, F. A. Aharonian, and J. G. Kirk. External Compton emission from relativistic jets in Galactic black hole candidates and ultraluminous X-ray sources. , 388: L25–L28, June 2002. doi: 10.1051/0004-6361:20020567.

G. Ghisellini and F. Tavecchio. Canonical high-power blazars. , 397(2):985–1002, Aug. 2009. doi: 10.1111/j.1365-2966.2009.15007.x.

G. Ghisellini, A. Celotti, G. Fossati, L. Maraschi, and A. Comastri. A theoretical unifying scheme for gamma-ray bright blazars. , 301(2):451–468, Dec. 1998. doi: 10.1046/j.1365-8711.1998.02032.x.

G. Ghisellini, L. Maraschi, and F. Tavecchio. The Fermi blazars' divide. , 396(1):L105–L109, June 2009. doi: 10.1111/j.1745-3933.2009.00673.x.

G. Ghisellini, F. Tavecchio, L. Foschini, G. Ghirland a, L. Maraschi, and A. Celotti. General physical properties of bright Fermi blazars. , 402(1):497–518, Feb. 2010. doi: 10.1111/j.1365-2966.2009.15898.x.

G. Ghisellini, C. Righi, L. Costamante, and F. Tavecchio. The Fermi blazar sequence. , 469(1):255–266, July 2017. doi: 10.1093/mnras/stx806.

D. Giannios. Reconnection-driven plasmoids in blazars: fast flares on a slow envelope. , 431(1):355–363, May 2013. doi: 10.1093/mnras/stt167.

D. Giannios, D. A. Uzdensky, and M. C. Begelman. Fast TeV variability in blazars: jets in a jet. , 395(1):L29–L33, May 2009. doi: 10.1111/j.1745-3933.2009.00635.x.

R. C. Gilmore, R. S. Somerville, J. R. Primack, and A. Domínguez. Semi-analytic modelling of the extragalactic background light and consequences for extragalactic gamma-ray spectra. , 422(4):3189–3207, June 2012. doi: 10.1111/j.1365-2966.2012.20841.x.

P. W. Graham, I. G. Irastorza, S. K. Lamoreaux, A. Lindner, and K. A. van Bibber. Experimental Searches for the Axion and Axion-Like Particles. *Annual Review of Nuclear and Particle Science*, 65:485–514, Oct. 2015. doi: 10.1146/annurev-nucl-102014-022120.

J. L. Greenstein. Red-Shift of the Unusual Radio Source: 3C 48. , 197(4872):1041–1042, Mar. 1963. doi: 10.1038/1971041a0.

P. K. F. Grieder. *Extensive Air Showers: High Energy Phenomena and Astrophysical Aspects - A Tutorial, Reference Manual and Data Book*. 2010. doi: 10.1007/978-3-540-76941-5.

H. E. S. S. Collaboration, H. Abdalla, A. Abramowski, F. Aharonian, F. Ait Benkhali, E. O. Angüner, M. Arakawa, M. Arrieta, P. Aubert, M. Backes, A. Balzer, M. Barnard, Y. Becherini, J. Becker Tjus, D. Berge, S. Bernhard, K. Bernlöhr, R. Blackwell, M. Böttcher, C. Boisson, J. Bolmont, S. Bonnefoy, P. Bordas, J. Bregeon, F. Brun, P. Brun, M. Bryan, M. Büchele, T. Bulik, M. Capasso, S. Carrigan, S. Caroff, A. Carosi, S. Casanova, M. Cerruti, N. Chakraborty, R. C. G. Chaves, A. Chen, J. Chevalier, S. Colafrancesco, B. Condon, J. Conrad, I. D. Davids, J. Decock, C. Deil, J. Devin, P. deWilt, L. Dirson, A. Djannati-Ataï, W. Domainko, A. Donath, L. O. C. Drury, K. Dutson, J. Dyks, T. Edwards, K. Egberts, P. Eger, G. Emery, J. P. Ernenwein,

S. Eschbach, C. Farnier, S. Fegan, M. V. Fernandes, A. Fiasson, G. Fontaine, A. Förster, S. Funk, M. Füßling, S. Gabici, Y. A. Gallant, T. Garrigoux, H. Gast, F. Gaté, G. Giavitto, B. Giebels, D. Glawion, J. F. Glicenstein, D. Gottschall, M. H. Grondin, J. Hahn, M. Haupt, J. Hawkes, G. Heinzelmann, G. Henri, G. Hermann, J. A. Hinton, W. Hofmann, C. Hoischen, T. L. Holch, M. Holler, D. Horns, A. Ivascenko, H. Iwasaki, A. Jacholkowska, M. Jamrozy, D. Jankowsky, F. Jankowsky, M. Jingo, L. Jouvin, I. Jung-Richardt, M. A. Kastendieck, K. Katarzyński, M. Katsuragawa, U. Katz, D. Kerszberg, D. Khangulyan, B. Khélifi, J. King, S. Klepser, D. Klochkov, W. Kluźniak, N. Komin, K. Kosack, S. Krakau, M. Kraus, P. P. Krüger, H. Laffon, G. Lamanna, J. Lau, J. P. Lees, J. Lefaucheur, A. Lemière, M. Lemoine-Goumard, J. P. Lenain, E. Leser, T. Lohse, M. Lorentz, R. Liu, R. López-Coto, I. Lypova, V. Marandon, D. Malyshev, A. Marcowith, C. Mariaud, R. Marx, G. Maurin, N. Maxted, M. Mayer, P. J. Meintjes, M. Meyer, A. M. W. Mitchell, R. Moderski, M. Mohamed, L. Mohrmann, K. Morå, E. Moulin, T. Murach, S. Nakashima, M. de Naurois, H. Ndiyavala, F. Niederwanger, J. Niemiec, L. Oakes, P. O'Brien, H. Odaka, S. Ohm, M. Ostrowski, I. Oya, M. Padovani, M. Panter, R. D. Parsons, M. Paz Arribas, N. W. Pekeur, G. Pelletier, C. Perennes, P. O. Petrucci, B. Peyaud, Q. Piel, S. Pita, V. Poireau, H. Poon, D. Prokhorov, H. Prokoph, G. Pühlhofer, M. Punch, A. Quirrenbach, S. Raab, R. Rauth, A. Reimer, O. Reimer, M. Renaud, R. de los Reyes, F. Rieger, L. Rinchiuso, C. Romoli, G. Rowell, B. Rudak, C. B. Rulten, S. Safi-Harb, V. Sahakian, S. Saito, D. A. Sanchez, A. Santangelo, M. Sasaki, M. Schandri, R. Schlickeiser, F. Schüssler, A. Schulz, U. Schwanke, S. Schwemmer, M. Seglar-Arroyo, M. Settimo, A. S. Seyffert, N. Shafi, I. Shilon, K. Shiningayamwe, R. Simoni, H. Sol, F. Spanier, M. Spir-Jacob, Ł. Stawarz, R. Steenkamp, C. Stegmann, C. Steppa, I. Sushch, T. Takahashi, J. P. Tavernet, T. Tavernier, A. M. Taylor, R. Terrier, L. Tibaldo, D. Tiziani, M. Tluczykont, C. Trichard, M. Tsirou, N. Tsuji, R. Tuffs, Y. Uchiyama, D. J. van der Walt, C. van Eldik, C. van Rensburg, B. van Soelen, G. Vasileiadis, J. Veh, C. Venter, A. Viana, P. Vincent, J. Vink, F. Voisin, H. J. Völk, T. Vuillaume, Z. Wadiasingh, S. J. Wagner, P. Wagner, R. M. Wagner, R. White, A. Wierzcholska, P. Willmann, A. Wörnlein, D. Wouters, R. Yang, D. Zaborov, M. Zacharias, R. Zanin,

A. A. Zdziarski, A. Zech, F. Zefi, A. Ziegler, J. Zorn, and N. Żywucka. The H.E.S.S. Galactic plane survey. , 612:A1, Apr. 2018. doi: 10.1051/0004-6361/201732098.

H. E. S. S. Collaboration, H. Abdalla, R. Adam, F. Aharonian, F. Ait Benkhali, E. O. Angüner, M. Arakawa, C. Arcaro, C. Armand, H. Ashkar, M. Backes, V. Barbosa Martins, M. Barnard, Y. Becherini, D. Berge, K. Bernlöhr, R. Blackwell, M. Böttcher, C. Boisson, J. Bolmont, S. Bonnefoy, J. Bregeon, M. Breuhaus, F. Brun, P. Brun, M. Bryan, M. Büchele, T. Bulik, T. Bylund, M. Capasso, S. Caroff, A. Carosi, S. Casanova, M. Cerruti, T. Chand, S. Chandra, A. Chen, S. Colafrancesco, M. Curyło, I. D. Davids, C. Deil, J. Devin, P. deWilt, L. Dirson, A. Djannati-Ataï, A. Dmytriiev, A. Donath, V. Doroshenko, L. O. C. Drury, J. Dyks, K. Egberts, G. Emery, J. P. Ernenwein, S. Eschbach, K. Feijen, S. Fegan, A. Fiasson, G. Fontaine, S. Funk, M. Füßling, S. Gabici, Y. A. Gallant, F. Gaté, G. Giavitto, D. Glawion, J. F. Glicenstein, D. Gottschall, M. H. Grondin, J. Hahn, M. Haupt, G. Heinzelmann, G. Henri, G. Hermann, J. A. Hinton, W. Hofmann, C. Hoischen, T. L. Holch, M. Holler, D. Horns, D. Huber, H. Iwasaki, M. Jamrozy, D. Jankowsky, F. Jankowsky, A. Jardin-Blicq, I. Jung-Richardt, M. A. Kastendieck, K. Katarzyński, M. Katsuragawa, U. Katz, D. Khangulyan, B. Khélifi, J. King, S. Klepser, W. Kluźniak, N. Komin, K. Kosack, D. Kostunin, M. Kraus, G. Lamanna, J. Lau, A. Lemière, M. Lemoine-Goumard, J. P. Lenain, E. Leser, C. Levy, T. Lohse, I. Lypova, J. Mackey, J. Majumdar, D. Malyshev, V. Marandon, A. Marcowith, A. Mares, C. Mariaud, G. Martí-Devesa, R. Marx, G. Maurin, P. J. Meintjes, A. M. W. Mitchell, R. Moderski, M. Mohamed, L. Mohrmann, C. Moore, E. Moulin, J. Muller, T. Murach, S. Nakashima, M. de Naurois, H. Ndiyavala, F. Niederwanger, J. Niemiec, L. Oakes, P. O'Brien, H. Odaka, S. Ohm, E. de Ona Wilhelmi, M. Ostrowski, I. Oya, M. Panter, R. D. Parsons, C. Perennes, P. O. Petrucci, B. Peyaud, Q. Piel, S. Pita, V. Poireau, A. Priyana Noel, D. A. Prokhorov, H. Prokoph, G. Pühlhofer, M. Punch, A. Quirrenbach, S. Raab, R. Rauth, A. Reimer, O. Reimer, Q. Remy, M. Renaud, F. Rieger, L. Rinchiuso, C. Romoli, G. Rowell, B. Rudak, E. Ruiz-Velasco, V. Sahakian, S. Saito, D. A. Sanchez, A. Santangelo, M. Sasaki, R. Schlickeiser, F. Schüssler, A. Schulz, H. Schutte, U. Schwanke, S. Schwemmer, M. Seglar-Arroyo, M. Senniappan, A. S. Sey-

ffert, N. Shafi, K. Shiningayamwe, R. Simoni, A. Sinha, H. Sol, A. Specovius, M. Spir-Jacob, L. Stawarz, R. Steenkamp, C. Stegmann, C. Steppa, T. Takahashi, T. Tavernier, A. M. Taylor, R. Terrier, D. Tiziani, M. Tluczykont, C. Trichard, M. Tsirou, N. Tsuji, R. Tuffs, Y. Uchiyama, D. J. van der Walt, C. van Eldik, C. van Rensburg, B. van Soelen, G. Vasileiadis, J. Veh, C. Venter, P. Vincent, J. Vink, F. Voisin, H. J. Völk, T. Vuillaume, Z. Wadiasingh, S. J. Wagner, R. White, A. Wierzcholska, R. Yang, H. Yoneda, M. Zacharias, R. Zanin, A. A. Zdziarski, A. Zech, A. Ziegler, J. Zorn, N. Żywucka, and M. Meyer. Constraints on the emission region of <ASTROBJ>3C 279</ASTROBJ> during strong flares in 2014 and 2015 through VHE γ-ray observations with H.E.S.S. , 627:A159, July 2019. doi: 10.1051/0004-6361/201935704.

F. Halzen and E. Zas. Neutrino Fluxes from Active Galaxies: A Model-Independent Estimate. , 488(2):669–674, Oct. 1997. doi: 10.1086/304741.

J. Harris, M. K. Daniel, and P. M. Chadwick. Identifying Breaks and Curvature in the Fermi Spectra of Bright Flat Spectrum Radio Quasars. , 761(1):2, Dec. 2012. doi: 10.1088/0004-637X/761/1/2.

T. Hassan, L. Arrabito, K. Bernlöhr, J. Bregeon, J. Cortina, P. Cumani, F. Di Pierro, D. Falceta-Goncalves, R. G. Lang, J. Hinton, T. Jogler, G. Maier, A. Moralejo, A. Morselli, C. J. Todero Peixoto, and M. Wood. Monte Carlo performance studies for the site selection of the Cherenkov Telescope Array. *Astroparticle Physics*, 93: 76–85, July 2017a. doi: 10.1016/j.astropartphys.2017.05.001.

T. Hassan, A. Dominguez, J. Lefaucheur, D. Mazin, S. Pita, A. Zech, and C. Consortium. Extragalactic source population studies at very high energies in the Cherenkov Telescope Array era. In *35th International Cosmic Ray Conference (ICRC2017)*, volume 301 of *International Cosmic Ray Conference*, page 632, Jan. 2017b.

E. Hatziminaoglou, A. Siemiginowska, and M. Elvis. Accretion Disk Instabilities, Cold Dark Matter Models, and Their Role in Quasar Evolution. , 547(1):90–98, Jan. 2001. doi: 10.1086/318325.

G. S. Hawkins. Expansion of the Universe. , 194(4828):563–564, May 1962. doi: 10.1038/194563a0.

M. Hayashida, Ł. Stawarz, C. C. Cheung, K. Bechtol, G. M. Madejski, M. Ajello, F. Massaro, I. V. Moskalenko, A. Strong, and L. Tibaldo. Discovery of GeV Emission from the Circinus Galaxy with the Fermi Large Area Telescope. , 779(2):131, Dec. 2013. doi: 10.1088/0004-637X/779/2/131.

M. Hayashida, K. Nalewajko, G. M. Madejski, M. Sikora, R. Itoh, M. Ajello, R. D. Blandford, S. Buson, J. Chiang, Y. Fukazawa, A. K. Furniss, C. M. Urry, I. Hasan, F. A. Harrison, D. M. Alexand er, M. Baloković, D. Barret, S. E. Boggs, F. E. Christensen, W. W. Craig, K. Forster, P. Giommi, B. Grefenstette, C. Hailey, A. Hornstrup, T. Kitaguchi, J. E. Koglin, K. K. Madsen, P. H. Mao, H. Miyasaka, K. Mori, M. Perri, M. J. Pivovaroff, S. Puccetti, V. Rana, D. Stern, G. Tagliaferri, N. J. Westergaard, W. W. Zhang, A. Zoglauer, M. A. Gurwell, M. Uemura, H. Akitaya, K. S. Kawabata, K. Kawaguchi, Y. Kanda, Y. Moritani, K. Takaki, T. Ui, M. Yoshida, A. Agarwal, and A. C. Gupta. Rapid Variability of Blazar 3C 279 during Flaring States in 2013-2014 with Joint Fermi-LAT, NuSTAR, Swift, and Ground-Based Multiwavelength Observations. , 807(1):79, July 2015. doi: 10.1088/0004-637X/807/1/79.

C. Hazard, M. B. Mackey, and A. J. Shimmins. Investigation of the Radio Source 3C 273 By The Method of Lunar Occultations. , 197(4872):1037–1039, Mar. 1963. doi: 10.1038/1971037a0.

W. Heitler. *Quantum theory of radiation*. 1954.

HESS Collaboration, A. Abramowski, F. Aharonian, F. A. Benkhali, A. G. Akhperjanian, E. O. Angüner, M. Backes, A. Balzer, Y. Becherini, J. B. Tjus, D. Berge, S. Bernhard, K. Bernlöhr, E. Birsin, R. Blackwell, M. Böttcher, C. Boisson, J. Bolmont, P. Bordas, J. Bregeon, F. Brun, P. Brun, M. Bryan, T. Bulik, J. Carr, S. Casanova, N. Chakraborty, R. Chalme-Calvet, R. C. G. Chaves, A. Chen, M. Chrétien, S. Colafrancesco, G. Cologna, J. Conrad, C. Couturier, Y. Cui, I. D. Davids, B. Degrange, C. Deil, P. Dewilt, A. Djannati-Ataï, W. Domainko, A. Donath, L. O. Drury, G. Dubus, K. Dutson, J. Dyks, M. Dyrda,

T. Edwards, K. Egberts, P. Eger, J. P. Ernenwein, P. Espigat, C. Farnier, S. Fegan, F. Feinstein, M. V. Fernandes, D. Fernand ez, A. Fiasson, G. Fontaine, A. Förster, M. Füßling, S. Gabici, M. Gajdus, Y. A. Gallant, T. Garrigoux, G. Giavitto, B. Giebels, J. F. Glicenstein, D. Gottschall, A. Goyal, M. H. Grondin, M. Grudzińska, D. Hadasch, S. Häffner, J. Hahn, J. Hawkes, G. Heinzelmann, G. Henri, G. Hermann, O. Hervet, A. Hillert, J. A. Hinton, W. Hofmann, P. Hofverberg, C. Hoischen, M. Holler, D. Horns, A. Ivascenko, A. Jacholkowska, M. Jamrozy, M. Janiak, F. Jankowsky, I. Jung-Richardt, M. A. Kastendieck, K. Katarzyński, U. Katz, D. Kerszberg, B. Khélifi, M. Kieffer, S. Klepser, D. Klochkov, W. Kluźniak, D. Kolitzus, N. Komin, K. Kosack, S. Krakau, F. Krayzel, P. P. Krüger, H. Laffon, G. Lamanna, J. Lau, J. Lefaucheur, V. Lefranc, A. Lemiére, M. Lemoine-Goumard, J. P. Lenain, T. Lohse, A. Lopatin, C. C. Lu, R. Lui, V. Marand on, A. Marcowith, C. Mariaud, R. Marx, G. Maurin, N. Maxted, M. Mayer, P. J. Meintjes, U. Menzler, M. Meyer, A. M. W. Mitchell, R. Moderski, M. Mohamed, K. Morå, E. Moulin, T. Murach, M. de Naurois, J. Niemiec, L. Oakes, H. Odaka, S. Öttl, S. Ohm, B. Opitz, M. Ostrowski, I. Oya, M. Panter, R. D. Parsons, M. P. Arribas, N. W. Pekeur, G. Pelletier, P. O. Petrucci, B. Peyaud, S. Pita, H. Poon, H. Prokoph, G. Pühlhofer, M. Punch, A. Quirrenbach, S. Raab, I. Reichardt, A. Reimer, O. Reimer, M. Renaud, R. de Los Reyes, F. Rieger, C. Romoli, S. Rosier-Lees, G. Rowell, B. Rudak, C. B. Rulten, V. Sahakian, D. Salek, D. A. Sanchez, A. Santangelo, M. Sasaki, R. Schlickeiser, F. Schüssler, A. Schulz, U. Schwanke, S. Schwemmer, A. S. Seyffert, R. Simoni, H. Sol, F. Spanier, G. Spengler, F. Spies, Ł. Stawarz, R. Steenkamp, C. Stegmann, F. Stinzing, K. Stycz, I. Sushch, J. P. Tavernet, T. Tavernier, A. M. Taylor, R. Terrier, M. Tluczykont, C. Trichard, R. Tuffs, K. Valerius, J. van der Walt, C. van Eldik, B. van Soelen, G. Vasileiadis, J. Veh, C. Venter, A. Viana, P. Vincent, J. Vink, F. Voisin, H. J. Völk, T. Vuillaume, S. J. Wagner, P. Wagner, R. M. Wagner, M. Weidinger, Q. Weitzel, R. White, A. Wierzcholska, P. Willmann, A. Wörnlein, D. Wouters, R. Yang, V. Zabalza, D. Zaborov, M. Zacharias, A. A. Zdziarski, A. Zech, F. Zefi, and N. Żywucka. Acceleration of petaelectronvolt protons in the Galactic Centre. , 531(7595):476–479, Mar. 2016. doi: 10.1038/nature17147.

P. C. Hewett and V. Wild. Improved redshifts for SDSS quasar spectra. , 405(4):2302–2316, July 2010. doi: 10.1111/j.1365-2966.2010.16648.x.

A. M. Hillas. Cerenkov Light Images of EAS Produced by Primary Gamma Rays and by Nuclei. In *19th International Cosmic Ray Conference (ICRC19), Volume 3*, volume 3 of *International Cosmic Ray Conference*, page 445, Aug. 1985.

D. W. Hogg. Distance measures in cosmology. *arXiv e-prints*, art. astro-ph/9905116, May 1999.

D. W. Hogg and D. Foreman-Mackey. Data Analysis Recipes: Using Markov Chain Monte Carlo. , 236(1):11, May 2018. doi: 10.3847/1538-4365/aab76e.

J. Holder. Detection of Persistent VHE emission from PKS 1222+216 (4C +21.35) with VERITAS. *The Astronomer's Telegram*, 5981:1, Mar. 2014.

F. Hoyle. On the Nature of the Quasi-stellar Sources. , 209(5025):751–753, Feb. 1966. doi: 10.1038/209751a0.

F. Hoyle and W. A. Fowler. On the nature of strong radio sources. , 125:169, Jan. 1963. doi: 10.1093/mnras/125.2.169.

I. Hughes and T. Hase. *Measurements and their uncertainties: a practical guide to modern error analysis*. Oxford University Press, 2010.

J. D. Hunter. Matplotlib: A 2d graphics environment. *Computing in Science & Engineering*, 9(3):90–95, 2007. doi: 10.1109/MCSE.2007.55.

C. Ilie. Gamma-Ray Polarimetry: A New Window for the Nonthermal Universe. , 131 (1005):111001, Nov. 2019. doi: 10.1088/1538-3873/ab2a3a.

Y. Inoue, Y. T. Tanaka, G. M. Madejski, and A. Domínguez. Upper Bound on the First Star Formation History. , 781(2):L35, Feb. 2014. doi: 10.1088/2041-8205/781/2/L35.

K. G. Jansky. Radio Waves from Outside the Solar System. , 132(3323):66, July 1933. doi: 10.1038/132066a0.

R. C. Jennison and M. K. Das Gupta. Fine Structure of the Extra-terrestrial Radio Source Cygnus I. , 172(4387):996–997, Nov. 1953. doi: 10.1038/172996a0.

S. G. Jorstad, A. P. Marscher, M. L. Lister, A. M. Stirling, T. V. Cawthorne, W. K. Gear, J. L. Gómez, J. A. Stevens, P. S. Smith, J. R. Forster, and E. I. Robson. Polarimetric Observations of 15 Active Galactic Nuclei at High Frequencies: Jet Kinematics from Bimonthly Monitoring with the Very Long Baseline Array. , 130(4):1418–1465, Oct. 2005. doi: 10.1086/444593.

S. G. Jorstad, A. P. Marscher, P. S. Smith, V. M. Larionov, I. Agudo, M. Gurwell, A. E. Wehrle, A. Lähteenmäki, M. G. Nikolashvili, G. D. Schmidt, A. A. Arkharov, D. A. Blinov, K. Blumenthal, C. Casadio, R. A. Chigladze, N. V. Efimova, J. R. Eggen, J. L. Gómez, D. Grupe, V. A. Hagen-Thorn, M. Joshi, G. N. Kimeridze, T. S. Konstantinova, E. N. Kopatskaya, O. M. Kurtanidze, S. O. Kurtanidze, E. G. Larionova, L. V. Larionova, L. A. Sigua, N. R. MacDonald, J. D. Maune, I. M. McHardy, H. R. Miller, S. N. Molina, D. A. Morozova, T. Scott, B. W. Taylor, M. Tornikoski, I. S. Troitsky, C. Thum, G. Walker, K. E. Williamson, S. Sallum, S. Consiglio, and V. Strelnitski. A Tight Connection between Gamma-Ray Outbursts and Parsec-scale Jet Activity in the Quasar 3C 454.3. , 773(2):147, Aug. 2013. doi: 10.1088/0004-637X/773/2/147.

S. G. Jorstad, A. P. Marscher, D. A. Morozova, I. S. Troitsky, I. Agudo, C. Casadio, A. Foord, J. L. Gómez, N. R. MacDonald, S. N. Molina, A. Lähteenmäki, J. Tammi, and M. Tornikoski. Kinematics of Parsec-scale Jets of Gamma-Ray Blazars at 43 GHz within the VLBA-BU-BLAZAR Program. , 846(2):98, Sept. 2017. doi: 10.3847/1538-4357/aa8407.

M. Kadler, F. Krauß, K. Mannheim, R. Ojha, C. Müller, R. Schulz, G. Anton, W. Baumgartner, T. Beuchert, S. Buson, B. Carpenter, T. Eberl, P. G. Edwards, D. Eisenacher Glawion, D. Elsässer, N. Gehrels, C. Gräfe, S. Gulyaev, H. Hase, S. Horiuchi, C. W. James, A. Kappes, A. Kappes, U. Katz, A. Kreikenbohm, M. Kreter, I. Kreykenbohm, M. Langejahn, K. Leiter, E. Litzinger, F. Longo, J. E. J. Lovell, J. McEnery, T. Natusch, C. Phillips, C. Plötz, J. Quick, E. Ros, F. W. Stecker, T. Steinbring, J. Stevens, D. J.

Thompson, J. Trüstedt, A. K. Tzioumis, S. Weston, J. Wilms, and J. A. Zensus. Coincidence of a high-fluence blazar outburst with a PeV-energy neutrino event. *Nature Physics*, 12(8):807–814, Aug. 2016. doi: 10.1038/nphys3715.

S. Kaspi, P. S. Smith, D. Maoz, H. Netzer, and B. T. Jannuzi. Measurement of the Broad Line Region Size in Two Bright Quasars. , 471:L75, Nov. 1996. doi: 10.1086/310339.

R. C. Keenan, A. J. Barger, L. L. Cowie, and W. H. Wang. The Resolved Near-infrared Extragalactic Background. , 723(1):40–46, Nov. 2010. doi: 10.1088/0004-637X/723/1/40.

E. Y. Khachikian and D. W. Weedman. An atlas of Seyfert galaxies. , 192:581–589, Sept. 1974. doi: 10.1086/153093.

J. Knödlseder, P. Jean, V. Lonjou, G. Weidenspointner, N. Guessoum, W. Gillard, G. Skinner, P. von Ballmoos, G. Vedrenne, J. P. Roques, S. Schanne, B. Teegarden, V. Schönfelder, and C. Winkler. The all-sky distribution of 511 keV electron-positron annihilation emission. , 441(2):513–532, Oct. 2005. doi: 10.1051/0004-6361:20042063.

J. Knödlseder, M. Mayer, C. Deil, J. B. Cayrou, E. Owen, N. Kelley-Hoskins, C. C. Lu, R. Buehler, F. Forest, T. Louge, H. Siejkowski, K. Kosack, L. Gerard, A. Schulz, P. Martin, D. Sanchez, S. Ohm, T. Hassan, and S. Brau-Nogué. GammaLib and ctools. A software framework for the analysis of astronomical gamma-ray data. , 593:A1, Aug. 2016. doi: 10.1051/0004-6361/201628822.

E. Komatsu, J. Dunkley, M. R. Nolta, C. L. Bennett, B. Gold, G. Hinshaw, N. Jarosik, D. Larson, M. Limon, L. Page, D. N. Spergel, M. Halpern, R. S. Hill, A. Kogut, S. S. Meyer, G. S. Tucker, J. L. Weiland, E. Wollack, and E. L. Wright. Five-Year Wilkinson Microwave Anisotropy Probe Observations: Cosmological Interpretation. , 180(2):330–376, Feb. 2009. doi: 10.1088/0067-0049/180/2/330.

J. H. Krolik. *Active galactic nuclei : from the central black hole to the galactic environment*. 1999.

J. H. Krolik and M. C. Begelman. Molecular Tori in Seyfert Galaxies: Feeding the Monster and Hiding It. , 329:702, June 1988. doi: 10.1086/166414.

J. P. Lenain, C. Boisson, H. Sol, and K. Katarzyński. A synchrotron self-Compton scenario for the very high energy γ-ray emission of the radiogalaxy M 87. Unifying the TeV emission of blazars and other AGNs? , 478(1):111–120, Jan. 2008. doi: 10.1051/0004-6361:20077995.

F. Lewis, A. Butler, and L. Gilbert. A unified approach to model selection using the likelihood ratio test. *Methods in Ecology and Evolution*, 2(2):155–162, 2011. doi: 10.1111/j.2041-210X.2010.00063.x. URL `https://besjournals.onlinelibrary.wiley.com/doi/abs/10.1111/j.2041-210X.2010.00063.x`.

H. T. Liu and J. M. Bai. Absorption of 10-200 GeV Gamma Rays by Radiation from Broad-Line Regions in Blazars. , 653(2):1089–1097, Dec 2006. doi: 10.1086/509097.

H. T. Liu, J. M. Bai, and L. Ma. Absorption of 10 GeV-1 TeV Gamma Rays by Radiation from the Broad-Line Region in 3C 279. , 688(1):148–158, Nov. 2008. doi: 10.1086/592039.

M. S. Longair. *High Energy Astrophysics*. 2011.

D. Lynden-Bell. Galactic Nuclei as Collapsed Old Quasars. , 223(5207):690–694, Aug. 1969. doi: 10.1038/223690a0.

N. R. MacDonald, S. G. Jorstad, and A. P. Marscher. "Orphan" γ-Ray Flares and Stationary Sheaths of Blazar Jets. , 850(1):87, Nov. 2017. doi: 10.3847/1538-4357/aa92c8.

P. Madau and L. Pozzetti. Deep galaxy counts, extragalactic background light and the stellar baryon budget. , 312(2):L9–L15, Feb. 2000. doi: 10.1046/j.1365-8711.2000.03268.x.

MAGIC Collaboration, J. Albert, E. Aliu, H. Anderhub, L. A. Antonelli, P. Antoranz, M. Backes, C. Baixeras, J. A. Barrio, H. Bartko, D. Bastieri, J. K. Becker, W. Bednarek, K. Berger, E. Bernardini, C. Bigongiari, A. Biland, R. K. Bock, G. Bonnoli, P. Bordas, V. Bosch-Ramon, T. Bretz, I. Britvitch, M. Camara, E. Carmona, A. Chilingarian,

S. Commichau, J. L. Contreras, J. Cortina, M. T. Costado, S. Covino, V. Curtef, F. Dazzi, A. De Angelis, E. de Cea del Pozo, R. de los Reyes, B. De Lotto, M. De Maria, F. De Sabata, C. Delgado Mendez, A. Dominguez, D. Dorner, M. Doro, M. Errando, M. Fagiolini, D. Ferenc, E. Fernández, R. Firpo, M. V. Fonseca, L. Font, N. Galante, R. J. García López, M. Garczarczyk, M. Gaug, F. Goebel, M. Hayashida, A. Herrero, D. Höhne, J. Hose, C. C. Hsu, S. Huber, T. Jogler, T. M. Kneiske, D. Kranich, A. La Barbera, A. Laille, E. Leonardo, E. Lindfors, S. Lombardi, F. Longo, M. López, E. Lorenz, P. Majumdar, G. Maneva, N. Mankuzhiyil, K. Mannheim, L. Maraschi, M. Mariotti, M. Martínez, D. Mazin, M. Meucci, M. Meyer, J. M. Miranda, R. Mirzoyan, S. Mizobuchi, M. Moles, A. Moralejo, D. Nieto, K. Nilsson, J. Ninkovic, N. Otte, I. Oya, M. Panniello, R. Paoletti, J. M. Paredes, M. Pasanen, D. Pascoli, F. Pauss, R. G. Pegna, M. A. Perez-Torres, M. Persic, L. Peruzzo, A. Piccioli, F. Prada, E. Prandini, N. Puchades, A. Raymers, W. Rhode, M. Ribó, J. Rico, M. Rissi, A. Robert, S. Rügamer, A. Saggion, T. Y. Saito, M. Salvati, M. Sanchez-Conde, P. Sartori, K. Satalecka, V. Scalzotto, V. Scapin, R. Schmitt, T. Schweizer, M. Shayduk, K. Shinozaki, S. N. Shore, N. Sidro, A. Sierpowska-Bartosik, A. Sillanpää, D. Sobczynska, F. Spanier, A. Stamerra, L. S. Stark, L. Takalo, F. Tavecchio, P. Temnikov, D. Tescaro, M. Teshima, M. Tluczykont, D. F. Torres, N. Turini, H. Vankov, A. Venturini, V. Vitale, R. M. Wagner, W. Wittek, V. Zabalza, F. Zandanel, R. Zanin, and J. Zapatero. Very-High-Energy gamma rays from a Distant Quasar: How Transparent Is the Universe? *Science*, 320(5884):1752, June 2008. doi: 10.1126/science.1157087.

K. Mannheim. The proton blazar. , 269:67–76, Mar. 1993.

M. J. M. Marchã and A. Caccianiga. The CLASS BL Lac sample: the radio luminosity function. , 430(3):2464–2475, Apr. 2013. doi: 10.1093/mnras/stt065.

A. P. Marscher and W. K. Gear. Models for high-frequency radio outbursts in extragalactic sources, with application to the early 1983 millimeter-to-infrared flare of 3C 273. , 298: 114–127, Nov. 1985. doi: 10.1086/163592.

A. P. Marscher, S. G. Jorstad, V. M. Larionov, M. F. Aller, H. D. Aller, A. Lähteenmäki,

I. Agudo, P. S. Smith, M. Gurwell, V. A. Hagen-Thorn, T. S. Konstantinova, E. G. Larionova, L. V. Larionova, D. A. Melnichuk, D. A. Blinov, E. N. Kopatskaya, I. S. Troitsky, M. Tornikoski, T. Hovatta, G. D. Schmidt, F. D. D'Arcangelo, D. Bhattarai, B. Taylor, A. R. Olmstead, E. Manne-Nicholas, M. Roca-Sogorb, J. L. Gómez, I. M. McHardy, O. Kurtanidze, M. G. Nikolashvili, G. N. Kimeridze, and L. A. Sigua. Probing the Inner Jet of the Quasar PKS 1510-089 with Multi-Waveband Monitoring During Strong Gamma-Ray Activity. , 710(2):L126–L131, Feb. 2010. doi: 10.1088/2041-8205/710/2/L126.

H. L. Marshall, H. Tananbaum, Y. Avni, and G. Zamorani. Analysis of complete quasar samples to obtain parameters of luminosity and evolution functions. , 269:35–41, June 1983. doi: 10.1086/161016.

P. Marziani, J. W. Sulentic, D. Dultzin-Hacyan, M. Calvani, and M. Moles. Comparative Analysis of the High- and Low-Ionization Lines in the Broad-Line Region of Active Galactic Nuclei. , 104:37, May 1996. doi: 10.1086/192291.

J. Matthews. A Heitler model of extensive air showers. *Astroparticle Physics*, 22(5-6): 387–397, Jan. 2005. doi: 10.1016/j.astropartphys.2004.09.003.

T. A. Matthews and A. R. Sandage. Optical Identification of 3C 48, 3C 196, and 3C 286 with Stellar Objects. , 138:30, July 1963. doi: 10.1086/147615.

J. R. Mattox, D. L. Bertsch, J. Chiang, B. L. Dingus, S. W. Digel, J. A. Esposito, J. M. Fierro, R. C. Hartman, S. D. Hunter, G. Kanbach, D. A. Kniffen, Y. C. Lin, D. J. Macomb, H. A. Mayer-Hasselwander, P. F. Michelson, C. von Montigny, R. Mukherjee, P. L. Nolan, P. V. Ramanamurthy, E. Schneid, P. Sreekumar, D. J. Thompson, and T. D. Willis. The Likelihood Analysis of EGRET Data. , 461:396, Apr. 1996. doi: 10.1086/177068.

W. Max-Moerbeck, T. Hovatta, J. L. Richards, O. G. King, T. J. Pearson, A. C. S. Readhead, R. Reeves, M. C. Shepherd, M. A. Stevenson, E. Angelakis, L. Fuhrmann, K. J. B. Grainge, V. Pavlidou, R. W. Romani, and J. A. Zensus. Time correlation between

the radio and gamma-ray activity in blazars and the production site of the gamma-ray emission. , 445(1):428–436, Nov. 2014a. doi: 10.1093/mnras/stu1749.

W. Max-Moerbeck, J. L. Richards, T. Hovatta, V. Pavlidou, T. J. Pearson, and A. C. S. Readhead. A method for the estimation of the significance of cross-correlations in unevenly sampled red-noise time series. , 445(1):437–459, Nov. 2014b. doi: 10.1093/mnras/stu1707.

H. A. Mayer-Hasselwander, R. Buccheri, G. Kanbach, K. Bennett, G. G. Lichti, G. F. Bignami, N. Damico, W. Hermsen, F. Lebrun, and J. L. Masnou. COS-B observation of the Milky Way in high-energy gamma rays. In *Ninth Texas Symposium on Relativistic Astrophysics*, volume 336, pages 211–222, Feb. 1980. doi: 10.1111/j.1749-6632.1980.tb15931.x.

D. Mazin and M. Raue. New limits on the density of the extragalactic background light in the optical to the far infrared from the spectra of all known TeV blazars. , 471(2):439–452, Aug. 2007. doi: 10.1051/0004-6361:20077158.

J. C. McKinney. General relativistic magnetohydrodynamic simulations of the jet formation and large-scale propagation from black hole accretion systems. , 368(4):1561–1582, June 2006. doi: 10.1111/j.1365-2966.2006.10256.x.

C. Meegan, G. Lichti, P. N. Bhat, E. Bissaldi, M. S. Briggs, V. Connaughton, R. Diehl, G. Fishman, J. Greiner, A. S. Hoover, A. e. J. van der Horst, A. von Kienlin, R. M. Kippen, C. Kouveliotou, S. McBreen, W. S. Paciesas, R. Preece, H. Steinle, M. S. Wallace, R. B. Wilson, and C. Wilson-Hodge. The Fermi Gamma-ray Burst Monitor. , 702(1):791–804, Sept. 2009. doi: 10.1088/0004-637X/702/1/791.

A. Merloni. The anti-hierarchical growth of supermassive black holes. , 353(4):1035–1047, Oct. 2004. doi: 10.1111/j.1365-2966.2004.08147.x.

N. Metropolis, A. W. Rosenbluth, M. N. Rosenbluth, A. H. Teller, and E. Teller. Equation of State Calculations by Fast Computing Machines. , 21(6):1087–1092, June 1953. doi: 10.1063/1.1699114.

M. Meyer, J. D. Scargle, and R. D. Blandford. Characterizing the Gamma-Ray Variability of the Brightest Flat Spectrum Radio Quasars Observed with the Fermi LAT. , 877(1): 39, May 2019. doi: 10.3847/1538-4357/ab1651.

P. Meyer and R. Vogt. Electrons in the Primary Cosmic Radiation. , 6(4):193–196, Feb. 1961. doi: 10.1103/PhysRevLett.6.193.

Y. Mizuno, Z. Younsi, C. M. Fromm, O. Porth, M. De Laurentis, H. Olivares, H. Falcke, M. Kramer, and L. Rezzolla. The current ability to test theories of gravity with black hole shadows. *Nature Astronomy*, 2:585–590, Apr. 2018. doi: 10.1038/s41550-018-0449-5.

T. R. Monroe, J. X. Prochaska, N. Tejos, G. Worseck, J. F. Hennawi, T. Schmidt, J. Tumlinson, and Y. Shen. The UV-bright Quasar Survey (UVQS): DR1. , 152(1):25, July 2016. doi: 10.3847/0004-6256/152/1/25.

P. Morrison. On gamma-ray astronomy. *Il Nuovo Cimento*, 7(6):858–865, Mar. 1958. doi: 10.1007/BF02745590.

M. Mose Mariotti. MAGIC detects a VHE flare from 4C +21.35 (PKS 1222+21). *The Astronomer's Telegram*, 2684:1, June 2010.

K. Murase and J. F. Beacom. Constraining very heavy dark matter using diffuse backgrounds of neutrinos and cascaded gamma rays. , 2012(10):043, Oct. 2012. doi: 10.1088/1475-7516/2012/10/043.

K. Nalewajko. The brightest gamma-ray flares of blazars. , 430(2):1324–1333, Apr. 2013. doi: 10.1093/mnras/sts711.

K. Nalewajko, M. Sikora, G. M. Madejski, K. Exter, A. Szostek, R. Szczerba, M. R. Kidger, and R. Lorente. Herschel PACS and SPIRE Observations of Blazar PKS 1510-089: A Case for Two Blazar Zones. , 760(1):69, Nov. 2012. doi: 10.1088/0004-637X/760/1/69.

R. S. Nemmen, M. Georganopoulos, S. Guiriec, E. T. Meyer, N. Gehrels, and R. M. Sambruna. A Universal Scaling for the Energetics of Relativistic Jets from Black Hole Systems. *Science*, 338(6113):1445, Dec. 2012. doi: 10.1126/science.1227416.

C. Nigro, C. Deil, R. Zanin, T. Hassan, J. King, J. E. Ruiz, L. Saha, R. Terrier, K. Brügge, M. Nöthe, R. Bird, T. T. Y. Lin, J. Aleksić, C. Boisson, J. L. Contreras, A. Donath, L. Jouvin, N. Kelley-Hoskins, B. Khelifi, K. Kosack, J. Rico, and A. Sinha. Towards open and reproducible multi-instrument analysis in gamma-ray astronomy. , 625:A10, May 2019. doi: 10.1051/0004-6361/201834938.

J. B. Oke. Absolute Energy Distribution in the Optical Spectrum of 3C 273. , 197(4872): 1040–1041, Mar. 1963. doi: 10.1038/1971040b0.

D. E. Osterbrock and R. W. Pogge. Optical Spectra of Narrow Emission Line Palomar-Green Galaxies. , 323:108, Dec. 1987. doi: 10.1086/165810.

L. Pacciani, V. Vittorini, M. Tavani, M. T. Fiocchi, S. Vercellone, F. D'Ammando, T. Sakamoto, E. Pian, C. M. Raiteri, M. Villata, M. Sasada, R. Itoh, M. Yamanaka, M. Uemura, E. Striani, D. Fugazza, A. Tiengo, H. A. Krimm, M. C. Stroh, A. D. Falcone, P. A. Curran, A. C. Sadun, A. Lahteenmaki, M. Tornikoski, H. D. Aller, M. F. Aller, C. S. Lin, V. M. Larionov, P. Leto, L. O. Takalo, A. Berdyugin, M. A. Gurwell, A. Bulgarelli, A. W. Chen, I. Donnarumma, A. Giuliani, F. Longo, G. Pucella, A. Argan, G. Barbiellini, P. Caraveo, P. W. Cattaneo, E. Costa, G. De Paris, E. Del Monte, G. Di Cocco, Y. Evangelista, A. Ferrari, M. Feroci, M. Fiorini, F. Fuschino, M. Galli, F. Gianotti, C. Labanti, I. Lapshov, F. Lazzarotto, P. Lipari, M. Marisaldi, S. Mereghetti, E. Morelli, E. Moretti, A. Morselli, A. Pellizzoni, F. Perotti, G. Piano, P. Picozza, M. Pilia, M. Prest, M. Rapisarda, A. Rappoldi, A. Rubini, S. Sabatini, P. Soffitta, M. Trifoglio, A. Trois, E. Vallazza, D. Zanello, S. Colafrancesco, C. Pittori, F. Verrecchia, P. Santolamazza, F. Lucarelli, P. Giommi, and L. Salotti. The 2009 December Gamma-ray Flare of 3C 454.3: The Multifrequency Campaign. , 716(2):L170–L175, June 2010. doi: 10.1088/2041-8205/716/2/L170.

L. Pacciani, F. Tavecchio, I. Donnarumma, A. Stamerra, L. Carrasco, E. Recillas, A. Porras, and M. Uemura. Exploring the Blazar Zone in High-energy Flares of FSRQs. , 790(1): 45, Aug. 2014. doi: 10.1088/0004-637X/790/1/45.

P. Padovani. High energy emission from AGN and unified schemes. In F. Giovannelli and G. Mannocchi, editors, *Vulcano Workshop 1998: Frontier Objects in Astrophysics and Particle Physics*, volume 65, page 159, Jan. 1999.

P. Padovani. The blazar sequence: validity and predictions. , 309(1-4):63–71, June 2007. doi: 10.1007/s10509-007-9455-2.

P. Padovani, P. Giommi, H. Landt, and E. S. Perlman. The Deep X-Ray Radio Blazar Survey. III. Radio Number Counts, Evolutionary Properties, and Luminosity Function of Blazars. , 662(1):182–198, June 2007. doi: 10.1086/516815.

I. Pâris, P. Petitjean, É. Aubourg, N. P. Ross, A. D. Myers, A. Streblyanska, S. Bailey, P. B. Hall, M. A. Strauss, S. F. Anderson, D. Bizyaev, A. Borde, J. Brinkmann, J. Bovy, W. N. Brandt, H. Brewington, J. R. Brownstein, B. A. Cook, G. Ebelke, X. Fan, N. Filiz Ak, H. Finley, A. Font-Ribera, J. Ge, F. Hamann, S. Ho, L. Jiang, K. Kinemuchi, E. Malanushenko, V. Malanushenko, M. Marchante, I. D. McGreer, R. G. McMahon, J. Miralda-Escudé, D. Muna, P. Noterdaeme, D. Oravetz, N. Palanque-Delabrouille, K. Pan, I. Perez-Fournon, M. Pieri, R. Riffel, D. J. Schlegel, D. P. Schneider, A. Simmons, M. Viel, B. A. Weaver, W. M. Wood-Vasey, C. Yèche, and D. G. York. The Sloan Digital Sky Survey quasar catalog: tenth data release. , 563:A54, Mar. 2014. doi: 10.1051/0004-6361/201322691.

G. Paturel, P. Dubois, C. Petit, and F. Woelfel. Comparison LEDA/SIMBAD octobre 2002. Catalogue to be published in 2003. *LEDA*, page 0, Jan. 2002.

A. Pellizzoni, A. Trois, M. Tavani, M. Pilia, A. Giuliani, G. Pucella, P. Esposito, S. Sabatini, G. Piano, A. Argan, G. Barbiellini, A. Bulgarelli, M. Burgay, P. Caraveo, P. W. Cattaneo, A. W. Chen, V. Cocco, T. Contessi, E. Costa, F. D'Ammando, E. Del Monte, G. De Paris, G. Di Cocco, G. Di Persio, I. Donnarumma, Y. Evangelista, M. Feroci, A. Ferrari, M. Fiorini, F. Fuschino, M. Galli, F. Gianotti, A. Hotan, C. Labanti, I. Lapshov, F. Lazzarotto, P. Lipari, F. Longo, M. Marisaldi, M. Mastropietro, S. Mereghetti, E. Moretti, A. Morselli, L. Pacciani, J. Palfreyman, F. Perotti, P. Picozza, C. Pittori, A. Possenti, M. Prest, M. Rapisarda, A. Rappoldi, E. Rossi, A. Rubini, P. Santolamazza,

E. Scalise, P. Soffitta, E. Striani, M. Trifoglio, E. Vallazza, S. Vercellone, F. Verrecchia, V. Vittorini, A. Zambra, D. Zanello, P. Giommi, S. Colafrancesco, A. Antonelli, L. Salotti, N. D'Amico, and G. F. Bignami. Detection of Gamma-Ray Emission from the Vela Pulsar Wind Nebula with AGILE. *Science*, 327(5966):663, Feb. 2010. doi: 10.1126/science.1183844.

W. Pence, J. K. Blackburn, and E. Greene. FTOOLS—A FITS Utility Package for Multiple Environments. In R. J. Hanisch, R. J. V. Brissenden, and J. Barnes, editors, *Astronomical Data Analysis Software and Systems II*, volume 52 of *Astronomical Society of the Pacific Conference Series*, page 541, Jan. 1993.

B. M. Peterson. *An Introduction to Active Galactic Nuclei*. Cambridge University Press, 1997. doi: 10.1017/CBO9781139170901.

B. M. Peterson. *The Broad-Line Region in Active Galactic Nuclei*, volume 693, page 77. 2006. doi: 10.1007/3-540-34621-X_3.

D. Petry, V. Beckmann, H. Halloin, and A. Strong. Soft gamma-ray sources detected by INTEGRAL. , 507(1):549–571, Nov. 2009. doi: 10.1051/0004-6361/200912844.

B. G. Piner and P. G. Edwards. Multi-epoch VLBA Imaging of 20 New TeV Blazars: Apparent Jet Speeds. , 853(1):68, Jan. 2018. doi: 10.3847/1538-4357/aaa425.

B. G. Piner, M. Mahmud, A. L. Fey, and K. Gospodinova. Relativistic Jets in the Radio Reference Frame Image Database. I. Apparent Speeds from the First 5 Years of Data. , 133(5):2357–2388, May 2007. doi: 10.1086/514812.

W. J. Potter and G. Cotter. Synchrotron and inverse-Compton emission from blazar jets - III. Compton-dominant blazars. , 431(2):1840–1852, May 2013. doi: 10.1093/mnras/stt300.

J. Poutanen and B. Stern. GeV Breaks in Blazars as a Result of Gamma-ray Absorption Within the Broad-line Region. , 717(2):L118–L121, July 2010. doi: 10.1088/2041-8205/717/2/L118.

M. Punch, C. W. Akerlof, M. F. Cawley, M. Chantell, D. J. Fegan, S. Fennell, J. A. Gaidos, J. Hagan, A. M. Hillas, Y. Jiang, A. D. Kerrick, R. C. Lamb, M. A. Lawrence, D. A. Lewis, D. I. Meyer, G. Mohanty, K. S. O'Flaherty, P. T. Reynolds, A. C. Rovero, M. S. Schubnell, G. Sembroski, T. C. Weekes, T. Whitaker, and C. Wilson. Detection of TeV photons from the active galaxy Markarian 421. , 358(6386):477–478, Aug. 1992. doi: 10.1038/358477a0.

B. Rani, S. G. Jorstad, A. P. Marscher, I. Agudo, K. V. Sokolovsky, V. M. Larionov, P. Smith, D. A. Mosunova, G. A. Borman, T. S. Grishina, E. N. Kopatskaya, A. A. Mokrushina, D. A. Morozova, S. S. Savchenko, Y. V. Troitskaya, I. S. Troitsky, C. Thum, S. N. Molina, and C. Casadio. Exploring the Connection between Parsec-scale Jet Activity and Broadband Outbursts in 3C 279. , 858(2):80, May 2018. doi: 10.3847/1538-4357/aab785.

G. Reber. Cosmic Static. , 100:279, Nov. 1944. doi: 10.1086/144668.

M. J. Rees. Appearance of Relativistically Expanding Radio Sources. , 211(5048):468–470, July 1966. doi: 10.1038/211468a0.

M. J. Rees. Black Hole Models for Active Galactic Nuclei. , 22:471–506, Jan. 1984. doi: 10.1146/annurev.aa.22.090184.002351.

E. Resconi, D. Franco, A. Gross, L. Costamante, and E. Flaccomio. The classification of flaring states of blazars. , 502(2):499–504, Aug. 2009. doi: 10.1051/0004-6361/200911770.

C. S. Reynolds. Observing black holes spin. *Nature Astronomy*, 3:41–47, Jan. 2019. doi: 10.1038/s41550-018-0665-z.

M. M. Reynoso, M. C. Medina, and G. E. Romero. A lepto-hadronic model for high-energy emission from FR I radiogalaxies. , 531:A30, July 2011. doi: 10.1051/0004-6361/201014998.

P. Romano, S. Vercellone, L. Foschini, F. Tavecchio, M. Landoni, and J. Knödlseder. Prospects for gamma-ray observations of narrow-line Seyfert 1 galaxies with the Cherenkov Telescope Array. , 481(4):5046–5061, Dec. 2018. doi: 10.1093/mnras/sty2484.

G. E. Romero, D. F. Torres, M. M. Kaufman Bernadó, and I. F. Mirabel. Hadronic gamma-ray emission from windy microquasars. , 410:L1–L4, Oct. 2003. doi: 10.1051/0004-6361:20031314-1.

G. E. Romero, M. Boettcher, S. Markoff, and F. Tavecchio. Relativistic Jets in Active Galactic Nuclei and Microquasars. , 207(1-4):5–61, July 2017. doi: 10.1007/s11214-016-0328-2.

M. Ryle and F. G. Smith. A New Intense Source of Radio-Frequency Radiation in the Constellation of Cassiopeia. , 162(4116):462–463, Sept. 1948. doi: 10.1038/162462a0.

M. Ryle, F. G. Smith, and B. Elsmore. A preliminary survey of the radio stars in the Northern Hemisphere. , 110:508, Jan. 1950. doi: 10.1093/mnras/110.6.508.

N. Sahakyan. Investigation of the γ-ray spectrum of CTA 102 during the exceptional flaring state in 2016-2017. , 635:A25, Mar. 2020. doi: 10.1051/0004-6361/201936715.

S. Saito, Ł. Stawarz, Y. T. Tanaka, T. Takahashi, G. Madejski, and F. D'Ammando. Very Rapid High-amplitude Gamma-Ray Variability in Luminous Blazar PKS 1510-089 Studied with Fermi-LAT. , 766(1):L11, Mar. 2013. doi: 10.1088/2041-8205/766/1/L11.

E. E. Salpeter. Accretion of Interstellar Matter by Massive Objects. , 140:796–800, Aug. 1964. doi: 10.1086/147973.

A. Sandage and G. A. Tammann. Steps toward the Hubble constant. V. The Hubble constant from nearby galaxies and the regularity of the local velocity field. , 196:313–328, Mar. 1975. doi: 10.1086/153413.

J. D. Scargle, J. P. Norris, B. Jackson, and J. Chiang. Studies in Astronomical Time Series Analysis. VI. Bayesian Block Representations. , 764(2):167, Feb. 2013. doi: 10.1088/0004-637X/764/2/167.

P. Schechter. An analytic expression for the luminosity function for galaxies. , 203: 297–306, Jan. 1976. doi: 10.1086/154079.

P. A. G. Scheuer and A. C. S. Readhead. Superluminally expanding radio sources and the radio-quiet QSOs. , 277:182–185, Jan. 1979. doi: 10.1038/277182a0.

M. Schmidt. 3C 273 : A Star-Like Object with Large Red-Shift. , 197(4872):1040, Mar. 1963. doi: 10.1038/1971040a0.

M. Schmidt. Space Distribution and Luminosity Functions of Quasi-Stellar Radio Sources. , 151:393, Feb. 1968. doi: 10.1086/149446.

M. Schmidt and R. F. Green. Quasar evolution derived from the Palomar bright quasar survey and other complete quasar surveys. , 269:352–374, June 1983. doi: 10.1086/161048.

V. Schoenfelder. Gamma-Ray Properties of Active Galactic Nuclei. , 92:593, June 1994. doi: 10.1086/192021.

F. Schüssler, M. Seglar-Arroyo, M. Arrieta, M. Böttcher, C. Boisson, M. Cerruti, N. Chakraborty, I. D. Davids, J. Felix, J. P. Lenain, H. Prokoph, D. Sanchez, S. Wagner, M. Zacharias, A. Zech, and H. E. S. S. Collaboration. Target of Opportunity Observations of Blazars with H.E.S.S. In *35th International Cosmic Ray Conference (ICRC2017)*, volume 301 of *International Cosmic Ray Conference*, page 652, Jan. 2017.

C. K. Seyfert. Nuclear Emission in Spiral Nebulae. , 97:28, Jan. 1943. doi: 10.1086/144488.

F. Shankar, M. Bernardi, R. K. Sheth, L. Ferrarese, A. W. Graham, G. Savorgnan, V. Allevato, A. Marconi, R. Läsker, and A. Lapi. Selection bias in dynamically measured supermassive black hole samples: its consequences and the quest for the most fundamental relation. , 460(3):3119–3142, Aug. 2016. doi: 10.1093/mnras/stw678.

A. Shukla and K. Mannheim. Gamma-ray flares from relativistic magnetic reconnection in the jet of the quasar 3C 279. *Nature Communications*, 11:4176, Aug. 2020. doi: 10.1038/s41467-020-17912-z.

A. Shukla, K. Mannheim, S. R. Patel, J. Roy, V. R. Chitnis, D. Dorner, A. R. Rao, G. C. Anupama, and C. Wendel. Short-timescale γ-Ray Variability in CTA 102. , 854(2):L26, Feb. 2018. doi: 10.3847/2041-8213/aaacca.

V. M. Slipher. The spectrum and velocity of the nebula N.G.C. 1068 (M 77). *Lowell Observatory Bulletin*, 3:59–62, Jan. 1917.

F. G. Smith. An Accurate Determination of the Positions of Four Radio Stars. , 168(4274): 555, Sept. 1951. doi: 10.1038/168555a0.

H. J. Smith and D. Hoffleit. Light Variations in the Superluminous Radio Galaxy 3C273. , 198(4881):650–651, May 1963. doi: 10.1038/198650a0.

R. S. Somerville, K. Lee, H. C. Ferguson, J. P. Gardner, L. A. Moustakas, and M. Giavalisco. Cosmic Variance in the Great Observatories Origins Deep Survey. , 600(2):L171–L174, Jan. 2004. doi: 10.1086/378628.

B. E. Stern and J. Poutanen. The Mystery of Spectral Breaks: Lyman Continuum Absorption by Photon-Photon Pair Production in the Fermi GeV Spectra of Bright Blazars. , 794(1):8, Oct. 2014. doi: 10.1088/0004-637X/794/1/8.

M. Stickel, J. W. Fried, and H. Kuehr. Optical spectroscopy of 1 Jy BL Lacertae objects and flat spectrum radio sources. , 80:103–114, Oct. 1989.

E. Striani, F. Verrecchia, I. Donnarumma, S. Vercellone, M. Tavani, A. Bulgarelli, F. Gianotti, M. Trifoglio, A. Chen, A. Giuliani, S. Mereghetti, P. Caraveo, F. Perotti, F. D'Ammand o, E. Del Monte, Y. Evangelista, M. Feroci, F. Lazzarotto, L. Pacciani, P. Soffitta, E. Costa, I. Lapshov, M. Rapisarda, A. Argan, G. Piano, G. Pucella, S. Sabatini, A. Trois, V. Vittorini, F. Fuschino, M. Galli, C. Labanti, M. Marisaldi, G. Di Cocco, A. Pellizzoni, M. Pilia, G. Barbiellini, F. Longo, E. Moretti, E. Vallazza, A. Morselli, P. Picozza, M. Prest, P. Lipari, D. Zanello, P. W. Cattaneo, A. Rappoldi, C. Pittori, F. Lucarelli, P. Santolamazza, S. Colafrancesco, P. Giommi, and L. Salotti. AGILE detection of a gamma-ray flare from the blazar 4C+21.35 (PKS 1222+21). *The Astronomer's Telegram*, 2686:1, June 2010.

B. N. Swanenburg, K. Bennett, G. F. Bignami, R. Buccheri, P. Caraveo, W. Hermsen, G. Kanbach, G. G. Lichti, J. L. Masnou, H. A. Mayer-Hasselwander, J. A. Paul, B. Sacco, L. Scarsi, and R. D. Wills. Second COS-B catalogue of high-energy gamma-ray sources. , 243:L69–L73, Jan. 1981. doi: 10.1086/183445.

I. Tamm and I. Frank. Coherent radiation of fast electrons in a medium. In *Dokl. Akad. Nauk SSSR*, volume 14, pages 107–112, 1937.

Y. T. Tanaka, Ł. Stawarz, D. J. Thompson, F. D'Ammand o, S. J. Fegan, B. Lott, D. L. Wood, C. C. Cheung, J. Finke, S. Buson, L. Escande, S. Saito, M. Ohno, T. Takahashi, D. Donato, J. Chiang, M. Giroletti, F. K. Schinzel, G. Iafrate, F. Longo, and S. Ciprini. Fermi Large Area Telescope Detection of Bright γ-Ray Outbursts from the Peculiar Quasar 4C +21.35. , 733(1):19, May 2011. doi: 10.1088/0004-637X/733/1/19.

F. Tavecchio, G. Ghisellini, G. Bonnoli, and G. Ghirland a. Constraining the location of the emitting region in Fermi blazars through rapid γ-ray variability. , 405(1):L94–L98, June 2010. doi: 10.1111/j.1745-3933.2010.00867.x.

F. Tavecchio, J. Becerra-Gonzalez, G. Ghisellini, A. Stamerra, G. Bonnoli, L. Foschini, and L. Maraschi. On the origin of the γ-ray emission from the flaring blazar PKS 1222+216. , 534:A86, Oct. 2011. doi: 10.1051/0004-6361/201117204.

F. Tavecchio, M. Roncadelli, G. Galanti, and G. Bonnoli. Evidence for an axion-like particle from PKS 1222+216? , 86(8):085036, Oct. 2012. doi: 10.1103/PhysRevD.86.085036.

F. Tavecchio, L. Pacciani, I. Donnarumma, A. Stamerra, J. Isler, E. MacPherson, and C. M. Urry. The far emission region of the γ-ray blazar PKS B1424-418. , 435:L24–L28, Aug. 2013. doi: 10.1093/mnrasl/slt087.

P. Teerikorpi. A note on the velocity-distance relationship for nearby galaxies and galaxy groups. *The Observatory*, 95:105–107, June 1975.

The *Fermi*-LAT collaboration. Fermi Large Area Telescope Fourth Source Catalog. *arXiv e-prints*, art. arXiv:1902.10045, Feb 2019a.

The *Fermi*-LAT collaboration. Galactic Interstellar Emission Model for the 4FGL Catalog Analysis. `https://fermi.gsfc.nasa.gov/ssc/data/analysis/software/aux/4fgl/Galactic_Diffuse_Emission_Model_for_the_4FGL_Catalog_Analysis.pdf`, 2019b. [Online; accessed 14-March-2021].

D. Thompson, G. Djorgovski, and R. de Carvalho. Spectroscopy of radio sources from the parkes 2700 mhz survey. *Publications of the Astronomical Society of the Pacific*, 102: 1235–1240, 10 1990. doi: 10.1086/132758.

H. D. Tran. Hidden Broad-Line Seyfert 2 Galaxies in the CFA and 12 μM Samples. , 554 (1):L19–L23, June 2001. doi: 10.1086/320926.

Y. Ueda, M. Akiyama, K. Ohta, and T. Miyaji. Cosmological Evolution of the Hard X-Ray Active Galactic Nucleus Luminosity Function and the Origin of the Hard X-Ray Background. , 598(2):886–908, Dec. 2003. doi: 10.1086/378940.

M.-H. Ulrich, L. Maraschi, and C. M. Urry. Variability of Active Galactic Nuclei. , 35: 445–502, Jan. 1997. doi: 10.1146/annurev.astro.35.1.445.

C. M. Urry and P. Padovani. Unified Schemes for Radio-Loud Active Galactic Nuclei. , 107:803, Sep 1995. doi: 10.1086/133630.

P. Uttley, R. Edelson, I. M. McHardy, B. M. Peterson, and A. Markowitz. Correlated Long-Term Optical and X-Ray Variations in NGC 5548. , 584(2):L53–L56, Feb. 2003. doi: 10.1086/373887.

T. M. Venters and V. Pavlidou. The Spectral Index Distribution of EGRET Blazars: Prospects for GLAST. , 666(1):128–138, Sept. 2007. doi: 10.1086/519487.

S. Vercellone, A. W. Chen, A. Giuliani, A. Bulgarelli, I. Donnarumma, I. Lapshov, M. Tavani, A. Argan, G. Barbiellini, P. Caraveo, V. Cocco, E. Costa, F. D'Ammando, E. Del Monte, G. De Paris, G. Di Cocco, Y. Evangelista, M. Feroci, M. Fiorini, T. Froysland, F. Fuschino, M. Galli, F. Gianotti, C. Labanti, F. Lazzarotto, P. Lipari, F. Longo, M. Marisaldi, F. Mauri, S. Mereghetti, A. Morselli, L. Pacciani, A. Pellizzoni,

F. Perotti, P. Picozza, M. Prest, G. Pucella, M. Rapisarda, P. Soffitta, M. Trifoglio, A. Trois, E. Vallazza, V. Vittorini, A. Zambra, D. Zanello, C. Pittori, F. Verrecchia, D. Gasparrini, S. Cutini, P. Giommi, L. A. Antonelli, S. Colafrancesco, and L. Salotti. AGILE Detection of a Strong Gamma-Ray Flare from the Blazar 3C 454.3. , 676(1): L13, Mar. 2008. doi: 10.1086/587170.

S. Vercellone, E. Striani, V. Vittorini, I. Donnarumma, L. Pacciani, G. Pucella, M. Tavani, C. M. Raiteri, M. Villata, P. Romano, M. Fiocchi, A. Bazzano, V. Bianchin, C. Ferrigno, L. Maraschi, E. Pian, M. Türler, P. Ubertini, A. Bulgarelli, A. W. Chen, A. Giuliani, F. Longo, G. Barbiellini, M. Cardillo, P. W. Cattaneo, E. Del Monte, Y. Evangelista, M. Feroci, A. Ferrari, F. Fuschino, F. Gianotti, M. Giusti, F. Lazzarotto, A. Pellizzoni, G. Piano, M. Pilia, M. Rapisarda, A. Rappoldi, S. Sabatini, P. Soffitta, M. Trifoglio, A. Trois, P. Giommi, F. Lucarelli, C. Pittori, P. Santolamazza, F. Verrecchia, I. Agudo, H. D. Aller, M. F. Aller, A. A. Arkharov, U. Bach, A. Berdyugin, G. A. Borman, R. Chigladze, Y. S. Efimov, N. V. Efimova, J. L. Gómez, M. A. Gurwell, I. M. McHardy, M. Joshi, G. N. Kimeridze, T. Krajci, O. M. Kurtanidze, S. O. Kurtanidze, V. M. Larionov, E. Lindfors, S. N. Molina, D. A. Morozova, S. V. Nazarov, M. G. Nikolashvili, K. Nilsson, M. Pasanen, R. Reinthal, J. A. Ros, A. C. Sadun, T. Sakamoto, S. Sallum, S. G. Sergeev, R. D. Schwartz, L. A. Sigua, A. Sillanpää, K. V. Sokolovsky, V. Strelnitski, L. Takalo, B. Taylor, and G. Walker. The Brightest Gamma-Ray Flaring Blazar in the Sky: AGILE and Multi-wavelength Observations of 3C 454.3 During 2010 November. , 736(2):L38, Aug. 2011. doi: 10.1088/2041-8205/736/2/L38.

VERITAS Collaboration, V. A. Acciari, E. Aliu, T. Arlen, T. Aune, M. Bautista, M. Beilicke, W. Benbow, D. Boltuch, S. M. Bradbury, J. H. Buckley, V. Bugaev, K. Byrum, A. Cannon, O. Celik, A. Cesarini, Y. C. Chow, L. Ciupik, P. Cogan, P. Colin, W. Cui, R. Dickherber, C. Duke, S. J. Fegan, J. P. Finley, G. Finnegan, P. Fortin, L. Fortson, A. Furniss, N. Galante, D. Gall, K. Gibbs, G. H. Gillanders, S. Godambe, J. Grube, R. Guenette, G. Gyuk, D. Hanna, J. Holder, D. Horan, C. M. Hui, T. B. Humensky, A. Imran, P. Kaaret, N. Karlsson, M. Kertzman, D. Kieda, J. Kildea, A. Konopelko, H. Krawczynski, F. Krennrich, M. J. Lang, S. Lebohec, G. Maier, S. McArthur, A. McCann,

M. McCutcheon, J. Millis, P. Moriarty, R. Mukherjee, T. Nagai, R. A. Ong, A. N. Otte, D. Pandel, J. S. Perkins, F. Pizlo, M. Pohl, J. Quinn, K. Ragan, L. C. Reyes, P. T. Reynolds, E. Roache, H. J. Rose, M. Schroedter, G. H. Sembroski, A. W. Smith, D. Steele, S. P. Swordy, M. Theiling, S. Thibadeau, A. Varlotta, V. V. Vassiliev, S. Vincent, R. G. Wagner, S. P. Wakely, J. E. Ward, T. C. Weekes, A. Weinstein, T. Weisgarber, D. A. Williams, S. Wissel, M. Wood, and B. Zitzer. A connection between star formation activity and cosmic rays in the starburst galaxy M82. , 462(7274):770–772, Dec. 2009. doi: 10.1038/nature08557.

D. W. Weedman. Luminosities of Seyfert galaxies and QSOs. , 208:30–36, Aug. 1976. doi: 10.1086/154577.

T. C. Weekes. *Very high energy gamma-ray astronomy*. 2003.

S. Weinberg. A new light boson? *Phys. Rev. Lett.*, 40:223–226, Jan 1978. doi: 10.1103/PhysRevLett.40.223. URL `https://link.aps.org/doi/10.1103/PhysRevLett.40.223`.

W. F. Welsh. On the Reliability of Cross-Correlation Function Lag Determinations in Active Galactic Nuclei. , 111(765):1347–1366, Nov. 1999. doi: 10.1086/316457.

M. Wood, R. Caputo, E. Charles, M. Di Mauro, J. Magill, J. S. Perkins, and Fermi-LAT Collaboration. Fermipy: An open-source Python package for analysis of Fermi-LAT Data. In *35th International Cosmic Ray Conference (ICRC2017)*, volume 301 of *International Cosmic Ray Conference*, page 824, Jan. 2017.

F. Yusef-Zadeh, J. W. Hewitt, M. Wardle, V. Tatischeff, D. A. Roberts, W. Cotton, H. Uchiyama, M. Nobukawa, T. G. Tsuru, C. Heinke, and M. Royster. Interacting Cosmic Rays with Molecular Clouds: A Bremsstrahlung Origin of Diffuse High-energy Emission from the Inner 2°×1° of the Galactic Center. , 762(1):33, Jan. 2013. doi: 10.1088/0004-637X/762/1/33.

M. Zacharias, M. Böttcher, F. Jankowsky, J. P. Lenain, S. J. Wagner, and A. Wierzcholska. Cloud Ablation by a Relativistic Jet and the Extended Flare in CTA 102 in 2016 and 2017. , 851(2):72, Dec. 2017. doi: 10.3847/1538-4357/aa9bee.

A. A. Zdziarski, P. Pjanka, M. Sikora, and Ł. Stawarz. Jet contributions to the broad-band spectrum of Cyg X-1 in the hard state. , 442(4):3243–3255, Aug. 2014. doi: 10.1093/mnras/stu1009.

Y. B. Zel'dovich and I. D. Novikov. The Radiation of Gravity Waves by Bodies Moving in the Field of a Collapsing Star. *Soviet Physics Doklady*, 9:246, Oct. 1964.

H. Zeng, D. Yan, and L. Zhang. Gamma-ray luminosity function of BL Lac objects. , 441 (2):1760–1768, June 2014. doi: 10.1093/mnras/stu644.

Colophon

This thesis is based on a template developed by Matthew Townson and Andrew Reeves. It was typeset with LaTeX 2_ε. It was created using the *memoir* package, maintained by Lars Madsen, with the *madsen* chapter style. The font used is Latin Modern, derived from fonts designed by Donald E. Knuth.